AVERTISSEMENT

Ce document est le fruit d'un long travail approuvé par le jury de soutenance et mis à disposition de l'ensemble de la communauté universitaire élargie.

Il est soumis à la propriété intellectuelle de l'auteur. Ceci implique une obligation de citation et de référencement lors de l'utilisation de ce document.

D'autre part, toute contrefaçon, plagiat, reproduction illicite encourt une poursuite pénale.

Contact : ddoc-theses-contact@univ-lorraine.fr

LIENS

Code de la Propriété Intellectuelle. articles L 122. 4
Code de la Propriété Intellectuelle. articles L 335.2- L 335.10
http://www.cfcopies.com/V2/leg/leg_droi.php
http://www.culture.gouv.fr/culture/infos-pratiques/droits/protection.htm

École doctorale RP2E-Resources Procédés Produits Environnement
Université de Lorraine
Centre de Recherches Pétrographiques et Géochimiques

Melt-rock interaction signatures in peridotite from sub-continental mantle (French Massif Central): A trace element, H, Li and δ^7Li approach

Signatures des interactions fluide-roche dans le manteau souscontinental (Massif Central Français): Une approche H, Li, δ^7Li, et éléments trace

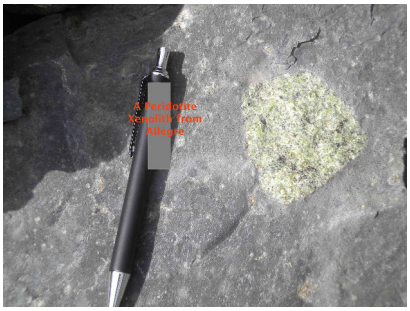

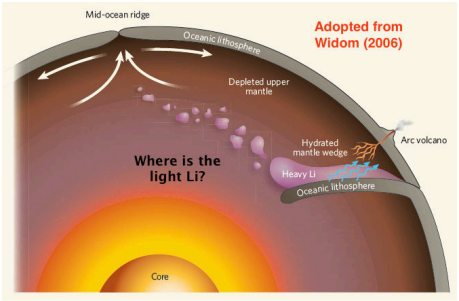

Par

Xiaoyan GU

Thèse présentée pour l'obtention du grade de Docteur en Géosciences
de l'Université de Lorraine
Soutenance publique 3 Juin 2016

Le jury composé de:

Laurie REISBERG	**Directeur de recherche CNRS, CRPG, Nancy**	**Examinateur**
Julien BERGER	**Maître de conférences, Université Paul Sabatier, Toulouse**	**Examinateur**
Sylvie DEMOUCHY	**Chargée de recherché CNRS, Université Montpellieré 2, Montpellier**	**Rapporteur**
Qunke XIA	**Professeur, Université de Zhejiang, Chine**	**Rapporteur**
Etienne DELOULE	**Directeur de recherche CNRS, CRPG, Nancy**	**Directeur**
Jannick INGRIN	**Directeur de recherche CNRS, Université Lille 1, Lille**	**Co-Directeur**

Avant propos

Le manuscrit de ma thèse est rédigé en anglais pour quelques raisons. Mon français n'est pas assez bon pour écrire un long manuscrit et présenter minutieusement tout mon travail au cours de mon PhD dans quatre dernières années. L'anglais sera en effet la seule langue commune de mon jury de thèse, qui comporte notamment un professeur chinois, et l'anglais est la langue internationale reconnue de notre discipline, celles de nos principaux journaux scientifiques, et une thèse rédigée en Anglais sera lisible pour la communauté chinoise, dans la quelle je compte poursuivre ma carrière. Un résumé étendu en français est inclus au manuscript.

Acknowledgement

After more than four years' work, now my thesis comes to the end. Here, my heart overflowed with deepest gratitude to many persons.

Firstly, my research has been financially supported by the INSU SYSTER program and the State Scholarship Fund of China has born my living expenses in France for four years.

I thank the members of the jury that accepted to judge my work, Laurie Reisberg, Christiane Wagner, Julien Berger, Qunke Xia, and Sylvie Demouchy.

I am very grateful to my thesis directors for all their help. Etienne have offered much assistance to make me quickly adapt to a new life style and make my life in France much easier. Thanks to his patient direction in use of the ion probe and studies on Li isotopes, I have almost grasped the essential operation of the ion probe and smoothly completed the part of my thesis concerning on Li isotopes, from measurements to discussions of the results. He has always opened the access to the ion probe whenever I needed. I also want to thank him to help me to obtain a salary from CRPG for the four last months after the scholarship from the Chinese government ended in January 2016. Jannick have given me much help in either life or work when I stayed in Lille for water analysis. It is the discussion with him on the results of water content that deepened my understandings of the water distribution in NAMs. His many directions will greatly benefit to my future career. Another thesis director, Lydéric France, has taught me a lot from the petrographic observations to the understandings on the major and trace element compositions. He has given me great encouragement to continue the work and many directions in writing a paper.

Here, I also would like to express my deep gratitude to Prof. Xia Qunke. From 2008 to 2011, I was in his lab and under his direction I finished the undergraduate thesis and the studies of my master stage in China. From him, I learned too much. And, it is he who introduced me into the field of the geochemical research, encouraged me to start the studies on water content in mantle minerals, and helped me to obtain the opportunity to come to CRPG and continue my research.

In addition, I also thank Christiane Wagner and Michel Grégoire for preliminary preparations for thesis, such as, polishing the thin sections for EMPA, instructing me

how to make typical petrographic observations, and selecting the representative samples for further analysis.

Li Pei, a senior fellow of mine, has helped me a lot to understand Li isotope results and improve Li diffusion modeling. Chen Huan is also thanked for his unselfish aide and allowed me to eat at his home during my staying in Lille in June 2015.

I appreciate Marc Chaussidon, Andrey Gurenko and Johan Villeneuve for direction in the use of SIMS at CRPG. Special gratitude is expressed to Nordine Bouden for not only direction in the use of SIMS but also assistance in guaranteeing the operation of IMS 1270 when I used it.

I also want to thank Olivier Rouer for access to EMP analysis, Marie-Christine Boiron and Chantal Peiffert for help in analyzing trace elements using LA-ICPMS, and Isabelle De Waele for her patient direction and aide when I utilized the FTIR-microscope to analyze the water content in Université Lille 1.

I also can't forget all the colleagues at CRPG whose help has facilitated my life in a foreign country. All of them, especially Evelyn Füri and Camille Soulié, have always been very friendly to me and offered me lots of nice advice, in either life or work.

Without the help from the secretaries, for example, Aurélie Didot at CRPG and Christine Fivet in the college of RP2E, I could not have so easily completed all the administrative formalities in the past four years.

Many friends, who have been accompanied with me in Nancy and made me never feel lonely in the alien land, deserve my deep gratitude. They are, for example, Zhang Xin, Chen Fengwei, Xu Yong and Ye Jing, etc.

Last but never the least, I would like to appreciate my devoted family. My wife have given up the comfortable life in her hometown and been in France to bear the loneliness and the hardships of studying the French. It is her love and companionship that support my persistence to complete this thesis work. The deepest gratitude are expressed to my parents, who has devoted all their love and attention to my elder sister and elder brother, me. Over the past four years I have not returned home once to see them, but they have never complaint against me. Every time I phoned to them, I always heard 'Don't worry about us and we are fine. You need to keep healthy and then work hard'.

Abstract

Melt-rock interactions are capable of modifying the chemical and modal compositions of peridotites and related lithologies, leaving imprints on their chemical properties. Peridotite xenoliths sampled from two volcanoes erupting in different modes in two localities, Allègre and Mont Coupet, in the southern domain of the French Massif Central (FMC), have been investigated to constrain the evolution of the sub-continental lithospheric mantle beneath the FMC and the behaviors of Li and H during melt-rock reactions.

To answer these questions, a set of several representative xenoliths was selected for each locality, and described for their mineralogy and petrography. In-situ measurements were then performed for major and trace elements in Ol, Cpx and Amp when existing, via EPMA and LA-ICP-MS respectively, for Li concentrations and isotopic compositions in pyroxenes and Ol (via SIMS), and water concentrations in minerals (via FTIR and SIMS).

Negative HFSE anomalies and markedly high LREE/HREE ratios reflect a mantle metasomatism by carbonatitic melts/fluids or melts/fluids related to subducting slabs following an earlier partial melting process in the lithospheric mantle under Allègre. The Ti and Nb negative anomalies in Cpx from all the Mont Coupet samples and Zr-Hf negative anomalies in Cpx from two most strongly metasomatized samples MC38 and MC34 also point to a mantle metasomatism. Amp in samples MC36 and MC53, whose origin should be associated with fluids from the subducting slab, have equilibrated most of the trace element composition with coexisting Cpx and the modal metasomatism responsible for the Amp genesis haven't refertilized Cpx in LREE and LILE.

Lithium isotope systematics indicates that Allègre xenoliths were overprinted by (at least) a two-stage metasomatism by melts of different origins. Exceptionally high Li concentrations in Cpx (up to 50 ppm by weight) and slightly increased Li contents at Ol rims are ascribed to a diffusive Li uptake from infiltrating melts derived from the host magma. On the other hand, extremely light Li isotopic compositions preserved in Ol cores (with δ^7Li as low as -25‰) suggest another metasomatic event prior to xenolith entrainment by the host magma. In contrast, xenoliths from Mont Coupet

have Li concentrations in constituent minerals similar to the normal mantle, and display nearly equilibrated inter-mineral Li partitioning and homogeneous intragranular Li distribution in every phase. The negative δ^7Li values of Cpx and Opx in some samples were brought by the exchange with a small-volume melt with Li concentration similar to the normal mantle and light Li isotopic compositions. The preservation of inter-mineral large Li isotopic fractionation currently observed in these samples indicates that the percolation of the melt should occur shortly prior to the entrainment of Mont Coupet peridotite xenoliths by the host magmas. The metasomatic agents, accounting for negative δ^7Li values in Ol cores in Allègre xenoliths and in Cpx and Opx in some Mont Coupet xenoliths, are related to a subduction environment. In the regional framework of the FMC, the subduction event most likely occurred during the Variscan orogeny.

Water content in Allègre xenoliths ranges from 10.6 to 12.4 ppm in weight, much lower than the water content in the MORB source mantle. It implies that water were lost during the degassing of the host magma during slow cooling of the lava lake. No core-rim variations from profile analysis suggest that xenoliths have achieved water diffusive equilibrium with the host magmas. Peridotite xenoliths from Mont Coupet have retained their original water content from the mantle depths. Partial melting has controlled the water content in most samples from Mont Coupet. However, the subsequent metasomatism characterized by LREE enrichment and HFSE negative anomalies has affected the sample MC34, which had the highest water content among the Mont Coupet xenoliths. The aqueous agent responsible for presence of Amp in samples MC36 and MC53 has not lead to the considerable increase of water content.

Résumé de la thèse

Introduction et objectif

Les xénolites de péridotite sont de petits fragments du manteau lithosphérique transportés à la surface de la terre par les basaltes alcalins ou les kimberlites lors des éruptions volcaniques. Ces échantillons peuvent donner un aperçu direct de la composition minéralogique et géochimique du manteau supérieur et des processus géologiques qui se déroulent en profondeur. Comparés aux échantillons des massifs de péridotite mis en place tectoniquement en association avec des ophiolites, qui ont généralement subi des processus de déformation et de recristallisation lors de leur exhumation lente ou leur mise en place, les xénolites ont généralement préservé les structures et signatures originales acquises avant ou au moment de leur entraînement en raison de l'éruption rapide de leurs magmas hôtes à la surface de la terre. Les magmas peuvent capturer des nodules de péridotite à différentes profondeurs au cours de leur remonté et échantillonner la diversité verticale du manteau lithosphérique dans une plus grande gamme de profondeur. Néanmoins, des xénolites de péridotite ont également leurs propres limites pour l'étude du manteau lithosphérique. En raison de la petite taille des xénolites, peu d'informations structurels modales peuvent être extraites sur le terrain ou lors de l'observation macroscopique des échantillons, contrairement aux péridotites des massifs. En outre, durant la montée, les magmas peuvent parfois avoir percoler au sein des xénolites et avoir changer leurs compositions minéralogique et géochimique, ce qui peut brouiller les signatures des agents métasomatiques ayant agi en profondeur. Ainsi, pour l'étude des xénolites, distinguer les processus métasomatiques ayant eu lieu en profondeur de ceux ayant eu lieu lors de la remontée des xénolites est d'une grande importance pour bien comprendre les processus métasomatiques qui ont affecté le manteau lithosphérique.

Des xénolites de péridotite provenant de deux localités du sud du Massif Central Français (Allègre et Mont Coupet), ont été étudiés pour définir l'évolution du manteau sous continentale et pour étudier le comportement de Li et H lors des

réactions fluides-roches pendant leur remonté vers la surface. La carrière de Ringue à Allègre est située dans un lac de lave solidifiée qui a rempli un maar il y a ~ 3 Ma. Les xénolites retrouvés dans ces basaltes devraient donc avoir refroidi lentement. La carrière de Razas Grand à Mont Coupet exploite les retombées d'un ancien volcan avec des éruptions de type stromboliennes, datées de 2 Ma. Les xénolites sont trouvés dans des bombes volcaniques de taille décimétrique, qui ont connu une trempe rapide à l'atmosphère.

A partir de l'étude de quelques dizaines d'échantillons, un ensemble de 6 xénolites représentatifs a été sélectionné pour chaque localité. La description pétrologique et minéralogique de chaque échantillon a été associée à la mesure des compositions chimiques en éléments majeur (par microsonde électronique) et trace (par LA-ICP-MS) des principales phases minéralogiques (Olivine, Pyroxène, Amphibole). La teneur et la composition isotopique du Li ont été mesurées par microsonde ionique (SIMS), et la teneur en eau par spectroscopie infrarouge à transformée de Fourrier (FTIR) et SIMS dans les pyroxènes et les olivines.

Résultat et conclusion

Distribution des éléments trace

Pour les xénolites de peridotite des deux localités, les compositions en éléments majeur et trace des Cpx (clinopyroxène) (Fig. R1) montrent que les xénolites ont subi une étape de fusion partielle et l'extraction de composants basaltiques, qui les ont enrichi en éléments compatibles réfractaires et les ont appauvris en éléments incompatibles. Les taux de fusion calculés à partir des teneurs en éléments trace varient de moins de 1% à 19%, la plupart des valeurs étant inférieur à 10%. La composition en éléments majeurs des cpx de la plupart de ces xénolites se situe dans le domaine de composition défini par Downes et al. (2003) pour les cpx du domaine du sud du Massif Central. Cela montre que les échantillons d'Allègre n'ont pas subi de modification sensible de leur composition en élément majeur malgré leur long temps de séjour dans un lac de lave et les interactions possibles avec le magma hôte.

Seul l'échantillon MC38 montre une composition plus appauvrie, qui est caractéristique habituellement du domaine du Nord du Massif Central.

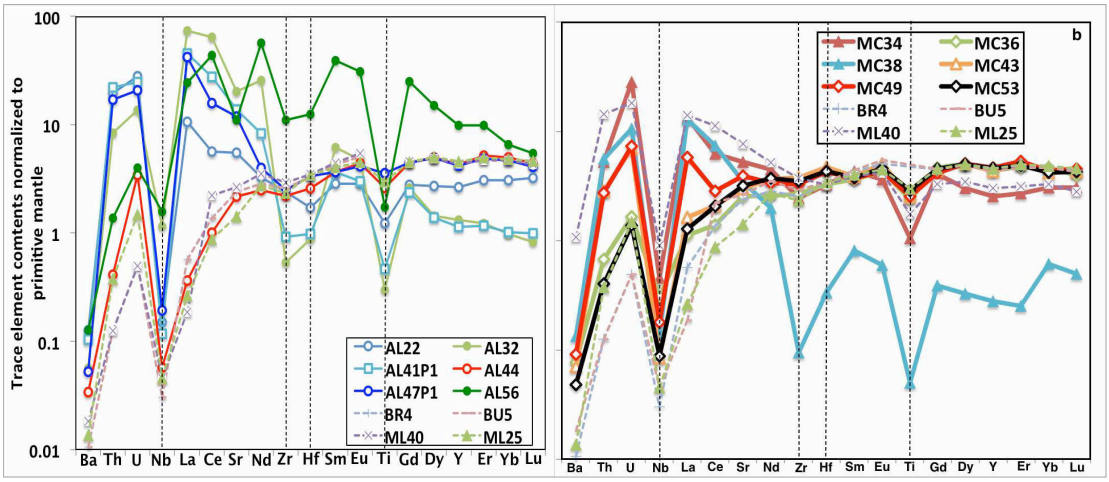

Figure R1: Distribution des teneurs en terres rares et éléments traces normalisées aux chondrites (McDonough and Sun, 1995), mesurées dans les clinopyroxènes des échantillons de Allègre (AL) et de Mont Coupet (MC). Les lignes pointillées représentent pour comparaison 4 échantillons d'autres localités du Sud du Massif Central, (ML40 et ML25 de Touron et al. (2008); BR4 et BU5 de Yoshikawa et al. (2010)).

Pour les xénolites d'Allègre, les anomalies négatives en HFSE (éléments à fort effets de champs) et les rapports LREE/HREE (terres rares légères sur terres rares lourdes) élevés reflètent un métasomatisme lié à des liquides carbonatitiques ou associés aux dalles de subduction (Fig. R2), postérieur au processus de fusion partielle. Pour les échantillons du Mont Coupet, les anomalies négatives en Ti et Nb des Cpx de tous les échantillons et les anomalies négatives de Zr et Hf pour deux échantillons plus fortement métasomatisés (Fig. R1; MC38 et MC34) soulignent également un métasomatisme. Les amphiboles des échantillons MC36 et MC53, dont l'origine doit être associée à des fluides riches en eau libérés par la subduction varisque, sont à l'équilibre avec les Cpx coexistant, ce qui indique que le fluide qui a permis leur formation n'a pas enrichi les Cpx en éléments incompatibles tels que les LREE ou les LILE (Large Ion lithophile Elements).

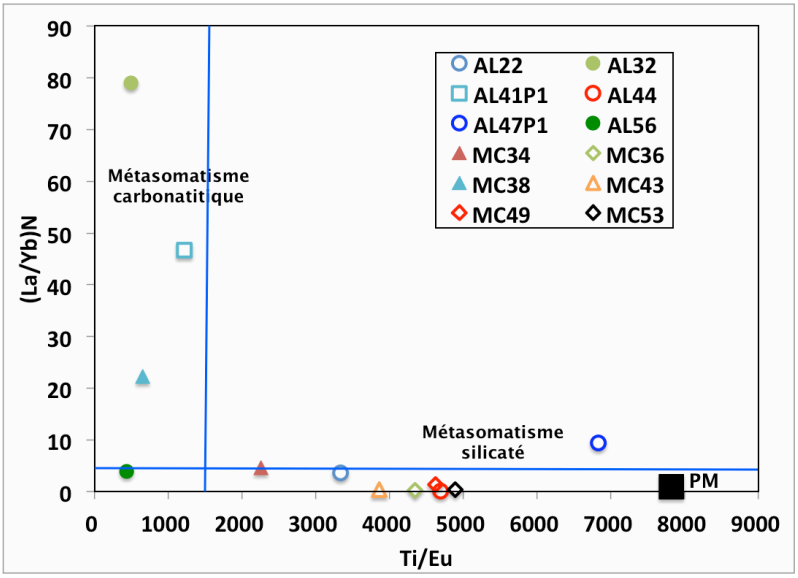

Figure R2 : Variation du rapport $(La/Yb)_N$ en fonction du rapport Ti/Eu dans les Cpx des xénolites de péridotite. La valeur de Ti/Eu du manteau primitif (McDonough et Sun, 1995) est montrée pour comparaison. Coltorti et al. (1999) ont suggéré que la relation entre $(La/Yb)_N$ et Ti/Eu pour les Cpx pourrait être considérée comme un indicateur pour distinguer le métasomatisme silicaté du métasomatisme carbonatitique (les lignes bleues).

Distribution du Lithium

Dans les xénolites d'Allègre, les teneurs en Li varient de 0,9 à 7,7 ppm pour les olivines, de 0,6 à 18,5 ppm pour les Opx (Orthopyroxène), de 3,4 à 49,5 ppm pour les Cpx. Les valeurs de δ^7Li varient de -32 à +15‰ pour les olivines, de -74,7 +30,9‰ pour les Opx et de -11,6 à +23,7‰ pour les Cpx (Fig. R3). Les variations observées à l'échelle du minéral ou entre les différents minéraux pour les teneurs en Li et pour sa composition isotopique suggèrent un métasomatisme en au moins deux étapes par des fluides différents. Les teneurs très élevées en Li des Cpx (par comparaison avec le manteau normal), ainsi que l'augmentation des teneurs en bordure des olivines, sont une conséquence de la diffusion de Li depuis le magma hôte vers les minéraux du xénolites, pendant ou après leur entrainement vers la surface (Fig. R4). En raison de la plus grande vitesse de diffusion du Li dans les Cpx que dans les olivines, la signature des processus métasomatiques ayant eu lieu en profondeur dans le manteau avant l'épisode volcanique ont été effacées dans les grains de Cpx, qui présentent des compositions isotopiques en équilibre avec le magma hôte, avec des δ^7Li positifs. Par contre les compositions isotopiques au coeurs de la plupart des olivines sont négatives

(δ^7L aussi bas que - 25‰; par exemple, les profils de deux grains d'olivine dans Fig. R4), bien en dessous des valeurs habituelles du manteau terrestre (+2 à +5 ‰). Ces signatures négatives sont dues à un apport de Li avec un δ^7Li négative, qui peut être associé au métasomatisme carbonatitique, ou à un fluide métasomatique plus tardif.

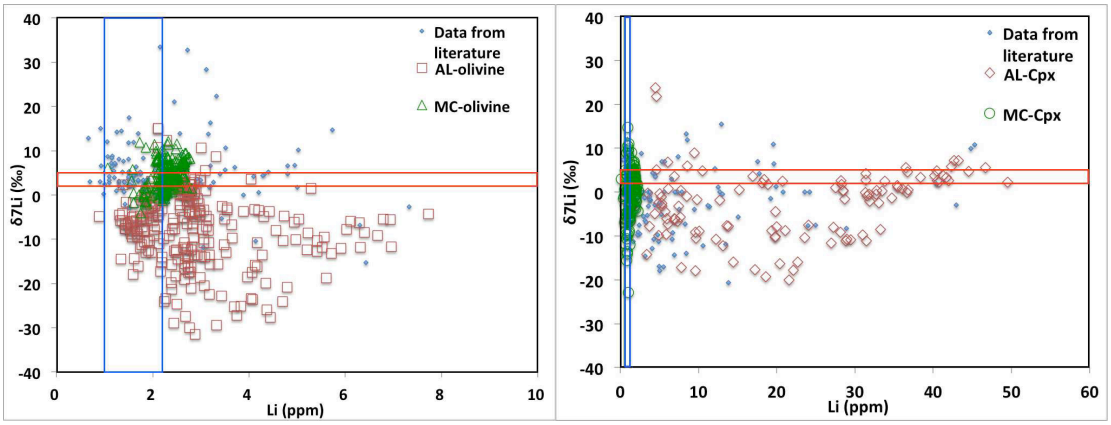

Figure R3 : Variation de δ^7Li contre les teneurs en Li des olivines (a) et des Cpx (b) dans les échantillons d'Allègre (AL) et de Mont Coupet (MC) pour comparaison avec les données de la littérature. Dans chaque parcelle, les valeurs d'Allègre et de Mont Coupet comprennent l'ensemble des données des olivines et des Cpx. La composition isotopique et le teneur du Li du manteau supérieur sont délimitées par des vitres en rouge et en bleu, respectivement.

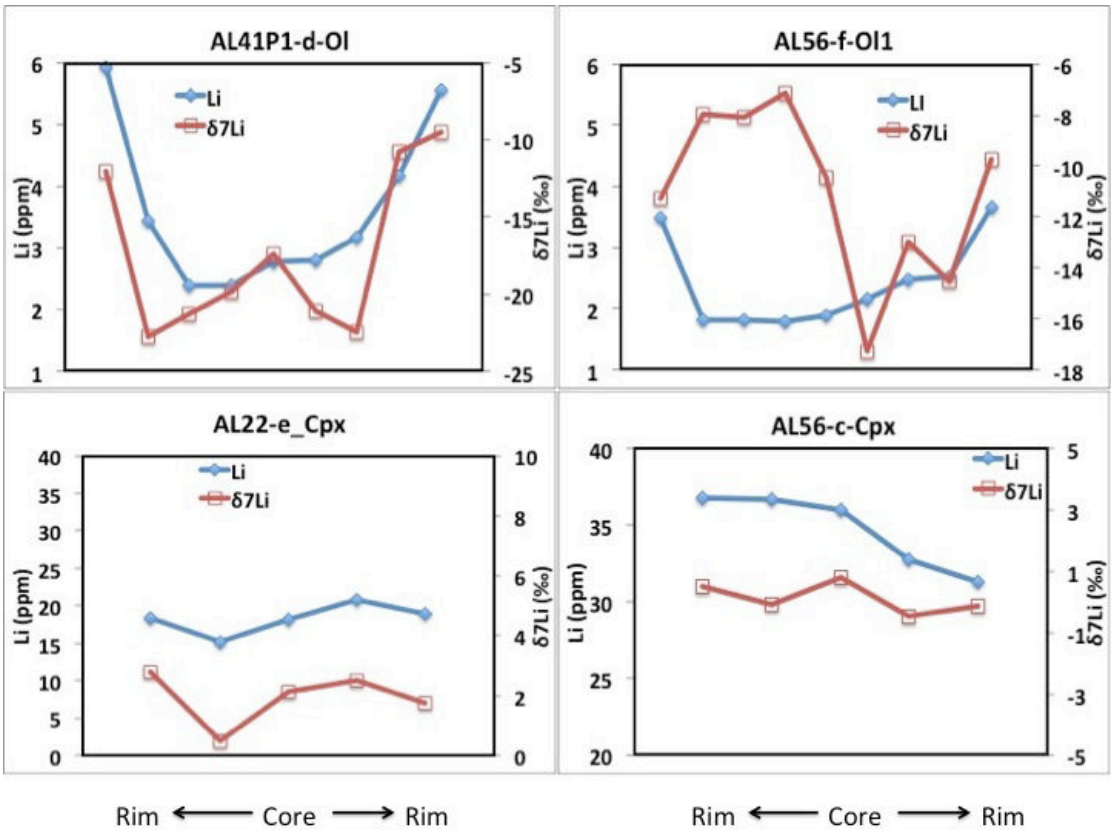

Figure R4 : Profils de variation cœur-bord des teneurs en Li et des δ^7Li des olivines et des Cpx dans les échantillons provenant d'Allègre.

Dans les xénolites de Mont Coupet, les teneurs en Li varient de 1,1 à 2,8 ppm pour les olivines, de 0,5 à 2,0 ppm pour les Opx et de 0,4 à 2,3 ppm pour les Cpx, et les valeurs de δ^7Li de -4.1 à +12,1‰ pour les olivines, -19,9 à +7,6‰ pour les Opx et de -22,9 à +14,7‰ pour les Cpx (Fig. R3). La distribution du Li est donc totalement différente pour le Mont Coupet que pour Allègre (Fig. R3), puisque les minéraux des xénolites de péridotite du Mont Coupet ont des teneurs en Li semblables à celles décrites pour le manteau normal, et montre une distribution à l'équilibre du Li entre les minéraux et une distribution homogène dans les grains de chaque minéral. Cependant des valeurs de δ^7Li négatives sont observées dans quelques grains de Cpx et d'Opx de certains échantillons, ce qui suggèrent une interaction avec un fluide en quantité limitée ayant une composition isotopique du Li négative (Fig. R5). La préservation du fractionnement isotopique du Li entre les pyroxènes et les olivines indique que cette interaction a du avoir lieu peu de temps avant l'entrainement des xénolites vers la surface. Les fluides métasomatiques à l'origine des valeurs de δ^7Li négatives observées à Allègre et à Mont Coupet sont liés à un environnement de subduction, probablement lié à l'orogenèse varisque dans le cadre régional du Massif Central.

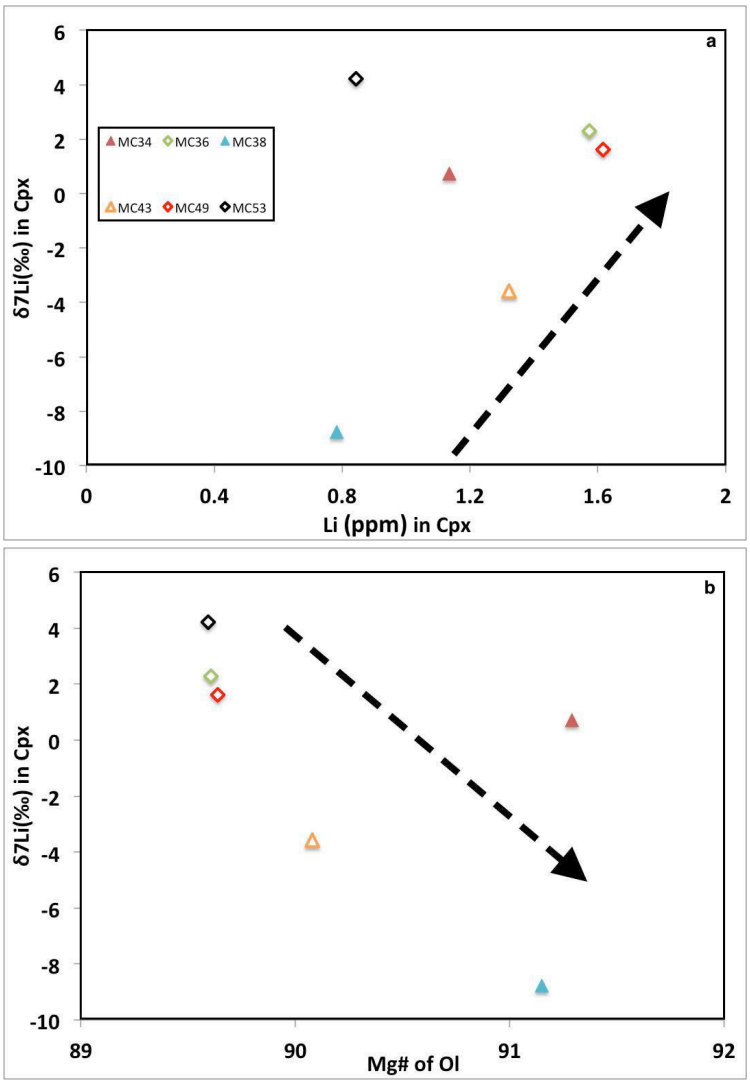

Figure R5: δ^7Li moyenne des Cpx contre les teneurs en Li des Cpx (a) et Mg# des olivines (b) dans les échantillons de Mont Coupet. Dans le graphique a, vers la direction de la ligne pointillée, δ^7Li des Cpx augmentent avec les teneurs en Li, affirmant que l'absorption du Li par diffusion induit la composition isotopique du Li portative. La relation négative entre δ^7Li des Cpx et Mg# des olivines (b) est compatible avec le phénomène que l'harzburgite est sensible à la percolation des fluides.

Distribution de l'eau

Les teneurs en eau des xénolites d'Allègre varient entre 23 et 41 ppm pour les Opx, 112 et 161 ppm pour les Cpx, en considérant les trois échantillons mesurés par FTIR (spectroscopie InfraRouge à Transformées de Fourrier). AL44 est le seul échantillon pour lequel les olivines montrent des bandes d'absorption dans les spectres infrarouges, avec une teneur en eau estimée à 1,4 ppm. Pour les autres échantillons, les teneurs en eau des olivines sont en dessous des seuils de détection. Les teneurs en eau des roches totales pour les échantillons d'Allègre varient de 10,6 à 12,4 ppm, c'est à dire moins que la teneur en eau de la source des MORB. Ceci implique que les xénolites aient perdu leur eau pendant le dégazage du magma hôte durant le refroidissement à basse pression du lac de lave. L'absence de variation cœur-bord

suggère que la distribution de l'eau dans les minéraux a atteint l'équilibre par diffusion entre les xénolites et les magmas hôtes.

Échantillon	t (cm)	Opx			Cpx			Ol					
									Ol Group I_{un}		Ol Group II_{un}		
		n	Intégral (cm-1)	Teneur en eau (ppm)	n	Intégral (cm-1)	Teneur en eau (ppm)	n	Intégral (cm-1)	OH_B (ppm)	Intégral (cm-1)	OH_L (ppm)	Teneur en eau (ppm)
MC34	0.015	21(31)	11.3	152	29(31)	15.2	428	38	0.01	0.4	0.123	1	1.4
MC36	0.016	32(32)	5.6	71	37(37)	12	318	32	0.04	1.4	0.09	0.7	2.1
MC38	0.016	33(40)	2.3	28	7(12)	1.6	41	34	-	-	-	-	
MC43	0.017	29(29)	10.6	126	24(29)	12.2	304	17	0.006	0.2	0.061	0.4	0.6
MC49	0.015	27(28)	9.9	133	29(31)	12.7	358	26	0.01	0.4	0.09	0.7	1.1
MC53	0.016	23(23)	7.3	92	28(28)	15.2	402	29	0.04	1.4	0.075	0.6	2
AL22	0.018	22(23)	3.6	41	14(19)	6.7	161	20	-	-	-	-	
AL41P1	0.016	27(31)	2.6	34	21(24)	4.1	112	26	-	-	-	-	
AL44	0.017	30(33)	1.9	23	29(31)	4.4	113	28	0.04	1.4	-	-	1.4

Table R1 : Les teneurs en eau pour les olivines, les Opx et les Cpx dans les échantillons d'Allègre et de Mont Coupet, calculé par des spectres infrarouges non-polarisés. Les indices "B" et "L" désignent les calculs basés sur les méthodes de Bell et al. (2003) et Libowitzky et Rossman (1997), respectivement.

Les teneurs en eau des xénolites de Mont Coupet varient de 0,6 à 2,1 ppm pour les olivines, de 28 à 152 ppm pour les Opx et de 41 à 428 ppm pour les Cpx, a l'exception de l'échantillon MC38, pour lequel aucune bande d'absorption n'est observée pour les olivines. Les teneurs en eau des roches totales pour les échantillons de Mont Coupet varient de 4,7 à 87,6 ppm. Nous pouvons considérer que ces xénolites ont conservé les teneurs en eau qu'ils avaient à l'équilibre en profondeur dans le manteau, et que ces teneurs étaient contrôlées par le processus de fusion partielle mis en évidence par les éléments traces. Toutefois, les teneurs en eau plus élevées observées pour l'échantillon MC34 peuvent être liées à un apport en eau pendant le métasomatisme du manteau. Enfin il faut noter que les fluides aqueux qui sont responsables de la formation d'amphiboles dans les échantillons MC36 et MC53, n'ont pas entrainé d'augmentation des teneurs en eau des cpx et des olivines de ces deux échantillons.

Conclusions

Les résultats présentés dans ce travail montrent que la mesure rigoureuse in situ des teneurs en Li et de sa compositions isotopique dans les différents minéraux des xénolites de péridotite permettent de distinguer les différents processus métasomatiques qui ont affectés les péridotites avant ou pendant leur remonté à la surface, et de discuter de leur ordre de succession et de leur durée. Ces interprétations

se basent sur les vitesses de diffusion différentes des isotopes du Li dans les différentes phases, notamment les Cpx et les olivines, qui sont donc capable de conserver différemment les signatures des évènements qui les affectent successivement. La distribution de l'hydrogène dans les minéraux du manteau est également influencée par les différents processus se produisant dans le manteau profond ou lors du refroidissement des magmas hôtes. Le lithium et l'hydrogène ayant des vitesses de diffusion différentes, ils seront affectés de façons différentes par l'évolution de leur magma hôte. Ainsi bien que ces deux localités étudiées ici sont toutes les deux situées dans le domaine sud du Massif Central, les signatures des isotopes du Li et de distribution d'eau reflètent les histoires évolutives différentes et compliqués des xénolites provenant d'Allègre et de Mont Coupet.

Table of Contents

Acknowledgement I

Abstract III

Résumé de la thèse V

Table of contents XV

List of figures XIX

List of table XXIII

1. Introduction 1

1.1 The lithospheric mantle 1

1.2 Lithium 4

1.2.1 Geochemical features *4*

1.2.2 The current research state of Li in the lithospheric mantle *6*

1.3 water in the NAMs 8

1.3.1 Water in the earth mantle *8*

1.3.2 The current research state of water in the NAMs *8*

1.4 Objective of this thesis 12

2. Geological background 13

2.1 The pre-Cenozoic tectonic evolution of the FMC 13

2.2 The Cenozoic volcanism in the FMC 14

2.3 The lithospheric mantle beneath the FMC 17

2.4 The sampling localities 18

3. Analytical methods 21

3.1 Sample preparations 21

3.2 Electron micro-probe analysis (EPMA) 21

3.3 Laser ablation inductively coupled plasma mass spectrometry (LA-ICP-MS) 22

3.4 Secondary ion mass spectrometry (SIMS) 22

3.4.1 Basic working principles *22*

3.4.2 Standards for Li isotopes measuring by SIMS *27*

3.4.3 Measuring procedure for Li isotopes by SIMS *27*

3.4.4 Measuring procedure for water content by SIMS *29*

3.5 Fourier transform infrared (FTIR) spectrometer 31

3.5.1 The rationale *31*

3.5.2 Measuring procedure for water content by FTIR *32*

3.5.3 Quantitative calculation procedure *35*

4. Results 41

4.1 Petrological description 41

4.1.1 Mineral proportions and textures *41*

4.1.2 Spongy textures in sample AL47P1 ..... *45*

4.2 Mineral major element compositions 46
4.2.1 Ol *47*
4.2.2 Opx *47*
4.2.3 Cpx *49*
4.2.4 Spl *50*
4.2.5 Amp *50*
4.2.6 AL47P1 ..... *51*
4.3 Trace element compositions 51
4.3.1 Cpx in samples from Allègre *52*
4.3.2 Cpx in samples from Mont Coupet *55*
4.3.3 Amp in samples MC36 and MC53 ..... *57*
4.3.4 Al, Ti, Cr and Ni in Ol from Allègre and Mont Coupet *58*
4.4 Li concentrations and isotopic compositions in minerals 61
4.4.1 Samples from Allègre *62*
4.4.2 Samples from Mont Coupet *64*
4.5 Water content results measured by FTIR 65
4.5.1 Infrared spectra *65*
4.5.2 Calculated water content from infrared spectra *73*
4.6 Water content results from SIMS measurements 75

5. Thermobarometry 77

6. Discussion 79

6.1 Depletion by partial melting 79

6.2 Mantle metasomatism revealed by trace element compositions 85
6.2.1 Trace element variations in Cpx from Allègre 85
6.2.2 Trace element variations in Cpx from Mont Coupet 90
6.2.3 Trace element partition between Cpx and Amp in samples MC36 and MC53 92
6.2.4 Trace element compositions of metasomatic melts/fluids and melt-rock reaction kinetics 97

6.3 Li distribution and isotopic composition variations 101
6.3.1 intra- and inter-mineral Li and Li isotopes distribution in Allègre samples 101
6.3.1.1 Intra-granular and inter-mineral lithium concentration disequilibrium 102
6.3.1.2 Distinctive Li isotopic offsets among mineral phases induced by asynchronous metasomatic events 111
6.3.2 No obvious Li addition but large inter-sample Li isotopic composition variations in peridotite xenoliths from Mont Coupet 118
6.3.2.1 Nearly equilibrated Li partitioning among minerals phases and no concentration zoning in grains 119
6.3.2.2 Large isotopic composition variations caused by a recent metasoamtism 121
6.3.3 Origin of melts with exceptionally light Li isotopic compositions 130
6.3.4 Precedence relationship of the carbannatitic mantle metasomatism and percolation of the negative δ^7Li melt 132

6.4. Water content of minerals in peridotite xenoliths from the French Massif

Central 135
6.4.1 Assignment of bands in the infrared spectra 135
6.4.2 Water partitioning among mineral phases 137
6.4.3 The low water content in minerals from Allègre samples - equilibrated with degassed host magmas 140
6.4.4 Mineral water concentration variations in xenoliths from Mont Coupet 143
6.4.4.1 Preservation of original water content during xenolith ascent 143
6.4.4.2 The processes controlling the water content in peridotite xenoliths from Mont Coupet 145
6.4.4.3 Relationship between water content and trace element concentrations in Ol . 148
6.4.5 Water content in the lithospheric mantle beneath the French Massif Central 149
Conclusion 151
References 155
Appendix 179

List of figures

Figure R1: Distribution des teneurs en terres rares et éléments traces normalisées aux chondrites (McDonough and Sun, 1995), mesurées dans les clinopyroxènes des échantillons de Allègre (AL) et de Mont Coupet (MC). VII

Figure R2 : Variation du rapport $(La/Yb)_N$ en fonction du rapport Ti/Eu dans les Cpx des xénolites de péridotite VIII

Figure R3 : Variation de δ^7Li contre les teneurs en Li des olivines (a) et des Cpx (b) dans les échantillons d'Allègre (AL) et de Mont Coupet (MC) pour comparaison avec les données de la littérature IX

Figure R4 : Profils de variation cœur-bord des teneurs en Li et des δ^7Li des olivines et des Cpx dans les échantillons provenant d'Allègre X

Figure R5: δ^7Li moyenne des Cpx contre les teneurs en Li des Cpx (a) et Mg# des olivines (b) dans les échantillons de Mont Coupet XI

Figure 1-1: Li isotopic compositions of Earth reservoirs, modified from Tang et al. (2010) expressed in δ^7Li values 5

Figure 2-1: A sketch showing the evolution of the Variscan belt in the sector of the Western Europe, adopted from Matt (1991) 13

Figure 2-2: Simplified geological map of the FMC and the spatial distribution of Cenozoic volcanoe 15

Figure 2-3: Vertical north-south section through the FMC showing the S velocity variation from 50-1200 km depth, adopted from Fichtner and Villaseñor (2015) 16

Figure 2-4: a. Sampling in the Ringue quarry in Allègre. b. The Razas Grand quarry in Mont Coupet 19

Figure 3-1: Photos of representative samples after being cut into small pieces 21

Figure 3-2: The simplified instrumental configuration of the ion probe 24

Figure 3-3: A sketch illustrating the process generating the secondary ions 24

Figure 3-4: a. The detailed internal configuration of IMS 1280. b. The photo of IMS 1270 at CRPG. This machine has been upgraded to IMS 1280 in 2015. c. The photo of IMS 1280 (HR2) 26

Figure 3-5: (a) Instrumental mass fractionation plotted against Mg# of olivine standards. As the R^2 values are much lower than one, there should be no compositional influence on Δ_i. We used the averaged Δ_i of individual standard minerals (pyroxenes in red and Ol in blue) to calculate the δ^7Li values of the corresponding sample minerals. (b) Lithium ion yields ([Li]) plotted against Mg# of Ol standards. No co-variation exists. For calculation, the averages of individual phases are utilized 29

Figure 3-6: The ratios of H_2O/SiO_2 vs. measured $^{16}O^1H/^{30}Si$ ratios of standards 31

Figure 3-7: A photo of the Bruker Vertex 70 spectrometer coupled with a Bruker Hyperion 3000 FTIR-microscope 33

Figure 3-8: The IR spectra in the wavenumber range of 1200 to 2200 cm^{-1} with E parallel to Ol principle axes x, y and z, adopted from Lemaire et al. (2004). Si-O vibrations generate these bands ... 34

Figure 3-9: The averaged IR spectra of Ol in the structural H stretching region for each analyzed sample. All the spectra are normalized to 1 cm in thickness ... 35

Figure 3-10: (a) The baseline obtained by polynomial fitting with aide of software KaleidaGraph. (b) The spectrum after baseline deduction (in red) ... 37

Figure 3-11: Representative Ol spectra collected under polarized light with E parallel to X, Y and Z axes. The spectra are normalized to 1 cm in thickness ... 39

Figure 4-1: Modal compositions of samples in this study compared with literature data (smaller blue symbols) ... 42

Figure 4-2: The representative photos of protogranular (a) and porphyroclastic (b) textures under transmission cross-polarized light (a) and mono-polarized light (b) ... 43

Figure 4-3: (a) Protogranular-textured sample AL56. (b) Porphyroclastic-textured sample AL37P1. Fined-grained Ol and Cpx are included in an Opx porphyroclast of about 4 mm across. (c) Cluster composed of Cpx, Ol, Opx and Spl in sample AL56. (d) Spinel with spongy-textured rim in sample AL47P1. (e) Back-scattered images of spongy texture around one spinel grain (d2). (f) Thin spongy rim around an Opx grain (d3). (g) Protogranular-textured sample MC50. Small-grained Cpx and Spl disperse interstitially with larger coexisting Ol and Opx. (h) Porphyroclastic sample MC30 with fine Cpx exsolutions in a large Opx porphyroclast. (i) Kink-banded texture in an Ol grain from sample MC30. (j) Cribriform-shaped Opx grain boundaries in sample MC53. ... 45

Figure 4-4: Mg# of Opx (a), Mg# of Cpx (b) plotted against Mg# of Ol in samples from Allègre and Mon Coupet ... 48

Figure 4-5: Relative difference values of MgO (a) and variation of MgO and CaO contents (b) from cores to rims in Cpx grains of AL47P1 (filled symbols) and AL43 (empty symbols) ... 49

Figure 4-6: REE composition patterns normalized to Chondrite (a) and extended trace element composition patterns normalized to the primitive mantle (b) ... 54

Figure 4-7: REE composition patterns in Cpx from Mont Coupet samples normalized to Chondrite (a) and extended trace element composition patterns normalized to the primitive mantle (b) ... 56

Figure 4-8: REE composition patterns in Amp from Mont Coupet samples normalized to Chondrite (a) and extended trace element composition patterns normalized to the primitive mantle (b) ... 58

Figure 4-9: Al, Ti, Cr and Ni concentrations in Ol plotted against Mg# of Ol and temperature ... 61

Figure 4-10: Averaged unpolarized Ol infrared spectra for all the peridotite xenoliths from Allègre and Mont Coupet in the wavenumber range from 4000 to 3000 cm^{-1} ... 67

Figure 4-11: Unpolarized infrared spectra of two representative profiles made on Ol grains ... 68

Figure 4-12: Representative polarized Ol infrared spectra collected with E parallel to principle axes X, Y and Z 69

Figure 4-13: Averaged unpolarized Opx infrared spectra for all the peridotite xenoliths from Allègre and Mont Coupet in the wavenumber range from 4000 to 2800 cm^{-1} 70

Figure 4-14: Unpolarized infrared spectra of two representative profiles made on Opx grains 71

Figure 4-15: Averaged unpolarized Cpx infrared spectra for all the peridotite xenoliths from Allègre and Mont Coupet in the wavenumber range from 4000 to 3000 cm^{-1} 73

Figure 5-1: T_{BK} (℃) plotted against averaged temperatures calculated using four thermometers 78

Figure 6-1: Co-variation of major element compositions in minerals 80

Figure 6-2: Plots of Ol Mg# versus abundances of La, Sm and Lu in Cpx (a, b and c, respectively) and Cr# of Spl versus abundance of Lu in Cpx (d) 81

Figure 6-3: The fractional melting modeling results based on Y and Yb contents in Cpx 82

Figure 6-4: A sketch modeling the chromatographic effect of a percolating melt, adopted from Mundl et al. (2015) 86

Figure 6-5: Progressive Cpx REE variations, normalized to chondrite, in the Allègre peridotite xenoliths due to the chromatographic effect of the percolating melt 87

Figure 6-6: Variation of $(La/Yb)_N$ versus Ti/Eu (a) and Zr^* (b) in Cpx from Allègre peridotite xenoliths 89

Figure 6-7: Variation of $(La/Yb)_N$ versus Ti/Eu (a) and Zr^* (b) in Cpx from Mont Coupet peridotite xenoliths 91

Figure 6-8: The trace element concentration ratios between co-existing Amp and Cpx ($K_d^{Amp/Cpx}$) in samples MC36 and MC53 compared with literature data in table 6-1 93

Figure 6-9: Zr/Nb ratios vs. Ti/Nb ratios (a) and Ti/Zr (b) of Amp in samples MC36 and MC53 96

Figure 6-10: The primitive mantle-normalized trace element distribution patterns of the hypothetical silicate and carbonatite melts in equilibrium with Cpx from samples AL56 (a) and MC34 (b), and the primitive mantle-normalized trace element distribution patterns of the hypothetical silicate melts in equilibrium with Amp in samples MC36 and MC53 (c) 99

Figure 6-11: Li concentrations in Allègre samples including the minimum and maximum values compared with the Li concentration ranges estimated for the normal mantle (Seitz and Woodland, 2000; Ottolini et al., 2004) 102

Figure 6-12: Li partitioning between Ol and Cpx (a) and between Opx and Cpx (b) in Allègre samples 103

Figure 6-13: Representative Li concentration and δ^7Li profiles of core-rim variations in Ol, Opx and Cpx grains from Allègre samples 105

Figure 6-14: The Li concentration plotted against Mg# measured at the same position in Ol cores from Allègre samples 110

Figure 6-15: Propagation of the δ^7Li tough into a Cpx crystal using the open-system numerical model, adopted from Parkinson et al. (2007) 112

Figure 6-16: Variation of δ^7Li versus Li concentration in Cpx (a), Ol (b) and Opx (c) from Allègre and Mont Coupet samples compared with literature data 114

Figure 6-17: δ^7Li against Li concentrations in Ol grain cores of Allègre samples 115

Figure 6-18: A profile measured on one Opx grain in sample AL32 (AL32-f-Opx) 117

Figure 6-19: Li isotopic discrepancy between Ol and Cpx in samples from Allègre (represented by 'AL') compared with literature data 118

Figure 6-20: Li concentrations in samples from Mont Coupet including the minimum and maximum values compared with the Li concentration ranges estimated for the normal mantle (Seitz and Woodland, 2000; Ottolini et al., 2004) 120

Figure 6-21: Li partitioning between Ol and Cpx (a), between Opx and Cpx (b) in samples from Mont Coupet 120

Figure 6-22: Representative Li concentration and δ^7Li profiles of core-rim variations in Ol, Opx, Cpx and Amp grains from Mont Coupet samples 122

Figure 6-23: Averaged δ^7Li of Cpx versus Li concentrations in Cpx (a) and Mg# of coexisting Ol (b) in samples from Mont Coupet 129

Figure 6-24: The water partitioning between Cpx and Opx in xenoliths from Allègre and Mont Coupet, compared with the $C_{H_2O}^{Cpx} / C_{H_2O}^{Opx}$ range from literature (a), and the linear fitting on water concentrations of Opx and Cpx in mantle xenoliths from worldwide localities 140

Figure 6-25: The fractional melting modeling results for whole rock water content in Allègre xenoliths plotted against primitive mantle-normalized Yb content in Cpx 141

Figure 6-26: Water content in Ol versus water content in Cpx in Mont Coupet xenoliths 144

Figure 6-27: Water content in Cpx (a) and in Opx (b) plotted against Ol of coexisting Ol; water content in Cpx versus $Fe^{3+}/\Sigma Fe$ values of coexisting Spl (c) and Sm content in Cpx (d) in xenoliths from Mont Coupet 147

Figure 7-1: A schematic diagram modeling the evolution of peridotite xenoliths from the lithospheric mantle beneath Allègre 148

List of tables

Table R1 : Les teneurs en eau pour les olivines, les Opx et les Cpx dans les échantillons d'Allègre et de Mont Coupet, calculé par des spectres infrarouges non-polarisés XII

Table 3-1: The major element compositions, Li concentrations and isotopic compositions of standard minerals measured by ICP-MS (Su et al., 2015) 27

Table 4-1: Mineral modes, textures, P-T conditions, origin depths and the degrees of partial melting calculated based on Spl Cr# 41

Table 4-2: The results of electron microprobe analysis on minerals from xenoliths from Allègre and Mont Coupet 47

Table 4-3: The results of electron microprobe analysis on cores and rims of spongy-textured Cpx from sample AL47P1 51

Table 4-4: Trace element abundances in ppm for Cpx in Allègre xenoliths, Cpx and Amp in xenoliths from Mont Coupe 53

Table 4-5: Al, Ti, Cr and Ti concentrations (in ppm) in Ol from Allègre and Mont Coupet samples, measured by LA-ICPMS 59

Table 4-6: The average Li concentration and δ^7Li values for Ol, Opx and Cpx in every sample, including the averages of values in cores and rims 62

Table 4-7: Ol water content in Allègre and Mont Coupet peridotite xenoliths calculated from infrared spectra 74

Table 4-8: Water content of Opx and Cpx in Allègre and Mont Coupet peridotite xenoliths calculated from unpolarized infrared spectra 75

Table 4-9: The results of water content measured by SIMS 75

Table 5-1: Calculated equilibrium temperatures of Allègre and Mont Coupet peridotite xenoliths 77

Table 6-1: The trace element concentration ratios between co-existing Amp and Cpx ($K_d^{Amp/Cpx}$) in samples MC36 and MC53 93

Table 6-2: The average Li concentrations and isotopic compositions at cores and rims, Li concentration ratios and Li isotopic differences (e.g., $\Delta^7Li_{Ol\text{-}Cpx}=\delta^7Li_{Ol}-\delta^7Li_{Cpx}$) among individual phases in Allègre samples 101

Table 6-3: The average Li concentrations and isotopic compositions at cores and rims, Li concentration ratios and Li isotopic differences (e.g., $\Delta^7Li_{Ol\text{-}Cpx}=\delta^7Li_{Ol}-\delta^7Li_{Cpx}$) among individual phases in samples from Mont Coupet 119

Table 6-4: $D_{H_2O}^{Cpx/Opx}$ estimated using Al_2O_3 content in Cpx and Opx, and water concentration ratios between different phases in analyzed samples 138

Table 6-5: Water content calculated from Ti concentrations in Ol from Mont Coupet 149

1. Introduction

1.1 The continental lithospheric mantle

The composition and evolutional history of the Earth are undoubtedly unique. Earth is ~4.54 billion years old and becomes a totally different planet from it formed initially. In spite of space exploration technologies highly developed nowadays, Earth is still the only planet known to be suitable for the human being to live.

The solid earth is composed of three main layers: crust, mantle, and core. The crust is the shallowest layer and large part of it is accessible to direct researches. While the accumulation of the knowledge of the deeper layers, the mantle and the core, have to rely on studies of materials accidentally brought to the surface by geologic processes, indirect inferences based on high T-P experiments and geophysical observations.

The lithosphere is the rigid outer portion of the earth, extending from the surface to the depth of a few tens of kilometers to >200 km. It includes the crust and the upper fraction of the mantle. The chemical compositions of the lithosphere are layered and, the crust and the underlying lithospheric mantle are clearly different from each other in compositions. The former has been created by partial melting of the depleted upper mantle (or lager proportion of the mantle), although there are still some questionable points, for instance: the average composition of the crust is andesitic, but the experimentally melting products of peridotite (the dominate rock type composed of the shallow mantle) are basaltic (Rudnick, 1995). Even so, the continental lithospheric mantle has been identified to be depleted of the basaltic components (CaO, Al_2O_3 and FeO) and of the incompatible trace elements, which makes it gravitationally buoyant and thermally cooler relative to the asthenosphere due to iron contents controlling the density of peridotite and radioactive elements (K, Rb and U) dominating the production of energy at depth (Carlson et al., 2005). That is the reason why the lithospheric mantle domains could keep long-term stability, separation from the asthenosphere underneath them, and, avoiding the delamination by the asthenospheric convection.

The continental lithospheric mantle is not uniform on different scales, including the compositions, ages and evolutional histories. On a global scale, the sub-continental

lithospheric mantle can be subdivided into cratonic and non-cratonic types. The former is of large thickness (from crust bottom to >200 km), has highly depleted compositions and underlies the crust of Archean or Proterozoic ages, while the latter is much thinner (from crust bottom to <120 km), more fertile and much younger (Phanerozoic). Even in a single region, the geochemical compositions of the lithospheric mantle exhibit large variations. In most cases, these variations can't be explained merely by partial melting in various degrees, especially in respect of the trace element compositions (e.g., Frey and Green, 1974; Menzies, 1983; McDonough and Frey, 1989). Postdating infiltration events of exotic melts and/or fluids in the mantle depth can refertilize the depleted upper mantle to bring mineralogical and geochemical modification, defined as mantle metasomatism. The metasomatism, creating new additional minerals (e.g., amphibole (Amp), apatite and phlogopite) lying interstitially or replacing primary minerals, has been called modal (patent) metasomatism. Whereas the other type, cryptic metasomatism, has been proposed to cause only chemical modifications and no mineralogical changes (Menzies and Hawkesworth, 1987 and references therein). Up to present, three main metasomatic agents have been proposed to be responsible for mantle metasomatism, those are: silicate melts, carbonatite melts and volatile-rich fluids (Giuliani et al., 2012; O'Reilly and Griffin, 2013). The properties of certain metasomatic melts/fluids have intimate relation to localized geological backgrounds and tectonic activities occurring in their sources, e.g., the fluids generated during dehydration of a subducting slab enriched in the fluid-mobile elements (LREE, LILE...), and depleted in immobile elements (HFSE). .

The trace elements are constituent elements occupying minor fraction of a system of interest. They, or groups of them, usually have somewhat unique physicochemical characteristics and behave more sensitively to certain geological processes compared with the major elements. During melt/fluid-related processes, many trace elements are incompatible, and readily enter into melts/fluids, and are depleted in solid phases. Hence, the concentrations of these trace elements in samples from the lithospheric mantle are often a few orders of magnitude lower than those in metasomatic melts/fluids. Even small amount of melts/fluids can introduce significant deviation of

trace element distributions in metasomatized rocks from in their protoliths. Meantime, because trace elements have low concentrations in a studied system and can be considered to approximately obey Henry's Law, their behaviors are relatively simple and can be easily simulated. Combining with the experimental results and theoretical modeling, the trace element signature of metasomatism has, in turn, been used to identify the type of metasomatic agents and to track the history of the local evolution of the lithospheric mantle. Some trace element couples (e.g., Ti/Eu, Th/U and B/La), each of which has similar incompatibility to its counterpart during melting and crystallization, are especially useful. For example, the ratio of Ti/Eu in clinopyroxene from peridotites has been proposed as an indicator of metasomatic agents distinguishing between carbonatite melts and silicate melts (Coltorti et al., 1999), while the partition coefficient differences of Th and U in the system of Cpx coexisting with silicate melts will diminish markedly with decreasing oxygen fugacity (LaTourrette and Burnett, 1992).

Peridotite xenoliths are small fragments of the lithospheric mantle transported to the earth surface by alkaline basalts or kimberlites and can provide direct insight into the mineralogical and geochemical compositions of the upper mantle and its evolutional processes at depth (e.g., Nixon, 1987; Pearson et al., 2003). Compared with samples from tectonically emplaced ultramafic bodies, the information from which have usually been obscured by deformation and recrystallization occurring during slow exhumation and emplacement, xenoliths can, generally, preserve the original signatures at the time of entrainment due to the rapid eruption of their host magmas to the earth surface (Pearson et al., 2003). Meantime, magmas en route to the surface can capture peridotite nodules from different depths and exhume the vertical diversity of the lithospheric mantle in a larger depth range. Nevertheless, peridotite xenoliths also have their own drawbacks to studying the lithospheric mantle. Due to small sizes of xenoliths, little modal structural information could be extracted from fieldwork or macroscopic observations on samples, unlike peridotite massifs (e.g., Bodinier et al., 1990; Bodinier and Godard, 2003; Le Roux et al., 2007). Additionally, the percolation of host magmas within xenoliths during ascent may occasionally change the mineralogical and geochemical compositions of xenoliths and render the

identification of the origin of metasomatic agents ambiguous (Shaw et al., 2006; Shaw and Dingwell, 2008; Bonadiman et al., 2008; Wagner et al., 2013). Thus, for xenolith studies, discriminating two types of metasomatism (mantle metasomatism or host magma-xenolith interaction) is of prime importance to better understand metasomatic processes of the lithospheric mantle in some cases, for example, when studying xenoliths derived from a solidified lava lake or entrained by a slowly rising magma.

1.2 Lithium

1.2.1 Geochemical features

Lithium is a chemical element with atomic number 3 and belongs to the alkali metal group in the chemical periodic table. Like other elements in the same group, Li has a single valence electron that is easily lost to form a monovalent cation. This property makes Li very reactive and it doesn't exist in the pattern of simple substance and only bonds with other anions to develop ionic compounds in nature. Wenger and Armbruster (1991) systematically investigated the oxygen coordination of Li based on structural data and concluded that Li could bond with different numbers of O in the form of LiO_n (n=3, 4, 6, 8) polyhedral. Meantime, due to a diagonal relationship with magnesium (Mg) in the periodic table, Li^+ has a similar ionic radius (0.78 Å; Huh et al., 1998) to that of Mg^{2+} (0.72 Å) that is a major constituent element of most mantle minerals, for example, olivine and pyroxenes, etc. Thus, Li usually incorporates into these minerals by substituting Mg^{2+} (Fe^{2+}) in octahedral coordination, perhaps coupled with some trivalent cations to keep the electroneutrality (Seitz and Woodland, 2000; Grant and Wood, 2010; Zhang and Wright, 2012). In contrast, Li has been proposed to preferentially form tetrahedral LiO_4 in melts and fluids (Cormier et al., 1998).

^6Li and ^7Li are the two stable isotopes of lithium in nature, with isotopic abundances of 7.52% and 92.48%, respectively. The Li isotopic composition is currently expressed as:

$$\delta^7Li=[(^7Li/^6Li)_{sample}/(^7Li/^6Li)_{L\text{-}SVEC}-1]\times1000, \quad (1)$$

where L-SVEC is highly purified Li_2CO_3 as the international standard for Li isotopes with $^7Li/^6Li$ abundance ratio at 12.0192 (Flesch et al., 1973). As two major reservoirs of interest, the upper continental crust is estimated to contain Li at 35±11 ppm with a δ^7Li value of 0±2‰ (Teng et al., 2004), while the upper mantle is estimated to contain at 1.7±0.1 ppm with a higher δ^7Li value of 3.5±0.5‰ (Ottilini et al., 2004; Pogge von Strandmann et al., 2011). The large mass difference between ^6Li and ^7Li (∽16%) results in significant isotopic fractionation during various geochemical processes and produces large Li isotopic variation in the different reservoirs (Fig. 1-1; see Tomascak (2004) for a review). Theoretically speaking, for a two-atom molecule, the one composed of the heavy isotope has a lower vibrational frequency than that composed of light isotope, due to the inverse relationship between frequency and mass (Chacko et al., 2001). Moreover, the lower vibrational frequency determine a lower zero point energy (ZPE), which makes the bond between the two atoms much more stable. Meantime, the bond energy also depends on the bond length, which is closely related to the coordination number of each element. Generally, when coordination numbers are higher, the bonds are longer and thus the bond energies are lower, and as with heavy isotopes of other elements, ^7Li prefers the higher-energy bonds. That is probably why ^7Li preferentially enter into melts/fluids in a system of minerals co-existing with melts/fluids, where Li occurs in tetrahedral coordination. Both observations from natural samples (e.g., Huh et al., 1998; Pistiner and Henderson, 2003; Rudnick et al., 2004) and experiments (Wunder et al., 2006) have evidenced this behavior.

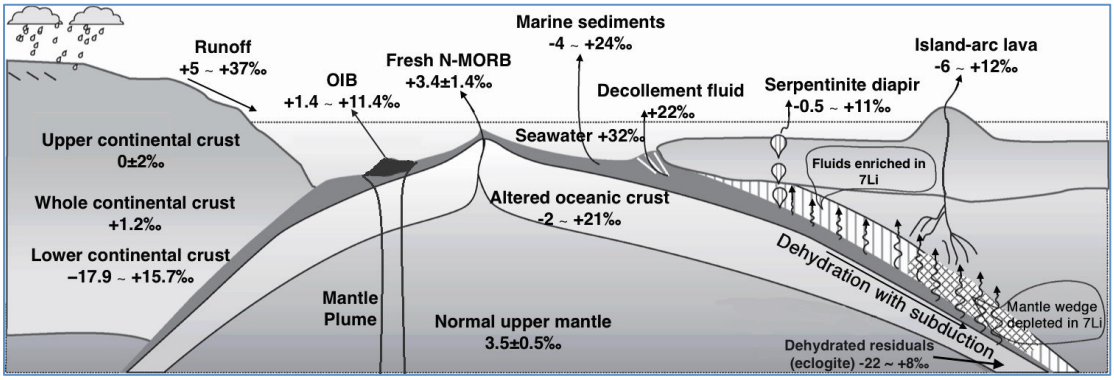

Figure 1-1: Li isotopic compositions of Earth reservoirs, modified from Tang et al. (2010) expressed in δ^7Li values. The data are from: seawater (Chan and Edmond, 1988; You and Chan, 1996), river water (Huh et al., 1998, 2001; Millot et al., 2010; Dellinger et al., 2015), arc lavas (Moriguti and Nakamura,

1998b; Tomascak et al., 2002; Chan et al., 2002a; Agostini et a., 2008; Košler et al., 2009), Fresh N-MORB (Tomascak et al., 2008), OIB (Tomascak et al., 1999; Chan and Frey, 2003; Kobayashi et al., 2004; Ryan and Kyle, 2004; Nishio et al., 2005; Jeffcoate et al., 2007; Chan et al., 2009), altered oceanic crust (Chan et al., 19992, 2002b), marine sediments (Chan et al., 1994, 2006; Chan and Kastner, 2000; Bouman et al., 2004), upper continental crust (Teng et al., 2004), lower continental crust (Teng et al., 2008), normal upper mantle (Von Strandmann et al., 2011), eclogite (Zack et al., 2003; Marschall et al., 2007; Penniston-Dorland et al., 2010).

Consequently, Li partitioning between melts/fluids and minerals (e.g., during partial melting process, subduction-induced dehydration of slabs, and melt/fluid-rock interactions) will induce Li isotopic fractionation. In addition, recent experimental simulations have revealed that the diffusivity of Li under mantle conditions is several orders of magnitude higher than that of other incompatible elements (Coogan et al., 2005; Dohmen et al., 2010), with ^{6}Li diffusing faster than ^{7}Li in either melts or minerals (Richter et al., 2003, 2014). The kinetic fractionation resulting from the diffusivity difference between ^{6}Li and ^{7}Li has been involved to account for the large Li isotopic variations observed in samples of different sizes (e.g., Lundstrom et al., 2005; Teng et al., 2006; Rudnick and Ionov, 2007; Penniston-Dorland et al., 2012). Especially, detailed Li diffusive profiles in mineral grains are considered to have the potential as a high-resolution geospeedometer for timescales as short as a few to hundreds of days (Jeffcoate et al., 2007; Parkinson et al., 2007).

1.2.2 The Current Research State of Li in the Lithospheric Mantle

Because Li^{+} can substitute Mg^{2+}, Fe^{2+}, and even Al^{3+} to incorporate into silicate minerals, it behaves as intermediately incompatible during partial melting processes (Brenan et al., 1998a; Ottolini et al., 2009). Li has an incompatibility similar to Yb (Ryan and Langmuir, 1987; Brenan et al., 1998a), with partition coefficient between clinopyroxene (s; Cpx) and melts varying from 0.229 to 0.264 (Ottolini et al., 2009), which means that the two elements will not fractionate significantly during melt-rock interaction. Nevertheless, observations from experiments show that in the presence of aqueous fluids, Li tends to enter in the fluids while, on the contrary, Yb stays in Cpx (Brenan et al., 1998b). The elevated ratio of Li/Yb in island arc lavas has been ascribed as the result of the fluid-mobile feature of Li (Brenan et al., 1998b). In light of this, in association with B and sometimes Be, Li has been used as a tracer for fluid

activities, especially for fluids released from subducted slabs towards the overlying mantle (e.g., Paquin and Altherr, 2002; Paquin et al., 2004; Kaeser et al., 2007; Marschall et al., 2009). Elsewise, as mentioned before, during dehydration of subducted slabs, ^{7}Li preferentially enters into the released fluids. Thus, the released fluids will be enriched in ^{7}Li whereas the residuals will have light Li isotopic compositions, as observed in eclogites formed from the altered oceanic crust basalts having undergone high-pressure metamorphism (Zack et al., 2003). These low-δ^{7}Li materials continue subducting and may become a new reservoir in the deep mantle (Zack et al., 2003). Nevertheless, there is still a controversy on the longevity of the mantle Li isotopic composition heterogeneity (e.g., Halama et al., 2008; Vlastéli et al., 2009), and whether the dehydration process during slab subduction could indeed induce large Li isotopic fractionation and then the low-δ^{7}Li materials are delivered into the deep mantle (e.g., Marschall et al., 2007). But light Li isotopic compositions have been subsequently observed in peridotites (Nishio et al., 2004; Brooker et al., 2004; Tang et al., 2007, 2012, 2014) as well as in magmas of mantle origin (Agostini et al., 2008; Bouvier et al., 2010; Abdelfadil et al., 2014), as a signature of the subduction factory.

As an extensive process in the upper mantle, mantle metasomatism could also bring significant changes to Li concentrations and isotopic compositions of host peridotites (e.g., Seitz and Woodland, 2000; Seitz et al., 2004; Woodland et al., 2004; Tang et al., 2007, 2011; Albach and Rudnick, 2009; Zhang et al., 2009; Su et al., 2012, 2014). Given the high diffusive rates of Li in mantle minerals, metasomatic events responsible for the currently observed Li signatures were often considered as a recent occurrence (Aulbach and Rudnick, 2009). Commonly, due to lower diffusivity of Li in olivine (s; Ol) relative to Cpx, negative δ^{7}Li values associated with high Li concentrations were observed in Cpx and ascribed to a kinetic fractionation produced by Li diffusive ingress from infiltrating metasomatic melts/fluids and Ol may have preserved pre-metasomatic Li signatures. Moreover, in metasomatized mantle peridotites, some researchers observed that Li was selectively enriched in Ol (in case of carbonatite metasomatism) or Cpx (in case of silicate metasomatism). They suggest that tendentious partitioning of Li could be regarded as an indicator of the agent

responsible for metasomatic events (Seitz and Woodland, 2000; Su et al., 2014). However, sometimes host magmas infiltrated into xenoliths and distorted the imprints left by mantle metasomatism (discussed in this thesis). As a matter of fact, in some foregoing studies, the observed Li metasomatic signatures were thought to be the result of Li addition from host magmas during xenolith entrainment (e.g., Rudnick and Ionov, 2007). In this case, the role of Li distribution for tracking the type of metasomatic agents should be treated with caution.

1.3 Water in the nominally anhydrous minerals (NAMs)

1.3.1 Water in the earth mantle

Hydrogen is the lightest chemical element on the periodic table and it is one of the most abundant elements in the universe, although in earth its abundance is just at minor level. In nature, it commonly occurs in the form of covalent compounds with non-metallic elements, such as water (H_2O) and organic compounds. Sometimes in ionic compounds, hydrogen can also obtain or lose an electron to take a negative charge (H^-; e.g., anion in hydride) or positive charge (H^+; e.g., cation in acid solutions). The existence of liquid water, composed of two hydrogen atoms and one oxygen atom, is believed as the principal factor making the earth livable and full of vigor from its interior to the terrestrial space. Hydrogen is also present inside the earth, although sometimes at ppm (parts per mil) levels by weight (conventionally measured in ppm wt. H_2O). The mass of water in the bulk Earth and different Earth reservoirs has been estimated by previous studies (e.g., Mottl et al., 2007; Bernard, 2012; Bodnar et al., 2013; Nestola and Smyth, 2016). The recent estimates, by Nestola and Smyth (2016) mainly based on the great observation of a terrestrial ringwoodite found in a large diamond containing 1.4% water, proposed an amount of 12.1×10^{24} g total water in the Earth and 1.2×10^{23} g water in upper mantle. Water occurs in several forms: as hydrated fluid or hydrous melt when water contents exceed the water storage capacity of host minerals; as hydrous phases, which is limited by their instability with increasing pressure and temperature into the deep Earth; as melt or fluid inclusions carried by mantle minerals, where hydrogen might move into water-unsaturated host minerals through diffusive exchange (Chen et al., 2011, 2013);

and as impurities entering the crystalline lattices of nominally anhydrous minerals (NAMs), which don't have hydrogen in terms of structural formula.

It is worth to be mentioned that because oxygen is the only anion in most NAMs, hydrogen, proton, hydroxyl (OH), and water will be equivalently applied throughout my thesis and hydrogen concentrations are given by water parts per million in weight (wt. ppm water).

1.3.2 The current research state of water in the NAMs

In recent few decades, water in NAMs from mantle has become an increasing subject of research (e.g., Aines and Rossman, 1984a; Miller et al., 1987; Skogby et al., 1990; Bell and Rossman, 1992; Rossman, 1996; Ingrin and Skogby, 2000; Bolfan-Casanova, 2005; Hirschmann, 2006; Peslier, 2010). Even in tiny amounts, water can significantly affect the physical and chemical properties of its host minerals/rocks, such as electrical conductivity (e.g., Karato, 1990; Huang et al., 2005; Wang et al., 2006; Yoshino et al., 2006; Yoshino and Katsura, 2013), ionic diffusivities (e.g., Wang et al., 2004; Hier-Majumder et al., 2005; Demouchy et al., 2007; Costa and Chakraborty, 2008; Otsuka and Karato, 2015), rheology (e.g., Mackwell et al., 1985; Karato et al., 1986, 2015; Karato and Wu, 1993; Chen et al., 1998; Mei and Kohlstedt, 2000a, 2000b; Dixon et al., 20004; Hier-Majumder et al., 2005a; Karato, 2010a, 2010b; Manthilake et al., 2013), seismic velocity (e.g., Karato and Jung, 1998; Jung and Karato, 2001; Falus et al., 2008; Karato et al., 2008), partial melting of host rocks (i.e., compositions of melts and residuals, solidus temperature and thus onset depths and melting degrees; e.g., Hirth and Kohlstedt, 1996; Gaetani and Grove, 1998; Asimow and Langmuir, 2003; Hirschmann et al., 2009; Green et al., 2010, 2014; Kelley et al., 2010; Tenner et al., 2012a). These make water a key parameter in earth evolution, including plate movements, craton stabilization and vertical structural stratification. In order to further explore water-influenced processes, water distributions in mantle minerals (commonly NAMs) should be precisely constrained.

NAMs are believed as the major host of water in the mantle. In general, the water content in NAMs is estimated from experimental extrapolations and direct analysis on natural samples (e.g., peridotite xenoliths). As synthesizing in labs, water

concentrations in products are likely to vary with the designed ambient conditions, which have been used to identify parameters controlling the water content in different mineral phases: Ol (Bai and Kohlstedt, 1992, 1993; Kohlstedt et al., 1996; Matveev et al., 2001; Lemaire et al., 2004; Zhao et al., 2004; Grant et al., 2006; Smyth et al., 2006; Bali et al., 2008; Withers et al., 2011; Adia et al., 2012; Ferot and Bolfan-Casanova, 2012; Novella et al., 2014), orthopyroxene (Opx; Rauch and Keppler, 2002; Stalder and Skogby, 2002; Mierdel and Keppler, 2004; Mierdel et al., 2007; Zhang et al., 2013), Cpx (Skogby, 1994; Bromily et al., 2004; O'Leary et al., 2010). Meantime, the incorporation mechanisms of hydrogen into mineral crystals have also been deeply investigated (e.g., Ol, Matveev et al., 2001; Lemaire et al., 2004; Berry et al., 2005, 2007a, 2007b; Demouchy and Mackwell, 2006; Smyth et al., 2006; Grant et al., 2007a; Walker et al., 2007; Kovács et al., 2010; Ingrin et al., 2013, 2014; Opx, Stalder and Skogby, 2002; Rauch and Kepppler, 2002; Stalder, 2004; Smyth et al., 2007; Cpx, Ingrin et al., 1989; Bromiley et al., 2004; Andrut et al., 2007). Hydrogen totally occupies the ionic vacancies (multi-atoms to maintain charge neutrality; $2H \rightarrow V_{Me}$, $4H \rightarrow V_{si}$), or substitutes the pre-existing high-valence ions coupled with other heterovalent impurity ions (e.g., $H^{+}+Fe^{3+} \rightarrow V_{Me}+Fe^{2+}$; $H^{+}+Al^{3+} \rightarrow Si^{4+}$). Through analyzing the products of solubility experiments at higher P and T, water content of mantle at remote depths have been estimated (e.g., Bolfan-Casanova et al., 2000; Demouchy et al., 2005; Inoue et al., 2010; Nishi et al., 2014; Ohira et al., 2014). In most cases, minerals have been synthesized under water-saturated conditions and the ambient settings for mineral synthesis used to be simplified compared with natural environments. Thus, water content in synthesized NAMs is commonly higher than that measured in direct samples stemming from depth and, usually, is regarded as the water solubility in minerals under the given conditions. Additionally, the difference between infrared spectra of synthesized mantle minerals (Ol, Opx and Cpx) and those of minerals from peridotite xenoliths, is another obstacle to associate all the experimental observations with natural samples (e.g., Stalder et al., 2015).

Nominally anhydrous Ol, Opx, Cpx and garnet in peridotite xenoliths transported to the earth surface by alkali basalts or kimberlites have been extensively analyzed for

water concentrations in order to access the water content of the upper mantle. On earth whether the currently measured water concentrations in these minerals represent their original values is still quentioned (e.g., Bell and Rossman, 1992; Ingrin and Skogby, 2000). At present, although Ol grains have undergone more or less H loss due to decompression during ascent (e.g., Demouchy et al., 2006; Peslier and Luhr, 2006; Peslier et al., 2008; Denis et al., 2013; Thoraval and Demouchy, 2014; Peslier et al., 2015), especially in peridotites entrained by alkali basalts (large part to total loss; e.g., Yang et al., 2008; Xia et al., 2010; Yu et al., 2011; Schmädicke et al., 2013; Hao et al. 2014, 2016), Opx and Cpx are generally believed to preserve their original water content (e.g., Bonadiman et al., 2009; Sundvall and Stalder 2011; Warren and Hauri, 2014; Peslier and Bizimis, 2015). Alternatively, the water diffusive profiles in Ol have been used as a tool to calculate the uprising rates of host magmas (e.g., Demouchy et al., 2006). Assuming that water partitioning between Ol and pyroxenes achieving equilibrium in source regions, we can estimate the whole rock water content when only water in pyroxenes has been preserved based on the water partition coefficients between Ol and pyroxenes deduced from experiments (e.g., Yang et al., 2008; Xia et al., 2010).

As a minor element in the mantle, hydrogen also behaves incompatibly during partial melting and fractional crystallization, with incompatibility most similar to Ce (Michael, 1988, 1995). According to this observation, and by using the constant H_2O/Ce ratio in MORB, combined with the estimated Ce concentrations in MORB, the water content in the depleted upper mantle has been proposed to vary between 50 and 200 ppm (Michael, 1995; Dixon et al., 2002; Saal et al., 2002). Meanwhile, water is a common component of metasomatic agents at mantle depths. Like other trace elements, water content in NAMs is also influenced by mantle metasomatism (e.g., Peslier et al., 2012; Doucet et al., 2014; Demouchy et al., 2015; Denis et al., 2015). But in some cases, the variation of measured water content in NAMs from peridotite xenoliths is not correlated with metasomatism indicators (e.g., La/Yb ratio) and the water content is decoupled with Ce concentration (e.g., Hao et al., 2014; Demouchy et al., 2015; Denis et al., 2015). Furthermore, the heterogeneity of water content in the mantle has been ascribed as the variations of other ambient parameters, such as, the

oxygen fugacity (Peslier et al., 2002; Peslier, 2010), and pressure (e.g., Demouchy, 2015; Demouchy and Bolfan-Casanova, 2016). Up to now, different observations have been presented on whether the presence of Amp during metasomatism has affected the water distribution in pre-existing NAMs (Yang et al., 2008; Schmädicke et al., 2013; Denis et al., 2015). Anyway, the varying water content in mantle NAMs was generally associated with different geological backgrounds (Skogby, 1990; Sundvall and Stalder, 2011) and no single parameter or process could be responsible for the heterogeneous water distribution. Since hydrogen has high diffusivity in NAMs under mantle conditions (Mackwell and Kohlstedt, 1990; Ingrin et al., 1995; Kohlstedt and Mackwell, 1998; Hercule and Ingrin, 1999; Carpenter Woods et al., 2000; Demouchy and Mackwell, 2003; Stalder and Skogby, 2003; Sundvall et al., 2009; Padrón-Navarta et al., 2014), the water content of NAMs in peridotite xenoliths may has, in some case, been influenced by host magmas (Grant et al., 2007b; Li et al., 2008).

1.4 Objective of this thesis

The objective of this thesis is to depict the evolution of the lithospheric mantle underneath the FMC from the study on mantle xenoliths. In order to investigate the imprints left by the host magma-xenolith interaction, xenoliths entrained by two volcanoes erupting in different modes were analyzed, from the Ringue quarry (Allègre), where they are sampled in a solidified lava lake, and in the Mont Coupet quarry, where hey occured in volcanic bombs.

In-situ measurements were made to determine major element and trace element compositions, water content and Li isotopic composition in Cpx, Amp (if any) and Ol. From these results, we describe the behaviors of light elements (Li and H) in peridotite minerals during partial melting and mantle metasomatism, and distinguish the distinctive roles of individual indexes (trace elements, Li isotopes and water) in tracing the melt-rock interactions. We will see that the Li analyses performed on xenoliths sampled in a solidified lava lake can help to define the imprints left by the host magma-xenolith interaction, and, to separate it from mantle metasomatism in time order.

2. Geological background

The French Massif Central (FMC) is one of the most typical massifs in the Variscan belt. It is located in Western Europe, to the south of the Paris Basin, to the west of the Rhône-Saône trough, to the east of the Aquitaine Basin, and to the north of the hollow joining the Aquitaine to Lower Provence. The basement of the FMC exhibist several rock types: metamorphic rocks, formed during the Variscan orogeny; sedimentary rocks, products of deposition processes wrapping round the older metamorphites and filling the basins; and magmatic rocks left by the massive Tertiary-Quaternary volcanism.

2.1 The pre-Cenozoic tectonic evolution of the FMC

The evolution of the Variscan belt can be regarded as a typical Wilson cycle, exhibiting subduction and extinction of oceanic basins and collision of continental plates (Fig. 2; e.g., Behr et al., 1984; Matte, 1986, 1991; Pin, 1990; Faure et al., 2009). Prior to the onset of the Variscan orogeny, the Rheic Ocean firstly emerged in the early Ordovician and separated the two ancient continents Gonwana and Laurussia (Faure et al., 2009; Nance et al., 2010).

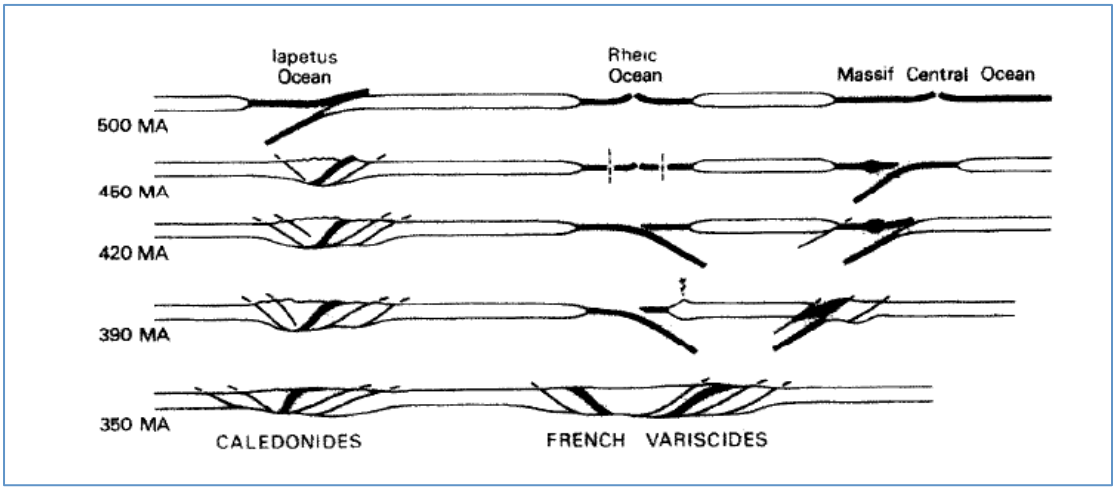

Figure 2-1: A sketch showing the evolution of the Variscan belt in the sector of the Western Europe, adopted from Matt (1991).

It continued expanding at the expense of the Iapetus Ocean, which subducted beneath Armorica (Matt, 1886, 1991; Faure et al., 2009). The Rheic Ocean achieved its largest width (~4000 km) in the Silurian and then commenced closing and subducting southward in the Devonian (Nance et al., 2010). The extinction of the Rheic Ocean

marked the onset of the Variscan orogeny, i.e., the collision between Gondwana and Laurussia during Devonian-Carboniferous times (Lardeaux et al., 2001; Nance et al., 2010), followed by two large-scale extension events and the gravitational collapse inside the continent (Faure et al., 2009). Many plutons distributing in the FMC (e.g., mostly granites) developed during this stage. After that, the sedimentation processes gradually predominated and filled the extension-induced basins through the Mesozoic. Then intense volcanic activities related to the West-European Rift system occurred during Cenozoic times (Ziegler, 1992; Michon and Merle, 2001).

2.2 The Cenozoic volcanism in the FMC

The Cenozoic volcanism within the FMC made it the largest magmatic province in the Western Europe (Michon and Merle, 2001). The volcanic activitiy started in the Eocene and lasted until the most recent volcanism in the Chaîne des Puys ~6,900 yr ago (Juvigné, 1992). The spatial distribution of volcanic activities spread over several regions (Fig. 2-2), such as Cantal, Devès, Velay Oriental, Aubrac, Mont-Dore, and Chaîne des Puys. The entire volcanism has been classified as three magmatic phases: pre-rift, rift-related, and major magmatic events (Michon and Merle, 2001). They have outcrops of different volumes in different localities. The pre-rift phase started in the late Cretaceous and was active in the Paleocene and Eocene. It has minor volumes and mainly scatters in the northern part of the FMC. The lavas erupting in this stage are under-saturated (alkali basalt to melilitite; Wilson and Downes, 1991; Michon and Merle, 2001). The rift-related volcanism is spatially restricted in the northern part of the FMC and could be ascribed to low degrees partial melting resulting from decompression during extension. In the Oligocene, the crust in the northern part of the FMC underwent significant thinning associated with graben fromation, especially the Limagne graben (Merle et al., 1998; Michon and Merle, 2001, whereas the crust thinning was very subtle in the southern part of the FMC and no related volcanic activity has been reported there. The lavas associated with this phase are mainly alkaline basalts and nephelinite. The major magmatic phase commenced at different times in the northern and southern parts of the FMC (5.5 Ma and 15 Ma ago, respectively; Michon and Merle, 2001). It lasted from Miocene till recently and

produced the few large magmatic provinces presently observed in the FMC (Fig. 2-2).

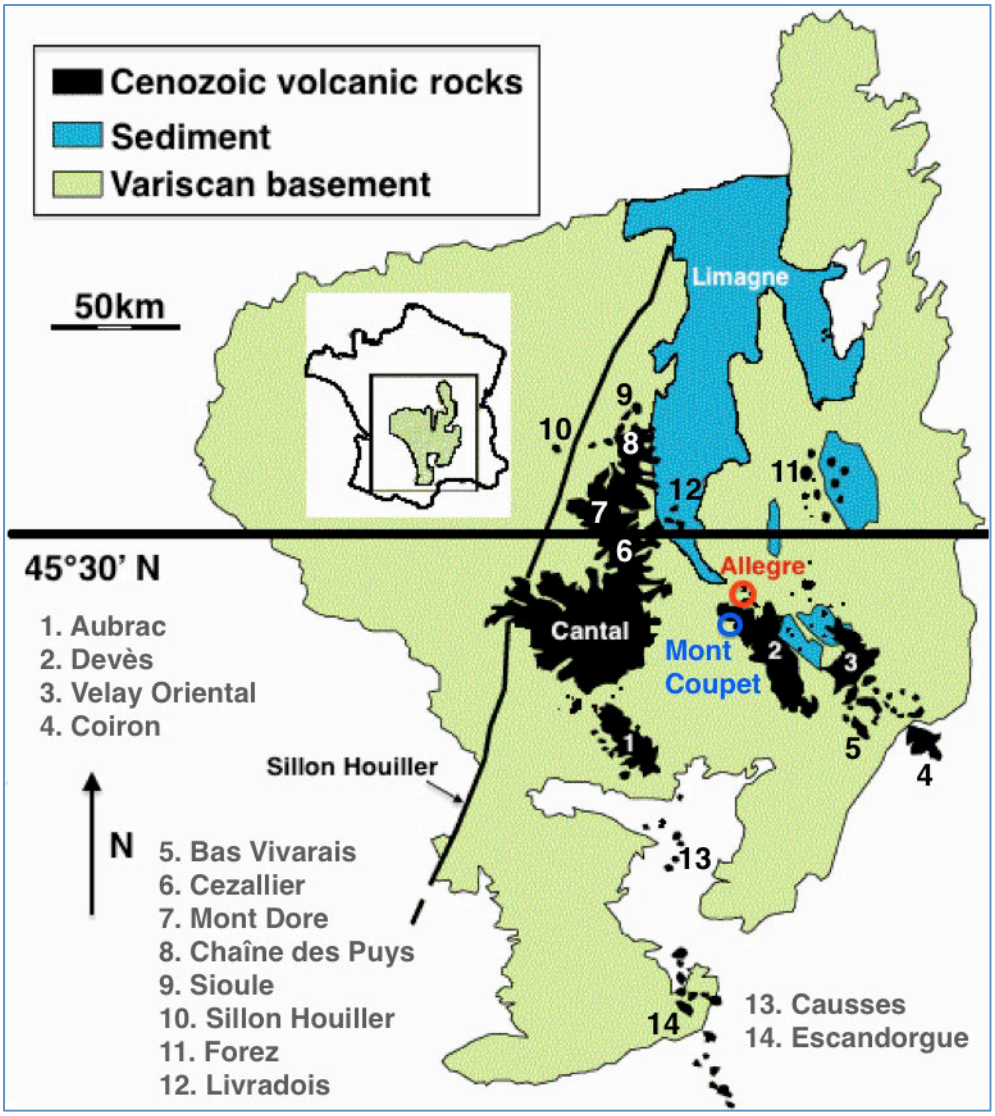

Figure 2-2: Simplified geological map of the FMC and the spatial distribution of Cenozoic volcanoes. The sampling localities of Allègre and Mont Coupet, both belonging to Dèves (region 2), are marked by the red and blue circles, respectively. The boundary between the northern and southern domains (the horizontal black line; Lenoir et al., 2000) is also drawn.

The lavas have alkali basaltic compositions and sometimes exhibit two series. Based on geochemical and Sr-Nd-Pb isotopic compositions, Wilson and Downes (1991) proposed that these lavas could be regarded as binary mixtures of two components of different origins: the primary magmas and the lithospheric mantle metasomatized during Variscan orogeny. The primary magmas probably had signatures between DM and HIMU, which has been explained by partial melting of subducted oceanic lithosphere during Variscan orogeny after it entered the convecting asthenosphere. Then they were contaminated by phlogopite or amphibole-bearing lithospheric mantle

during ascent towards the surface. Meantime, due to the harmony of major magmatic localities and the thermal anomalies underneath the FMC, the extensive volcanism during this stage has been considered to be prompted by an asthenospheric upwelling (Michon and Merle, 2001). Recently, it has been also suggested that the presence of fertile lithologies (pyroxenites and/or amphibolites) in the FMC mantle had also enhanced the volcanism (Pilet et al., 2008; France et al., 2015).

The existence of thermal anomalies underneath the FMC has been continuously verified by results of seismic tomography (Fig. 2-3; Hoernle et al., 1995; Granet et al., 1995; Sobolev et al., 1997; Zeyen et al., 1997; Goes et al., 1999; Fichtner and Villaseñor, 2015), but different interpretations of this observation have been given.

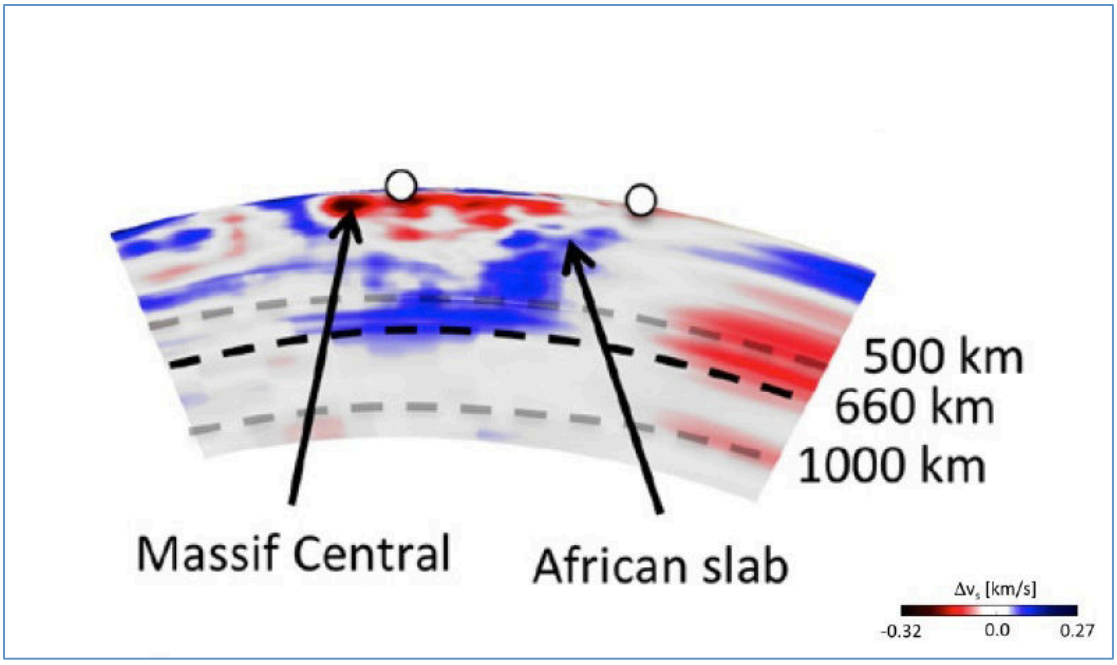

Figure 2-3: Vertical north-south section through the FMC showing the S velocity variation from 50-1200 km depth, adopted from Fichtner and Villaseñor (2015).

On the one hand, diapiric mantle upwelling deriving from an older mantle plume, whose head spread at a depth of 400 km, have been proposed to account for these thermal anomalies (Granet et al., 1995). Goes et al. (1999) have also observed a low-velocity anomaly located at the depth of 660 to 2000 km beneath central Europe and suggest that it had played the role of the root for mantle upwellings interspersing under western and central Europe. On the other hand, these thermal anomalies have been ascribed as hotspots that originated from the upper mantle only to the bottom of the transition zone, and not from the lower mantle (Hoernle et al., 1995). A recent

full-waveform tomographic model from Fichtner and Villaseñor (2015) has not shown the presence of mantle plumes beneath the FMC and they discussed the previous plume signatures observed in tomographic images as an artifact brought by vertical smearing in the upper mantle (Fichtner and Villaseñor, 2015). Alternatively, the mantle upwellings were temptatively associated with slab subduction or extension-induced lithosphere thinning during Alpine orogeny (Sobolev et al., 1997; Goes et al., 1999). In spite of the debate, upwellings of deep materials hotter than ambient lithosphere had brought heat and resulted in thinning and partial melting of lithosphere to generate a few magmatic provinces that carried large quantities of xenoliths from various depths to the surface.

2.3 The lithospheric mantle beneath the FMC

In the past decades, peridotite or pyroxenite xenoliths have been used to decipher the composition and evolution of the lithospheric mantle beneath the FMC (e.g., Mercier and Nicolas, 1975; Downes, 1987; Downes and Dupuy, 1987; Nicolas et al., 1987; Werling and Altherr, 1997; Zangana et al., 1997, 1999; Xu et al., 1998; Lenoir et al., 2000; Lorand and Alard, 2001; Lorand et al., 2003; Downes et al., 2003, 2015; Féménias et al., 2003, 2004, 2005; Berger et al., 2005, 2007; Wittig et al., 2006, 2007; Touron et al., 2008; Yoshikawa et al., 2010; Harvey et al., 2010; Uenver-Thiele et al., 2014; France et al., 2015).

Among these, Lenoir et al. (2000) integrated textural observations with bulk rock major and trace element compositions of peridotite xenoliths widely distributed in the FMC (25 volcanic centers) and identified two distinct lithospheric mantle domains to the North and South of a boundary at ~45°30'N (Fig. 2-2). They suggest that the northern domain could be considerd as a cratonic sub-continental lithospheric mantle. The southern domain lies surrounding the northern one and they merged together during the Variscan orogeny. Peridotites for the northern domain are mainly protogranular in texture, more refractory in chemical compositions with Sr-Nd isotopic compositions largely overlapping the compositional field of the European Asthenospheric Reservoir, whereas peridotites from the southern domain are coarse-granular, more fertile with MORB-like Sr-Nd isotopic compositions (Lenoir et

al., 2000; Downes et al., 2003). Both domains have been metasomatized to different degrees, with highly incompatible element and LREE enrichment more pronounced in the northern domain (Lenoir et al., 2000; Downes et al., 2003). Additionally, remarkable HFSE negative anomalies as an indicator of carbonatitic metasomatism have often been observed in xenoliths from the northern domain, but not in xenoliths from the southern domain (Lenoir et al., 2000; Downes et al., 2003; Witting et al., 2007). Thus, it has been proposed that the northern and southern domain of the FMC have been metasomatized by different types of agents, fluid/carbonatitic melt and silicate melt, respectively (Wittig et al., 2007). However, the metasomatic agents recorded in peridotites and pyroxenites from the FMC have sometimes been attributed to a deep, recycled, and enriched component, possibly related to Variscan subduction (Downes and Dupuy, 1987; Touron et al., 2008; Yoshikawa et al., 2010). *In-situ* measurements of amphibole D/H ratios in peridotites from the FMC have presented high values, which were associated with recycled surficial materials through Variscan subduction (Deloule et al., 1991).

2.4 The sampling localities

Peridotite xenoliths studied herein were sampled in two localities, both belonging to the southern FMC domain (Fig. 2-2). One is the Ringue quarry in Allègre (Fig. 2-4a), situated in a solidified lava lake that filled a maar ~3 Ma ago. In the field, xenoliths from different levels were found, including granite, gneisses, and spinel peridotites.

The other is the Razas Grand quarry in Mont Coupet (Fig. 2-4b). The volcano erupted in strombolian type 2 Ma years ago. Many wonderful volcanic bombs of different sizes containing peridotites xenoliths have been collected in this quarry.

Figure 2-4: a. Sampling in the Ringue quarry in Allègre. b. The Razas Grand quarry in Mont Coupet.

3. Analytical methods

3.1 Sample preparations

More than twenty peridotite xenoliths with diameters ranging from <1 to 15 cm were collected in each quarry. The outer basaltic shells were sawed off and the cores free of visible intrusive veins and of any weathering feature were cut into thin section size billets to retain (Fig. 3-1). After careful investigation under a binocular microscope, thin sections were polished for all the xenoliths. Then detailed petrological observations were performed on every thin section and nine samples from Allègre and eight samples from Mont Coupet were selected for electron micro-probe analysis. The rules for this first-step selection are based on different features under the microscope, e.g., modal compositions, textures, no visible veins connecting with host magmas, the colors of spinel. After EPMA, a representative subset of six samples for each locality, covering the total major element composition range, was used for trace element, Li isotope and water content measurements.

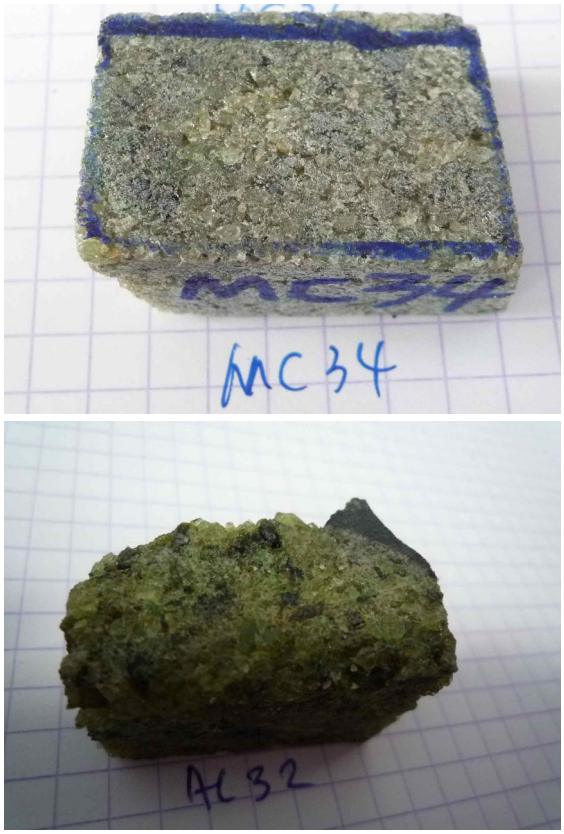

Figure 3-1: Photos of representative samples after being cut into small pieces.

3.2 Electron micro-probe analysis (EPMA)

Mineral major element compositions of Allègre samples were measured on thin sections using a Cameca SX100 electron microprobe at the Service Commun de

Microscopies Electroniques et de Microanalyses X (SCMEM), University of Lorraine (France). The operating conditions were set at an accelerating voltage of 20kV and a beam current of 20nA. Alkaline elements were analyzed first to minimize errors due to element migration with counting times of 10s on peak and 5s for backgrounds. For other elements, counting times were 20s on peak and 10s for backgrounds. A minimum of three grains was analyzed for each mineral phase in a single thin section; at least two points were analyzed on the cores and rims of each crystal (at least four points per crystal).

3.3 Laser ablation inductively coupled plasma mass spectrometry (LA-ICP-MS)

Cpx and Amp trace element compositions were determined using LA-ICP-MS at GeoRessources Laboratory, University of Lorraine (France). Double-polished thick sections (~0.15mm thick) or thin sections were ablated *in-situ* using a nanosecond excimer laser (GEOLAS Pro; 193 nm wavelength) with a spot size of 44 μm at 5 Hz with an energy density of 10 J/cm^2 per pulse. The ablation products were transported in a helium flow, mixed with argon gas, and then analyzed with an Agilent 7500 ICP-MS. A complete analysis comprises 30s for background acquisition and 50s for sample acquisition. The raw intensities of ions were recorded as a function of time. SiO_2 contents obtained from EPMA were used as an internal standard; NIST 612 and 614, analyzed at the beginning and end of the analytical session, were used as external standards. Some minor elements in Ol from Mont Coupet samples, such as Al, Ca, Ti, Cr and Ni, were also analyzed following the same procedure.

3.4 Secondary ion mass spectrometry (SIMS)

3.4.1 Basic working principles

The secondary ion mass spectrometry is an analytical technique with the ability to quantitatively detect in situ all the elements (especially for light elements, e.g., H, Li, Be, B) in the chemical periodic table with detection limits reaching part per million or below. The instrument mainly consists of a primary ion source, a mass spectrometer and a secondary ion detection system (Fig. 3-2). In present, the obstacle to the extensive application of SIMS is the dependence on standards to quantify the matrix effects strongly dependent on the chemical compositions of the analyzed materials, and the high cost for this equipment.

The primary ions, generally O^- or Cs^+ ions for geological materials (Fig. 3-3), are extracted from the sources and focused by a series of electrostatic lenses (L1, L2, L3 and L4 in Fig. 3-4a) onto the sample surface. These lenses can be adjusted to get the appropriate intensity and focusing for measuring. During an entire analytical session, the intensity of the primary ion beam usually fluctuates. If it deviates too much from the initial value, it should be adjusted again because its variation has a significant influence on the instrumental matrix fractionation (Fitzsimons et al., 2000; Hauri et al., 2006a). When the primary ion beam bombards the sample surface, ions will partly transfer their high energy (4 to 20 keV) to the matrix atoms by collision. The atoms that obtain energy in excess of their binding energy will break away from the matrix and be sputtered (Fig. 3-3). Many of the released atoms are neutral while parts of them are charged as ions (Fig. 3-3) that can be accelerated by an electric field and transferred to the mass spectrometer. These secondary ions subsequently can be selectively positive or negative depending on the polarity of the accelerating voltage. Here, it's worth noting that not only are the target ions sputtered by the primary beam, but also ions of the other elements froming the matrix and even complex ions formed by combination of two or more atoms of different elements. Commonly, complex ions with mass close to that of target ions can be produced and go through the entrance slit, which requires a mass spectrometer at high mass resolution to distinguish the ions concerned from the interference complex ions. It is achieved by combination of an electrostatic filter and a magnet sector, forming a double-focusing mass spectrometer (Fig. 3-2). The mass resolution can be controlled by adjusting the width of the entrance slit and the exit slit, which will significantly influence the intensities of secondary ions ultimately reaching the collectors. Some technical ways can be adopted to raise the secondary ion transmission (details referring to Hilton (1995)).

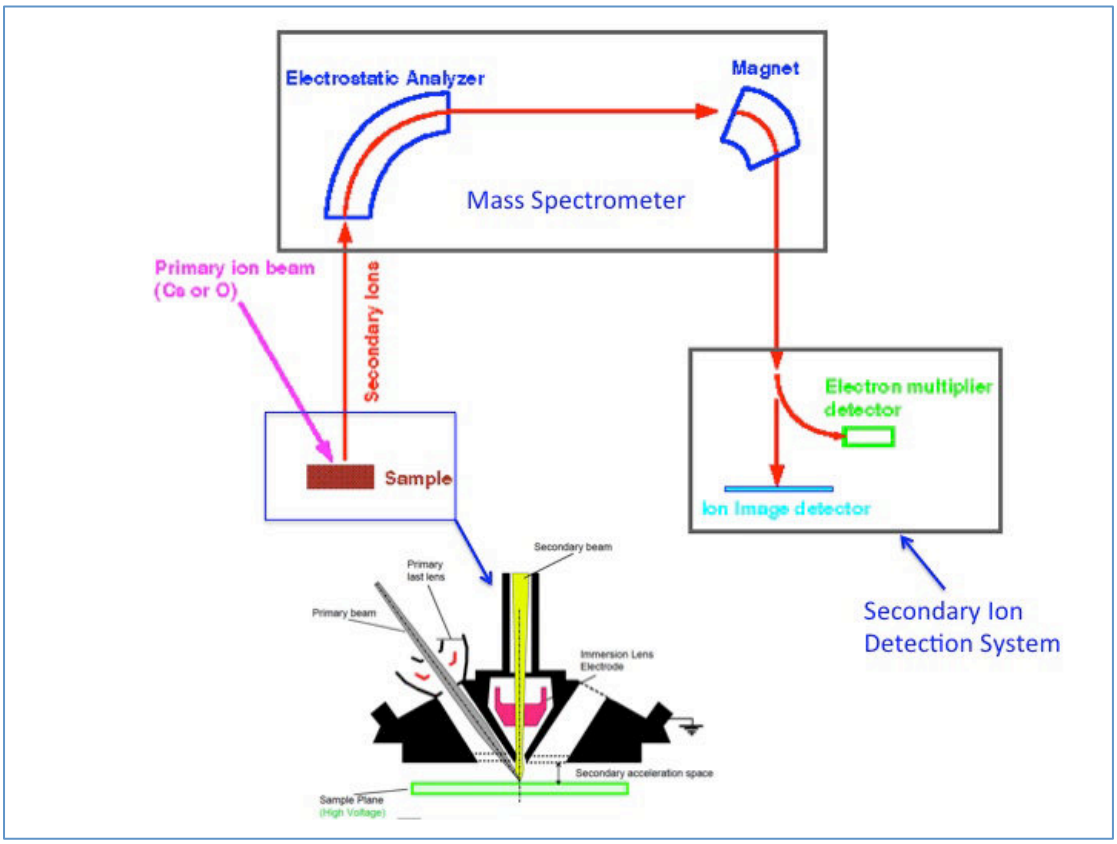

Figure 3-2: The simplified instrumental configuration of the ion probe.

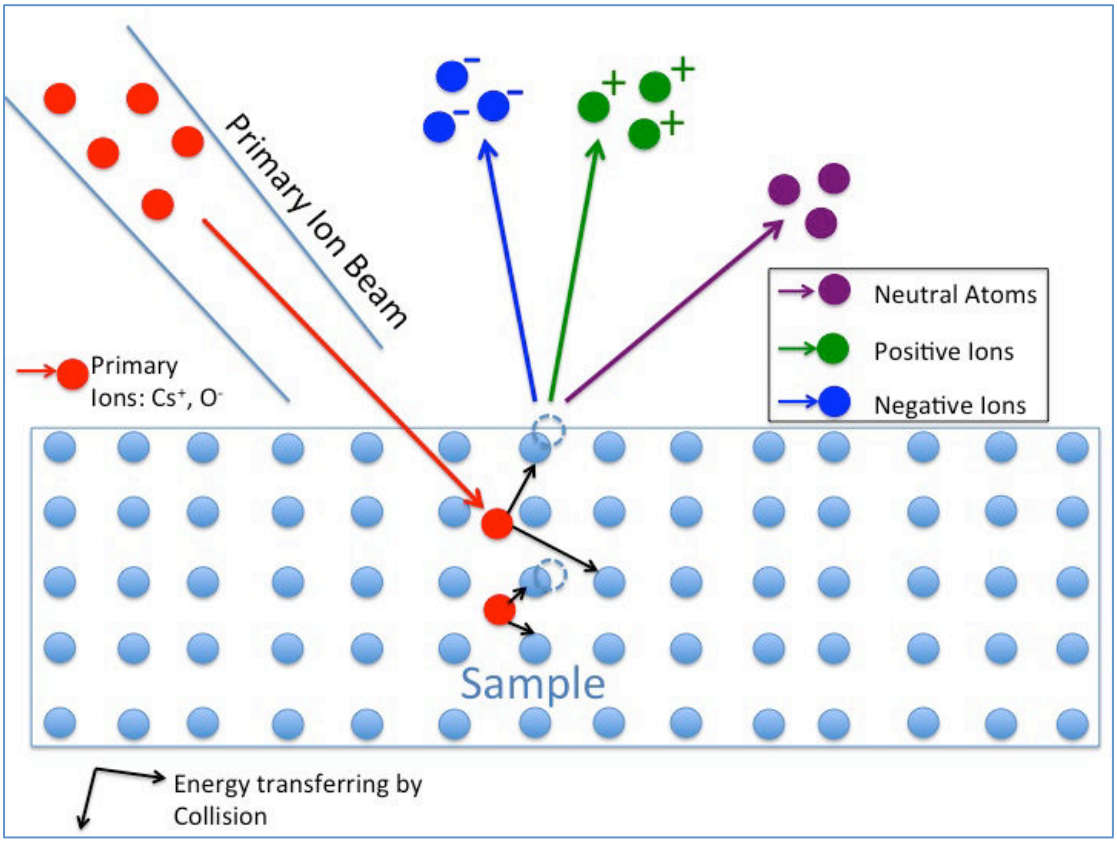

Figure 3-3: A sketch illustrating the process generating the secondary ions.

When the secondary ions pass through the exit slit, they can be detected by different devices depending on their intensities. The Faraday cup is generally used to collect ions with intensities higher than 10^6cps, whereas single-ion detectors, based on electron multiplier, will be employed if the intensities are lower than 10^6cps. A limitation of the ion counting systems is that, at high counting rates, two pulses may reach the detector almost simultaneously and that the second pulse will be lost if it arrive before the detector is reset. Therefore, the 'dead time' of the counting system need to be known to obtain accurate measurements independently of the counting rates (Deloule et al., 1991; Hilton, 1995). Moreover, each element and each isotope of the same element have their own dead times (Zinner et al., 1986), even in different analytical periods. Thus, dead times should be measured at the beginning of every analytical session.

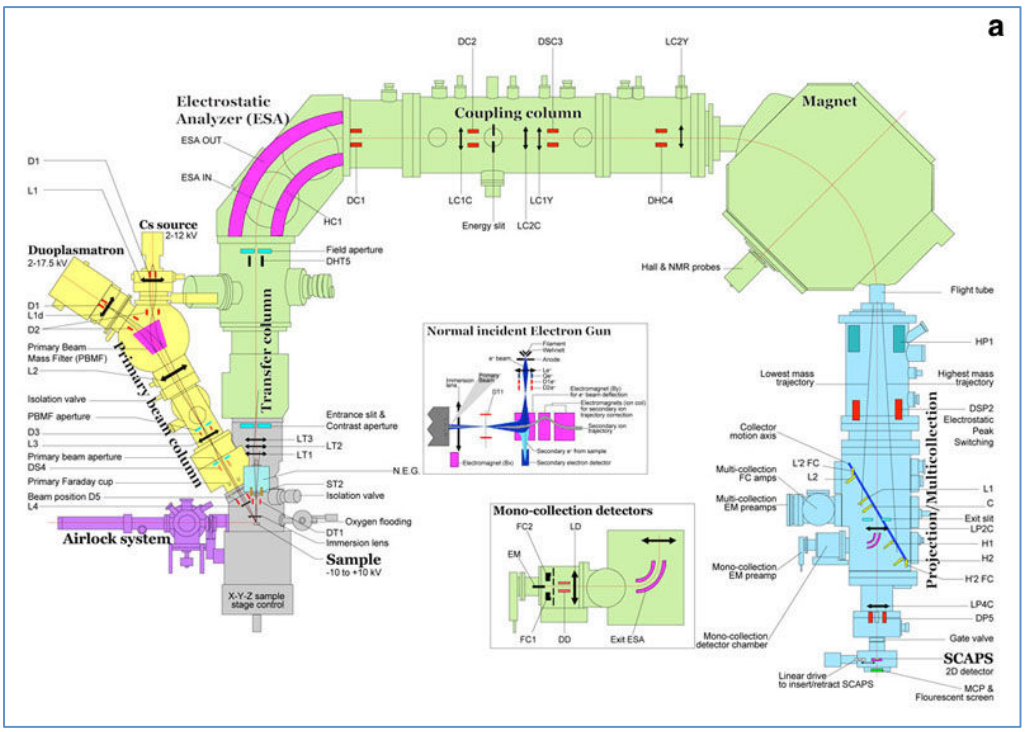

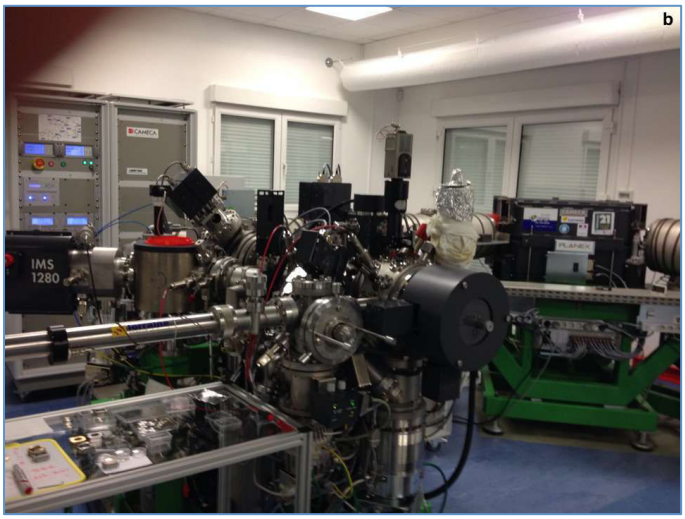

Figure 3-4: a. The detailed internal configuration of IMS 1280.
b. The photo of IMS 1270 at CRPG. This machine has been upgraded to IMS 1280 in 2015.
c. The photo of IMS 1280 (HR2).

3.4.2 Standards for Li isotopes measuring by SIMS

To better calibrate the instrumental fractionation during measuring Li isotopes in peridotite minerals by SIMS, a series of Ol, Cpx and Opx have been analyzed by electron probe and ion probe and been identified to have the potential as standards for *in-situ* Li isotope measurements (Table 4-1; Su et al., 2015). These standard minerals are from mantle xenoliths and have a wide compositional range, which can mitigate the matrix effects during calibration. Meanwhile, large quantities of measurements on different grains of each sample as well as on different positions in a single grain suggest homogeneous distributions of major elements, Li and its isotopes for each sample.

Minerals	SiO_2	FeO	MgO	Mg#	δ7Li	± 2σ	Li (ppm)
06JY06 Ol	41.5	10.1	48.3	89.48	5.3	0.29	2.2
06JY06 Opx	56.4	6.4	32.5	90.1	3.7	0.03	1.4
06JY06 Cpx	52.4	3	15.3	89.94	1.3	0.04	1.2
06JY31 Ol	42.2	9.3	48.3	90.19	4.5	0.33	2.7
06JY31 Opx	57.1	5.9	32.6	90.71	-0.2	0.21	1.3
06JY31 Cpx	53.6	2.8	16.2	91.04	-2.4	0.45	1.2
06JY29 Ol	41.9	8.6	49.5	91.12	3.1	0.13	1.7
06JY29 Cpx	53.6	2.4	15.5	91.85	-2.6	0.53	1
06JY34 Ol	41.8	8.3	49.7	91.41	3.3	0.16	1.5
06JY34 Opx	57.6	5.2	33.6	91.97	-0.8	0.25	1.1

Table 3-1: The major element compositions, Li concentrations and isotopic compositions of standard minerals measured by ICP-MS (Su et al., 2015).

3.4.3 Measuring procedure for Li isotopes

Li concentrations and isotopic compositions were measured with a Cameca IMS1270 ion microprobe at CRPG (Fig. 3-4b); thin sections were gold-coated before SIMS analysis. At least three points (the number of analyses depending on grain size) were measured from core to rim on each grain, in areas devoid of cracks and inclusions.

To sputter the secondary positive ions ($^{7}Li^{+}$ and $^{6}Li^{+}$), a primary $^{16}O^{-}$ beam was used at intensity ranging from 8 to 15nA, with diameters of 20-40 μm, slightly varying among individual analytical sessions. The 10kV secondary positive ions were counted without energy offset at a mass resolution of 1100 (M/ΔM) to separate the ^{6}LiH from ^{7}Li, in mono-collection mode. Counting rates for ^{7}Li ranged from 2×10^{4} to 2×10^{5}cps, varying with the Li content of samples and the primary beam intensities. Following a 120s pre-sputtering, twenty-five to forty cycles were accumulated with counting times of 4s, 12s and 4s for the backgrounds at mass 5.7, ^{6}Li and ^{7}Li,

respectively. Prior to each analytical session, the deadtime of the counting system was calculated according to Deloule et al. (1992). The standard minerals were used to calibrate the instrumental mass fractionation, defined as $\Delta_i = \delta^7Li_{SIMS}-\delta^7Li_{known}$ (Decitre et al., 2002). These reference minerals are from mantle xenoliths, with Mg# comparable to the corresponding mineral phases in our samples (Table 3-1). Throughout each analytical session, the standards were analyzed to monitor the fluctuation of Δ_i with temporal variations of instrumental parameters, including the primary beam intensity (Fitzsimons et al., 2000). Unlike previous studies using an IMS 3f ion probe (e.g., Beck et al., 2004; Decitre et al., 2002), reference pyroxenes and Ol do not produce the same Δ_i; pyroxenes and Ol have co-variations of -0.39 and -0.52 δ unit per Mg#, respectively (Fig. 3-5a). Thus, due to the narrow and similar range of Mg# in our samples relative to the standards, no large inaccuracy (±1‰) is introduced when applying an averaged Δ_i of individual standard minerals to calculate the δ^7Li values of the corresponding sample minerals. The absence of significant compositional variation across the analyzed grains, as well as the limited compositional range of our samples, dictate that variations in our results are not the consequence of matrix effects.

The lithium ionization yield ([Li ion counts / primary beam intensity] / Li concentration measured by ICP-MS)) was determined on the reference minerals (Fig. 3-5b), and Li concentrations were calculated by dividing the measured ^{7}Li intensity by the average ion yield of the standards. The estimated precision of this procedure is better than 20%.

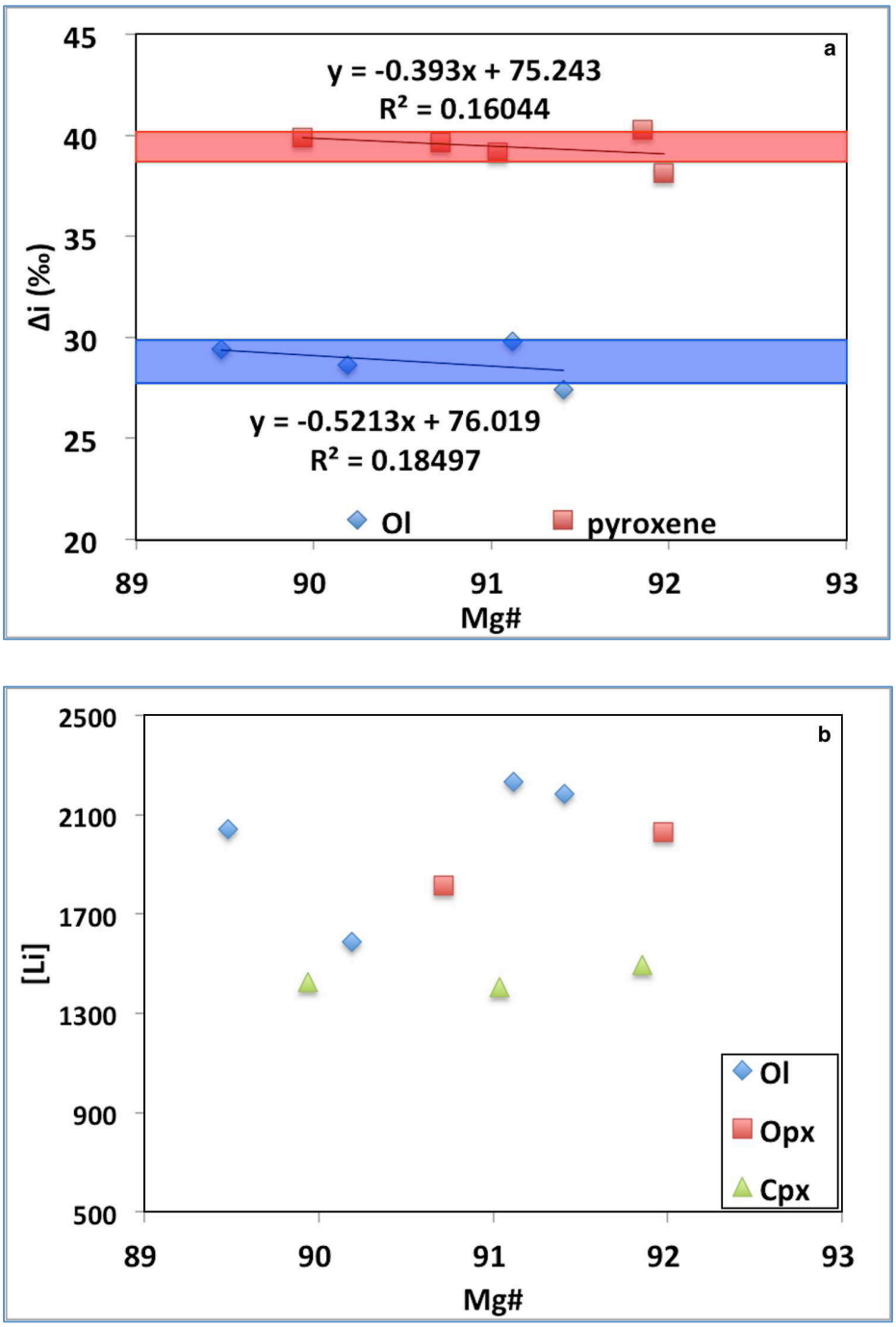

Figure 3-5: (a) Instrumental mass fractionation plotted against Mg# of olivine standards. As the R^2 values are much lower than one, there should be no compositional influence on Δ_i. We used the averaged Δ_i of individual standard minerals (pyroxenes in red and Ol in blue) to calculate the δ^7Li values of the corresponding sample minerals. (b) Lithium ion yields ([Li]) plotted against Mg# of Ol standards. No co-variation exists. For calculation, the averages of individual phases are utilized.

3.4.2 Water content by SIMS

For the samples AL32, AL47P1 and AL56, it was not possible to get thick sections

for FTIR measurements. Therefore, the water content of minerals in these samples were measured on thin sections by means of IMS 1280 ion probe (Fig. 4-3c) following a procedure similar to that of Füri et al. (2014). Several standards with known water content covering a wide range were used to calibrate the instrumental matrix effect and monitor the moisture in the sample chamber: synthetic forsterite (<0.4 ppm water); synthetic quartz (<1 ppm water); pyrope (56 ppm water); StHs glass (250 ppm water). Rims along with cores in several grains of each phase in individual samples were analyzed to check the intra-grain water homogeneity.

During analysis, the spectrometry was set to detect the signals of secondary ions, ^{17}O, $^{16}O^{1}H$, ^{18}O, ^{27}Al, ^{28}Si, and ^{30}Si, sputtered by 10 keV primary Cs^{+} ion beams of intensities 2.5-3nA with the spot size of 20μm in diameter. The electron gun has been always kept open during analysis for charge compensation. Given very low hydrogen concentrations in samples, the moisture in the background is a crucial factor to influence the accuracy of ultimate analytical results (Koga et al., 2003). A few ways have been used to diminish it. Through every measurement, the pressure of the sample chamber was always lower than 10^{-9} mbar and a liquid nitrogen trap was used to eliminate the moisture in the sample chamber. The samples were put in the airlock usually two days before being analyzed to remove water contamination on sample surface. When beginning measuring everyday morning, the degree of drying in the sample chamber was checked by operating the mass scan on the samples with the electron gun on solely. The everyday measured $^{16}O^{1}H/^{30}Si$ ratios of synthetic forsterite (<0.4 ppm water) were never higher than 0.0030. Each measurement lasted for about 15 minutes, composed of 60s pre-sputtering, 20 cycles with counting times of 2.96s for ^{17}O, and ^{18}O, and ^{27}Al, and ^{28}Si, and ^{30}Si, 12s for $^{16}O^{1}H$, 4s for the backgrounds at dummy mass 16.7 and 26.5. The mass resolving power (MRP; $M/\Delta M$) was set at 7000 to separate the peak of $^{16}O^{1}H$ from that of ^{17}O. An energy offset of 50±10 eV was applied to minimize the matrix effect. The H_2O/SiO_2 ratio of concerned samples can be calculated using an equation established by polynomial fitting between known H_2O/SiO_2 and currently measured $^{16}O^{1}H/^{30}Si$ of these standards (Fig. 3-6). The SiO_2 content of each sample is from EMPA results. The estimated errors for all the results are less than 40 ppm (±2σ).

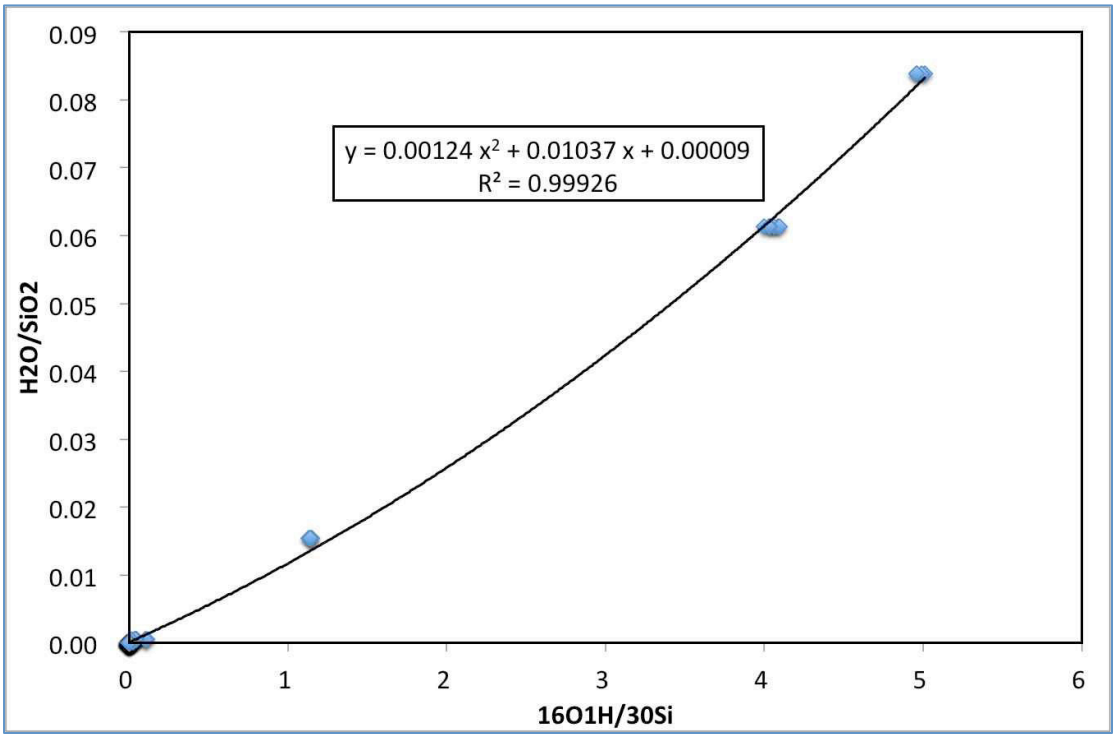

Figure 3-6: The ratios of H_2O/SiO_2 vs. measured $^{16}O^1H/^{30}Si$ ratios of standards. In this equation, y represents the H_2O/SiO_2 ratios of target samples and x represents the $^{16}O^1H/^{30}Si$ ratios of target samples measured by the ion probe. The H_2O/SiO_2 ratios of measuring samples can be calculated by substituting the obtained $^{16}O^1H/^{30}Si$ ratios into the equation, and then are multiplied by the SiO_2 content of samples from EMPA to get the water content value.

3.5 Fourier Transform Infrared (FTIR) Spectrometer

3.5.1 Rationale

When a beam of discrete-wavelength infrared light passes through a substance, and when the oscillation or rotation frequency of a group (an atom or a multi-atom assembly) in the constituent molecule is close to the frequency of the light, the atom will absorb energy of infrared light and complete the transition from the low and stable energy level to the high and excited energy level. That is, the light located at corresponding wavelengths is absorbed. The infrared spectrometry is using the information derived from the vibration and rotation frequency of the atoms consisting of a molecule to identify the molecular structure and elemental composition of a substance. An infrared spectrum of a substance can be obtained by recording the light intensity change as a function of wavelength after absorbance by the substance with a spectrometer. In an infrared spectrum, the horizontal axis represents wavelengths (λ) or wavenumbers (σ) to show the positions of absorption peaks whereas the ordinate

axis generally represents the transmittance (T%) or absorbance (A), which is intimately related to the concentration of corresponding chemical group.

Generally, each group composed of a molecule has its own distinctive absorption peaks on an IR spectrum. Even in different substances, the absorption peaks of the same functional group always occur in a narrow range of wavelengths but not at constant wavelengths, depending on the environment of the group in different molecules. Some ambient parameters can induce the absorption frequency shifting, e.g., temperature, pressure and oxygen fugacity.

Based on the Beer-Lambert law (equation 2), the concentration of absorbing species in question can be calculated using the absorbance:

$$A=kcd \qquad (2)$$

where A denotes absorbance, c the concentration of the species, d optical path, and k the absorption coefficient, which is related to chemical properties of the species (Withers, 2013). In other words, if equation 2 is invoked to calculate the concentration of the species, the absorption coefficient (k) should be firstly determined. Thus, this method is not self-calibrating and independent analytical methods are necessary to calibrate and obtain the substance-specific absorption coefficient.

3.5.2 Measuring procedure for water content

To ensure the spectra of high quality, samples are polished to wafers of 0.1 mm to 0.2 mm in thickness, much thicker than those for optical microscopy. During polishing, these sections were generally attached on glasses with epoxy, which has absorption bands at wavenumbers 2800-3000 cm^{-1} (Grant et al., 2007b). Therefore epoxy has to be thoroughly removed from sample wafers, to avoid any contribution of the epoxy on the mineral bands to calculate water content of analyzed minerals, especially for Opx. The sections were steeped in acetone for a few hours and then cleaned using ethanol for several times. Before formal measurements some spectra were collected in different zones of a wafer to check whether the epoxy remained. If

did, the same washing procedure would be repeated until no bands of epoxy in the spectra randomly collected. Prior to measurements, the samples were scanned for a full image of their thin sections under a Bruker Hyperion 3000 FTIR-microscope. Then twenty to forty grains for each phase (Ol, Opx and Cpx) were marked on the image, which will facilitate finding enough grains for analysis under the FTIR microscope.

After these preceding preparations, infrared spectra were acquired using a Bruker Hyperion 3000 FTIR-microscope attached to a Bruker Vertex 70 spectrometer (Fig. 3-7) equipped with a liquid nitrogen cooled MCT detector and a KBr beam splitter in the laboratory of infrared and Raman spectrochemistry (LASIR, Université Lille 1).

Figure 3-7: A photo of the Bruker Vertex 70 spectrometer coupled with a Bruker Hyperion 3000 FTIR-microscope.

The entire instrument was always flushed with dry air during analysis. More than twenty non-oriented grains of every mineral phase (Ol, Opx and Cpx) were analyzed under unpolarized light in the transmittance mode, with the exception of sample MC38, which is too depleted to find enough Cpx grains for analysis. Generally, one spectrum was collected close to the core of the grain, where optically clean, void of inclusion and crack, with accumulation of 256 scans at a resolution of 4 cm^{-1}. Before determining a measured position, the height of the object stage was adjusted to look

for the upper and lower surface of the grain and make sure that no visible inclusion or impurity are present along the light path. A squared aperture was used and was adjusted (30×30 to 100×100 μm^2) depending on the mineral grain size and quality. To check the intra-granular water distribution homogeneity, several large grains of Ol and Opx were selected to make profile measurements with interval of 60 μm between every two adjacent measured points.

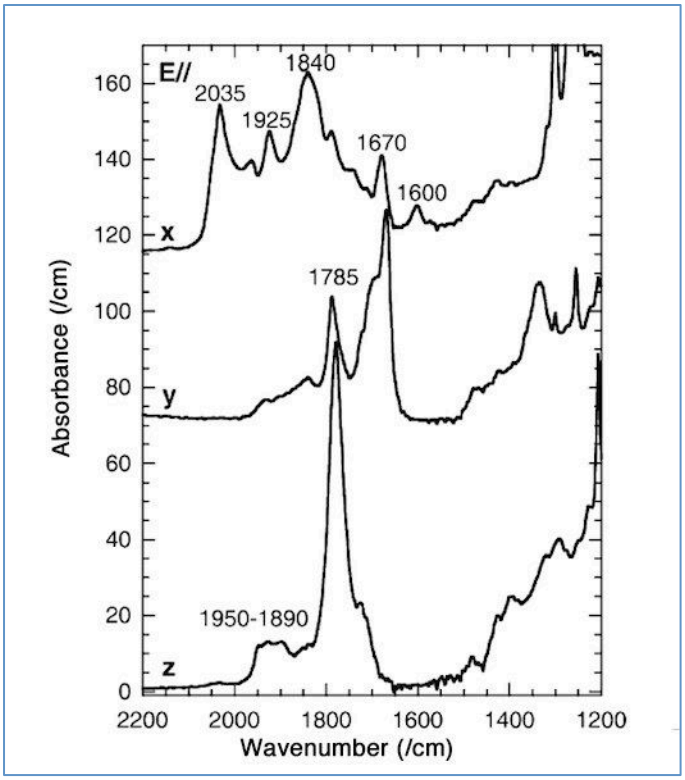

Figure 3-8: The IR spectra in the wavenumber range of 1200 to 2200 cm^{-1} with E parallel to Ol principle axes x, y and z, adopted from Lemaire et al. (2004). Si-O vibrations generate these bands.

Analyses by polarized infrared light were also performed on Ol grains where weak hydroxyl absorption peaks have occurred, mainly in sample AL44, MC34, MC36, and MC49. Different from the common method using grains whose directions relative to the principle axes have been oriented under microscope (e.g., Bell et al., 2003; Peslier and Luhr, 2006, Peslier et al., 2008, 2015), some Ol grains are identified to have directions along the principle axes of Ol because their IR spectra under unpolarized light have bands in the range of Si-O overtone vibrations (Fig. 3-8; 1200-2200 cm^{-1}), the same with those in spectra collected on grains oriented along the principle axes (Jamtveit et al., 2001; Lemaire et al., 2004). The polarized light was obtained by inserting an infrared Zn-Se grid polarizer in the beam pathway. For every grain, one spectrum was collected firstly putting the polarizer along 0° direction, then rotating the polarizer by 45° and 90° to collect one spectrum, respectively. Thus, three spectra

were acquired for each grain, among which one or two should have Si-O overtones resembling with those in the cystallographic directions. In every sample, two or three spectra can be obtained for each principle axis.

3.5.3 Quantitative calculation procedure

For Ol and pyroxene measured under unpolarized light, the averaged spectrum of all the spectra of a phase in one sample was applied to calculate the water content in that mineral (e.g., Ol; Fig. 3-9). The averaging was carried out with the aide of the KaleidaGraph software.

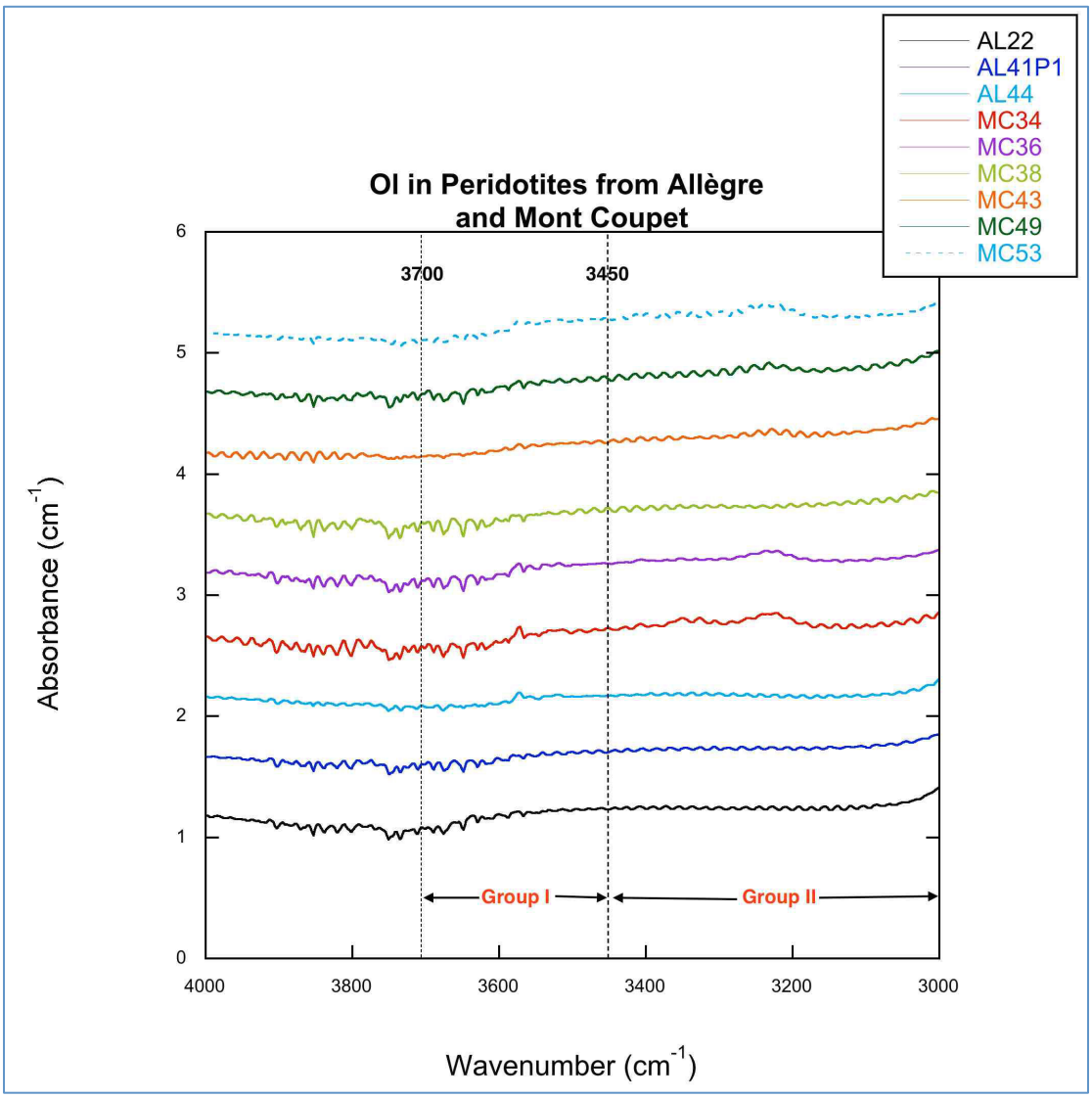

Figure 3-9: The averaged IR spectra of Ol in the structural H stretching region for each analyzed sample. All the spectra are normalized to 1 cm in thickness.

An equation modified from the Beer-Lambert law was used to transfer the

absorbance to the water H_2O content:

$$C_{H_2O}=A/\varepsilon t\gamma \quad (3)$$

in which, C_{H_2O} is the OH concentration (H_2O in wt. ppm), A is the integral absorbance which is represented here by the integrated area beneath the hydroxyl absorption bands (cm^{-2}), ε is the molar absorption coefficient ($ppm^{-1}cm^{-2}$), t is the thickness of the sample (cm), and γ is the orientation factor (Paterson, 1982). For the absorbance, the bands located at wavenumbers between 3700 and 2800 cm^{-1} for Opx, at wavenumbers between 3700 and 3000 cm^{-1} for Cpx were under consideration when integrating. The absorption coefficients determined by Bell et al. (1995) were used: 14.84 $ppm^{-1}cm^{-2}$ for Opx and 7.09 $ppm^{-1}cm^{-2}$ for Cpx. The calculation procedure for Ol is a little bit different from that for pyroxene. OH in Ol from mantle xenoliths is usually characteristiized by two types of bands in the IR absorption spectra: the group I located at wavenumbers between 3450-3700 cm^{-1}, the group II located at wavenumbers between 3000-3450 cm^{-1} (Fig. 3-9; Bai and Kohlstedt, 1993; Peslier et al., 2015). The spectra of Ol used to estimate the absorption coefficient in Bell et al. (2003) solely have bands of group I. Thus, when calculating the water content in Ol, the bands will integrated separately and equation 2 will be applied along with the absorption coefficient (0.188 $ppm^{-1}cm^{-2}$) from Bell et al. (2003) for bands in group I, whereas for bands in group II the calculation method established by Libowitzky and Rossman (1997) was used:

$$C_{H_2O}=18000\times 3A/\varepsilon_i tD \quad (4)$$

$$\varepsilon_i=246.6\times(3753-\nu) \quad (5)$$

where ε_i is the integrated molar absorption coefficient (L cm^{-2} mol^{-1}) depending on the hydrogen bond strength, which associate ε_i with the wavenumbers (ν; cm^{-1}) of corresponding bands, D is the density of concerned mineral (g cm^{-3}; here 3.3 g cm^{-3} is used for Ol). In the original pattern of equation 4, the absorbance A_i is the sum of the areas beneath the bands in the spectra acquired with the electric vector of light (E)

parallel to three principle axes (Libowitzky and Rossman, 1997), while here triple the absorbance integrated in the average spectra (3×A) takes place of A_i. The thickness of samples was measured using a digital micrometer. 1/3 was assigned to the orientation factor due to the unpolarized radiation (Paterson, 1982). The baseline was drawn by 3rd order polynomial fitting using KaleidaGraph software after chosing a few points on the spectra at higher and lower wavenumbers beyond the integrated zones. The fitted baseline was then subtracted to the primary spectrum (e.g., the calculating process of MC43 in Fig. 3-10).

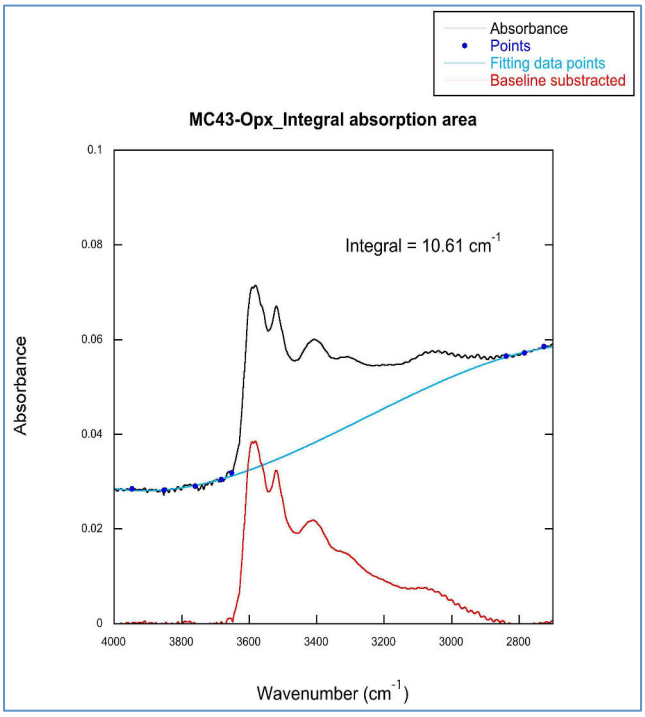

Figure 3-10: (a) The baseline obtained by polynomial fitting with aide of software KaleidaGraph. (b) The spectrum after baseline deduction (in red).

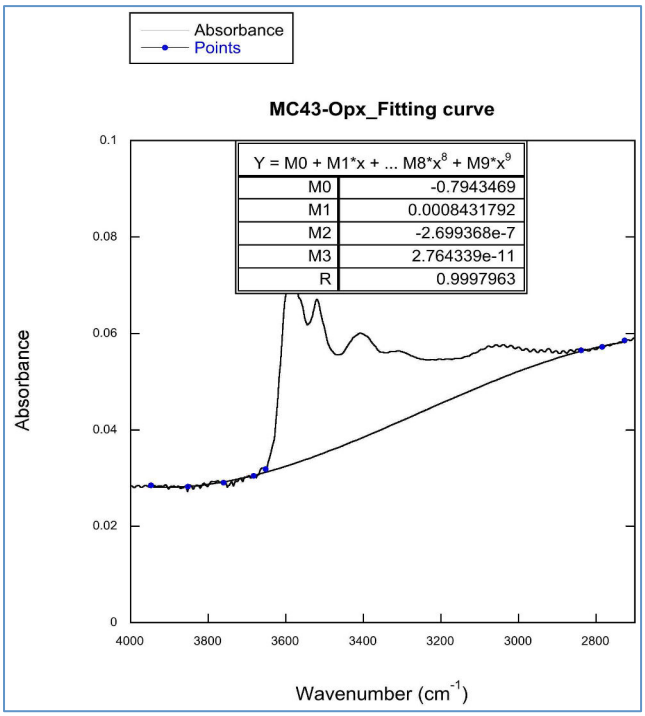

As for the spectra obtained under polarized light, the integrated absorbances when E is parallel to three principle axes (X ([100]), Y ([010]) and Z ([001]); Fig. 3-11) were added together to take place of A in equation 2 and the direction factor was assigned as one when calculating the content of water whose IR absorption caused the Group I bands. The absorption coefficient from Bell et al. (2003; 0.188 $ppm^{-1}cm^{-2}$) was applied. The content of water associated with the Group II bands was calculated using the method of Libowitzky and Rossman (1997; equation 4), where 3A was replaced by the sum of the absorbance of different directions ($A_X+A_Y+A_Z$).

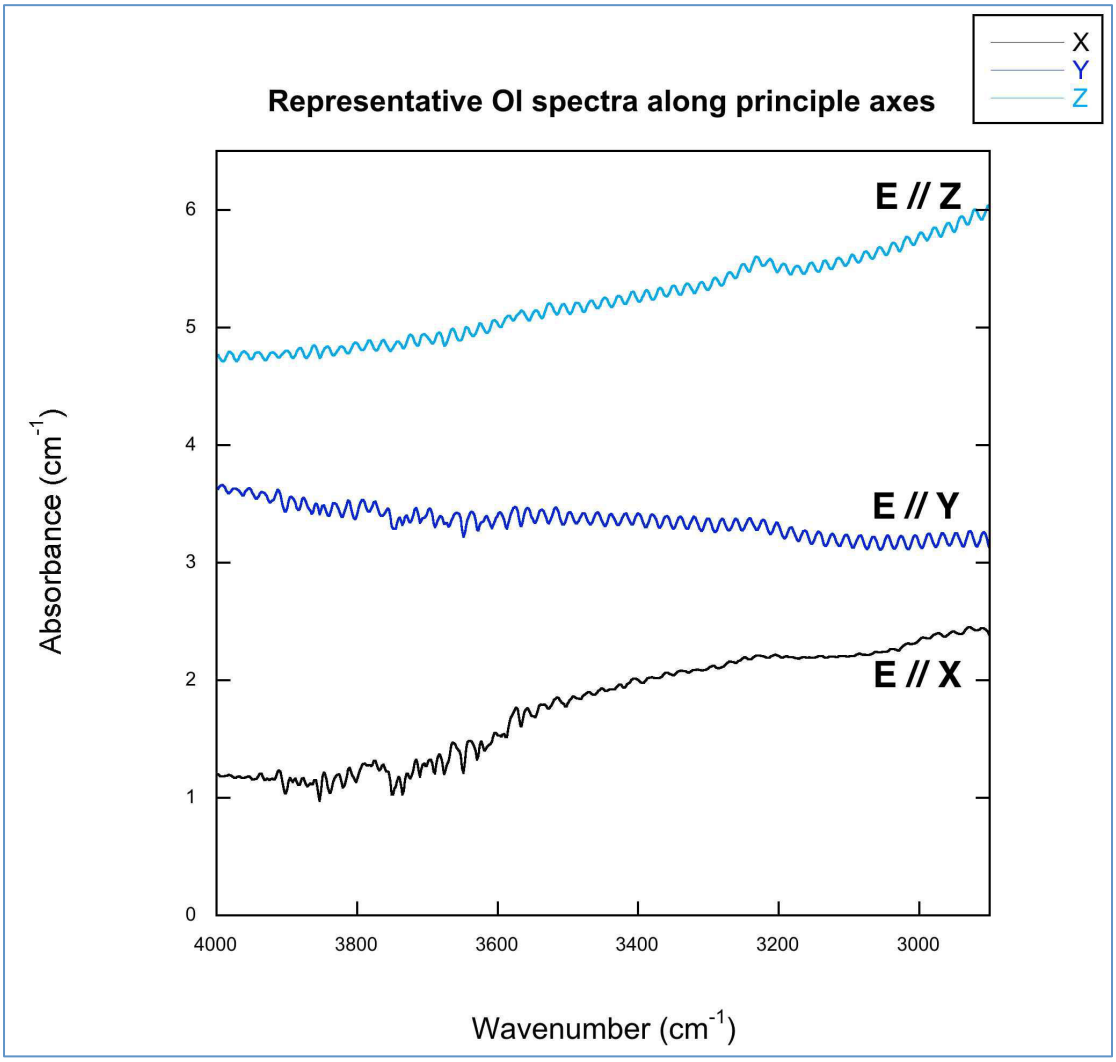

Figure 3-11: Representative Ol spectra in sample MC36 collected under polarized light with E parallel to X, Y and Z axes. The spectra are normalized to 1 cm in thickness.

4. Results

4.1 Petrological description

4.1.1 Mineral proportions and textures

According to the petrographical observations, the selected eighteen samples for petrographical observation can be divided into two groups based on the Cpx modal proportions, spinel lherzolite (Cpx up to 15%) and spinel harzburgite (Cpx < 5%; Fig. 4-1 and Table 4-1). Mineral abundances in each sample were estimated in each thin section by point counting. For each mineral phase in a given sample, the estimation was made three times in different sessions and the ultimate results shown in Table 1 are averages of three values. No hydrous phases were observed in samples from Allègre, while two samples from Mont Coupet (MC36 and MC53) contain amphibole in small proportions (less than 1%; Table 4-1).

Sample	Lithology	Proportions of minerals					Texture	T_{BK} (℃)	P (kbar)	Depth (km)	Degrees of fractional melting (%)
		Ol	Opx	Cpx	Spl	Amp					
AL22	Lherzolite	84	10	5	1	-	Protogranular	973	14.8	52	8.2
AL27P2	Lherzolite	79	10	10	1	-	Protogranular	855	10.3	36.4	-
AL32	Harzburgite	74	20	3	3	-	Protogranular	1071	9	31.6	14.8
AL41P1	Lherzolite	79	15	5	1	-	Porphyroclastic	840	9.9	34.7	13.2
AL43	Lherzolite	74	20	5	1	-	Porphyroclastic	1012	5.4	18.9	12.1
AL44	Lherzolite	70	25	5	5	-	Porphyroclastic	945	10.8	37.9	1.3
AL47P1	Lherzolite	79	12	8	1	-	Protogranular	925	9.3	32.6	2
AL48	Harzburgite	83	15	1	1	-	Protogranular	879	10.3	36.1	18.6
AL56	Harzburgite	81	15	3	1	-	Protogranular	1077	11.2	39.1	14.9
MC30	Lherzolite	60	30	5	1	-	Porphyroclastic	807	7.7	26.8	1.2
MC34	Harzburgite	80	15	3	2	-	Protogranular	834	9	31.4	10.4
MC36	Lherzolite	68	20	8	3	1	Porphyroclastic	810	15.2	53.3	-
MC38	Harzburgite	82	15	1	2	-	Protogranular	802	10.3	36.1	16.1
MC43	Lherzolite	74	15	10	1	-	Protogranular	963	8.8	30.9	2.9
MC49	Lherzolite	58	25	15	2	-	Protogranular	908	7.8	27.5	2.2
MC50	Lherzolite	64	25	10	1	-	Protogranular	779	10.9	38.3	3.8
MC53	Lherzolite	57	35	5	2	1	Porphyroclastic	763	4.9	17	-

Table 4-1: Mineral modes, textures, P-T conditions, origin depths and the degrees of partial melting calculated based on Spl Cr#. The partial melting degrees of sample AL27P2, MC36 and MC53 were not calculated due to their Cr# of Spl lower than the lower limit of the available range for the equation between Spl Cr# and partial melting degrees (Hellebrand et al., 2001). The prefixes “AL” and “MC” represent the samples from Allègre and Mont Coupet. See section 5 for P-T-depth estimates, and section 6.1 for estimates of partial melting degrees.

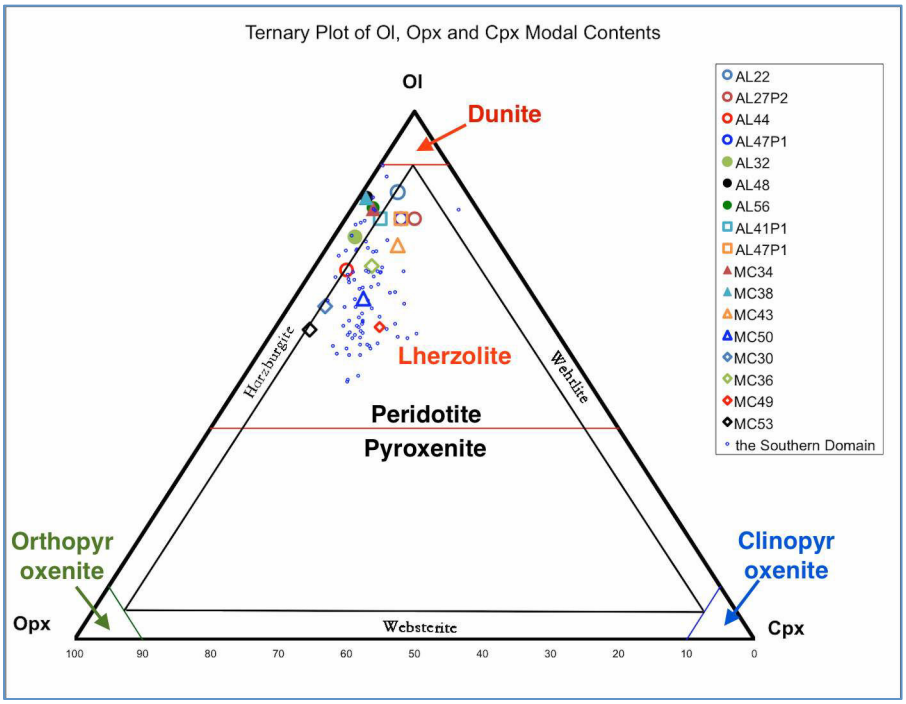

Figure 4-1: Modal compositions of samples in this study compared with literature data (smaller blue symbols). The data of samples from the southern domain are from Lenoir et al. (2000) and Zangana et al. (1997). Circles, squares, triangles and diamonds represent protogranular Allègre samples, porphyroclastic Allègre samples, protogranular Mont Coupet samples and porphyroclastic Mont Coupet samples, respectively. Filled symbols denote harzburgites and empty symbols denote lherzolites.

According to microscopic features, for example, grain size, mutual contact relationships between minerals and grain shape of minerals, a statistical survey carried out by Mercier and Nicolas (1975) has classified peridotite xenoliths from the FMC into three textural groups: protogranular, porphyroclastic and equigranular textures. The protogranular texture, the most common in our samples, is regarded as an original texture that evolved (through plastic flow and recrystallization) to porphyroclastic, and further to equigranular textures (Mercier and Nicolas, 1975; Downes and Dupuy, 1987). In protogranular samples (Fig. 4-2a; Fig. 4-3a), Ol and Opx are coarse-grained and of similar sizes (1.5-2.5mm). Cpx is either clustered with spinel (s; Spl) as a characteristic feature of this textural type (Lenoir et al., 2000; Downes et al., 2003), mainly in sample AL56 (Fig. 4-3c), or dispersed interstitially with similar-sized or larger coexisting Ol and Opx (Fig. 4-3g). No samples from Mont Coupet have the Cpx-Spl clustering texture. The intergrowth of Cpx and Spl has been considered as a result of decompression reaction between garnet and olivine during

the diapiric uprise of the lithosphere (Nicolas et al., 1987), or alternatively as an evidence for modal metasomatism. In samples with the porphyroclastic texture (Fig. 4-2b), large Ol and Opx porphyroclasts (up to 4 mm across) are embedded in smaller Ol, Opx, Cpx and Spl granuloblasts (<1mm; Fig. 4-3b, h). Some Ol grains have kink-banded texture (Fig. 4-3i). Many Opx grain boundaries are cribriform-shaped (Fig. 4-3j) and fine Cpx exsolutions have been observed in large Opx grains under the orthogonal polarized light (Fig. 4-3h). The rare equigranular samples are characterized by uniform small grains (<1mm) that display triple junctions. In several samples from Mont Coupet (e.g., MC49, MC36 and MC53), minerals don't uniformly distribute in a single thin section; Cpx is more enriched in some zones where the grain sizes are much smaller (perhaps related to stronger reaction with metasomatic melts, similar to observations of Zagana et al. (1997). Inside these zones, around some Cpx and Opx grains there exist minor hydrous minerals (perhaps Amp) can be observed via FTIR, but they are so negligible that they have been ignored and these samples, except MC36 and MC53, are still thought to be anhydrous.

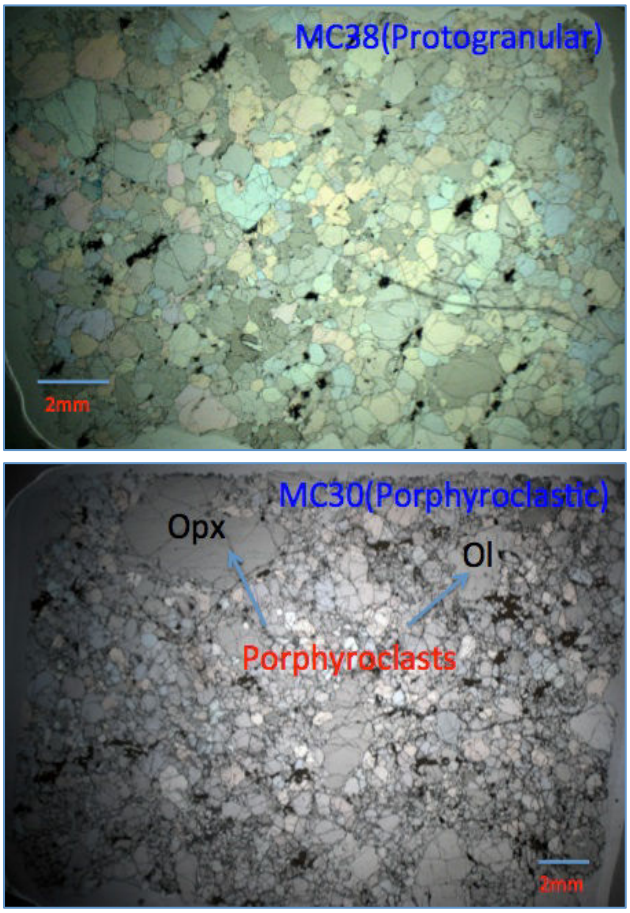

Figure 4-2: The representative photos of protogranular (a) and porphyroclastic (b) textures under transmission cross-polarized light (a) and mono-polarized light (b).

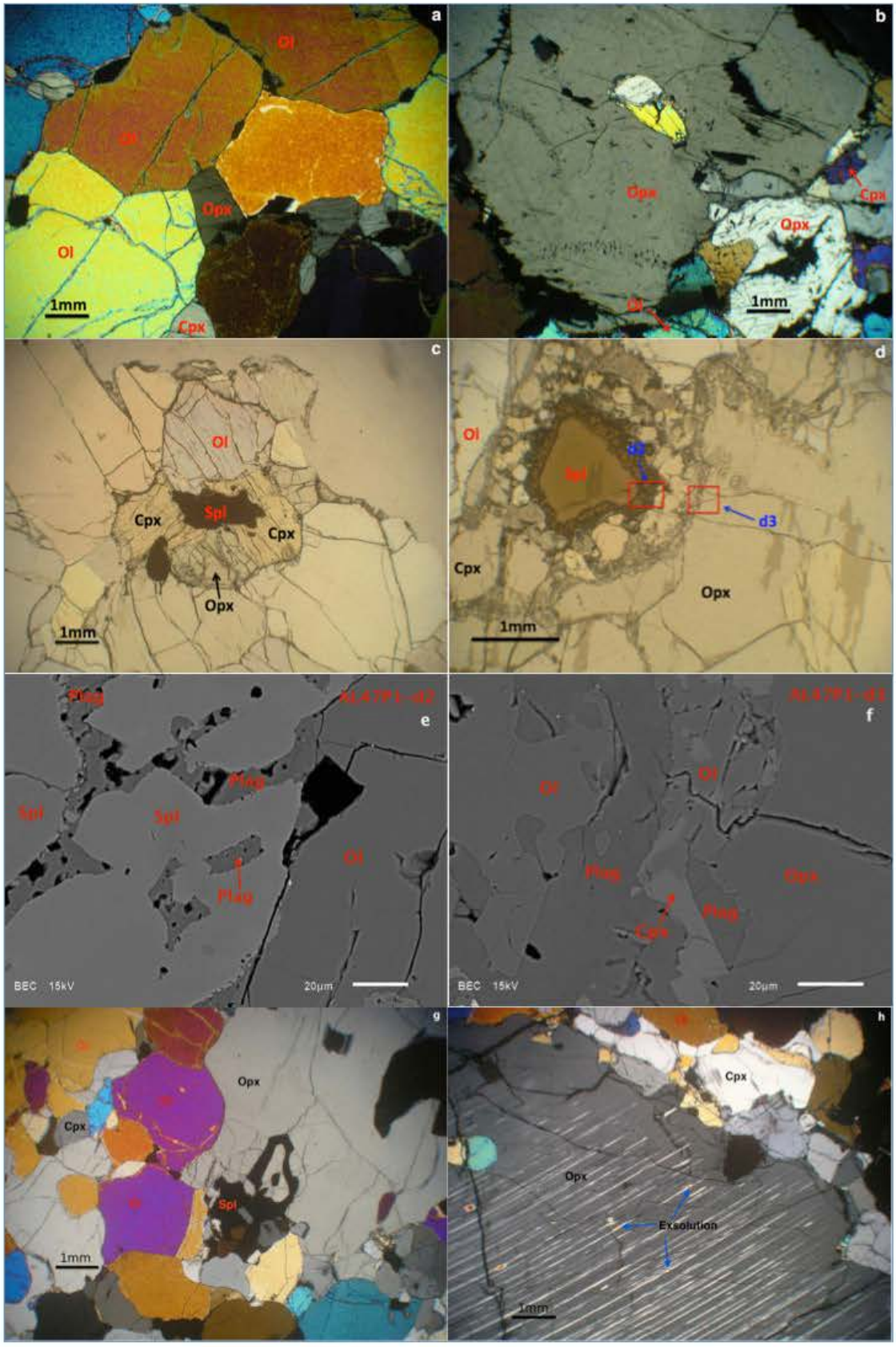
a
Ol
Ol
Opx
Ol
1mm
Cpx
b
Opx
Cpx
Opx
Ol
1mm
c
Ol
Cpx
Spl
Cpx
Opx
1mm
d
Ol
Spl
d2
d3
Cpx
Opx
1mm
e
KL4791-d2
Plag
Spl
Spl
Plag
Ol
BEC 15kV
20µm
f
KL4791-d3
Ol
Ol
Plag
Opx
Cpx
Plag
BEC 15kV
20µm
g
Opx
Cpx
Spl
1mm
h
Cpx
Opx
Exsolution
1mm

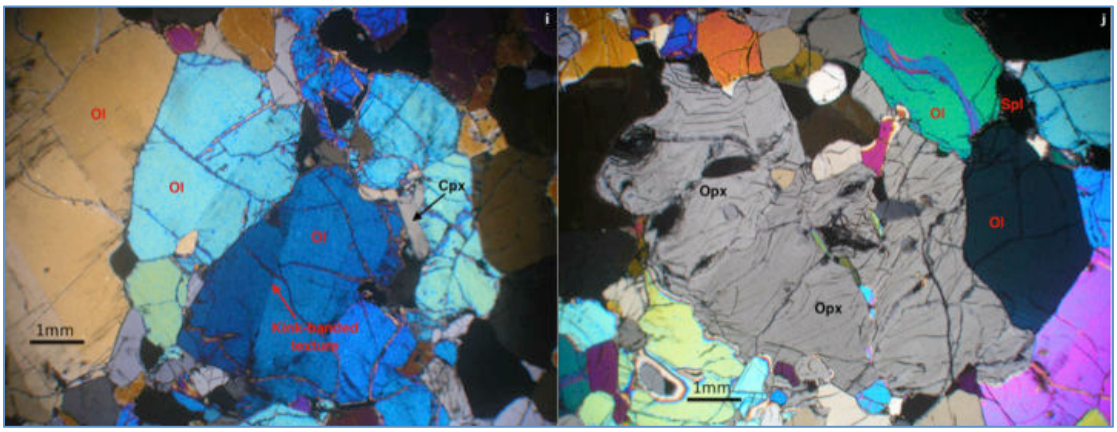

Figure 4-3: (a) Protogranular-textured sample AL56. (b) Porphyroclastic-textured sample AL37P1. Fined-grained Ol and Cpx are included in an Opx porphyroclast of about 4 mm across. (c) Cluster composed of Cpx, Ol, Opx and Spl in sample AL56. (d) Spinel with spongy-textured rim in sample AL47P1. (e) Back-scattered images of spongy texture around one spinel grain (d2). (f) Thin spongy rim around an Opx grain (d3). (g) Protogranular-textured sample MC50. Small-grained Cpx and Spl disperse interstitially with larger coexisting Ol and Opx. (h) Porphyroclastic sample MC30 with fine Cpx exsolutions in a large Opx porphyroclast. (i) Kink-banded texture in an Ol grain from sample MC30. (j) Cribriform-shaped Opx grain boundaries in sample MC53. Plag, plagioclase.

In some samples from Allègre, some signatures of interaction with the host magma (possibly once it had pooled in the lava lake) are shown as both small microlitic veins that crosscut some minerals and glass pools.

4.1.2 Spongy textures in sample AL47P1

The sample AL47P1 displays spongy-textured rims of various widths (from <50μm to 300μm; Fig. 4-3d), most commonly around Cpx and Spl. Mineral constituents in these zones mainly include fined-grained Cpx, plagioclase, Opx, Ol and Spl (Fig. 4-3e, f). Some of spongy rims are glass bearing. Although no consensus has been achieved on the origin of spongy texture in peridotite xenoliths (Ionov et al., 1995; Coltorti et al., 2000; Xu et al., 2000; Carpenter et al., 2002; Bonadiman et al., 2005, 2008; Shaw et al., 2006; Shaw and Dingwell, 2008; Su et al., 2011; Wagner et al., 2013), the interpretation of decompression-induced partial melting (Nicolas et al., 1987; Xu et al., 2000; Su et al., 2011) will be adopted in the present study. However, according to the BSE images, we can observe that the plagioclase, which exists in most reaction zones, is interwoven with primary minerals. This mineral should be produced simultaneously to the formation of the texture. And the modal contents of plag are so

high in the reaction zones that we can't believe that it is generated solely by partial melting. Additionally, the existence of plagioclase, especially the K-riched plagioclase, indicates that the process is not isochemical and the participation of exotic materials is indispensable. Thus, a participation of the infiltrated host melts is also possible (Ionov et al., 1995; Carpenter et al., 2002).

4.2 Mineral major element compositions

The EMPA results are shown in Table 4-2. The values are the averages of all the measured points on the same phase in a single sample. No significant core-rim variation was observed in any sample except sample AL4P1.

Ol	n	SiO_2	Al_2O_3	TiO_2	CaO	Na_2O	K_2O	MnO	MgO	Fe^TO	Cr_2O_3	Total	Mg#
AL22	18	41.5	0.01	0	0.05	0.01	0	0.13	49.75	9.5	0.01	101	90.3
AL27P2	12	41.28	0.01	0	0.07	0.01	0.01	0.13	49.12	10.55	0.01	101.2	89.23
AL32	14	41.62	0.02	0	0.1	0.01	0	0.12	50.68	8.38	0.03	101	91.49
AL41P1	43	40.36	0.01	0.01	0.05	0.01	0.01	0.12	52.04	8.67	0.12	101.4	91.44
AL43	16	41.53	0.03	0	0.12	0.02	0.01	0.14	50.37	8.69	0.02	100.9	91.16
AL44	13	41.26	0.02	0	0.09	0.02	0	0.13	49.43	9.66	0.02	100.6	90.1
AL47P1	16	41.54	0.02	0	0.1	0.01	0.01	0.15	49.58	9.84	0.01	101.3	89.96
AL48	12	41.49	0	0	0.04	0.01	0	0.14	50.31	8.9	0.02	100.9	90.95
AL56	38	41.9	0.02	0	0.1	0.02	0	0.15	49.76	7.26	0.02	99.23	92.42
MC30	23	40.65	0.02	0.02	0.03	0.01	0	0.16	48.42	9.64	0.01	98.96	89.93
MC34	18	41.37	0.01	0.01	0.03	0.01	0	0.12	49.84	8.46	0.02	99.88	91.29
MC36	19	41.21	0	0.02	0.02	0.01	0.01	0.14	48.51	10.01	0.04	99.96	89.6
MC38	32	41.58	0.01	0.02	0.03	0.01	0.01	0.12	49.64	8.57	0.04	100	91.15
MC43	21	41.66	0.02	0.01	0.06	0.01	0	0.13	49.16	9.63	0	100.7	90.08
MC49	33	41.98	0.01	0	0.05	0.01	0	0.13	48.66	10.01	0	100.8	89.64
MC50	15	40.92	0	0	0.02	0	0	0.13	48.54	9.61	0	99.21	89.98
MC53	18	40.79	0.01	0.01	0.03	0.01	0	0.14	48.39	10	0.01	99.39	89.59

Opx	n	SiO_2	Al_2O_3	TiO_2	CaO	Na_2O	K_2O	MnO	MgO	Fe^TO	Cr_2O_3	Total	Mg#
AL22	7	56.99	3.15	0.05	0.45	0.06	0	0.15	34.1	6.27	0.41	101.6	90.63
AL27P2	10	56.43	3.66	0.09	0.5	0.07	0.01	0.12	33.62	6.91	0.2	101.6	89.65
AL32	11	57.09	2.97	0.02	0.97	0.1	0.01	0.1	34.21	5.38	0.57	101.4	91.87
AL41P1	20	55.97	2.43	0.03	0.49	0.05	0	0.12	36.23	5.45	0.52	101.3	92.19
AL43	12	56.42	3.37	0.05	1.01	0.11	0.01	0.13	33.79	5.69	0.52	101.1	91.35
AL44	12	56.57	3.68	0.08	0.63	0.15	0.01	0.13	33.65	6.14	0.23	101.3	90.69
AL47P1	10	56.55	3.91	0.08	0.72	0.08	0.01	0.12	33.63	6.18	0.28	101.6	90.63
AL48	12	58.05	1.72	0.03	0.45	0.09	0	0.16	35.05	5.78	0.35	101.7	91.51
AL56	18	57.12	2.53	0.08	0.98	0.11	0	0.16	33.99	4.63	0.5	100.1	92.89
MC30	15	54.99	4.01	0.11	0.41	0.05	0	0.14	32.53	6.37	0.36	98.97	90.08
MC34	23	56.18	2.87	0.06	0.43	0.04	0	0.1	34.25	5.67	0.46	100.1	91.49
MC36	19	55.74	3.85	0.1	0.43	0.04	0	0.13	32.98	6.64	0.27	100.2	89.83
MC38	14	57.24	2	0.01	0.5	0.04	0.01	0.14	34.31	5.78	0.41	100.4	91.34
MC43	21	56.7	3.64	0.1	0.45	0.06	0	0.12	33.51	6.36	0.32	101.3	90.36
MC49	12	57.11	3.44	0.12	0.43	0.05	0	0.15	33.23	6.56	0.27	101.4	90.01
MC50	18	56.5	3.57	0.06	0.31	0.03	0.01	0.13	33.21	6.33	0.39	100.6	90.32
MC53	24	54.98	4	0.1	0.4	0.05	0.01	0.14	32.92	6.61	0.27	99.48	89.86

Cpx	n	SiO_2	Al_2O_3	TiO_2	CaO	Na_2O	K_2O	MnO	MgO	Fe^TO	Cr_2O_3	Total	Mg#
AL22	4	53.32	5.75	0.25	21.28	1.8	0.01	0.12	14.99	2.75	1.38	101.6	90.66
AL27P2	14	52.38	6.48	0.67	21.7	1.45	0.01	0.06	15.1	2.99	0.59	101.5	89.99
AL32	45	52.71	3.72	0.06	20.3	1.05	0	0.05	17.84	2.55	1.07	99.35	92.57
AL41P1	40	52.18	3.37	0.09	22.17	1.02	0	0.04	17.29	2.44	1.02	99.62	92.66
AL43	76	52.07	5.03	0.19	20.21	1.16	0.01	0.08	17.66	2.97	1.4	100.8	91.37
AL44	52	51.74	6.89	0.53	20.8	1.81	0.02	0.07	15.21	2.66	0.77	100.5	91.04
AL47P1	11	51.76	6.03	0.72	21.79	1.1	0	0.08	15.51	3.59	0.8	101.5	88.47
AL48	4	50.75	4.58	0.52	22.68	0.51	0.02	0.06	16.66	2.83	1.27	99.87	91.29
AL56	23	53.21	4.65	0.35	20.3	1.22	0.01	0.11	16.79	2.56	1.59	101.1	92.11
MC30	32	51.64	6.66	0.62	20.67	1.91	0	0.05	13.93	2.34	0.77	98.61	91.37
MC34	17	52.4	5.21	0.23	21.23	1.65	0.01	0.01	15.07	2.29	1.38	99.48	92.11
MC36	22	52.34	6.4	0.55	21.31	1.64	0	0.05	14.29	2.33	0.69	99.62	91.59
MC38	11	54.41	1.94	0.06	23.05	0.62	0.01	0.04	16.75	2.15	0.61	99.64	93.27
MC43	23	52.83	6.44	0.56	20.76	1.6	0	0.03	14.93	2.82	0.86	100.8	90.4
MC49	30	53.41	6.46	0.56	20.89	1.78	0	0.07	14.65	2.64	0.82	101.3	90.79
MC50	18	52.74	6.02	0.37	21.41	1.81	0	0.05	14.44	2.3	1	100.1	91.79
MC53	20	51.45	6.99	0.69	20.94	1.89	0	0.06	14.21	2.45	0.66	99.33	91.17

Spl	n	SiO_2	Al_2O_3	TiO_2	CaO	Na_2O	K_2O	MnO	MgO	Fe^TO	Cr_2O_3	Total	Mg#	Cr#
AL22	6	0.01	48.38	0.05	0.01	0.01	0.01	0.1	19.11	13.85	18.81	100.3	71.05	20.69
AL27P2	6	0.01	59.84	0.06	0	0.01	0.01	0.08	20.8	11.89	7	99.69	75.68	7.28
AL32	5	0.02	34.5	0.19	0.01	0.02	0	0.16	17.65	14.17	33.83	100.6	68.89	39.68
AL41P1	16	0.04	37.22	0.07	0.01	0.01	0.01	0.13	18.72	14.76	28.58	99.54	69.29	34
AL43	5	0.04	40.68	0.22	0.01	0.01	0.01	0.14	18.47	13.93	26.54	100	70.22	30.45
AL44	5	0.05	57.56	0.12	0.01	0.02	0	0.07	21.03	10.85	9.86	99.57	77.52	10.3
AL47P1	5	0.02	56.78	0.09	0.01	0	0	0.07	20.91	11.86	10.53	100.3	75.83	11.06
AL48	5	0.02	21.5	0.12	0.01	0.01	0	0.18	13.83	19.29	44.97	99.92	56.05	58.39
AL56	5	0.04	33.62	0.69	0.01	0.01	0	0.17	17.26	13.12	33.71	98.63	70.06	40.22
MC30	8	0.03	55.54	0.05	0	0	0	0	19.32	11.89	9.48	96.31	74.29	10.28
MC34	6	0.02	44.33	0.05	0.01	0.01	0.01	0	18.23	13.97	22.85	99.48	69.89	25.69
MC36	6	0.04	57.78	0.04	0	0	0	0	19.77	12.02	8.54	98.19	74.52	9.02
MC38	6	0.03	28.3	0.03	0	0	0	0	14.48	19.59	34.8	97.23	56.8	45.2
MC43	7	0.04	54.43	0.05	0	0	0	0	20.38	11.88	11.25	97.66	75.32	12.18
MC49	7	0.03	55.38	0.05	0.01	0	0	0	19.84	12.75	10.47	98.15	73.46	11.25
MC50	7	-0.01	54.26	0.03	0	0	0.01	0	19.41	11.9	12.44	97.62	74.38	13.33
MC53	5	0.05	59.59	0.08	0	0.01	0	0	20.01	10.95	8	98.7	76.48	8.26

Amp	n	SiO_2	Al_2O_3	TiO_2	CaO	Na_2O	K_2O	MnO	MgO	Fe^TO	Cr_2O_3	Total	Mg#	Cr#
MC36	12	42.75	14.3	2.76	11.39	3.62	0.12	0.02	16.71	4	0.78	96.46	88.15	3.55
MC53	15	42.87	14.53	3.46	11.33	3.48	0.2	0.03	16.61	4	0.78	97.28	88.08	3.48

Table 4-2: The results of electron microprobe analysis on minerals from xenoliths from Allègre and Mont Coupet. The values are the averages of all the analyzed points ('n' denotes the number) on every mineral phase in a single sample. Abbreviations: Fe^TO, total Fe; Mg#=molar (100×Mg/(Mg+Fe^T)); Cr#= molar (100×Cr/(Cr+Al)).

4.2.1 Ol

Ol forsterite (Fo) content (or Mg# = 100×molarMg/(Mg+Fe)) in samples from Allègre has larger variation range than in samples from Mont Coupet, from 89.2 to 92.4 and from 89.6 to 91.3, respectively. The former nearly encompasses the range of

Fo content in off-craton peridotites worldwide, and overlaps the Fo content range of cratonic peridotites (Boyd, 1989; Rudnick et al., 2004). The NiO content in samples from Allègre varies from 0.33 to 0.38 wt.%, seemingly lower than, although overlapping with, that in samples from Mont Coupet (0.36-0.41 wt.%). No large inter-grain variation has been observed in individual samples (for example, the standard deviation of MgO contents within every sample is less than 0.56 (in sample AL47P1)).

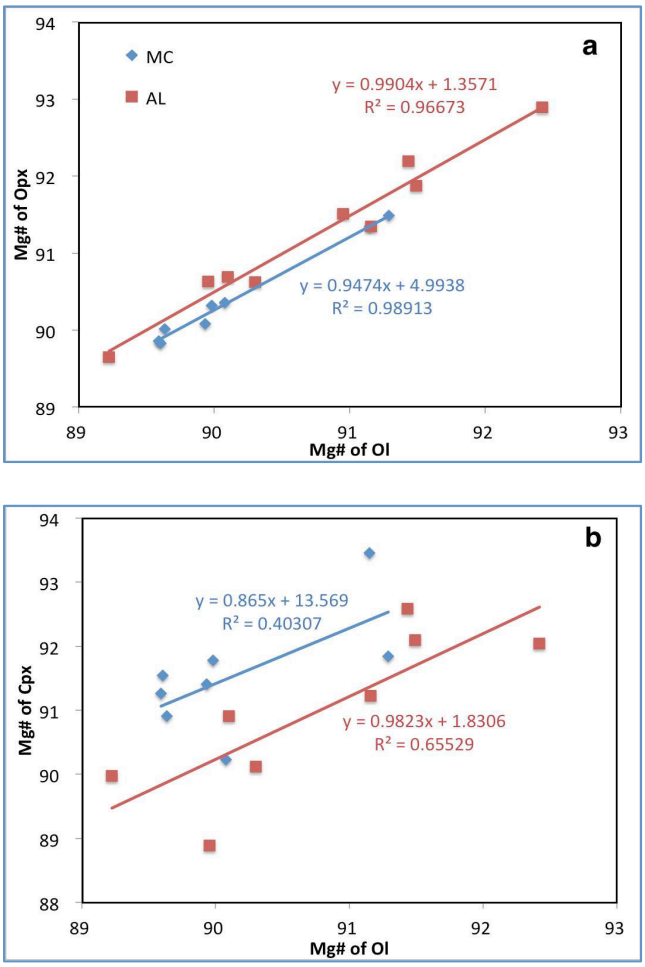

Figure 4-4: Mg# of Opx (a), Mg# of Cpx (b) plotted against Mg# of Ol in samples from Allègre and Mon Coupet. Samples from both localities have nice positive correlation between Mg# of Opx and Mg# of Ol (R^2=0.97 and 0.99, respectively). But the correlation of Cpx Mg# with Ol Mg# is not very good, reflecting the influence of metasomatism after partial melting.

4.2.2 Opx

Opx Mg# varies from 89.7 to 92.9 in samples from Allègre, and from 89.8 to 91.49 in samples from Mont Coupet, both similar to the Fo content range in respective co-existing Ol (Fig. 4-4a), which suggests a chemical equilibrium between Ol and opx after partial melting in samples from the two localities (Lee and Rudnick, 1999; Ottoloni et al., 2004). No remarkable difference occurs between Al_2O_3 content range

of Allègre and Mont Coupet samples, from 1.72 to 3.91 wt.% and from 2.00 to 4.01 wt.%, respectively. CaO content in samples from Mont Coupet cover a range of 0.31 to 0.50 wt.%, much narrower than in samples from Allègre (0.45 to 1.01 wt.%). TiO_2 content in samples from both localities has similar ranges (0.01 to 0.12 wt.%) and is slightly lower than in other peridotites worldwide; similar low TiO_2 contents have been reported in peridotites metasomatized by subduction-related melts (e.g., Zanetti et al., 1999; Grégoire et al., 2009; Woo et al., 2014).

4.2.3 Cpx

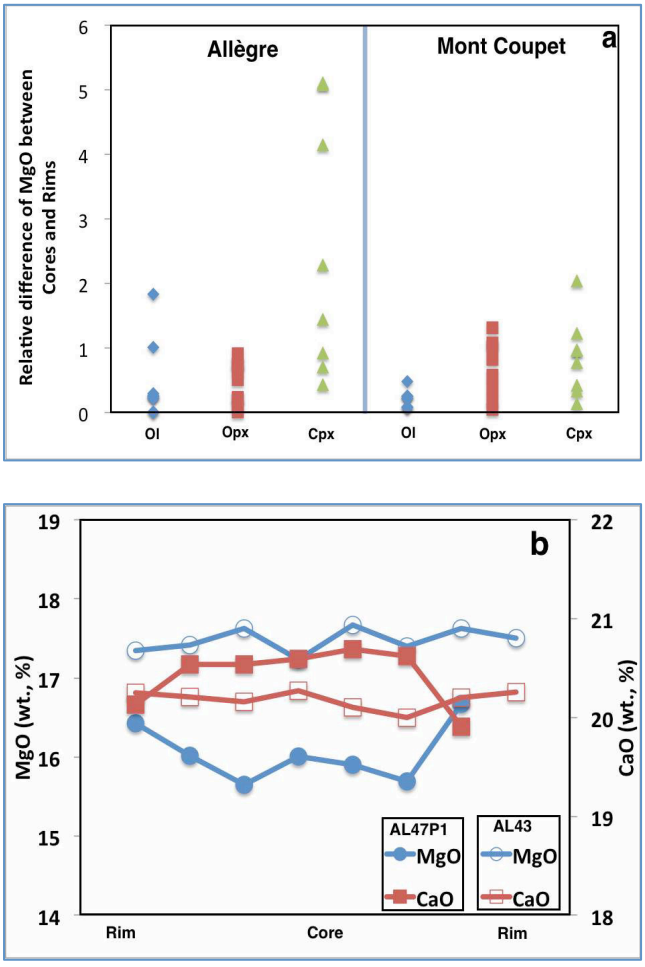

Figure 4-5: Relative difference values of MgO (a) and variation of MgO and CaO contents (b) from cores to rims in Cpx grains of AL47P1 (filled symbols) and AL43 (empty symbols). Relative difference=$(|C_{core}-C_{rim}|)/C_{core}\times100$, C_{core} (C_{rim}) denotes the MgO contents in the cores (at the rims).

Cpx in samples from both localities is Cr-diopside. Cr_2O_3 content in samples from Allègre ranges from 0.55 to 1.58 wt.%, which embraces the range of Cr_2O_3 content in samples from Mont Coupet (0.57 to 1.34 wt.%). In both localities, Mg# of Cpx in samples is higher than Fo content of coexisting Ol and Mg# of coexisting Opx, consistent with the onset order of partial melting (4-4b). Otherwise, Mg# of Cpx in

samples from both localities varies more largely than Fo content and Mg# of Opx, reflecting that Cpx is more sensitive to metasomatism following partial melting (4-4b), which is consistent with larger core-rim variations of the major element content for Cpx than for Ol and Opx (Fig. 4-5a). In some samples from Allègre, no compositional difference was observed between Cpx clustered with Spl and those scattered interstitially. Al_2O_3 content in Cpx from both localities ranges from 1.88 to 6.89 wt.%, and the lowest value occurs in sample MC38.

4.2.4 Spl

Spl is present in all the studied samples at modal abundances of 1 to 5%. Cr# (=100×molarCr/(Cr+Al)) in samples from Allègre and Mont Coupet varies from 7.3 to 58.4, and from 8.3 to 45.2, respectively. There is no Cr# distinction between Spl in Spl-pyroxene clusters and those in interstitial positions. Spl Cr# of xenoliths from both localities falls in the Cr# range of Spl from subcontinental peridotite xenoliths (Arai, 1994). The ratio of $Fe^{3+}/\Sigma Fe$, as an indicator of the redox state, has been calculated ranging from 0.18 to 0.30 in samples from Allègre, and from 0.07 to 0.24 in samples from Mont Coupet. The former falls in the range of the FMC (0.16 to 0.46), identified on the basis of a comprehensive study on xenolithic Spl in the FMC (Uenver-Thiele et al., 2014), but some values from Mont Coupet samples are much lower.

4.2.5 Amp

Only two samples from Mont Coupet (samples MC36 and MC53) contain low amount of Amp (< 1%). Eight Amp grains (four for each sample) were analyzed using electron microprobe. No large variation has been observed between different grains in a single sample as well as between core and rim in a grain. According to the amphibole nomenclature approved by the International Mineralogical Association (Leake et al., 1997), Amp in both samples can be classified into pargasite. Most major elements have similar content values in the two samples, with the exception of TiO_2, 2.76 and 3.46 wt.% in MC36 and MC53, respectively. Compared with results reported in previous studies (Touron et al., 2008; Uenve-Thiele et al., 2014), no obvious

distinction occurs in samples from Mont Coupet.

4.2.6 AL47P1

In sample AL47P1, Cpx and Spl exhibiting spongy-textured rims have major element variations only in narrow zones approaching the spongy rims of mineral grains. MgO, Cr_2O_3 and SiO_2 are enriched toward the Cpx rims while Na_2O, CaO, Al_2O_3 and TiO_2 are depleted (Table 4-3; Fig. 4-5b). It is consistent with the interpretation of the formation of the spongy texture; the basaltic components were extracted into the interstitial melt during decompression-induced partial melting while the compatible elements resided in Cpx. In other domains, no significant core-to-rim variation is observed.

Sample	Position	SiO_2	Al_2O_3	TiO_2	CaO	Na_2O	K_2O	MnO	MgO	Fe^TO	Cr_2O_3	Total
AL47P1-a	Core	51.95	6.92	0.53	20.84	1.43	0	0.2	15.8	3.04	0.78	101.5
	Rim	52.51	6.28	0.28	20.13	1.39	0.02	0	16.54	3.44	0.58	101.2
AL47P1-f	Core	52.11	7.08	0.58	20.59	1.55	0	0.09	16.01	3.37	0.78	102.2
	Rim	52.71	6.14	0.37	20.13	1.41	0	0.13	16.43	3.2	0.7	101.2
AL47P1-j1	Core	52.09	6.73	0.55	20.46	1.42	0	0.13	15.83	3.09	0.79	101.1
	Rim	52.9	6.05	0.36	19.6	1.28	0	0.1	16.99	3.38	0.58	101.2
AL47P1-j2	Core	51.13	6.59	0.54	20.53	1.46	0.01	0.05	15.97	3.2	0.76	100.2
	Rim	51.73	6.16	0.4	20.12	1.3	0.01	0.2	16.55	3.23	0.72	100.4
AL47P1-j4	Core	52.16	6.04	0.48	20.17	1.26	0.01	0.01	16.54	3.42	0.71	100.8
	Rim	51.47	5.95	0.3	20.12	1.39	0.01	0.1	16.71	3.53	0.62	100.2

Table 4-3: The results of electron microprobe analysis on cores and rims of spongy-textured Cpx from sample AL47P1. Abbreviations: Fe^TO, total Fe.

4.3 Trace element compositions

Cpx and Amp trace element compositions are reported in Table 4-4. In each sample, more than 7 Cpx grains were analyzed at the cores, and the rims of 1 to 4 large grains were analyzed to monitor core-to-rim trace element homogeneity. Cpx rims are largely enriched in Sr, La, and Ce only in sample AL47P1. In sample MC36 and MC53, ten and six Amp grains, respectively, were analyzed at the cores for trace element compositions. The Amp grains are too small to find grains to make separate measurements at rims. No significant variation was observed among different Cpx (or Amp) grains in any given sample; thus, we will use the average contents of individual samples in the following discussion.

4.3.1 Cpx in samples from Allègre

The Cpx chondrite-normalized rare earth element (REE) distribution patterns vary greatly among the six analyzed samples from Allègre (Fig. 4-6a). Cpx in sample AL44 is highly depleted in light REE (LREE) relative to middle REE (MREE), and has a nearly flat transition from MREE to heavy REE (HREE) ($(La/Yb)_N$=0.1; $(Sm/Yb)_N$=0.8, the subscript 'N' represents normalization to chrondrite; McDonough and Sun, 1995). In contrast, REE distributions of Cpx in samples AL22 and AL47P1 are spoon-shaped, with steep inflections from Nd to La, and nearly flat from MREEs to HREEs ($(La/Sm)_N$=3.9 and 11.8, respectively; $(Sm/Yb)_N$=0.9 and 0.8, respectively). Cpx from samples AL32 and AL41P1 are enriched in LREE compared to HREE, and chondrite-normalized element contents decrease continuously from La to Lu ($(La/Yb)_N$=79 and 46.7, respectively; $(Sm/Yb)_N$=6.4 and 3.7, respectively). The REE distribution pattern of Cpx in sample AL56 is distinct due to higher contents of most elements except La and Ce (ΣREE=211.1ppm). Moreover, in this sample, the chondrite-normalized concentrations are depleted in LREE compared to MREE, and decrease nearly linearly from Nd to Lu.

Allègre	Cpx						Mont Coupet	Cpx						Amp	
Sample	AL22	AL32	AL41P1	AL44	AL47P1	AL56		MC34	MC36	MC38	MC43	MC49	MC53	MC36	MC53
n	13	13	14	18	14	12		16	21	13	13	12	18	10	6
Ba	0.84	0.37	0.68	0.22	0.35	0.84		0.56	0.51	0.89	0.47	0.6	0.32	118.96	3.55
Th	1.55	0.66	1.75	0.03	1.36	0.11		0.42	0.05	0.45	0.23	0.22	0.03	0.05	0.06
U	0.57	0.28	0.5	0.07	0.42	0.08		0.57	0.03	0.22	0.14	0.15	0.03	0.03	0.05
Nb	0.1	0.75	0.08	0.04	0.13	1.03		0.3	0.2	0.09	0.06	0.12	0.06	11.24	0.64
La	6.9	47.32	29.33	0.24	27.05	15.75		8.66	0.72	8.41	1.06	3.77	0.83	1.33	1.31
Ce	9.43	107.68	45.99	1.69	26.53	72.68		10.43	2.33	12.43	3.52	4.77	3.46	3.44	5.25
Sr	109.59	400.02	272.78	43.32	236.5	218.35		104.31	50.47	69.16	59.58	78.13	63.34	141.05	186.32
Nd	4.1	31.81	10.36	3.11	4.97	70.78		5.6	3.22	2.5	4.6	4.21	4.68	4.85	7.14
Zr	25.12	5.61	9.62	23.11	25.92	116.2		25.81	28.1	1	39.76	34.82	36.86	27.63	35.5
Hf	0.48	0.25	0.28	0.73	0.95	3.52		0.92	0.94	0.1	1.34	1.2	1.23	0.8	1.11
Sm	1.15	2.49	1.49	1.48	1.48	15.88		1.75	1.47	0.33	1.58	1.51	1.53	2.01	2.52
Eu	0.44	0.73	0.46	0.67	0.63	4.76		0.56	0.66	0.09	0.78	0.66	0.71	0.98	1.08
Ti #	1468.39	359.61	559.39	3146.55	4305.28	2080.58		1261.63	2888.48	59.95	3018.46	3072.17	3470.61	13685	17021.67
Gd	1.52	1.42	1.28	2.43	2.42	13.61		2.21	2.53	0.21	2.41	2.26	2.49	3.52	4.32
Dy	1.82	0.97	0.93	3.35	3.31	10.13		2.04	3.43	0.22	3.42	3.43	3.36	5.01	5.5
Y	11.36	5.67	4.87	18.36	18.04	42.38		11	18.77	1.21	18.51	20.03	19.76	29.63	31.67
Er	1.35	0.54	0.51	2.26	2.13	4.32		1.19	2.1	0.11	2.23	2.34	2.14	3.37	3.62
Yb	1.36	0.43	0.45	2.18	2.06	2.87		1.35	2.05	0.27	1.83	1.94	1.87	3.65	3.1
Lu	0.22	0.06	0.07	0.3	0.28	0.37		0.21	0.27	0.03	0.29	0.31	0.29	0.52	0.49
$(La/Yb)_N$	3.6	79	46.7	0.1	9.4	3.9		3.2	0.3	16.4	0.4	1.6	0.3	0.4	0.3
$(La/Sm)_N$	3.9	12.3	12.7	0.1	11.8	0.6		4.6	0.3	22.2	0.4	1.4	0.3	0.3	0.3
$(Sm/Yb)_N$	0.9	6.4	3.7	0.8	0.8	6.2		1.4	0.8	1.4	1	0.9	0.9	0.6	0.9
Zr/Hf	52	23	35	32	27	33		28	29.9	10.5	29.7	29	30.1	34.6	31.9
Ti*	0.43	0.08	0.17	0.59	0.83	0.06		0.3	0.5	0.1	0.5	0.6	0.6	1.77	1.89
Zr*	0.78	0.03	0.15	0.72	0.65	0.23		0.6	0.9	0.1	1	0.9	0.9	0.6	0.57
Ti/Eu	3337.3	492.6	1216.3	4696.3	6833.8	437.1		2258	4348	653	3858	4626	4892	13950	15785
U/Th	0.4	0.4	0.3	2.3	0.3	0.7		1.4	0.6	0.5	0.6	0.7	0.9	0.6	0.8

Table 4-4: Trace element abundances in ppm for Cpx in Allègre xenoliths, Cpx and Amp in xenoliths from Mont Coupet. # The Ti concentrations in Allègre Cpx are calculated from EMPA results. The subscript 'N' represents normalization to the compositions of Chondrite (McDonough and Sun, 1995). $Ti^*=2\times Ti_n/(Eu_n+Gd_n)$; $Zr^*=2\times Zr_n/(Nd_n+Sm_n)$ where the subscript 'n' represents normalization to the primitive mantle. 'n' denotes the analyzed numbers on Cpx or Amp in each sample.

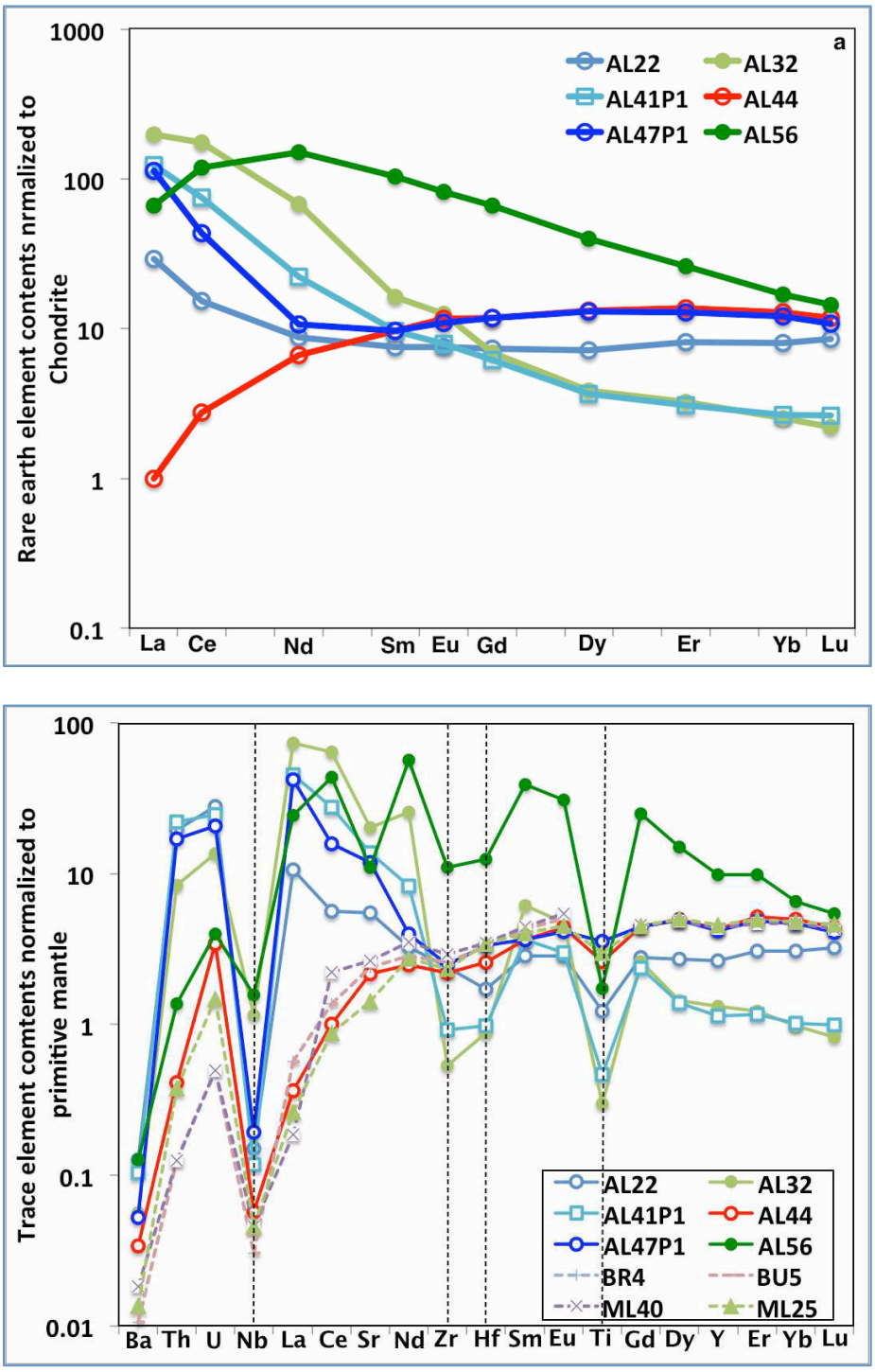

Figure 4-6: REE composition patterns normalized to Chondrite (a) and extended trace element composition patterns normalized to the primitive mantle (b). The dashed lines in (b) represent three samples from other localities in the southern domain for comparison with samples from Allegre (ML40 and ML25 from Touron et al. (2008); BR4 and BU5 from Yoshikawa et al. (2010)). Normalized values are from McDonough and Sun (1995).

Extended trace element compositions of Cpx (Table 4-3) exhibit negative High Field Strength Elements (HFSE; Nb, Zr, Hf, and Ti in this study) anomalies when

element abundances are normalized to the primitive mantle (McDonough and Sun, 1995; Fig. 4-6b). All samples exhibit strong negative Nb anomalies. The magnitudes of negative Ti anomalies ($Ti^*=2\times Ti_n/(Eu_n+Gd_n)$; the subscript 'n' represents normalization to the primitive mantle) gradually decrease from sample AL56 ($Ti^*=0.06$) to sample AL47P1 ($Ti^*=0.83$). Samples AL32, AL41P1 and AL56 exhibit strong negative Zr and Hf anomalies; sample AL47P1 displays small negative Zr and Hf anomalies, and samples AL22 and AL44 do not show anomalies (Table 4-3). Due to high LREE contents, Cpx from samples AL32 and AL56 display negative Sr_n anomalies compared to adjacent elements (Ce_n and Sm_n), in contrast to absent or weak positive anomalies in other samples. In all the Allègre samples, Th and U are enriched to different degrees (Th_n and U_n values as high as 19.5 and 27.9, respectively, in sample AL22; Fig. 4-6b).

4.3.2 Cpx in samples from Mont Coupet

The chondrite-normalized REE distribution patterns of Cpx in Mont Coupet peridotites are significantly different from those in Allègre samples (Fig. 4-6a and 4-7a). Cpx in sample MC43 is slightly depleted in LREE relative to middle MREE, and has a nearly flat transition from MREE to HREE ($(La/Yb)_N=0.41$; $(Sm/Yb)_N=0.96$). It is similar to sample AL44 but less depleted than the latter. Cpx chondrite-normalized REE distribution patterns in Amp-bearing sample MC36 and MC53 ($(La/Yb)_N=0.25$ and 0.32, respectively; $(Sm/Yb)_N=0.80$ and 0.91, respectively), resemble with that in sample MC43. In sample MC49, the normalized pattern of Cpx shows obvious enrichment in La compared with other elements and nearly no variation from Ce_N to Lu_N with $(La/Yb)_N$ and $(Sm/Yb)_N$ values of 1.39 and 0.87, respectively. The sample MC34 is similar to the sample AL22, exhibiting upward inflection from Nd to La, and flat transition from MREE to HREE ($(La/Sm)_N=3.20$; $(Sm/Yb)_N=1.44$). The chondrite-normalized REE distribution pattern of Cpx in sample MC38 is totally different. The sample is extremely depleted in MREE and HREE with Gd_N and Er_N values of 1.03 and 0.67, respectively, whereas it is highly enriched in LREE with La_N value of 35.47. The pattern shows linearly rising from Er to La. On the whole, to compare the patterns of Cpx from the two localities, a much

stronger LREE enrichment is a characteristic of Cpx in xenoliths from Allègre, and Cpx in one sample from Mont Coupet (MC38) displays the most pronounced depletions in MREE relative to HREE.

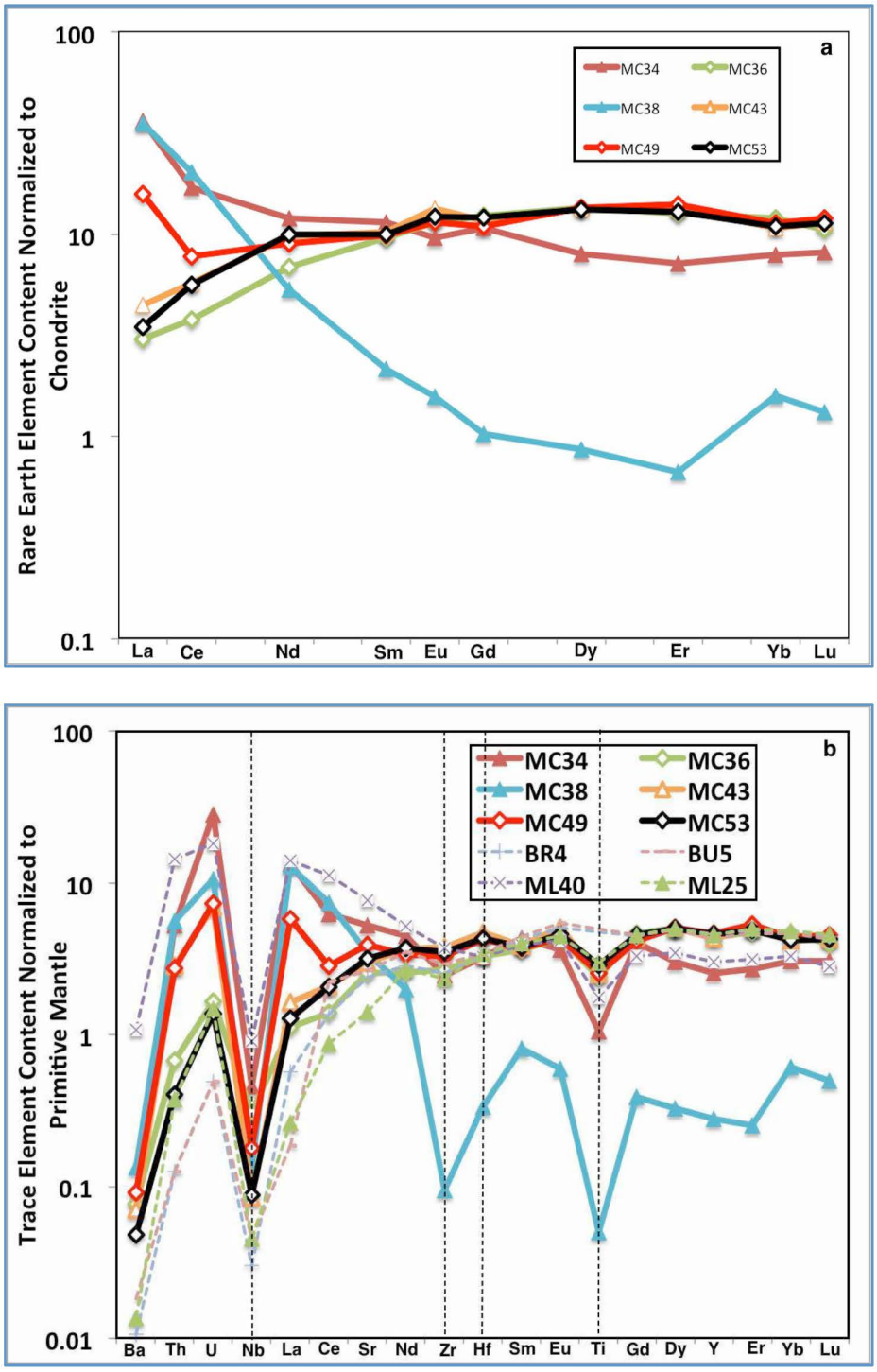

Figure 4-7: REE composition patterns in Cpx from Mont Coupet samples normalized to Chondrite (a) and extended trace element composition patterns normalized to the primitive mantle (b). The dashed lines in (b) represent four samples from other localities in the southern domain for comparison with samples from Allègre (ML25 and ML40 from Touron et al. (2008); BR4 and BU5 from Yoshikawa et

al. (2010)). Normalized values are from McDonough and Sun (1995).

When considering the extended trace element compositions of Cpx in xenoliths from Mont Coupet, they also show negative Ti and Nb anomalies when element abundances are normalized to the primitive mantle (Fig. 4-7b). The Nb anomaly also occurs in all the Mont Coupet samples. The magnitude of negative Ti anomalies gradually decreases from sample MC38 (Ti*=0.10) to sample MC53 (Ti*=0.63). A very strong negative Zr anomaly is shown by sample MC38. Sample MC34 displays a slight negative Zr anomaly and in other samples no Zr anomaly is observed. Similar to LREE, U and Th enrichment in samples from Mont Coupet is not as high as that in samples from Allègre.

4.3.3 Amp in sample MC36 and MC53

Amp REE have similar chondrite-normalized distribution patterns in sample MC36 and MC53 (Fig. 4-8a). They are very comparable with the patterns of coexisting Cpx, exhibiting LREE depletion and nearly flat transition from MREE to HREE in spider diagrams ($(La/Yb)_N$=0.26 and 0.30; $(Sm/Yb)_N$=0.61 and 0.90 in sample MC36 and MC53, respectively). This similarity between REE content in Cpx and Amp attests for the equilibrium between those two phases (e.g., Chazot et al., 1996).

According to the extended trace element spiderdiagrams, Amp in these two samples have a slightly different patterns (Fig. 4-8b). Amp in sample MC36 is enriched in Nb relative to neighboring elements (U and La) whereas for sample MC53 the diagram displays a slight negative anomaly in Nb. The similar difference also occurs in Ba. Compared with the distribution patterns of coexisting Cpx, those of Amp have significant distinctions: Sr, Ti enrichment, and Zr, Hf depletion.

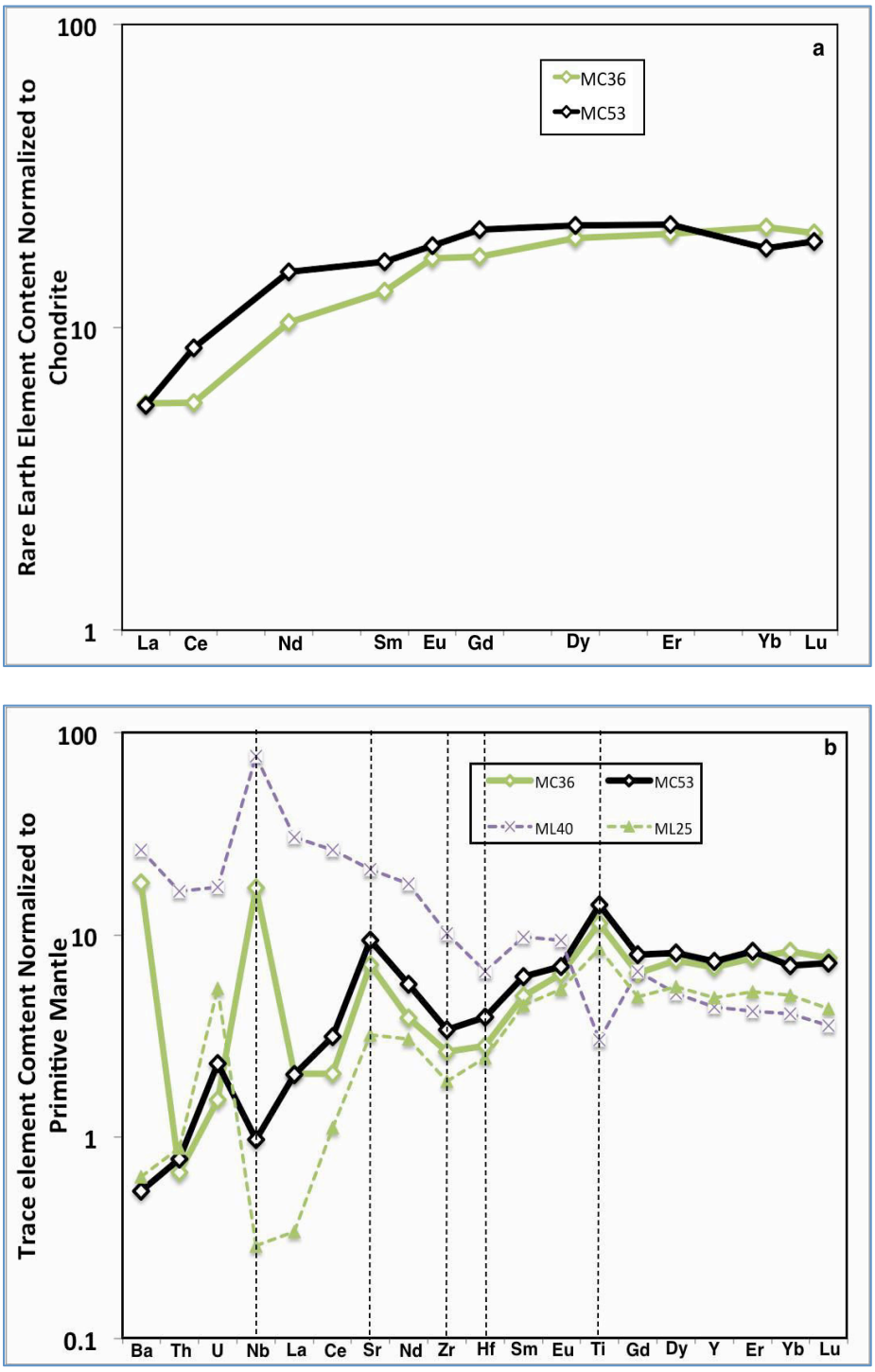

Figure 4-8: REE composition patterns in Amp from Mont Coupet samples normalized to Chondrite (a) and extended trace element composition patterns normalized to the primitive mantle (b). The dashed lines in (b) represent two samples from other localities in the southern domain for comparison with samples from Allègre (ML25 and ML40 from Touron et al. (2008)). Normalized values are from McDonough and Sun (1995).

4.3.4 Al, Ti, Cr and Ni in Ol from Allègre and Mont Coupet

Although Ca concentrations in Ol from Allègre and Mont Coupet have also been measured, the results of different analyzed points in a single sample, even on a same grain, vary so largely that they will not be discussed. The results of Al, Ti, Cr and Ni concentrations are reported in Table 4-5.

Sample	n	Al	Ti	Cr	Ni
AL22	16	44.8	8.0	52.4	3071.7
AL32	12	130.2	8.5	172.6	3255.6
AL41P1	14	48.5	8.4	66.7	3162.0
AL44	12	135.7	22.8	67.0	3303.3
AL47P1	16	125.2	19.7	87.2	2901.1
AL56	18	134.6	42.0	192.0	3072.3
MC34	12	37.3	6.0	28.4	3145.1
MC36	14	16.6	6.9	3.7	3105.6
MC38	11	13.9	3.7	23.7	3140.5
MC43	10	92.5	14.0	46.8	3267.0
MC49	8	51.3	8.9	23.4	3113.9
MC53	13	27.6	8.3	8.0	3085.4

Table 4-5: Al, Ti, Cr and Ti concentrations (in ppm) in Ol from Allègre and Mont Coupet samples, measured by LA-ICPMS. 'n' denotes the numbers of analyzed points on Ol in each sample.

Al concentrations ranging from 13.9 to 135.7 ppm don't have obvious co-variation with Fo but show a positive relationship with the calculated temperatures, consistent with temperature dependence of this element (Fig. 4-9a and b; De Hoog et al., 2010). Ti concentrations have a range of 3.7-42.0 ppm, falling in the range of most mantle Ol (<70 ppm; Foley et al., 2013) and closer to the lower end of the range defined by De Hoog et al. (2010; <0.4-290 ppm) on the basis of a large dataset. Weak dependence on temperatures can be observed (Fig. 4-9c) and the highest Ti concentration was obtained in sample AL56. De Hoog et al. (2010) have established a linear relation connecting Ti concentrations in Ol with TiO_2 in coexisting Cpx (wt. %): TiO_2^{Cpx} (wt. %)=Ti^{Ol} (ppm)/100 for spinel peridotites. However, the Ti concentrations in Ol from Allègre and Mont Coupet samples calculated according to this equation are much higher than those measured values from LA-ICPMS. The cause of this inconsistence is likely to lie in a Ti partitioning disequilibrium between Ol and Cpx indeed existing in Mont Coupet samples, which is verified by the ratios of Ti concentrations in these two phases by LA-ICP-MS (C_{Ti}^{Cpx}/C_{Ti}^{Ol}) much higher than the equilibrated partition coefficient (D_{Ti}^{Cpx}/D_{Ti}^{Ol}=43.14; Ionov et al., 2002). Cr

concentrations in Ol from Allègre and Mont Coupet vary from 3.7 to 192.0 ppm, the highest value also occurring in AL56. Except the two Amp-bearing samples (MC36 and MC53), other samples fall in the range defined by Cr concentrations in spinel and garnet-facies Ol (23-754 ppm; De Hoog et al., 2010). A strict positive co-relation (R^2=0.85) exists between Cr# of Ol and Cr# of Spl (Fig. 4-9d). A rough positive co-relation can also be observed between calculated temperatures and Cr concentration in Ol (Fig. 4-9e). Ni concentrations in Ol from Allègre and Mont Coupet vary less compared with other fore-mentioned elements. The range from 2901.1 ppm in sample AL47P1 to 3303.3 ppm in sample AL44 falls in the mantle Ol ranges defined by De Hoog et al. (2010) and Foley et al. (2013). The samples from both localities have a weak positive co-variation between their Fo and Ni concentrations in Ol (Fig. 4-9f). This agrees with the compatible behavior in Ol of this element during mantle partial melting, which is supported by the similar charge and ionic radius of Ni^{2+} to Mg^{2+} and Fe^{2+}, making Ni incorporation into Ol quite feasible.

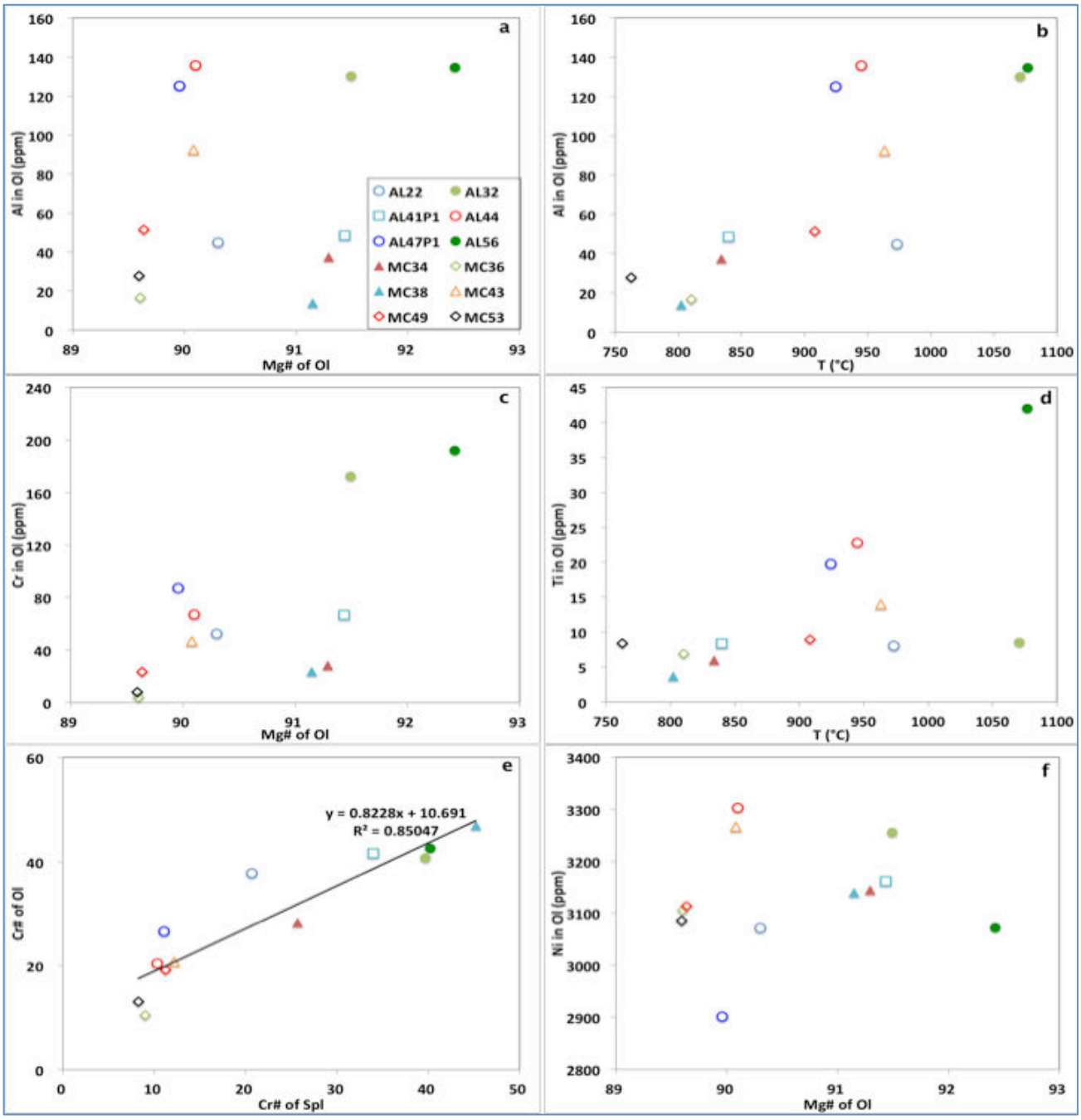

Figure 4-9: Al, Ti, Cr and Ni concentrations in Ol plotted against Mg# of Ol and temperature.

4.4 Li concentrations and isotopic compositions in minerals

The mineral Li concentrations and isotopic compositions in samples from Allègre and Mont Coupet are reported in Table 4-6.

Sample	Mineral	n	Li (ppm)						δ^7Li (‰)					
			Aver	±2σ	Max	Min	Core	Rim	Aver	±2σ	Max	Min	Core	Rim
AL22	Ol	39	1.7	0.1	3	1.3	1.7	1.7	-6.5	1.1	0.6	-14.4	-6.3	-7.2
	Opx	30	3.8	1.1	13.5	0.6	4.7	1.2	-5	0.9	0.1	-8.2	-4.6	-3.4
	Cpx	11	19.8	5.8	33.5	3.5	25.8	12.4	1.5	1.4	6	-2.2	1.2	2.6
AL32	Ol	29	2	0.3	4.3	0.9	1.9	2.5	-4.6	3.8	1.4	-31.6	-3.4	-6.5
	Opx	46	4.9	1.4	18.5	0.9	5.7	3.4	-25.1	6.1	-2.8	-74.7	-30.2	-15.4
	Cpx	14	20.5	4.7	34.7	5.9	16.2	18.3	-7.6	1.7	-1.4	-10.4	-5.9	-5.1
AL41P1	Ol	48	3.4	0.4	6.9	2.2	2.8	4.7	-15.7	2.3	-3.7	-31.6	-14.1	-10.7
	Opx	31	3.1	0.4	4.9	0.7	3.4	2.9	-11.8	2.7	0	-24.3	-12.1	-12.2
	Cpx	14	13.3	3.8	22.7	3.4	13.5	7.6	-14.5	2.4	-4.9	-20	-14.1	-12.3
AL44	Ol	12	2.6	0.2	3.1	2	2	2.9	-9.6	2.1	-3.4	-14.1	-9.2	-9.2
	Opx	24	2.8	0.7	8.7	1.4	3.8	2	-8.6	3.4	3.6	-19.3	-7.2	-10.4
	Cpx	15	27.9	2.5	33.3	12.7	30.9	24	-5.9	2.7	1.7	-11.6	-4.1	-4.4
AL47P1	Ol	42	4	0.5	7.7	1.6	3.1	5.2	-7.8	3.8	15.1	-27.6	-6.7	-3.6
	Opx	9	2.2	0.4	3.6	1.8	1.9	3	20.1	4.3	30.9	10.7	20.4	20.5
	Cpx	24	7.3	1.1	10.5	4.5	7.8	6.9	0.3	3.6	23.7	-6.2	2.1	2.9
AL56	Ol	85	3	0.2	6.3	1.8	2.5	3.8	-4.9	1.3	4.5	-17.3	-3	-6
	Opx	34	2.9	0.4	5.9	1.3	3.1	3.2	-2.5	1.9	5.4	-13.8	1.1	-6.1
	Cpx	32	34.6	3.9	49.5	4.9	39.9	33.6	1.8	1.4	7.2	-9.9	2.7	2.1
MC34	Ol	28	2.3	0.1	2.8	1.1	2.4	2.2	2.7	0.6	6.2	-0.7	4.1	2.7
	Opx	11	1.2	0.1	1.4	0.8	1.1	1.1	0.1	1.5	3.5	-5.3	2.4	-1.9
	Cpx	12	1.1	0.1	1.5	0.7	1.1	1	0.7	2.3	6.2	-9.3	0.9	-2.7
MC36	Ol	18	2.2	0	2.5	2.1	2.3	2.1	7.7	0.6	9.7	4.9	7.9	8.6
	Opx	35	1.4	0.1	2	0.9	1.8	1.2	3.3	0.7	6.5	-3.5	1.5	4.5
	Cpx	30	1.6	0.2	2.3	0.6	1.9	1.1	2.3	1	9.4	-3.1	2.9	2.4
	Amp	10	1	0.2	1.4	0.7	1	1.1	-3.8	1	-2.1	-7.4	-3.4	-4.6
MC38	Ol	45	2.1	0.1	2.4	1.6	2	2	0.5	0.4	3.6	-4.1	-0.3	0.6
	Opx	42	1.1	0	1.3	0.9	1.2	1.2	-5	1.2	-0.8	-19.9	-4.4	-11.7
	Cpx	16	0.8	0.1	1.3	0.4	0.8	0.9	-8.8	3.1	1	-22.9	-9.6	-13.5
MC43	Ol	16	2.2	0.1	2.5	1.7	2	2.2	6.1	1.8	11.9	2.1	7.2	5.1
	Opx	25	1.4	0.1	1.7	1	1.2	1.2	-2.3	1	1.8	-10.6	-3.2	-0.8
	Cpx	24	1.3	0.1	2.3	0.6	0.8	0.9	-3.6	1.4	1.7	-12	-3.2	-4.5
MC49	Ol	55	2.5	0	2.8	2.2	2.5	2.4	7	0.5	12.1	2.7	7.4	7.2
	Opx	27	1.5	0.1	1.7	1	1.7	1.4	4	0.8	7.6	-3.8	3.2	3.3
	Cpx	47	1.6	0.1	2.1	0.9	1.8	1.4	1.6	1.1	9	-9.7	1.5	0.8
MC53	Ol	16	2.3	0.1	2.7	2.1	2.2	2.4	3.3	0.6	5.2	0.5	4.3	2.5
	Opx	20	1.3	0.1	1.7	0.5	1.5	1.2	-0.5	1	4.5	-4.9	0.8	-0.9
	Cpx	12	0.9	0.2	1.8	0.5	0.9	0.9	4.3	3.8	14.7	-6.1	9.8	-0.7
	Amp	10	1	0.1	1.3	0.8	1	1.1	-7.1	1.4	-4.4	-11.4	-6.6	-7.6

Table 4-6: The average Li concentration and δ^7Li values for Ol, Opx and Cpx in every sample, including the averages of values in cores and rims.

4.4.1 Samples from Allègre

Li content in Ol cover a range of 0.9 to 7.7 ppm, with averages of individual samples varying from 1.7 to 4.0 ppm. Ol cores have lower or similar Li contents compared with their rims (Table 4-6), ranging from 1.3 to 4.4 ppm and from 1.4 to 7.7 ppm, respectively; the Li content increase at rims occurs within 900μm of the grain boundary. Li content in Opx ranges from 0.6 to 18.5 ppm, and, in most cases, is higher than those in coexisting Ol. The compositional zonation in Opx is variable; cores of some grains contain much more Li than their rims, whereas other grains show the opposite pattern. Cpx contain much more Li than coexisting Ol and exhibit much

larger variations, from 3.4 to 49.5 ppm, with averages of individual samples varying from 7.3 to 34.6 ppm. Cpx Li concentrations in sample AL47P1 are lower than Cpx in other samples.

Mineral lithium isotopic compositions in samples from Allègre display large variations. Ol δ^7Li values range from -32 to +15‰ with averages ranging from -9.6 to -4.6‰; Opx values range from -74.7 to +30.9‰ with averages from -25.1 to +20.1‰; Cpx values range from -11.6 to +23.7‰ with averages from -7.6 to +1.8‰ (Table 4-6). Despite their regular Li concentration zonations, Ol don't exhibit regular δ^7Li profiles; most samples have slightly higher average δ^7Li values in cores than in rims (Table 4-6). The δ^7Li distributions in Opx grains are more complicated. Their patterns can be divided into three groups: 1) δ^7Li values decrease from core to rim; 2) δ^7Li values increase systematically from core to rim; and 3) the δ^7Li profiles across the grains are irregularly sinuous. In Cpx grains, there is no large δ^7Li variation from core to rim. The average δ^7Li values of Ol and Opx in our samples, as well as some Cpx, fall outside the estimated Li isotopic composition of the upper mantle (+2 to +5‰), based on data from oceanic basalts (Chan et al., 1992; Tomascak et al., 2008), equilibrated fertile peridotites (Jeffcoate et al., 2007; Magna et al., 2006; Von Strandmann et al., 2011; Seitz et al., 2004), and mantle derived carbonatites (Halama et al., 2008).

To identify whether the host magma had influenced xenoliths with respect to Li concentration and isotopic composition, we carefully winnowed some phenocrysts and microcrystals of Cpx in the basaltic shells of xenoliths for SIMS analysis; the average Li concentration and δ^7Li value of the host magma Cpx are 16.5±5ppm and 3.2±0.6‰, respectively. Since no per mil-level Li isotopic fractionation occurs during crystal-melt differentiation at magmatic temperatures (Tomascak et al., 1999), the measured Cpx δ^7Li value can represent the Li isotopic composition of the host magma (and even the residual melts after a slight differentiation). Due to the temperature dependence of Li partition coefficient between Cpx and melts (Brenan et al., 1998a; Caciagli et al., 2011) and unawareness of the crystallization T and P of the measured Cpx, Li concentration in parental magma can only be estimated as no lower than 36 ppm (T=800°C; the partition coefficient between Cpx and melt calculated from

Caciagli et al. (2011)).

4.4.2 Samples from Mont Coupet

The Li distribution in Mont Coupet samples is totally different from that in Allègre samples. Li content in Ol ranges from 1.1 to 2.8 ppm, with small variation of averages in individual samples (2.1 to 2.5 ppm; Table 4-6). Li distributes nearly homogeneously from cores to rims of Ol grains. The Ol cores have a concentration range from 1.6 to 2.8 ppm similar to corresponding rims from 1.6 to 2.7 ppm. Opx in Mont Coupet samples contains Li ranging from 0.5 from 2.0 ppm. The average concentration for every sample has little inter-sample variation (1.1 to 1.5 ppm; Table 4-6). Resembling to co-exiting Ol grains, most Opx grains also have stable Li concentration transition from their cores to rims. Li content in Cpx covers a range of 0.4 to 2.3 ppm, with averages in individual samples ranging from 0.8 to 1.6 ppm (Table 4-6). The intragranular distribution in Cpx exhibits larger variation from cores to rims in some grains. On the whole, Cpx and Opx usually contain less Li than coexisting Ol in Mont Coupet samples. No significant difference in Li distribution can be observed between anhydrous samples and Amp-bearing samples.

Li isotopic compositions in Mont Coupet samples also display distinctive characteristics from those in Allègre samples. Ol δ^7Li values range from -4.1 to +12.1‰. None of the average Ol δ^7Li values in all the samples are negative, with a range of +0.5 to +7.7‰ (Table 4-6), the highest in sample MC36 and the lowest in sample MC38. No regular pattern can be summarized on the intragranular Li isotopic composition variation. In fact, the variation inside most grains is within analytical errors. The Li isotopic compositions of Opx have larger variation, with δ^7Li values varying from -19.9 to +7.6‰. The average δ^7Li value of Opx in each sample changes from -5.0 to +4.0‰ (Table 4-6), the former occurring in sample MC38 and the latter in sample MC49. In a few larger grains, the intragranular δ^7Li distribution patterns show steep decrease at the points closest to the grain boundaries. The patterns in other grains are totally irregular. Among the three mineral phases, Cpx in Mont Coupet samples have the widest Li isotopic composition varying range, from -22.9 to +14.7‰. The average δ^7Li values also cover a large range (-8.8 to +4.4‰; Table 4-6). It is worth noting that the lowest average δ^7Li values of Ol, Opx and Cpx in

individual samples are all obtained in sample MC38.

Amp in sample MC36 and MC53 have also been analyzed for Li concentrations and isotopic compositions using the ion probe (Table 4-6). Because of the similar crystalline structure of Amp to Cpx, the instrumental fractionation for measuring Li isotopic compositions of Amp was calibrated by Cpx standards. In these two samples, the Amp Li content cover a narrow range of 0.7 to 1.4 ppm. In spite of the very small grain size of Amp, the profiles have also been measured on each grain. And the core-rim heterogeneous Li distribution isn't present. The Li isotopic compositions of Amp in both samples are very light compared with other coexisting mineral phases, with δ^7Li values varying from -11.4 to -2.1‰. The intragranular variation can be regarded within the analytical errors.

4.5 Water content results measured by FTIR

4.5.1 Infrared spectra

More than 250 Ol, 270 Opx and 242 Cpx grains in aggregate were analyzed by FTIR under unpolarized light. Despite careful selection for optically clear grains, some spectra of Opx and Cpx (less Ol), especially from sample MC38, still exhibit bands located in higher wavenumbers (>3650 cm^{-1}), which have been previously ascribed as absorption of secondary hydrous phases (Amp at 3675 cm^{-1}, serpentine (alteration product) at 3709 and 3685 cm^{-1}), which may be present in the form of tiny inclusions and lamellae (Miller et al., 1987; Skogby et al., 1990; Skogby and Rossman, 1991; Matsyuk and Langer, 2004; Grant et al., 2007b; Gose et al., 2011; Baptiste et al., 2012; Mosenfelder and Rossman, 2013a). Meanwhile, in a few spectra, a broad band (peak centered at 3400 cm^{-1}) emerges to overlay the absorption bands of intrinsic hydroxyl. That band is likely related to molecular water (Sundvall and Stalder, 2011). These defective spectra have been eliminated when calculating the averaged infrared spectrum of each phase in individual samples.

The averaged Ol spectra collected under unpolarized light have bands similar to those of Ol sampled naturally or synthesized experimentally (Fig. 4-10; Miller et al., 1987; Bai and Kohlstedt, 1992, 1993; Bell et al., 2003, 2004; Matsyuk and Langer, 2004; Berry et al., 2005; Matveev et al., 2005; Demouchy et al., 2006; Peslier and

Luhr, 2006; Grant et al., 2007a, b; Matveev and Stachel, 2007; Walker et al., 2007; Peslier et al., 2008, 2015; Denis et al., 2013, 2015; Schämdicke et al., 2013; Doucet et al., 2014; Demouchy et al., 2015). The band at wavenumber 3572 cm^{-1} is dominant in Group I region for spectra of all the analyzed samples from Allègre and Mont Coupet. The other band at wavenumber 3520 cm^{-1} in the same group looks also present but is so weak in some spectra that it is at the limit of observation (Fig. 4-10). The bands belonging to Group II are not observed in spectra of Ol from Allègre, but they are present in in spectra of Ol from Mont Coupet, except sample MC38. A broad band centered at 3225 cm^{-1} occurs in all the samples from Mont Coupet, and in some samples (MC34, MC36 and MC53) this band seems even stronger than the 3572 cm^{-1} band (Fig. 4-10). Two other bands centered around 3350 and 3325 cm^{-1} are also present in the averaged spectrum of Ol from sample MC34, but not in spectra of Ol from other samples. Core-rim profiles have been made on some large Ol grains, but no significant changes have been observed in the spectra collected from grain cores to rims, including band position, band width, and peak height (Fig. 4-11).

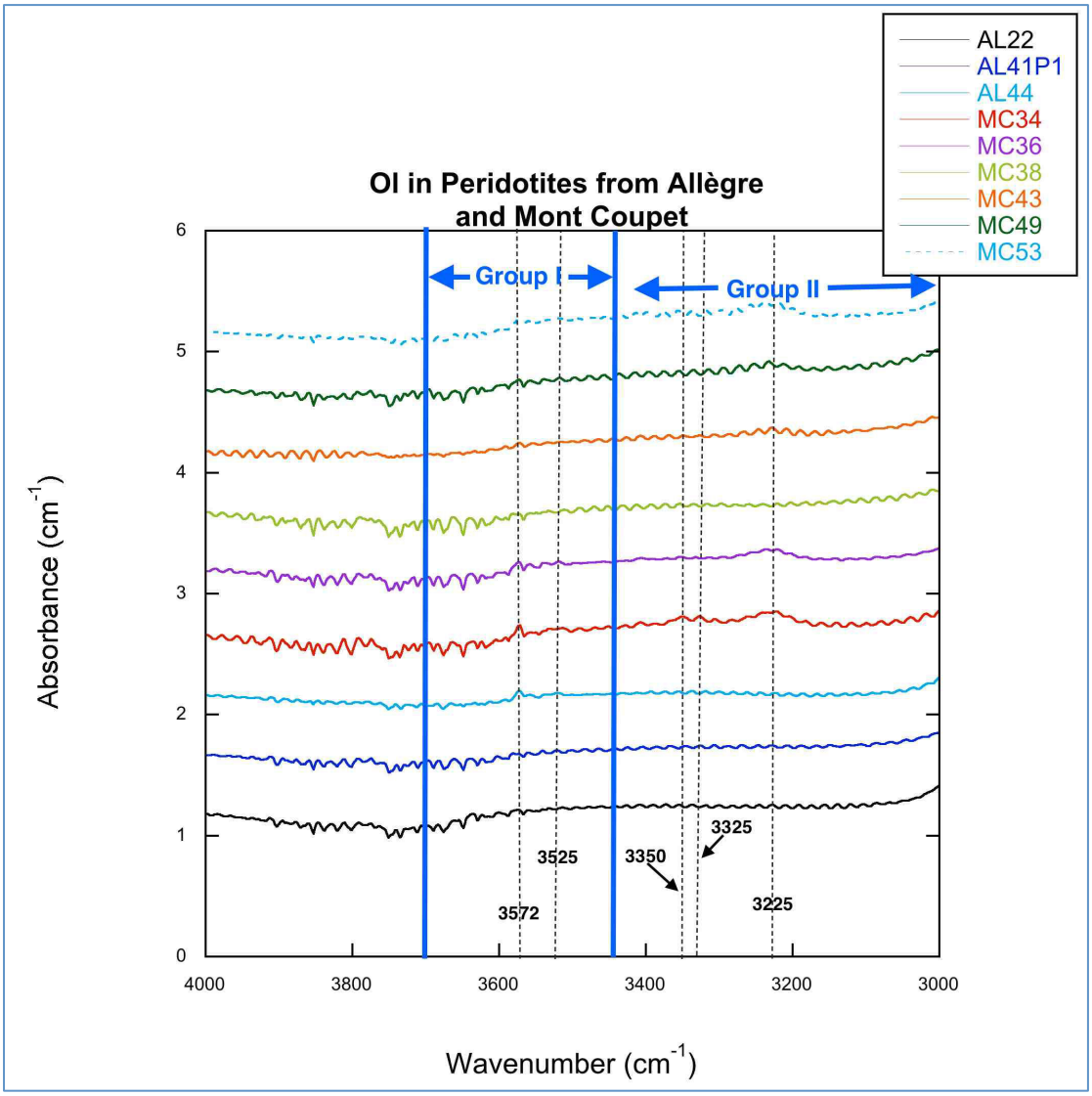

Figure 4-10: Averaged unpolarized Ol infrared spectra for all the peridotite xenoliths from Allègre and Mont Coupet in the wavenumber range from 4000 to 3000 cm^{-1}. The dashed lines represent the peak positions with the numbers in black presenting the corresponding wavenumbers. The blue solid lines are the wavenumber borders of each band group. The spectra have been normalized to 1cm in thickness.

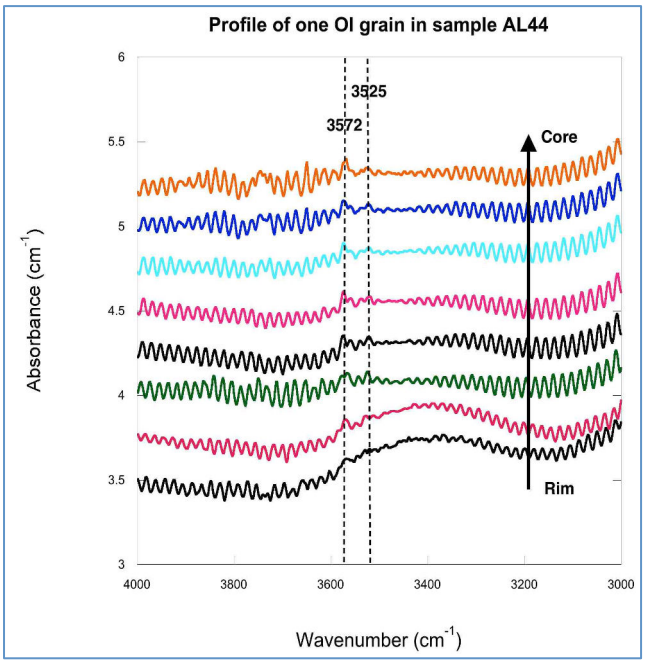

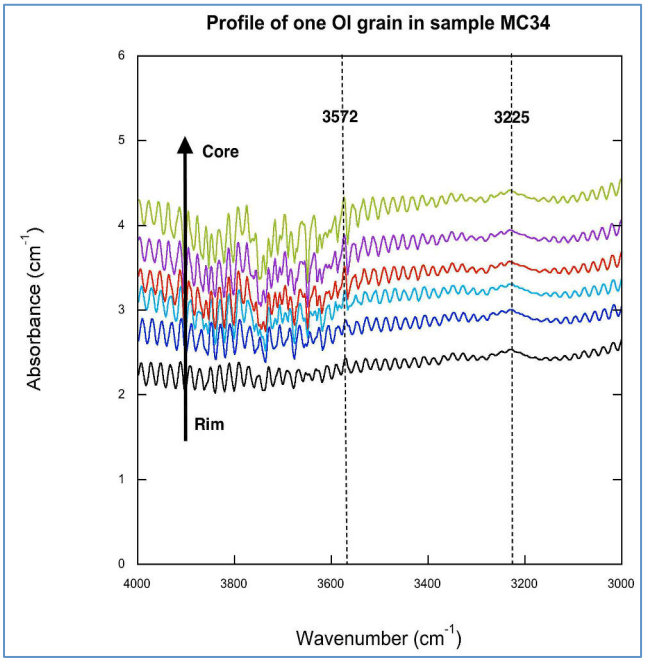

Figure 4-11: Unpolarized infrared spectra of two representative profiles made on Ol grains. The dashed lines represent the peak positions with the numbers in black presenting the corresponding wavenumbers. The thickness has been adjusted to 1cm.

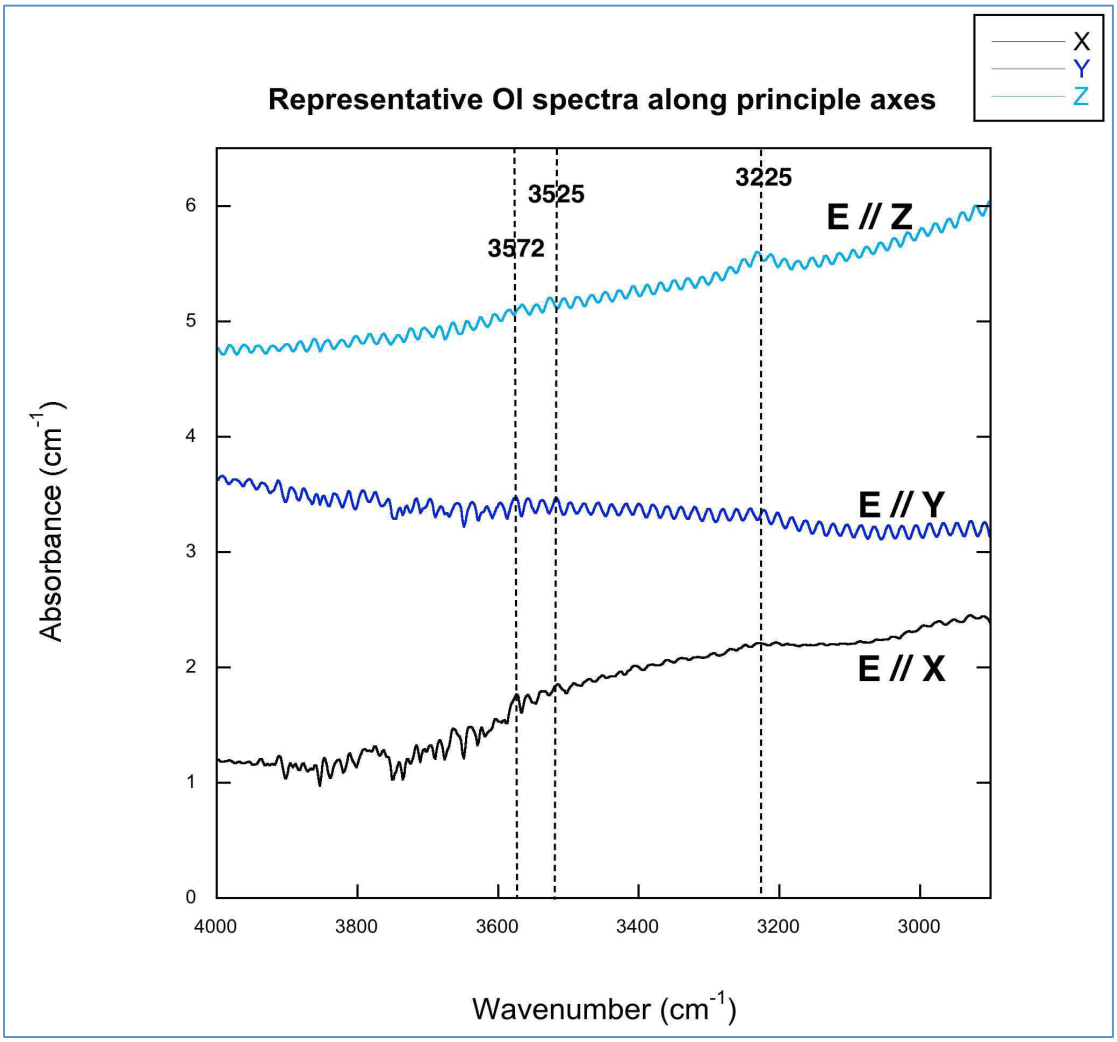

Figure 4-12: Representative polarized Ol infrared spectra collected in sample MC36 with E parallel to principle axes X, Y and Z. The dashed lines represent the peak positions with the numbers in black presenting the corresponding wavenumbers. The thickness has been adjusted to 1cm.

The spectra collected under polarized light with E parallel to X, Y and Z axes have the band allocation (Fig. 4-12) similar to that reported in Denis et al. (2013). The Group I bands mainly appear in spectra collected when E parallel to X axis. In the direction of Y axis, almost all the bands are present but very weak. While the band centered at 3225 cm^{-1} is dominant in the spectra collected along the Z axis. This remarkable anisotropic property of Ol partially induce the large variation of Ol spectra collected under unpolarized light in terms of band positions and intensities.

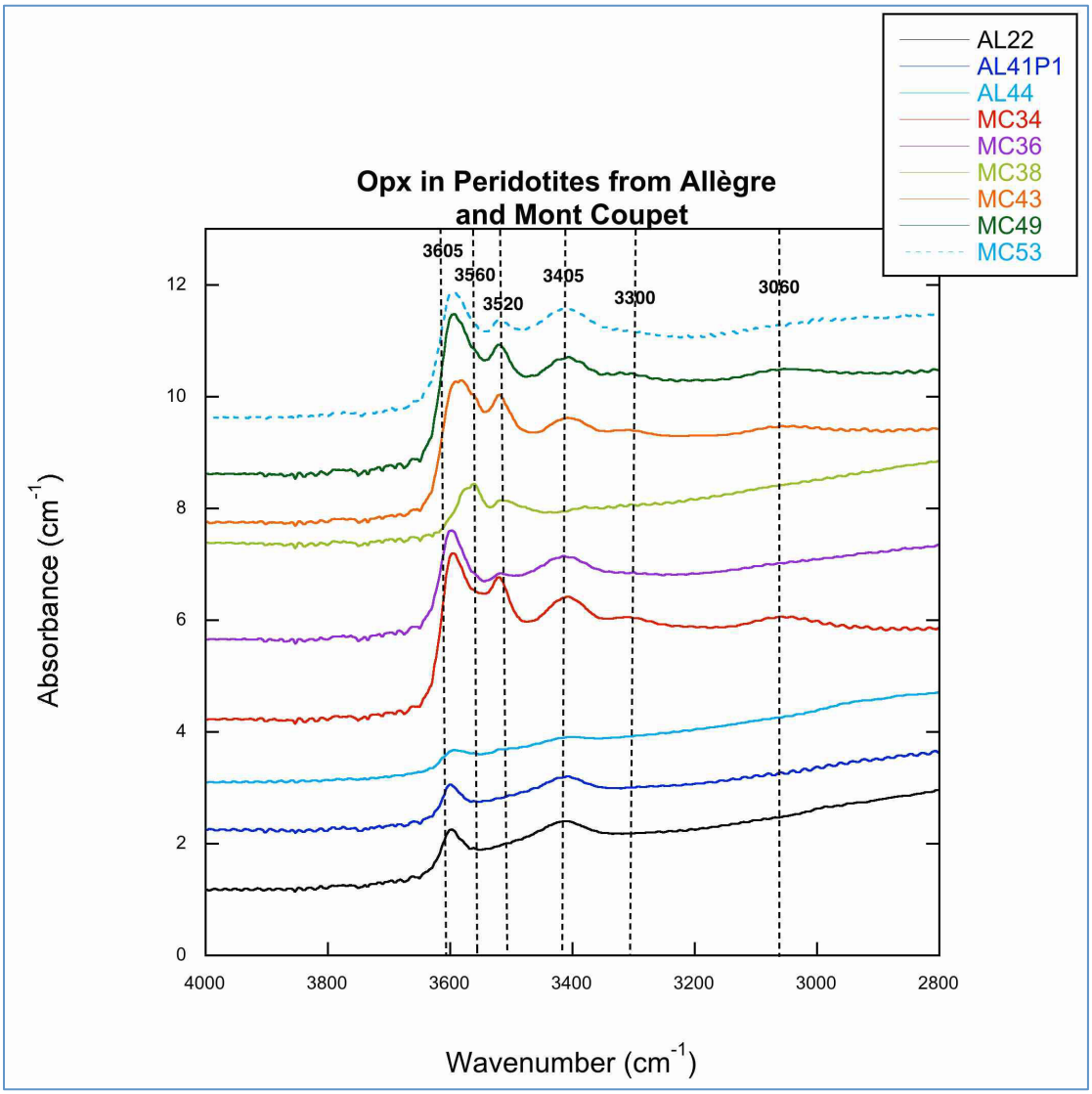

Figure 4-13: Averaged unpolarized Opx infrared spectra for all the peridotite xenoliths from Allègre and Mont Coupet in the wavenumber range from 4000 to 2800 cm^{-1}. For the bands located between 3605-3560 cm^{-1}, the wavenumber range is bordered by dashed lines with black numbers '3605' and '3560'. For other bands, the wavenumbers mostly centered are given on the dash lines. The spectra have been normalized to 1 cm in thickness.

The averaged Opx spectra are shown in Fig. 4-13. The band positions are similar to those reported in previous studies (e.g., Skogby et al., 1990; Peslier et al., 2002, 2012; Grant et al., 2007b; Goes et al., 2009; Xia et al., 2010; Sundvall and Stalder, 2011; Baptiste et al., 2012; Mosenfelder and Rossman, 2013a; Bizimis and Peslier, 2015; Demouchy et al., 2015; Denis et al., 2013, 2015; Doucet et al., 2014; Hui et al., 2015; Peslier and Bizimis, 2015; Hao et al., 2016). Each band in a certain wavenumber range is not centered at a constant wavenumber, so the bands are divided into several groups, between 3605-3590 cm^{-1}, 3525-3515 cm^{-1}, 3420-3390 cm^{-1}, 3315-3300 cm^{-1},

and 3080-3060 cm^{-1}. The latter two bands are less common than the former three ones in Opx spectra, on the basis of the large dataset from previous studies. In this study, the averaged spectra of Opx from sample MC34, MC43 and MC49 are very similar to each other, with the presence of all the aforementioned bands and the similar relative sizes of different bands (Fig. 4-13). In Opx spectrum of sample MC38, an additional band at wavenumbers between 3578 to 3560 cm^{-1} appears and it overwhelm the band 3605-3590 cm^{-1}. Meantime, the bands centered at 3315-3300 cm^{-1} and 3080-3060 cm^{-1} are absent in the spectrum. The spectra of Opx from two hydrous samples MC36 and MC53 resemble with each other. Bands centered at 3315-3300 cm^{-1} and 3080-3060 cm^{-1} also can't be observed. The band centered at 3525-3515 cm^{-1} contributes less to the total OH absorbance when compared with the same band in sample MC34, MC43 and MC49. The samples from Allègre have common band shapes in Opx spectra, which are distinctive to those from Mont Coupet. The bands centered at 3420-3390 cm^{-1}, 3315-3300 cm^{-1}, and 3080-3060 cm^{-1} are not observed in spectra of Opx from Allègre samples, and the band centered at 3525-3515 cm^{-1} is observed only in one spectrum, collected on one grain in sample AL44 (33 grains analyzed). The core-rim profiles were also measured on some large Opx grains, and the infrared spectra don't display any changes from grain cores to rims (Fig. 4-14).

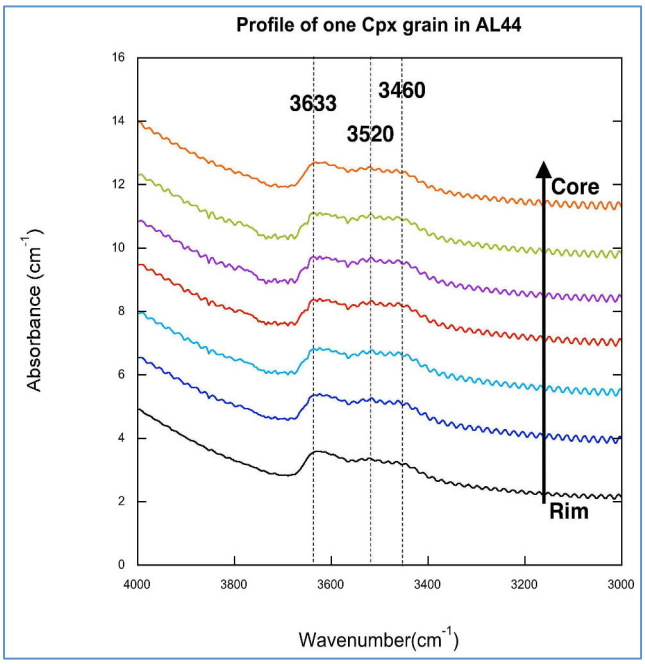

Figure 4-14: Unpolarized infrared spectra of two representative profiles made on Opx grains. The dashed lines represent the peak positions with the numbers in black presenting the corresponding wavenumbers. The thickness has been adjusted to 1cm.

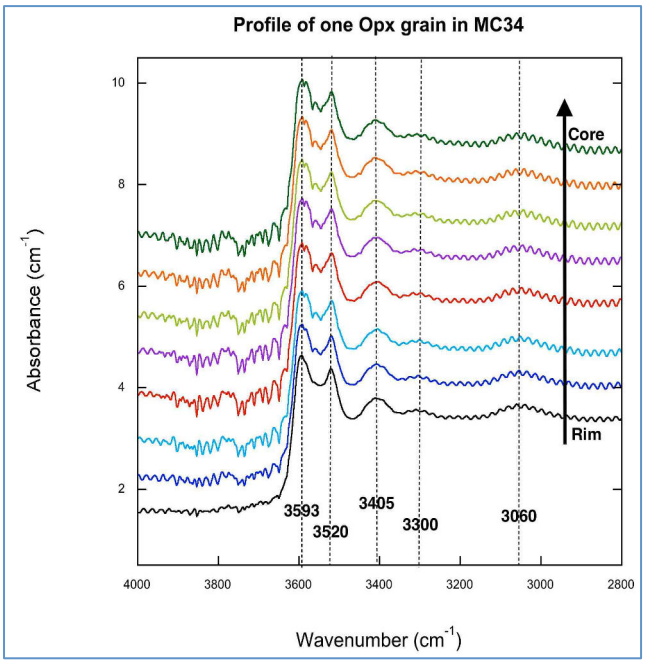

The OH absorption bands in the averaged Cpx spectra of Allègre and Mont Coupet samples are located in three narrow wavenumber ranges, between 3650-3630 cm^{-1}, 3540-3520 cm^{-1}, and 3465-3450 cm^{-1} (Fig. 4-15), comparable to literature (e.g., Skogby et al., 1990; Peslier et al., 2002, 2012; Grant et al., 2007b; Sundvall and Stalder, 2011; Baptiste et al., 2012; Hao et al., 2012, 2014; Mosenfelder and Rossman, 2013b; Bizimis and Peslier, 2015; Hui et al., 2015; Peslier and Bizimis, 2015). Among the spectra of these nine samples, that of sample MC38 is very particular in view of peak height and band position. The OH absorbance of Cpx in sample MC38 appears extremely low compared with that of other samples. The peak of 3650-3630 cm^{-1} band lies at higher wavenumber and the peaks of another two bands shift to lower wavenumbers in sample MC38 relative to other samples (Fig. 4-15). Averaged Cpx spectra collected on samples from Allègre and Mont Coupet (except sample MC38) are comparable with each other.

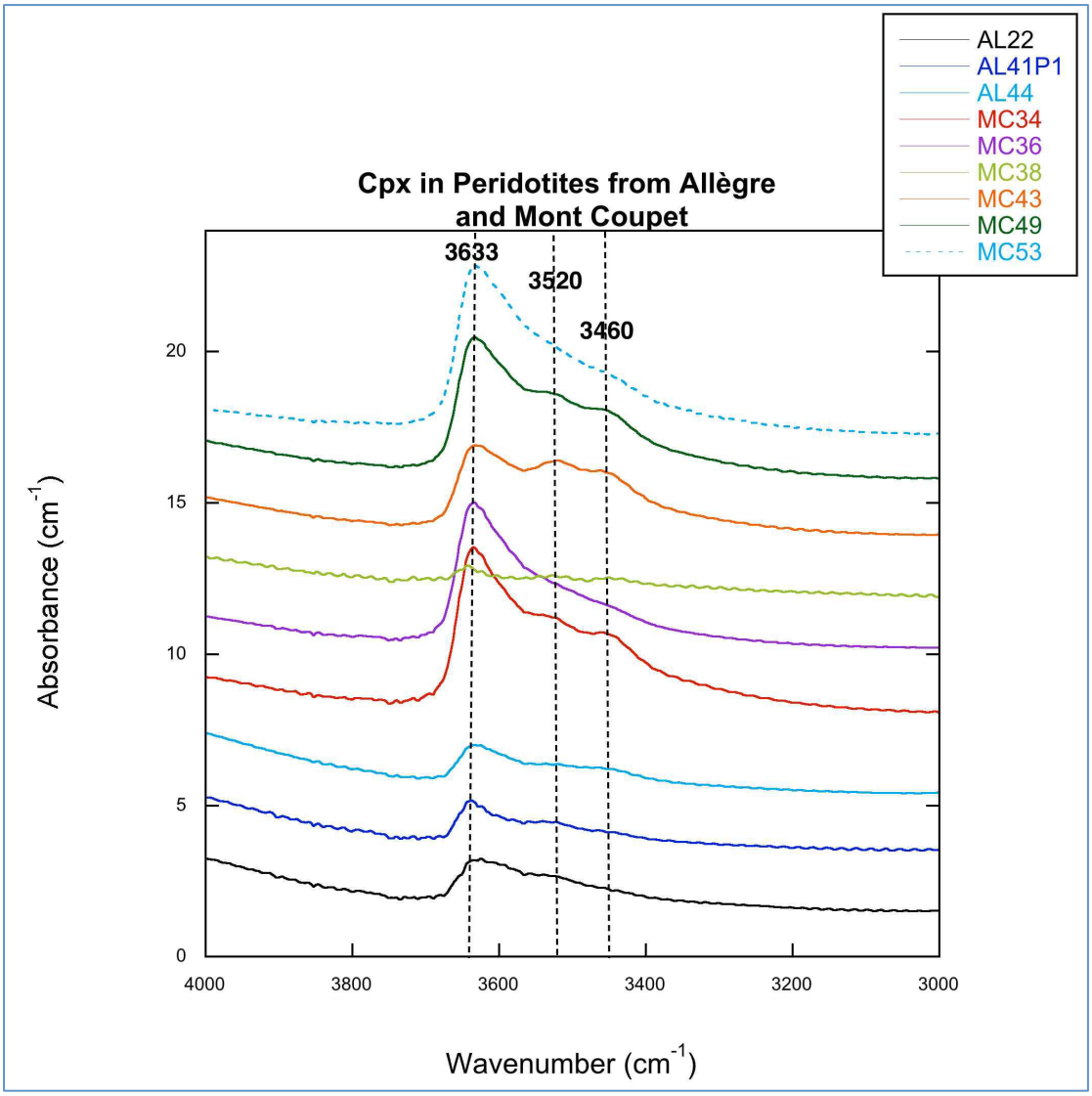

Figure 4-15: Averaged unpolarized Cpx infrared spectra for all the peridotite xenoliths from Allègre and Mont Coupet in the wavenumber range from 4000 to 3000 cm^{-1}. For three bands, the wavenumbers mostly centered are given on the dash lines. The spectra have been normalized to 1cm in thickness.

4.5.2 Calculated water content from infrared spectra

The results of water content in Ol calculated from IR spectra are shown in Table 4-7. No bands induced by structural OH vibration can be observed in the averaged spectra of Ol in sample MC38, AL22 and AL41P1 (Fig. 4-10). The averaging is carried out on spectra collected from more than twenty grains, so it is acceptable to assume that water content of Ol in these samples (<1 ppm) is 0 ppm. The deviation of total water content values calculated using unpolarized spectra relative to the values estimated from polarized spectra is within the analytical errors (<30%; Table 4-7) and similar to a comparison result from Doucet et al. (2014) where polarized and

unpolarized analysis on Ol from nine samples produce differences in results of less than 20%, so in the following parts the values from unpolarized spectra will be adopted to represent Ol water content. Ol in Mont Coupet samples (except sample MC38) contain 0.6 to 2.1 ppm water. The maximum value occurs in sample MC34. AL44 is the only Allègre sample in which Ol have OH absorption bands in infrared spectra. The water content estimated from the averaged spectrum is 1.4 ppm.

Sample	t (cm)		Ol Group I_{un}		Ol Group II_{un}		Ol Group I_p		Ol Group II_p		OH_{un} (ppm)	OH_p (ppm)	Deviation
		n	Integral (cm^{-1})	OH_B (ppm)	Integral (cm^{-1})	OH_L (ppm)	A_T (cm^{-1})	OH_B (ppm)	A_T (cm^{-1})	OH_L (ppm)			
MC34	0.015	38	0.01	0.4	0.123	1	0.024	0.3	0.29	0.7	1.4	1.1	0.27
MC36	0.016	32	0.04	1.4	0.09	0.7	0.107	1.3	0.215	0.6	2.1	1.9	0.11
MC38	0.016	34	-	-	-	-	-	-	-	-	-	-	-
MC43	0.017	17	0.006	0.2	0.061	0.4	-	-	-	-	0.6	-	-
MC49	0.015	26	0.01	0.4	0.09	0.7	0.025	0.3	0.243	0.7	1.1	1	0.1
MC53	0.016	29	0.04	1.4	0.075	0.6	-	-	-	-	2	-	-
AL22	0.018	20	-	-	-	-	-	-	-	-	-	-	-
AL41P1	0.016	26	-	-	-	-	-	-	-	-	-	-	-
AL44	0.017	28	0.04	1.4	-	-	-	-	-	-	1.4	-	-

Table 4-7: Ol water content in Allègre and Mont Coupet peridotite xenoliths calculated from infrared spectra. The subscripts "B" and "L" denote the calculation based on the methods from Bell et al. (2003) and Libowitzky and Rossman (1997), respectively. And the subscripts "un" and "p" represent the spectra collected under unpolarized and polarized light, respectively. Deviation=$(OH_{un}-OH_p)/OH_p\times100$, OH_{un} (OH_p) denotes the total water contents (Group I + Group II) calculated based on unpolarized (polarized) infrared spectra; $A_T= A_X+A_Y+A_Z$.

The Cpx and Opx water content estimated from the averaged spectra in each sample is shown in Table 4-8, where Ol water content is also included for comparison. Cpx water content in sample MC38 (41 ppm) is almost one order of magnitude lower than that in other Mont Coupet samples (304-428 ppm). Cpx in samples from Allègre contain much less water, the content covering a narrow range from 112 to 161 ppm, than Cpx in samples from Mont Coupet (except MC38). Opx water content in Mont Coupet samples ranges from 28 to 152 ppm, in which the maximum value was measured in sample MC34 and the minimum one from sample MC38. Opx in Allègre samples contain similar amounts of water, from 23 to 41 ppm, to Opx in sample MC38. The water content ratio between Cpx and coexisting Opx ($C_{H_2O}^{Cpx}/C_{H_2O}^{Opx}$) in each sample varies from 1.5 to 4.8.

Sample	t (cm)	Opx			Cpx			Ol
		n	Integral (cm^{-1})	Water Content (ppm)	n	Integral (cm^{-1})	Water Content (ppm)	Water Content (ppm)
MC34	0.015	21(31)	11.3	152	29(31)	15.2	428	1.4
MC36	0.016	32(32)	5.6	71	37(37)	12	318	2.1
MC38	0.016	33(40)	2.3	28	7(12)	1.6	41	
MC43	0.017	29(29)	10.6	126	24(29)	12.2	304	0.6
MC49	0.015	27(28)	9.9	133	29(31)	12.7	358	1.1
MC53	0.016	23(23)	7.3	92	28(28)	15.2	402	2
AL22	0.018	22(23)	3.6	41	14(19)	6.7	161	
AL41P1	0.016	27(31)	2.6	34	21(24)	4.1	112	
AL44	0.017	30(33)	1.9	23	29(31)	4.4	113	1.4

Table 4-8: Water content of Opx and Cpx in Allègre and Mont Coupet peridotite xenoliths calculated from unpolarized infrared spectra. "n" denote the numbers of analyzed grains whose spectra have been selected to calculate the averaged spectra . In that series, the numbers bracketed are the total numbers of analyzed grains. The Ol water content is also shown for comparison.

Combining the results of Ol, Opx and Cpx, one point is noteworthy, water content of the three phases in Amp-bearing samples (MC36 and MC53) is not higher than in other anhydrous samples but lies in the ranges of other samples (Table 4-8). This suggests that although samples MC36 and MC53 have once experienced hydrous metasomatism, water content of primary phases has not been changed at that time or imprint of water addition has been erased by subsequent metasomatic events.

4.6 Water content results from SIMS measurements

Sample	AL32			AL47P1			AL56		
	Ol	Opx	Cpx	Ol	Opx	Cpx	Ol	Opx	Cpx
$^{16}O^{1}H/^{30}Si$	0.011	0.017		0.006	0.014	0.03	0.007	0.014	0.016
H_2O (ppm)	90	160		66	140	217	73	143	143

Table 4-9: Results of water content measured by SIMS.

In order to better constrain the water content of minerals in Allègre peridotite xenoliths, another three samples (AL32, AL47P1 and AL56) were analyzed by SIMS for water content. The results are reported in Table 4-9. Ol water content is measured ranging from 66 to 90 ppm, totally different from the FTIR analyzed results of other three samples from the same locality. Considering that the $^{16}O^{1}H/^{30}Si$ ratios of synthetic forsterite, analyzed almost simultaneously, are lower than 0.003, the high Ol water content should not be ascribed as the background moisture, but probably originate from tiny aqueous inclusions in samples or molecular water attached on the surface of samples which has not been thoroughly removed during drying process in

the airlock. Although Opx water content measured by SIMS in AL32, AL47P1 and AL56 is uniformly higher than the Opx water content range identified from FTIR analysis on other samples also from Allègre, the SIMS results of Cpx from sample AL47P1 and AL56 are close to the FTIR results of other Allègre samples. Thus, the water content results measured by SIMS in this study will be just regarded as a reference during discussion and will not be used to represent the real water content of minerals in peridotite xenoliths from Allègre.

Here, the plus and minus of each analytical technique (SIMS and FTIR) to measure trace structural hydroxyl in NAMs are highlighted. Although the ion probe is capable of making in-situ measurements on very small crystals (spatial resolution of 10 μm), its strict requirements for lowering background moisture interference and drying measured samples are highly challenging. Moreover, analysis preformed by SIMS doesn't supply the information of the H incorporation modes into crystals and, additionally, the water in tiny aqueous inclusions can't be distinguished from the structural hydrogen in NAMs. In contrast, FTIR have the capability of providing constraints on H existing forms, intrinsic constituent (defects or substitution of other ions) or extrinsic impurity (inclusions, coexisting secondary hydrous minerals). If the thickness of samples is increased to certain values (e.g., 1 cm), the detection limit of FTIR for water measurements reaches as low as 1 ppm water by weight. But for FTIR, high accuracy of results demands orientation of anisotropic crystals, or large quantities of measurements on tens of non-oriented grains. Thus, the grain sizes or the amount of minerals could be an obstacle for using FTIR to measure some scarce natural samples or samples from high-pressure experiments.

5. Thermobarometry

Four thermometers, from Wood and Banno (1973), Wells (1977) and Brey and Köhler (1990; two-pyroxene and Ca-in-orthopyroxene thermometers), have been used to calculate the equilibrium temperatures (Table 5-1). The results derived from these four methods in all samples do not strongly differ (standard deviation<85) and the two-pyroxene thermometer from Brey and Köhler (1990; henceforth expressed as T_{BK}) is chosen as representative. This method was used in previous studies of the French Massif Central (Werling and Altherr, 1997; Zagana et al., 1997; Yoshikawa et al., 2010), allowing for direct comparison to other localities in the same region. The calculated equilibrium temperatures (T_{BK}) range from 840 to 1077℃ for Allègre xenoliths, and from 763 to 963℃ for xenoliths from Mont Coupet (Table 5-1), both falling within the range proposed by Werling and Altherr (1997; 721 to 1190℃). Equilibrium temperatures are correlated with the Mg# of Ol (in the next section). We do not observe any relationship between equilibrium temperatures and textural types (Fig. 5-1), as described by Zagana et al. (1997).

Sample	Wood and Banno (1973)	Wells (1977)	Brey and Kohler (1990; two-pyroxene, P=10kbar)			Brey and Kohler (1990; Ca in Opx, P=10kbar)			Average	Pressure (kbar)	Depth (km)
			WR	Core	Rim	WR	Core	Rim			
AL22	1056	955	973	851	1057	851	853	847	959	14.8	52
AL27P2	986	881	855	860	894	871	843	908	898	10.4	36
AL32	1162	1069	1071	1066	1089	1015	984	1050	1079	9	32
AL41P1	1042	924	840	833	862	869	853	883	919	9.9	35
AL43	1104	1005	1012	1076	1062	1028	1023	1034	1037	5.4	19
AL44	1060	959	945	885	988	918	876	955	970	10.8	38
AL47P1	1062	962	966	925	1010	945	905	981	984	9.3	33
AL48	1048	938	879	-	-	848	838	859	928	10.3	36
AL56	1142	1034	1077	1081	1075	1021	1001	1031	1069	11.2	39
MC30	949	835	807	806	848	838	864	819	857	7.7	27
MC34	988	869	834	822	839	843	868	828	884	9	31
MC36	949	837	810	817	806	843	851	839	860	15.2	53
MC38	983	864	802	820	793	874	929	839	881	10.3	36
MC43	1037	935	963	953	969	849	857	845	946	8.8	31
MC49	995	888	908	914	905	841	860	831	908	7.8	28
MC50	942	825	779	759	773	787	789	786	833	10.9	38
MC53	934	819	763	785	788	832	854	820	837	4.9	17

Table 5-1: Calculated equilibrium temperatures of Allègre and Mont Coupet peridotite xenoliths. 'WR' denotes that the results were calculated using the averaged mineral major element compositions in indivisual whole samples. The average is from temperatures calculated using four thermometers based on he averaged mineral major element compositions of all analyzed points in a single sample. All the values are in centidegree (℃).

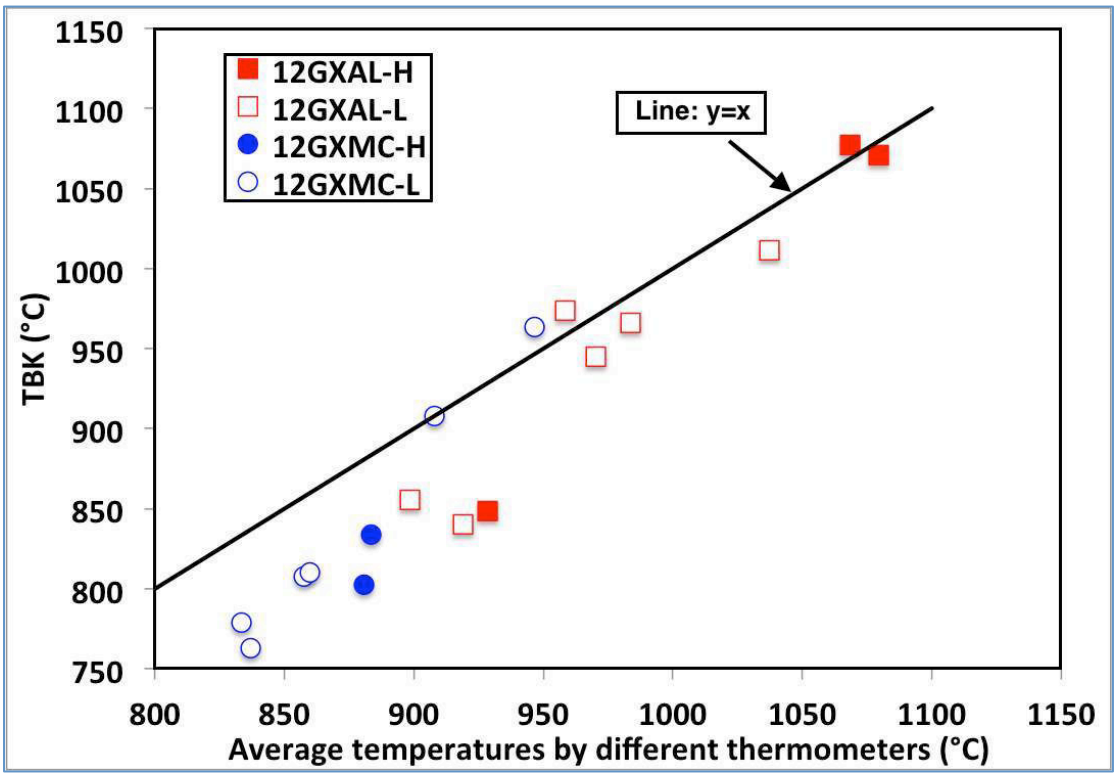

Figure 5-1: T_{BK} (℃) plotted against averaged temperatures calculated using four thermometers. For the samples of relatively low temperatures (T_{BK} <850℃), the averaged temperatures are a little higher than T_{BK} due to too high values calculated from the thermometer of Wood and Banno (1973) compared with other thermometers. The filled squares and circles represent harzburgites from Allègre and Mont Coupet, 12GXAL-H and 12GXMC-H, respectively), while lherzolites are represented by empty squares and circles, 12GXAL-L and 12GXMC-L, respectively.

Based on Ca-in-olivine geobarometer (Köhler and Brey, 1990), we calculate equilibrium pressures ranging from 9.3 to 14.8kbar for Allègre xenoliths and from 7.7 to 15.2kbar for xenoliths from Mont Coupet (Table 5-1), with the exception of AL43 and MC53, for which 5.4kbar and 4.9kbar, respectively, pressure is obtained. These low values may result from Ca disequilibrium between Ol and Cpx, and they are discarded in the following discussion. Given a lithospheric density of 2.85 g/cm^3 (Yoshikawa et al., 2010), our samples originate from depths of 27 to 53km, upper mantle depths, considering the depth of the Moho to be at 28 to 30km (Sobolev et al., 1996; Werling and Altherr, 1997; Michon and Merle, 2001).

6. Discussion

6.1 Depletion by partial melting

Partial melting of peridotites (extraction of partial melts) is one of the fundamental processes controlling the mantle evolution and giving rise to great compositional variations from the upper mantle to the crust (e.g., Carlson et al., 2005). During this process, the basaltic components (such as CaO, Al_2O_3, FeO and TiO_2) are extracted from the sources through the melt and, refractory depleted residues are formed. The compositions of these two differentiated members ultimately depend on the degrees of partial melting that are intimately related to temperature, pressure, and chemical compositions (including volatiles) of source rocks. The main indexes classically used to track partial melting are the modal compositions of Cpx, the Fo content in Ol, and Cr# of Spl in residual peridotites; those vary at different scales reflecting distinct degrees of partial melting.

Although the pressure-dependent aluminous minerals (plagioclase, Spl and garnet) are generally more susceptible to partial melting at lower pressures (<4-5 GPa), Cpx will follow up prior to Opx and Ol (Walter, 2014). With melting progressively proceeding, the Cpx modal proportions in residual rocks will decrease until Cpx is exhausted, leaving harzburgite peridotites. Meanwhile, the chemical composition of the residue is also changing. During melting, incompatible elements (e.g., Ca, Al) preferentially enter the melt, whereas other elements (e.g., Mg) selectively reside in the solid phase. Cr has a higher compatibility in solid phases than Al, and in dry and low-pressure environment, more Mg remains in residuals than Fe. Thus, when peridotites sufer partial melting in the normal upper mantle, the modal proportion of Cpx decreases, and the Fo content in Ol and Cr# of Spl increases in residuals with the increasing degrees of partial melting. As shown in Fig. 6-1a, the modal abundance of Cpx (1% to 15%) in xenoliths from Allègre and Mont Coupet systematically decreases with increasing Fo content (89.2 to 92.4), indicating an incremental degree of melting. Additionally, the positive correlation between Cr# of Spl (7.3 to 58.4) and Fo content (Fig. 6-1b) is consistent with the trend defined by sub-continental peridotites worldwide (Arai, 1994).

6.1 Depletion by partial melting

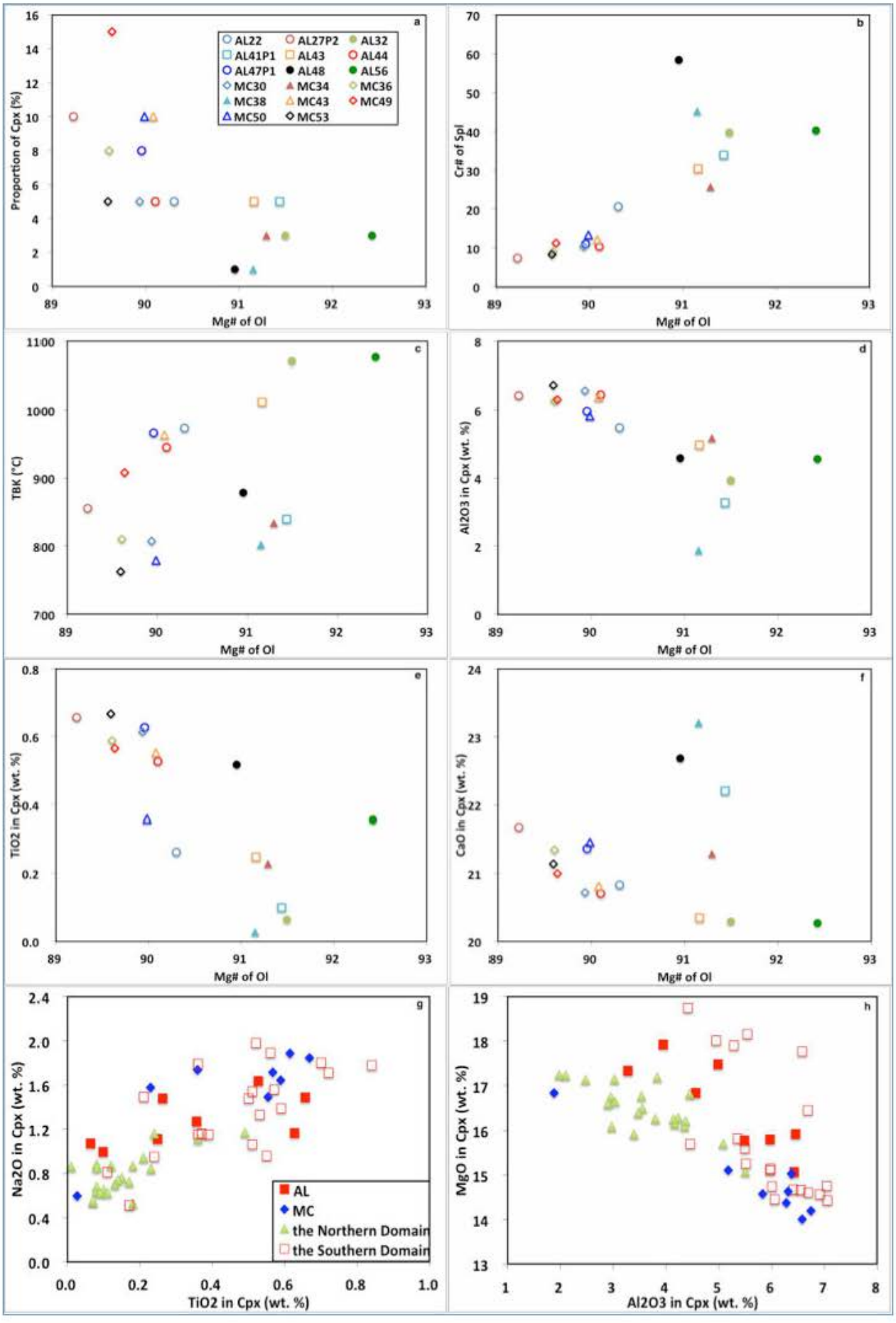

Figure 6-1: Co-variation of major element compositions in minerals. In (a-f), circles and triangles represent protogranular samples in Allègre and Mont Coupet, respectively; and squares and diamonds represent porphyroclastic samples in Allègre and Mont Coupet, respectively. Filled symbols denote harzburgites and empty symbols denote lherzolites. In (g-h), data from this study are plotted with literature data for the northern domain (Downes et al., 2003) and southern domain of the FMC (Xu et al., 1998; Touron et al., 2008; Yoshikawa et al., 2010). AL and MC in g and h denote the samples from Allègre and Mont Coupet, respectively.

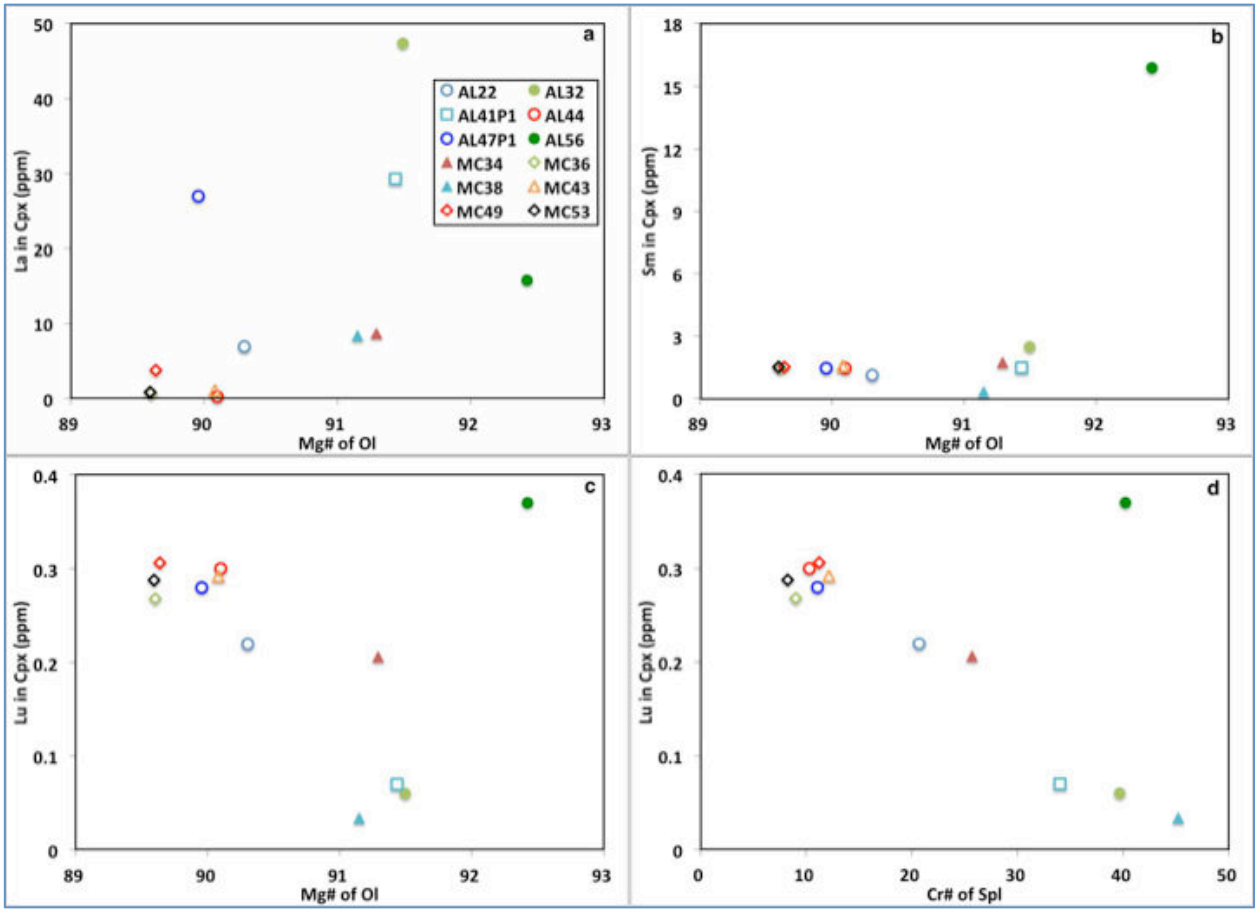

Figure 6-2: Plots of Ol Mg# versus abundances of La, Sm and Lu in Cpx (a, b and c, respectively) and Cr# of Spl versus abundance of Lu in Cpx (d).

When considering the major element compositions of Cpx (Na, Mg, Al , Ti in Fig. 6-1g and h), most of our samples fall in the field of the Massif Central southern domain defined by Downes et al. (2003). Al_2O_3, TiO_2 and CaO content in Cpx show a roughly negative relationship with Fo content in Ol (Fig. 6-1d, e and f), due to extraction of basaltic components during partial melting. Mildly incompatible elements in Cpx (HREE + Y) are mainly unaffected by later metasomatic events and record the partial melting event, along with Fo and Cr# of Spl (Fig. 6-2c and d). In contrast, LREE contents (Fig. 6-2a) seem to be affected by later metasomatic events, and do not display such correlations with Fo and Cr# of Spl. Only the HREE content

of sample AL56 falls outside the trends of Cpx modal proportions, Fo content, and Cr# of Spl; AL56 was therefore enriched by a metasomatic stage (Fig. 6-2c and d). In all other samples, the correlation between Cpx HREE content, Fo content of Ol, and Cr# of Spl indicate that Cpx is cogenetic with Ol, and thus suffered the partial melting event.

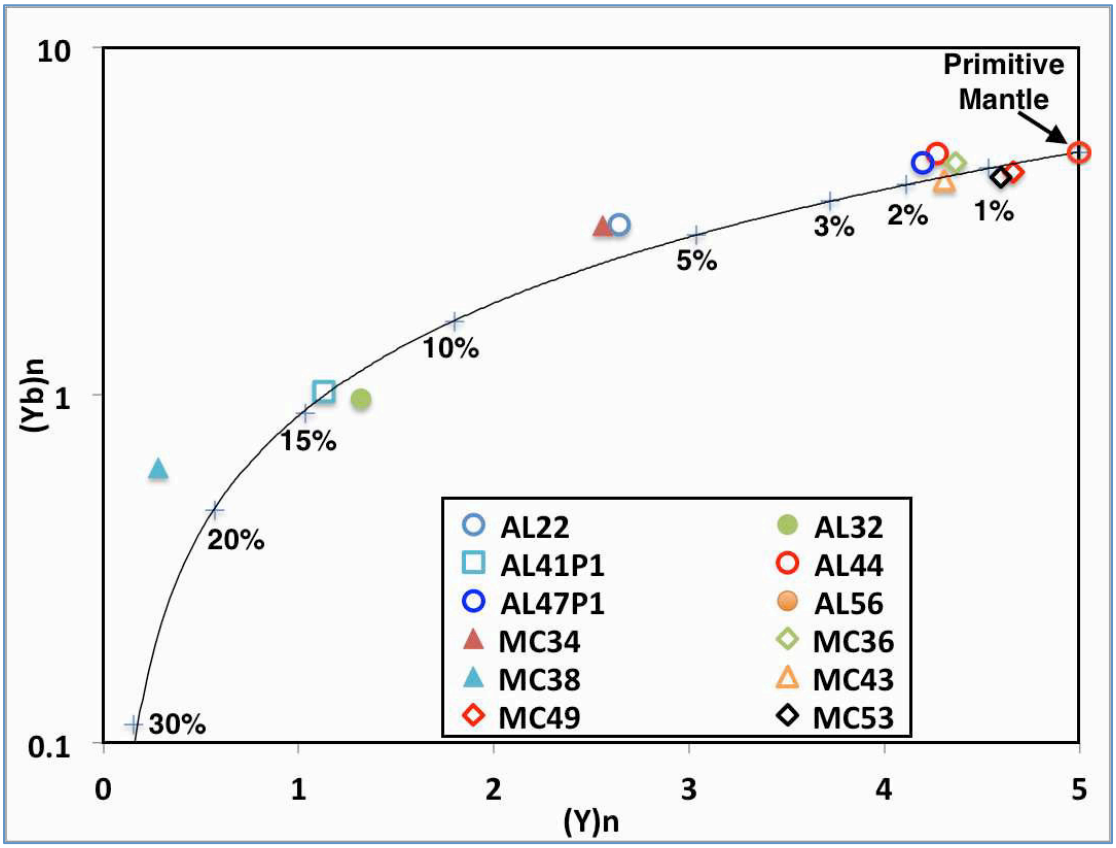

Figure 6-3: The fractional melting modeling results based on Y and Yb contents in Cpx. According to the model of Norman (1998), the initial contents of these two elements are chosen as the primitive mantle compositions from McDonough and Sun (1995), symbolized by the red cycle. Experimentally constrained partition coefficients between Cpx and melts by Hart and Dunn (1993) are used in the model (0.467 for Y; 0.43 for Yb). The modal composition of Cpx is assumed to be 20%, similar to Norman (1998). The subscript 'n' denotes normalization to primitive mantle compositions (McDonough and Sun, 1995). Cpx of sample AL56 contains enough Y and Yb that it plots outside the modeling zone (not shown here).

Hellebrand et al. (2001) have established a relationship linking Cr# of Spl in residual peridotites to the extent of partial melting. Using their equation, the degrees of partial melting of samples from Allègre and Mont Coupet were calculated to range from 1 to 19% (Table 4-1). No estimate could be made on samples AL27P2, MC36 and MC53, for which Spl Cr# of 7.28, 9.02 and 8.26, respectively, are lower than the

literature data (Touron et al., 2008; Werling and Altherr, 1997; Xu et al., 1998; Yoshikawa et al., 2010) and falls outside the available range of the equation. The fractional melting model of Norman (1998), based on HREE contents, has also been used to estimate the degrees of partial melting of samples in which the REE concentrations of Cpx have been measured (Fig. 6-3); the results, melting degrees ranging from <1% to 20%, are consistent with those calculated according to Hellebrand et al. (2001), with the exception of sample AL56, of which Cpx HREE were enriched by metasomatism (Fig. 6-2c and d) and the point of which in Fig. 6-3 falls out of the modeling zone (not shown).

6.2 Mantle metasomatism revealed by trace element compositions

The residual peridotites after various degrees of partial melting were usually refertilized by metasomatic melts/fluids at mantle depths. This is another important process to create heterogeneities in mantle rocks. The series of rare earth elements, of similar physical and chemical properties, can record the imprints of metasomatism and clearly present them by variations of relative element abundances in concerning specimens.

6.2.1 Trace element variations in Cpx from Allègre

In un-metasomatized peridotites, merely undergoing partial melting, Cpx should be depleted in incompatible elements (e.g., LREE, LILE, HFSE…) depending on the element partition coefficients. LREE are thus more depleted than HREE in residual peridotites. The trace element pattern of AL44 illustrates this tendency, whereas the trace element distribution patterns in Cpx from other samples deviate from this trend to different degrees (Fig. 4-6a), indicating that they have been modified by exotic melts or fluids percolating after partial melting (metasomatism). A series of fractionated REE patterns has been ascribed to the chromatographic effects during melt percolation into a porous matrix (Fig. 6-4; Navon and Stolper, 1987; Bodinier et al., 1990; Vasseur et al., 1991; Takazawa et al., 1992; Xu et al., 1998; Ionov et al., 2002; Mundl et al., 2015). The incipient percolating melt is presumed to be highly enriched in LREE relative to MREE and HREE (Ionov et al., 2002; Mundl et al., 2015). Elemental redistribution between peridotite minerals and the percolating melt is mainly controlled by the mineral-melt partition coefficient of a given element. Once the melt enters the host peridotite suite, the melt reacts first with peridotites closest to the melt conduit (Fig. 6-4). The peridotite minerals are quickly enriched in HREE (less incompatible than LREE), depleting the melt. Sample AL56 corresponds to the host peridotite at this stage (Fig. 6-5a) as the upward convex REE pattern is consistent with previous modeling results (Xu et al., 1998; Ionov et al., 2002; Mundl et al., 2015). With progressive percolation, the HREE-depleted melt (relatively LREE-enriched), no longer exchanging HREE with the host peridotites farther from the melt source, introduces a strong LREE enrichment in the ambient host peridotites.

Among our studied samples, AL34 and AL41P1 display the highest $LREE_N/MREE_N$ or $LREE_N/HREE_N$ ratios (Table 4-3; Fig. 6-5b) and can be assigned to this stage. As percolation continues, LREE continue to migrate from the melt to the host peridotites until the LREE/HREE fractionation diminishes. The progression from AL47P1 (La_N/Yb_N=9.4), to AL22 (La_N/Yb_N=3.9) and to AL44 (La_N/Yb_N=0.1) mirrors this process (Fig. 6-5c, d). Strongly metasomatized samples should record higher equilibrium temperatures due to their proximity to the melt source (Denis et al., 2015); indeed, samples AL56 and AL32 have equilibrium temperatures of 1077 and 1071℃, respectively. LREE enrichment of metasomatized Cpx in our samples is accompanied by different degrees of negative HFSE anomalies (Fig. 4-6b).

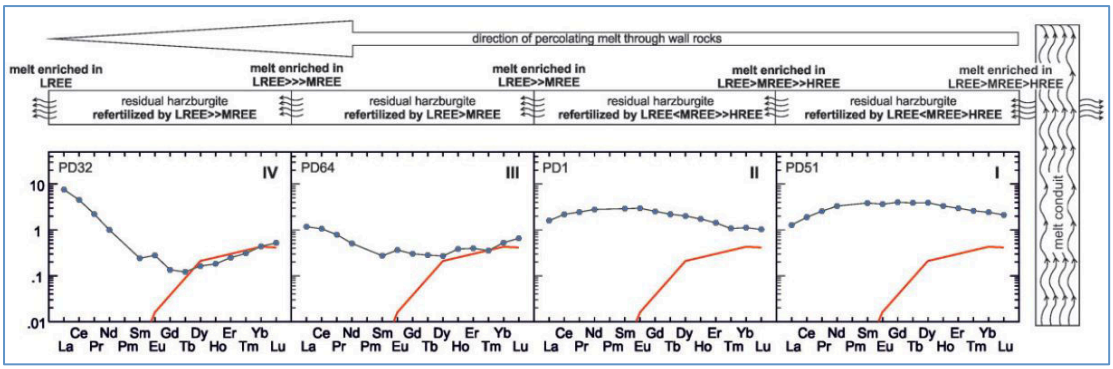

Figure 6-4: A sketch modeling the chromatographic effect of a percolating melt, adopted from Mundl et al. (2015). The melt was supposed to originate from a melt conduit in the mantle. With the melt progression, REE gradually fractionated due to the incompatibility differences among LREE, MREE and HREE. The graphs I, II, III, and IV show the primitive mantle-normalized Cpx REE patterns of samples from Mundl et al. (2015), at increasing distances from the melt source according to the modeling.

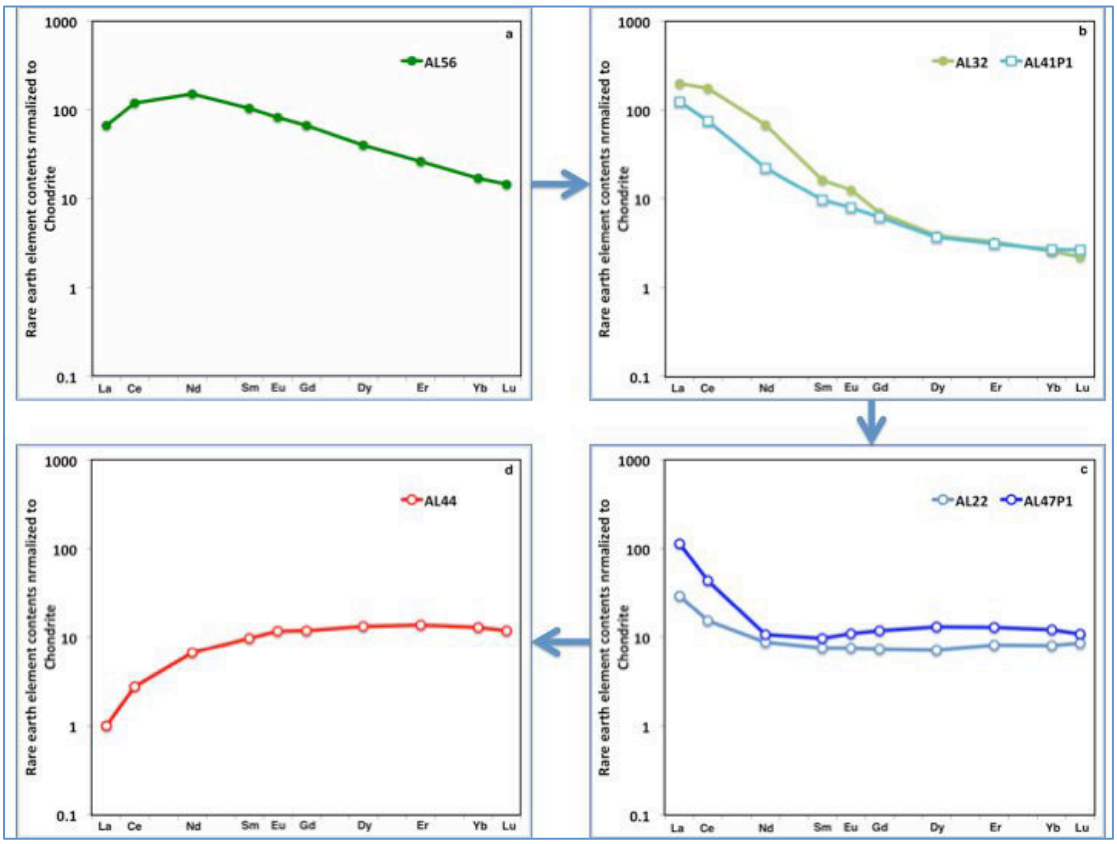

Figure 6-5: Progressive Cpx REE variations, normalized to chondrite, in the Allègre peridotite xenoliths due to the chromatographic effect of the percolating melt. (a) The sample AL53 has reacted with the melt near the melt source: not only LREE but also HREE have been added to the sample. (b) and (c) With the melt farther from the source, HREE was diluted and LREE was enriched in the melt. The Cpx chondrite-normalized REE patterns are prominent in LREE enrichment. HREE in Cpx display almost no variations and their concentrations agree well with the partial melting degrees. The degrees of LREE enrichment in samples are related to the sample distance from the melt source. (d) The sample AL44 is far from the melt source and the melt didn't influence the Cpx chondrite-normalized REE pattern in this sample.

In light of weak mobility of HFSE in aqueous fluids, negative HFSE anomalies were classically attributed to subduction settings, where mantle domains have been enriched in fluid-mobile elements (like LILE) and depleted in fluid-immobile elements (HFSE; e.g., Zanetti et al., 1999; Downes et al., 2004; Rivalent et al., 2007). However, HFSE anomalies associated with LREE enrichments have also been recognized as a signature of carbonate-bearing metasomatic silicate melts (e.g., Ionov et al., 2002; Grégoire et al., 2009). Experiments conducted at pressure and temperature that are pertinent to mantle conditions have shown that HFSE partition coefficients between Cpx and carbonatitic melts are much higher than those between

Cpx and silicate melts (Adam and Green, 2001; Blundy and Dalton, 2000; Klemme et al., 1995). Provided that Cpx present in the carbonatitic melt source controls the trace element budget of those melts, produced melts will be relatively depleted in HFSE, which will be recorded in the trace element distribution patterns of peridotites metasomatized by them. In natural peridotite samples, carbonatitic metasomatism is commonly associated with low Ti/Eu (Fig. 6-6a; usually<1500; Coltorti et al., 1999) and elevated Zr/Hf (>37) in Cpx (e.g., Ionov et al., 1993; Rudnick et al., 1993; Yaxley et al., 1998; Coltorti et al., 1999; Gorring et al., 2000). In Allègre samples, Ti/Eu values are as low as 437, consistent with previous observations. Sample AL56 have the lowest Ti/Eu ratio among the Allègre samples, but its $(La/Yb)_N$ ratio is not the highest one (Fig. 6-6a). This sample was most strongly metasomatized and metasomatic melts/fluids have also added relatively more HREE to Cpx. With respect to the Zr/Hf ratio of Cpx in Allègre samples, the highest value occurs in sample AL22 (52) rather than sample AL56 (33), the most metasomatized in term of REE addition and lowest Ti/Eu ratio in its Cpx. But Zr negative anomalies are indeed present in some strongly metasomatized samples (Fig. 6-6b). As proposed in some previous studies, the diagnostic trace element compositionas were commonly accompanied by the reaction textures (generation of secondary Cpx at expense of Opx; Coltori et al., 1999) or the presence of accessary minerals (e.g., Amp, apatite, or K-feldspar; Guzmics et al., 2008) in xenoliths metasomatized by a carbonatitic melt. Across the thin sections of all the Allègre samples, no reaction texture around Opx and no accessary minerals have been observed. Moreover, the present evidences are not enough to make us definitely conclude the metasomatic agent as a carbonatitic melt, rather than melts/fluids originally related to subducting slabs.

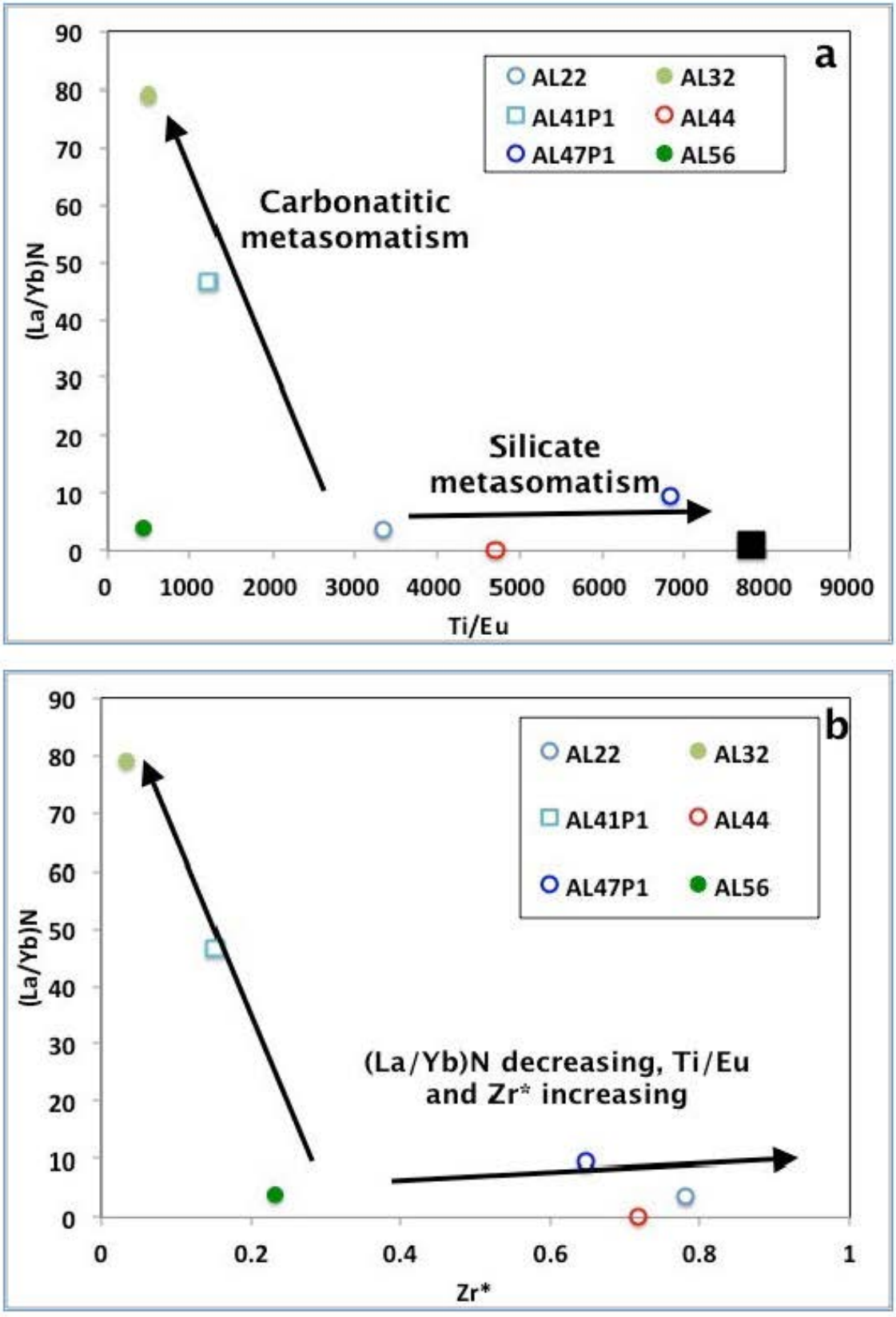

Figure 6-6: Variation of $(La/Yb)_N$ versus Ti/Eu (a) and Zr^* (b) in Cpx from Allègre peridotite xenoliths. The Ti/Eu value of the primitive mantle (McDonough and Sun, 1995) is also shown in black filled square for comparison (a). Coltorti et al. (1999) suggested the co-relation between $(La/Yb)_N$ and Ti/Eu in Cpx could be regarded as an indictor to distinguish the carbonatitic metasomatism from the silicate

metasomatism (a). Zr^* and Ti/Eu increase along with decreasing $(La/Yb)_N$ (the black lines). $Zr^*=2\times Zr_n/(Nd_n+Sm_n)$ where the subscript 'n' represents normalization to the primitive mantle.

At the same time, in the diagram of trace element variation normalized to the primitive mantle, all the analyzed Allègre samples, including sample AL44 that shows no LREE enrichment and very weak Ti negative anomaly, display a pronounced Nb negative anomaly. This can be ascribed to the strong Nb depletion resulted from foregoing partial melting due to the high incompatibility of Nb plus Nb deficiency in metasomatic melts/fluids. Nb negative anomalies in Cpx from Spitsbergen mantle xenoliths have been ascribed to the Amp precipitation in the vicinity of melt conduits (Ionov et al., 2002). This is also observed in Cpx from peridotite xenoliths from Ray Pic volcano (also belonging to the FMC southern domain; G1, G2 cpx in Denis et al. (2015)). These Ray Pic peridotites also have negative HFSE anomalies (Ti, Zr and Hf) and strong LREE enrichment in Cpx from the most strongly metasomatized samples (G3 Cpx in Denis et al. (2015)).

6.2.2 Trace element variations in Cpx from Mont Coupet

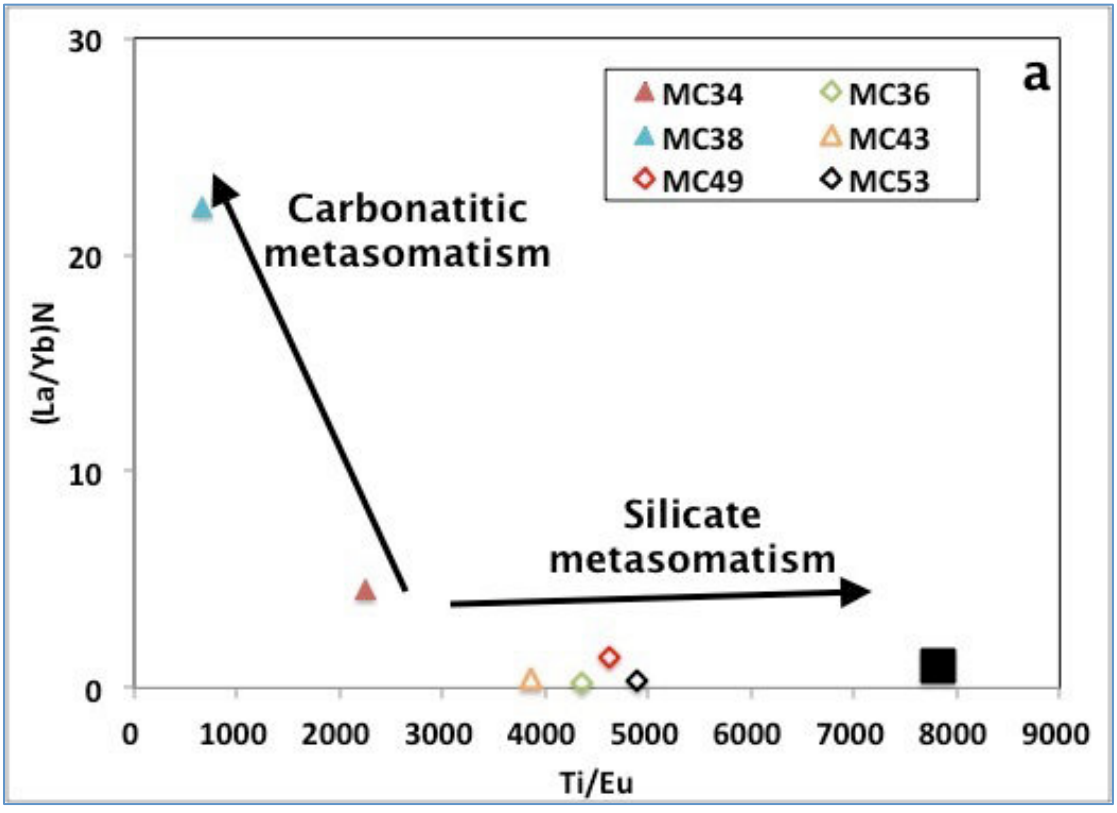

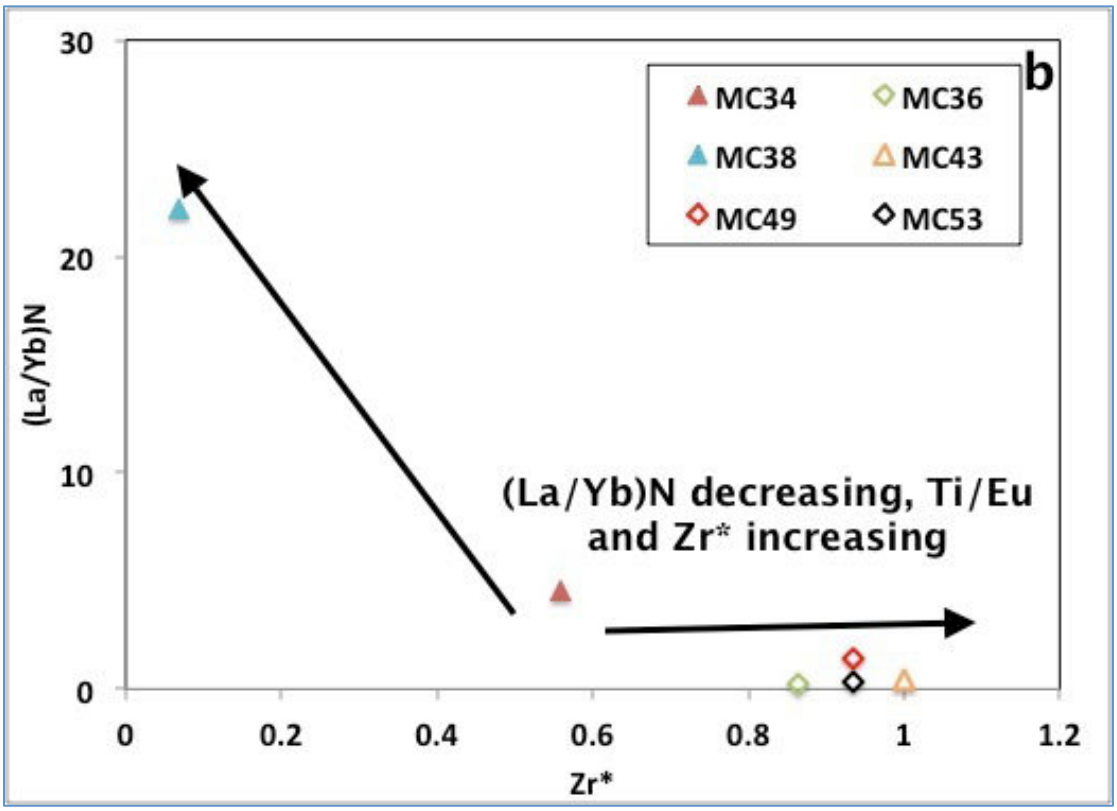

Figure 6-7: Variation of $(La/Yb)_N$ versus Ti/Eu (a) and Zr^* (b) in Cpx from Mont Coupet peridotite xenoliths.

The Cpx trace element compositions in Mont Coupet samples display a signature with a lower metasomatic influence than those in Allègre samples. In the chrondrite-normalized REE diagram, LREE depletion and flat transition from MREE to HREE indicate that the host samples have solely experienced partial melting and have not been refertilized by LREE-enriched metasomatic melts/fluids. Belong to this group not only sample MC43 but also the two Amp-bearing samples MC36 and MC53. Thus the modal metasomatism has not introduced significant LREE enrichment into samples MC36 and MC53. Cpx in sample MC49 have a nearly flat pattern from Ce to Lu with a steep uplift at La. Compared with the patterns in depleted samples, Ce should also have been added into sample MC49 by metasomatic melts/fluids but not in a similar degree to La. According to the calculated partial melting degree of sample MC34 (10%), the REE abundance in Cpx should be even lower than that in fore-mentioned four samples (MC43, MC36, MC53 and MC49). In the chrondrite-normalized REE diagram, HREE follow this intendancy but MREE and LREE appear to have been enriched. As the sample of highest partial melting

degree, sample MC38 have a distinctive chondrite-normalized REE distribution pattern compared with other samples from Mont Coupet (Fig. 4-7a). The strong depletion from Lu to Gd hasn't been replenished by the subsequent refertilization by metasomatic melts/fluids, which, however, induced the linear increase of the chondrite-normalized concentrations from Gd to La. But anyhow, the level of LREE enrichment relative to HREE in samples MC34 and MC38 is much weaker than the highest level observed in Allègre samples (e.g., sample AL32; Fig. 6-6a and 7a). According to the model for chromatographic effect from Mundl et al. (2015), the melt accounting for the Cpx chondrite-normalized REE distribution pattern of sample MC38 should be located at the end of the reaction series, occurring when a melt percolates into a porous matrix.

As for other trace elements in Cpx from Mont Coupet samples, the remarkable properties also lie in HFSE primitive mantle-normalized distribution. A Nb negative anomaly of high levels relative to neighboring elements is observed in all the samples from Mont Coupet in the primitive mantle-normalized REE diagram, which, comparable with Allègre samples, can be interpreted as a result of partial melting. The strength of Ti negative anomalies decreases from sample MC38 to MC53, roughly accompanied with the varying degrees of LREE enrichment. The lowest Ti/Eu ratio of Cpx in Mont Coupet samples is measured in Cpx from sample MC38 with the value of 653, suggestive of a metasomatic imprint by a carbonatite-related melt (Fig. 6-7a) or a melt/fluid released from a subducting slab. Similar to the Allègre samples, the samples from Mont Coupet don't have high Zr/Hf ratios in Cpx (11-30). And Zr negative anomaly is pronounced only in sample MC38 and very weak in sample MC34 (Fig. 6-7b).

6.2.3 Trace element partition between Cpx and Amp in samples MC36 and MC53

Sample	This study		Chazot et al. (1996)			Ionov et al. (1997)	Ionov et al. (2002)
	MC36	MC53	JK3	JK8	JK2		
Ba	233.3	11.1	1542.8	187.1	1745.9	880	-
Th	1	1.9	-	1	1.3	1	1.2
U	0.9	1.7	-	-	-	1	1.2
Nb	55.2	11	6.1	37.7	29	53	26
La	1.8	1.6	1.3	0.9	1.1	1.4	1.6
Ce	1.5	1.5	1.2	0.9	1.1	1.4	1.6
Sr	2.8	2.9	1.2	1	1.3	2.6	2.5
Nd	1.5	1.5	0.9	0.9	1.1	1.3	1.6
Zr	1	1	1.5	1.2	1.9	1.1	1.3
Hf	0.9	0.9	2.4	-	1.3	1	0.9
Sm	1.4	1.6	0.8	0.8	1.1	1.2	1.6
Eu	1.5	1.5	0.6	0.8	1.1	1.1	1.6
Ti	4.7	4.9	-	-	-	4.2	3.9
Gd	1.4	1.7	1.6	0.9	1.6	1.1	1.6
Dy	1.5	1.6	1.1	0.9	1.2	1	1.6
Y	1.6	1.6	1.1	0.9	1.1	1.2	-
Er	1.6	1.7	1.2	0.8	1.1	1	1.8
Yb	1.8	1.7	0.8	0.6	0.7	1	1.6
Lu	1.9	1.7	0.9	1.1	1.1	1	1.6

Table 6-1: The trace element concentration ratios between co-existing Amp and Cpx ($K_d^{Amp/Cpx}$) in samples MC36 and MC53. The ratios of three spinel Iherzolites from Chazot et al. (1996), and the average ratio of three mantle xenoliths from Ionov et al. (1997) are also shown for comparison. The trace element partition coefficients between Cpx and Amp are calculated from the partition coefficients between Cpx/Amp and melts, which were used to model the behaviors of trace elements during partial melting in Ionov et al. (2002).

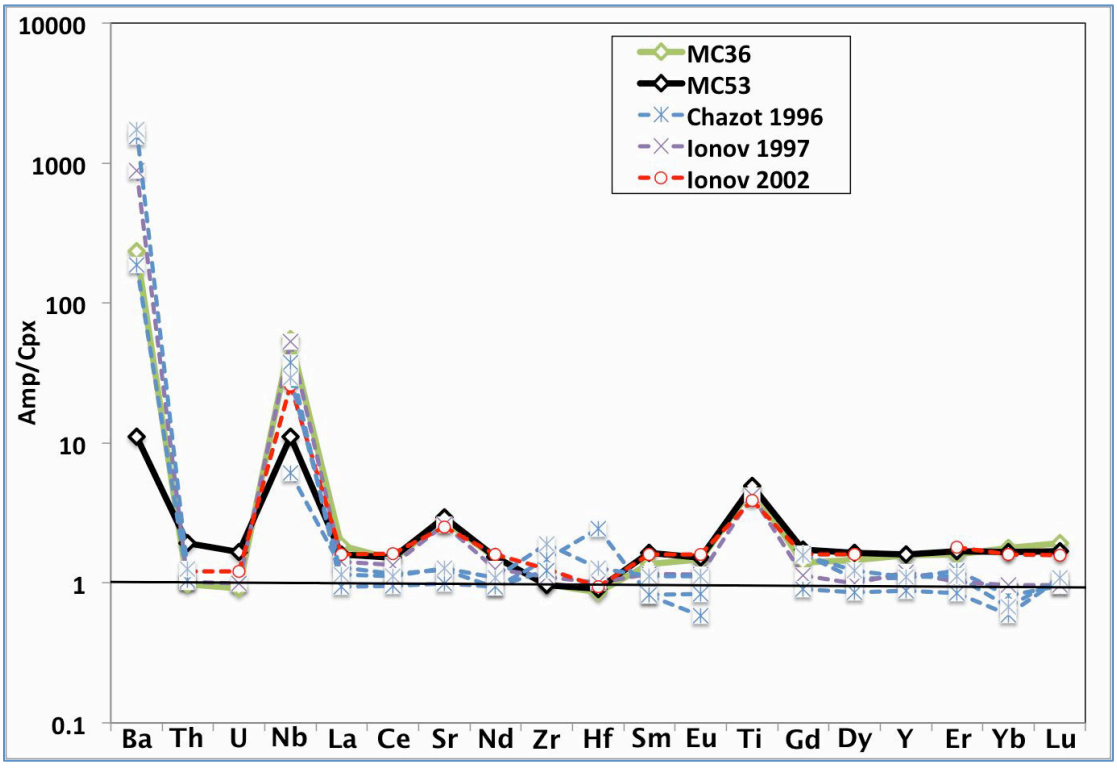

Figure 6-8: The trace element concentration ratios between co-existing Amp and Cpx ($K_d^{Amp/Cpx}$) in

samples MC36 and MC53 compared with literature data in table 6-1.

The trace element concentration ratios between co-existing Amp and Cpx ($K_d^{Amp/Cpx}$) in samples MC36 and MC53 are reported in Table 6-1. As shown in Fig. 6-8, the REE $K_d^{Amp/Cpx}$ of Mont Coupet xenoliths are close to those from the REE partition coefficients between Amp and Cpx measured in natural samples from previous studies (Chazot et al., 1996; Ionov et al., 1997) and those calculated from the partition coefficients between Cpx (and Amp) and melts (Ionov et al. 2002). Amp in sample MC36 and MC53 generally grow around Cpx and no significant core-rim variations have been observed in the REE concentrations of the two minerals. Combining with the similar Amp chondrite-normalized REE distribution patterns to those of Cpx (Fig. 4-7a and Fig. 4-8a), it can be concluded that REE partitioning has achieved equilibrium between co-existing Amp and Cpx in both samples.

However, when considering other trace elements (LILE and HFSE) in Amp, the situation becomes more complicated. Firstly, the large concentration discrepancy of Nb and Ba between sample MC36 and MC53 can only be interpreted as the inheritance from distinct sources, due to the distinctive mobility of these two elements in fluids. Coltorti et al. (2007) have compiled the major and trace element compositions of Amp in mantle xenoliths from many localities of various tectonic backgrounds and suggested that Nb concentrations in Amp can be used to discriminate the metasomatic fluids from supersubduction zones or from intraplate settings. Amp crystalized from intraplate metasomatic fluids contain Nb with a range of from 10 to 1000 ppm, much more than or little overlapping with Nb concentration range in Amp related to fluids from subducting slabs, which is mostly below 10 ppm (Coltorti et al., 2007). At this point, even though Amp in the sample MC36 contains much more Nb (11.2 ppm) than Amp in sample MC53 (0.6 ppm), it is not enough convincing to classify Amp in sample MC36 into those of intraplate origin. Otherwise, Zr/Nb ratios plotted against Ti/Nb ratios and Ti/Zr in Amp have also been proposed to trace the origin of Amp (Fig. 6-9; Coltorti et al., 2007). Sample MC53 falls in the field of Amp related to supersubduction fluids while sample MC36 isn't included by the fields of both Amp types and falls close to the overlap zone due to its relatively higher Nb content in Amp. The study of Touron (2005) based on a larger dataset of

Amp trace element compositions in peridotite xenoliths from the southern domain of the FMC also observed that Amp in sixteen xenoliths, even some from the same locality, have fall in different fields (Fig. 6-9). It indicates that the majority of Amp in peridotites from the FMC may crystalize from supersubduction fluids or from two end-member mixed fluids (supersubduction and intraplate). The model of a binary mixture, the residual Hercynian subducted oceanic lithosphere and the depleted upper mantle, has also been invoked to explain the Sr-Nd-Pb isotopic variations observed in the Tertiary-Quaternary mafic magmas from the FMC (Wilson and Downes, 1991).

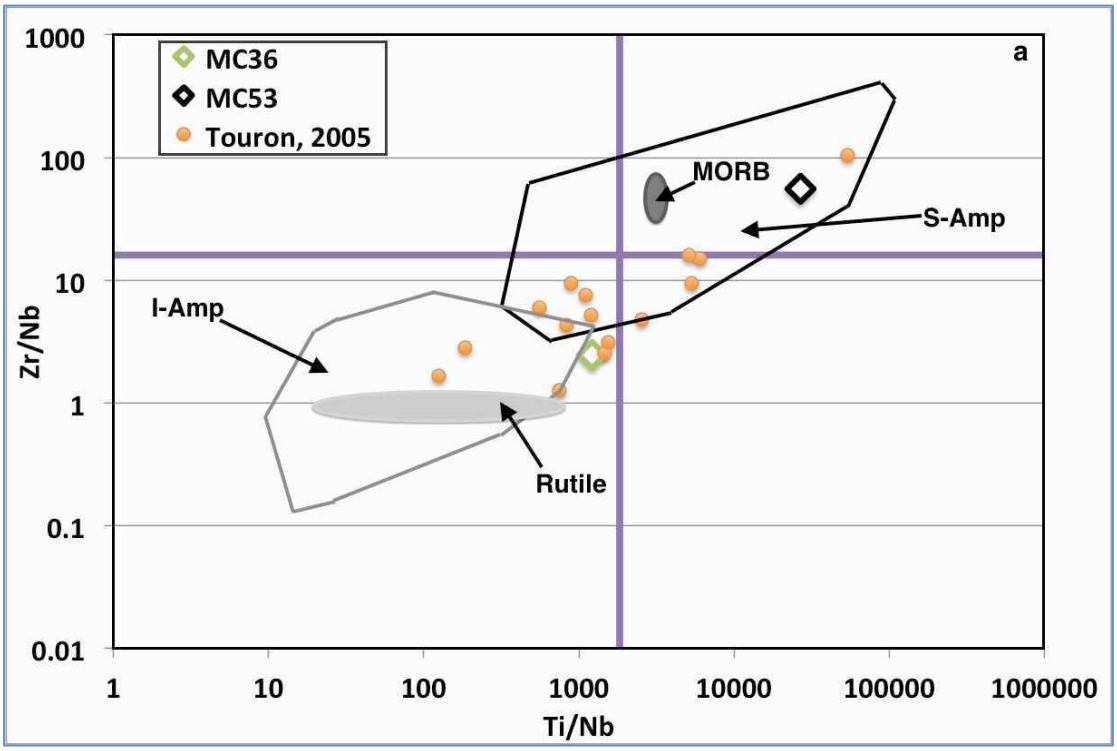

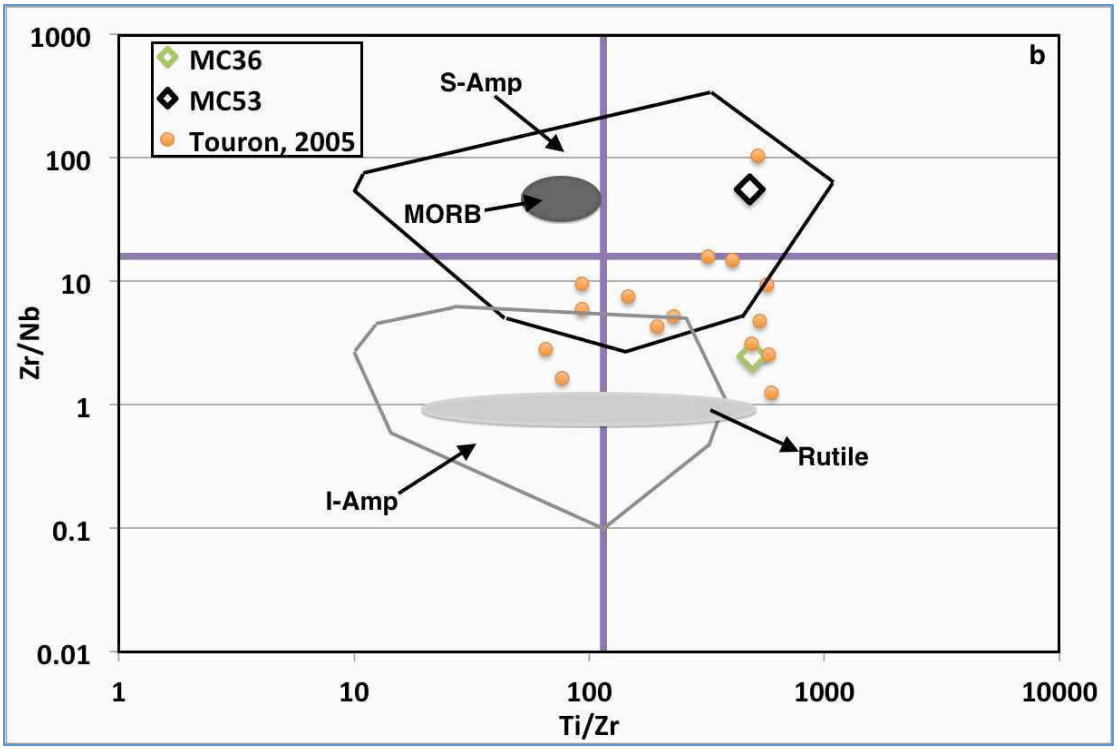

Figure 6-9: Zr/Nb ratios vs. Ti/Nb ratios (a) and Ti/Zr (b) of Amp in samples MC36 and MC53. S-Amp and I-Amp represent Amp originating from suprasubduction and intraplate environments, respectively. The fields for different Amp types are repainted according to Coltorti et al. (2007).

On the other hand, the Zr-Hf negative anomaly and Sr-Ti positive anomaly are present in Amp from both samples, totally different from coexisting Cpx, where there are weak Ti negative anomalies and no Sr-Zr-Hf anomalies. But $K_d^{Amp/Cpx}$ of each element in both samples is close to its equilibrated partition coefficient (Table 6-1). The different distribution patterns of Zr, Hf and Ti in coexisting Amp and Cpx from samples MC36 and MC53 can therefore be ascribed to concentration homogenization of each element between these two phases. Vannucci et al. (1995) have observed the same cases with samples MC36 and MC53. They integrated the trace element distribution of LREE-depleted Amp in 13 peridotites from different localities and found that Sr and Ti displayed positive anomalies and Zr (Hf not analyzed) displayed negative anomaly, which have been ascribed to the equilibrated redistribution at mantle depths (Vannucci et al. 1995). Some Amp grains in peridotite xenoliths sampled from other localities (Touron, 2005; Denis et al., 2015) also show similar trace element distribution patterns, with LREE depletion, Ti-Sr positive anomalies and Zr-Hf negative anomalies, and their coexisting Cpx grains are also poor in LREE and Ti.

6.2.4 Trace element compositions of metasomatic melts/fluids and melt-rock reaction kinetics

As Cpx grains in sample AL56 do not show trace element zoning from core to rim and sample AL56 is the most strongly metasomatized sample, proposed as the nearest sample to the metasomatic melt source by the modeling, we interpret that the trace element compositions of Cpx in that sample are the closest, from our sample suite, to the trace element compositions of Cpx that have equilibrated with the reactive melt. To assess the nature of the melt responsible for the trace element characteristics of our samples, the trace element compositions of melts in equilibrium with Cpx in sample AL56 were calculated based on the equation: $C_{melt}=C_{mineral}/D_p$, where C_{melt} and $C_{mineral}$ denote the concentrations of elements in the melt and Cpx, respectively, and D_p represents the experimentally measured partition coefficients of trace elements between Cpx and either a silicate melt (from Hart and Dunn, 1993, and Johnson, 1998) or a carbonatite melt (from Klemme et al., 1995). As shown in Fig. 6-10a, the calculated trace element patterns of reactive melts, using partition coefficients between a silicate melt and Cpx, do not match the trace element patterns of representative alkaline basalts in the FMC (Wilson and Downes, 1991), but display fractionation between the various trace elements similar to the pattern of a carbonatite melt originated from the mantle (Wagner et al., 2003). For xenoliths from Mont Coupet, we consider that no samples have the trace element compositions in Cpx equilibrated with the infiltrated melt according to the modeling for the chromatographic effect. However, from the calculated trace element compositions of melts in equilibrium with the most metasomatized sample MC34, some similar characteristics can be identified (Fig. 6-10b).

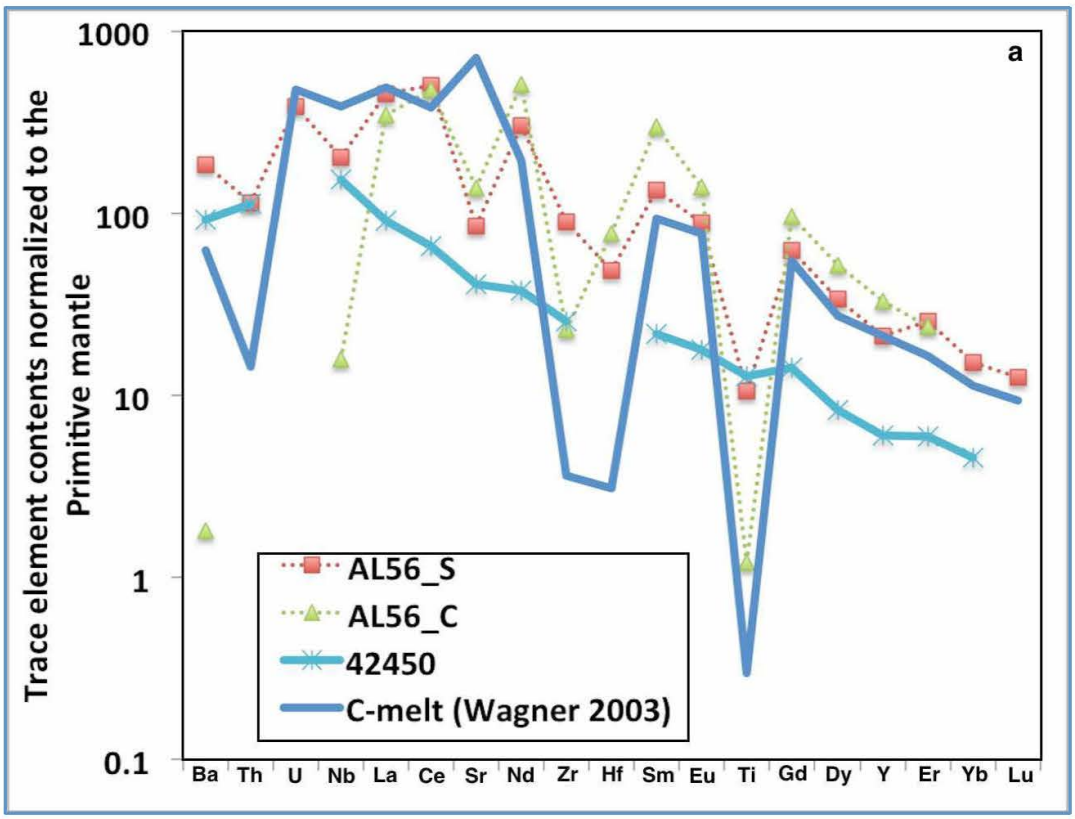
a
Trace element contents normalized to the Primitive mantle
1000
100
10
1
0.1
AL56_S
AL56_C
42450
C-melt (Wagner 2003)
Ba Th U Nb La Ce Sr Nd Zr Hf Sm Eu Ti Gd Dy Y Er Yb Lu

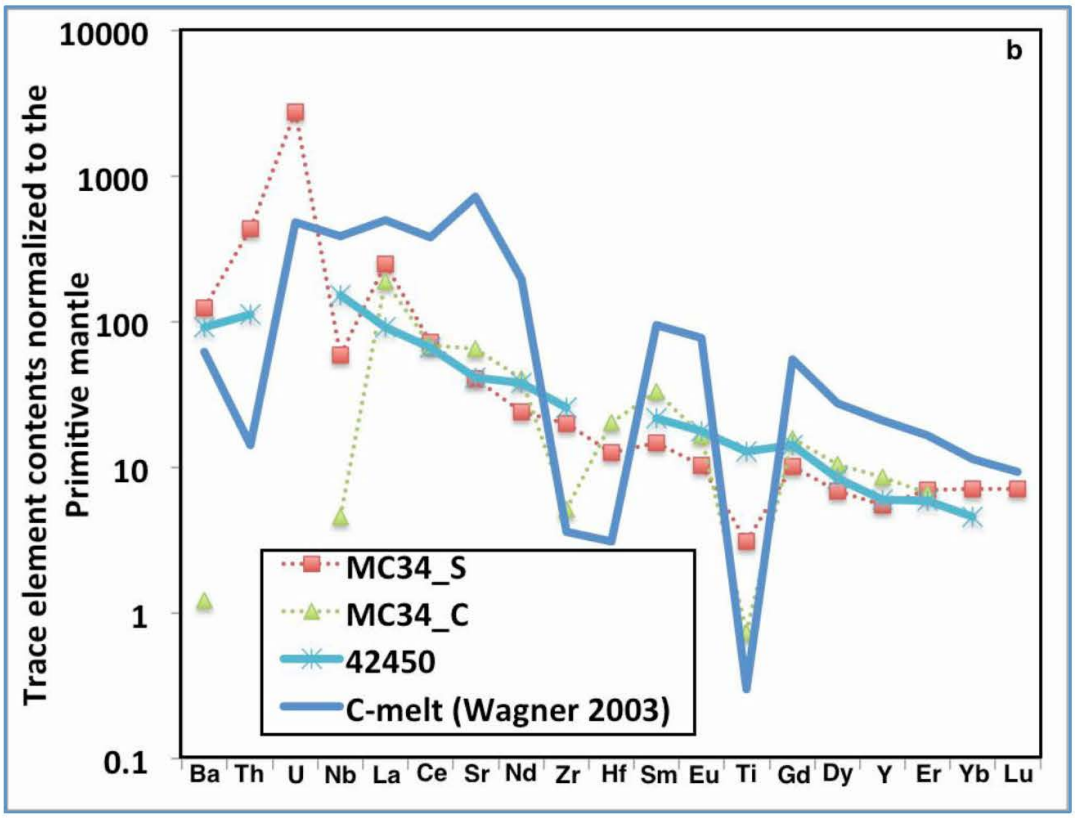
b
Trace element contents normalized to the Primitive mantle
10000
1000
100
10
1
0.1
MC34_S
MC34_C
42450
C-melt (Wagner 2003)
Ba Th U Nb La Ce Sr Nd Zr Hf Sm Eu Ti Gd Dy Y Er Yb Lu

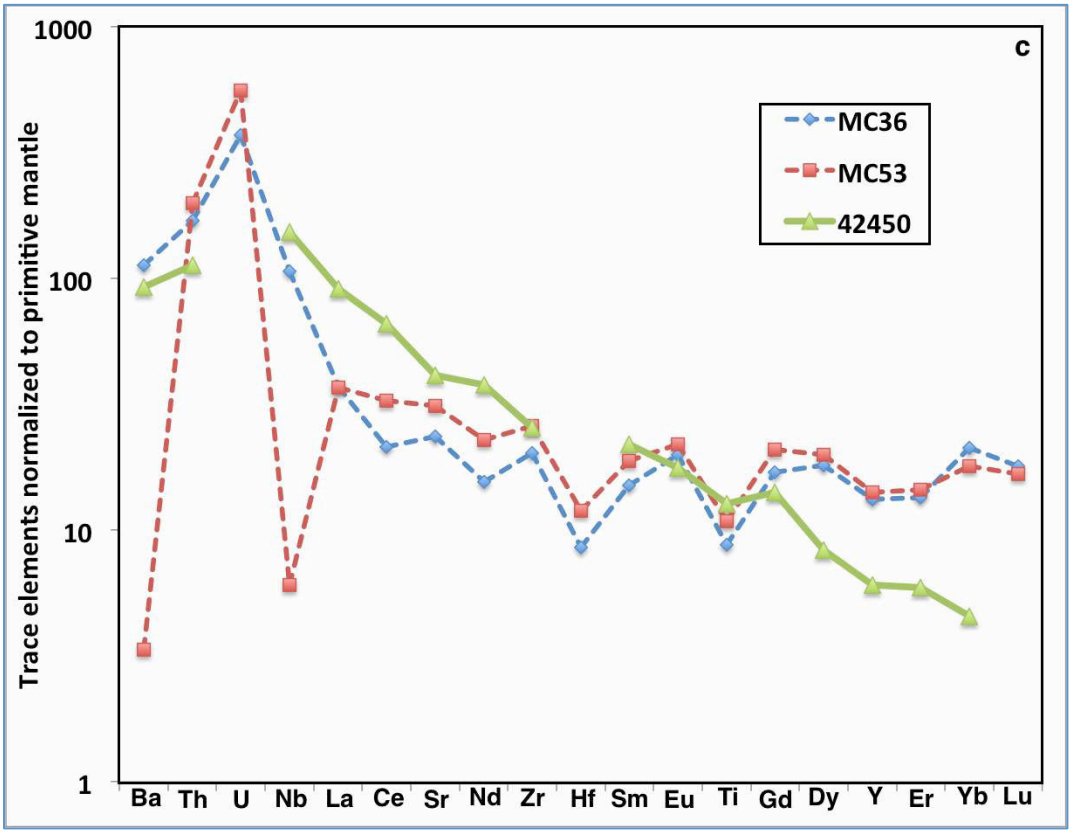

Figure 6-10: The primitive mantle-normalized trace element distribution patterns of the hypothetical silicate and carbonatite melts in equilibrium with Cpx from samples AL56 (a) and MC34 (b), and the primitive mantle-normalized trace element distribution patterns of the hypothetical silicate melts in equilibrium with Amp in samples MC36 and MC53 (c). The partition coefficients of trace elements between carbonatitic melts and Cpx refer to Hart and Dunn (1993) and the partition coefficients of trace elements between silicate melts and Cpx refer to Johnson (1998). The trace element compositions of representative alkaline basalts in the FMC are also shown for comparison (42450 from Wilson and Downes (1991)). The compositions of a carbonatitic melt are from Wagner et al. (2003) (the blue continuous line in a, b). The partition coefficients of most trace elements between basaltic melts and Amp are cited from LaTourrette et al. (1995). The coefficients of Sm, Eu and Dy have not been determined in LaTourrette et al. (1995) and refer to the calculated values in Ionov et al. (1997), due to the calculated partition coefficients of other elements in Ionov et al. (1997) very close to the experimentally determined values in LaTourrette et al. (1995).

As Amp are commonly generated by reaction of percolating melts/fluids with primary minerals (mainly Cpx) or are directly crystalized from metasomatic melts/fluids, the nature of melts/fluids can be unraveled from Amp compositions. Thus, the trace element compositions of melts/fluids equilibrated with Amp in samples MC36 and MC53 were calculated using the partition coefficients of trace elements between Amp and silicate melts (Latourette et al., 1995; Ionov et al., 1997).

The primitive mantle-normalized trace element distribution patterns of melts/fluids calculated from each sample are shown in Fig. 6-10c. No large differences exist between them, with exception of Ba and Nb concentrations.

To constrain the time needed for Cpx trace element compositions to equilibrate with a metasomatic melt, we apply a one-dimensional diffusion model simulating Sr concentrations, assuming that Sr diffuses from percolating melts of constant Sr concentration to Cpx grains acting as semi-infinite reservoirs:

$$\frac{C - C_s}{C_0 - C_s} = erf\left(\frac{x}{2\sqrt{Dt}}\right) \quad (6)$$

where C is the Sr concentration at any given distance x and time t after the onset of Sr diffusion, C_0 is the initial Sr concentration in the mineral core, C_s is the Sr concentration at the mineral boundary, D is the diffusion coefficient (Sr diffusion coefficient from Sneeringer et al., 1984), and *erf* is the error function. We assume that the Sr concentration of the average depleted MORB mantle (DMM; Workman and Hart, 2005) represents the initial concentration in pre-existing Cpx; the Sr concentration in the melt is constant (calculated above based on sample AL56). The model results imply that, to thoroughly equilibrate a 2mm-diameter Cpx grain in sample AL56, the percolating melt spent approximately 2.4 Ma at 850℃ or 200 years at 1100℃.

In summary, the trace element distribution in Cpx and Amp in peridotite xenoliths from Allègre and Mont Coupet reveals that the sub-continental lithospheric mantle beneath both localities has undergone mantle metasomatism by carbonatitic melts/fluids or melts/fluids released from subducting slabs in different degrees. The percolating melt left a spectrum of trace element variations (from strong enrichment to depletion) in Cpx from Allègre due to the chromatographic effect. The modal metasomatism in samples MC36 and MC53 haven't refertilized Cpx in LREE and LILE, and Amp in both samples have equilibrated most of the trace element composition with coexisting Cpx.

6.3 Li distribution and isotopic composition variations in peridotite xenoliths from Allègre and Mont Coupet

Li is one of fastest diffusing elements at high temperatures. As a trace element in peridotite, its distribution will inevitably be disturbed during melt-rock reactions occurring to peridotite xenoliths (either mantle metasomatism, or interactions between xenoliths and their host magmas). Its high diffusivity and its isotopic fractionation during diffusion (cf. section 6.3.1 and 6.3.2) make Li an effective tool to characterize the geological processes at short time scales (e.g., from days to years).

6.3.1 Intra- and inter-mineral Li and Li isotope distribution in Allègre samples

The Li concentration ratios and Li isotopic differences among individual minerals in each sample from Allègre are reported in Table 6-2. The average Li concentrations and isotopic compositions at cores and rims of all the grains for each phase are also shown for each sample.

Sample	Mineral	Li				δ^7Li (‰)			
		Core (ppm)	Rim (ppm)	$D_{Ol/Cpx}$	$D_{Opx/Cpx}$	Core	Rim	Δ^7Li_{Ol-Cpx}	$\Delta^7Li_{Opx-Cpx}$
	Ol	1.7	1.7			-6.3	-7.2		
AL22	Opx	4.7	1.2	0.1	0.2	-4.6	-3.4	-8	-6.5
	Cpx	25.8	12.4			1.2	2.6		
	Ol	1.9	2.5			-3.4	-6.5		
AL32	Opx	5.7	3.4	0.1	0.3	-30.2	-15.4	3	-17.5
	Cpx	16.2	18.3			-5.9	-5.1		
	Ol	2.8	4.7			-14.1	-10.7		
AL41P1	Opx	3.4	2.9	0.3	0.2	-12.1	-12.2	-1.3	2.6
	Cpx	13.5	7.6			-14.1	-12.3		
	Ol	2	2.9			-9.2	-9.2		
AL44	Opx	3.8	2	0.1	0.1	-7.2	-10.4	-3.7	-2.7
	Cpx	30.9	24			-4.1	-4.4		
	Ol	3.1	5.2			-6.7	-3.6		
AL47P1	Opx	1.9	3	0.5	0.3	20.4	20.5	-8.1	19.7
	Cpx	7.8	6.9			2.1	2.9		
	Ol	2.5	3.8			-3	-6		
AL56	Opx	3.1	3.2	0.1	0.1	1.1	-6.1	-6.7	-4.3
	Cpx	39.9	33.6			2.7	2.1		

Table 6-2: The average Li concentrations and isotopic compositions at cores and rims, Li concentration ratios and Li isotopic differences (e.g., $\Delta^7Li_{Ol-Cpx}=\delta^7Li_{Ol}-\delta^7Li_{Cpx}$) among individual phases in Allègre samples.

6.3.1.1 Intra-granular and inter-mineral lithium concentration disequilibrium

The Li content of the primitive mantle has been assessed to be 1.6±0.5 ppm (Jagoutz et al., 1979; McDonough and Sun, 1995). Using fertile equilibrated

peridotites, unaffected by metasomatic processes, as representative of the normal mantle, the Li partitioning sequence among mantle minerals is recognized as Ol>Cpx ≥Opx, with Li contents of 1.0-2.2 ppm for Ol, and 0.5-1.3 ppm for pyroxene (Seitz and Woodland, 2000; Ottolini et al., 2004). The definition of the 'normal' mantle is from Ottolini et al. (2004), who endowed the normal mantle with a homogenous pyrolitic composition and an evolutional history of only the crust extraction by partial melting. Spl and garnet contain even less Li, and, given their relatively low modal abundance in peridotite, those minerals are usually not considered (Seitz and Woodland, 2000; Jeffcoate et al., 2007).

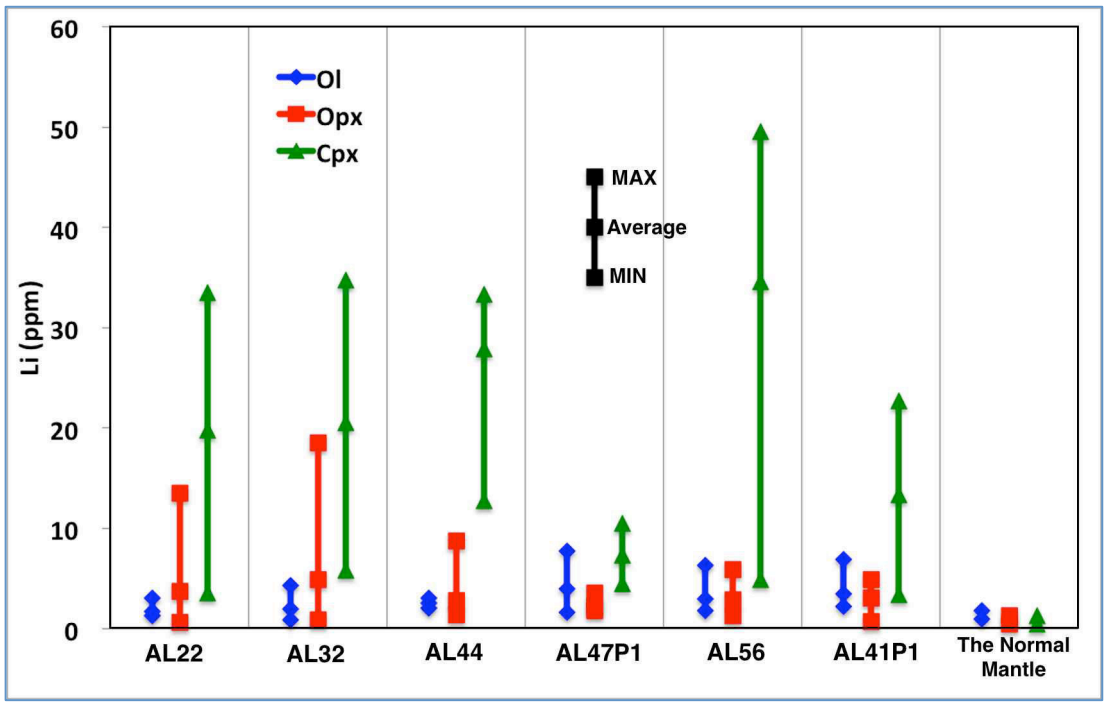

Figure 6-11: Li concentrations in Allègre samples including the minimum and maximum values compared with the Li concentration ranges estimated for the normal mantle (Seitz and Woodland, 2000; Ottolini et al., 2004).

The minerals in Allègre samples have incorporated additional Li (relative to the normal mantle), with concentrations up to 50 ppm in Cpx of AL56 (Fig. 6-11); Cpx in AL47P1, which display the lowest Li content (from 4.5 to 10.5 ppm), may have exchanged or lost Li to the interstitial melt during the formation of their spongy rims. Strong Li distribution disequilibria among mineral phases are concomitant with this Li addition (Fig. 6-12). The Li concentration ratios between Ol and Cpx ($D_{Li}^{Ol/Cpx}$) range from 0.08 to 0.54, much lower than the partition coefficient at equilibrium (Fig. 6-12a; 1.5~2.0, Seitz and Woodland, 2000; 1.74, Ottolini et al., 2009). Until now, the

inter-mineral nonequilibrium Li partitioning has been mostly ascribed to recent metasomatism by exotic melts/fluids (Rudnick and Ionov, 2007; Wagner and Deloule, 2007; Tang et al., 2007, 2011; Aulbach et al., 2008; Aulbach and Rudnick, 2009; Zhang et al., 2009; Su et al., 2012; Xu et al., 2013) or the Li re-distribution among mineral phases caused by the change of Li partition coefficient with decreasing temperature during ascent to the surface (Ionov and Seitz, 2008; Gallagher and Elliott, 2009; Kil, 2010; Gao et al., 2011; Xiao et al., 2015).

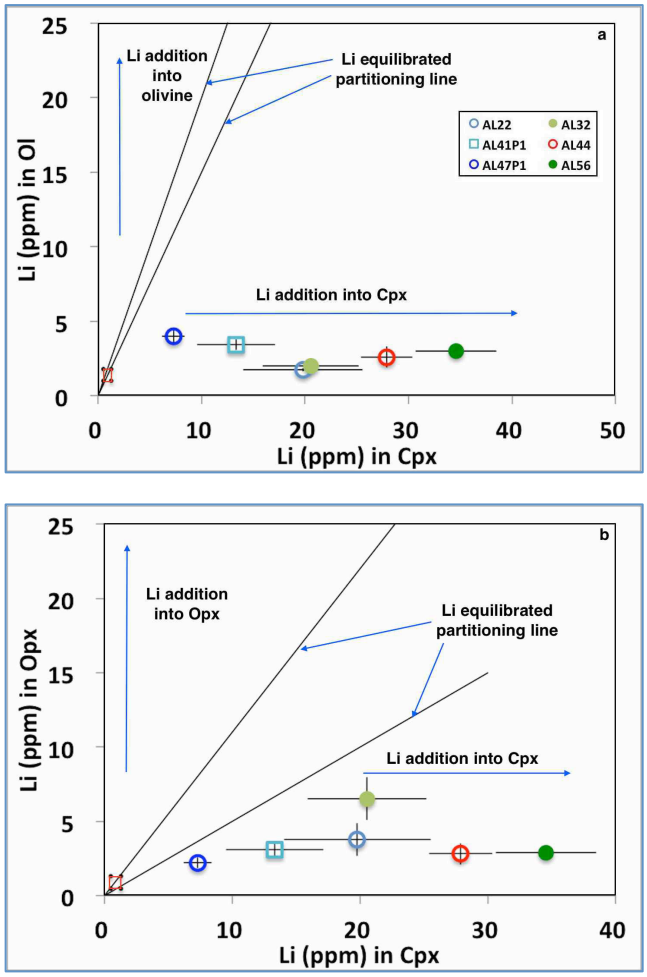

Figure 6-12: Li partitioning between Ol and Cpx (a) and between Opx and Cpx (b) in Allègre samples. The equilibrated partitioning lines are plotted according to the coefficients from Seitz and Woodland (2000), $D_{Ol/Cpx}$=1.5-2.0 and $D_{Opx/Cpx}$=0.5-1.1. The mineral Li content in the normal upper mantle is delimitated by the small red square. The metasomatic tendency is according to Seitz and Woodland (2000) and Su et al. (2014).

Yet, Kaliwoda et al. (2008) observed an increase of the Li partition coefficient between Ol and Cpx during cooling, in contrast with a decrease of this coefficient observed in other studies (Ionov and Seitz, 2008; Gao et al., 2011). Moreover, Yakob et al. (2012) have not detected any temperature dependence of the lithium partition coefficient between Ol and diopside (2.0±0.2) during experiments conducted from 700℃ to 1100℃. Thus, we will considere that the Li disequilibrated distribution observed in our samples results from melt/fluid metasomatism. Preferential Li

enrichment in either Ol or Cpx has been attributed to the type of interacting melt at mantle depth (Seitz and Woodland, 2000; Su et al., 2014). Silicate melts preferentially enrich Cpx in Li (e.g., Seitz and Woodland, 2000; Scambelluri et al., 2006; Tang et al., 2007; Wagner and Deloule, 2007; Rudnick and Ionov, 2007; Aulbach and Rudnick, 2009; Zhang et al., 2009), whereas carbonatitic melts preferentially enrich Ol (Ottolini et al., 2004; Woodland et al., 2004; Su et al., 2012). From this, the large Li enrichment in Allègre peridotite Cpx seems to result from mantle metasomatism by a silicate melt at first glance. Nevertheless, the xenoliths cooled slowly in a solidified lava lake, and host magma percolation was observed in some xenoliths. Consequently, the Li distributions in the xenoliths could have been modified in the lava lake due to the rapid diffusive rate of Li, and it is important to identify the respective effects of late infiltration of the host magma and of earlier mantle metasomatism on the final Li distribution in our samples.

The Li concentration profiles indicate that the Li addition not only induced inter-mineral disequilibria, but also disrupted the intra-granular Li elemental homogeneity (Fig. 6-11 and 6-13). Cpx cores show high Li concentrations (up to 40 ppm) similar to Cpx rims, within error. The most common case in Opx is that the cores contain much more Li than their corresponding rims, with some exceptional grains in which the inverse Li distribution pattern exists (Fig. 6-13). Ol are more variable; some grains have constant lithium contents from cores to rims, and, in other grains, Li contents rise suddenly just near grain boundaries (Fig. 6-13).

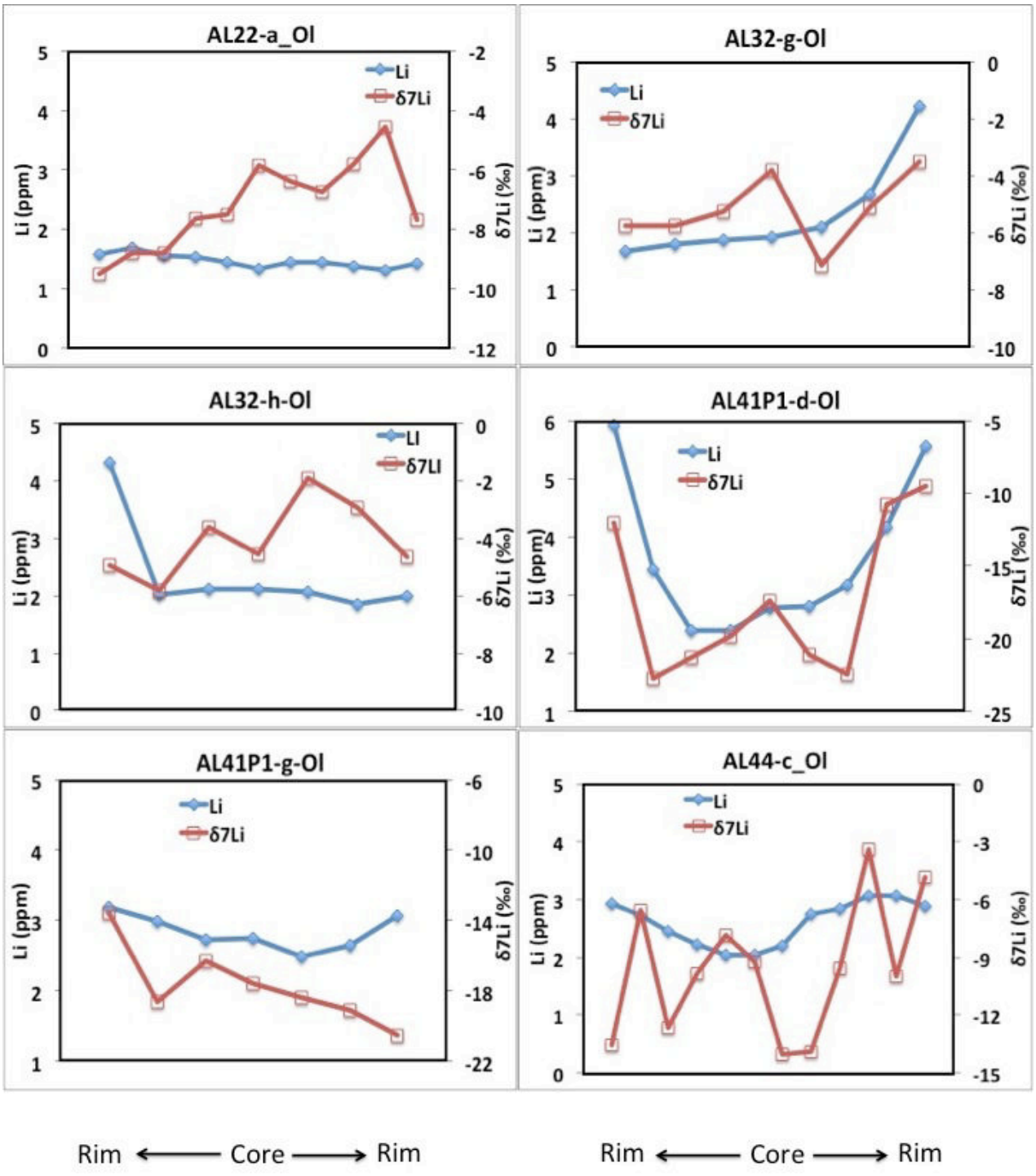

Figure 6-13: Representative Li concentration and δ^7Li profiles of core-rim variations in Ol, Opx and Cpx grains from Allègre samples.

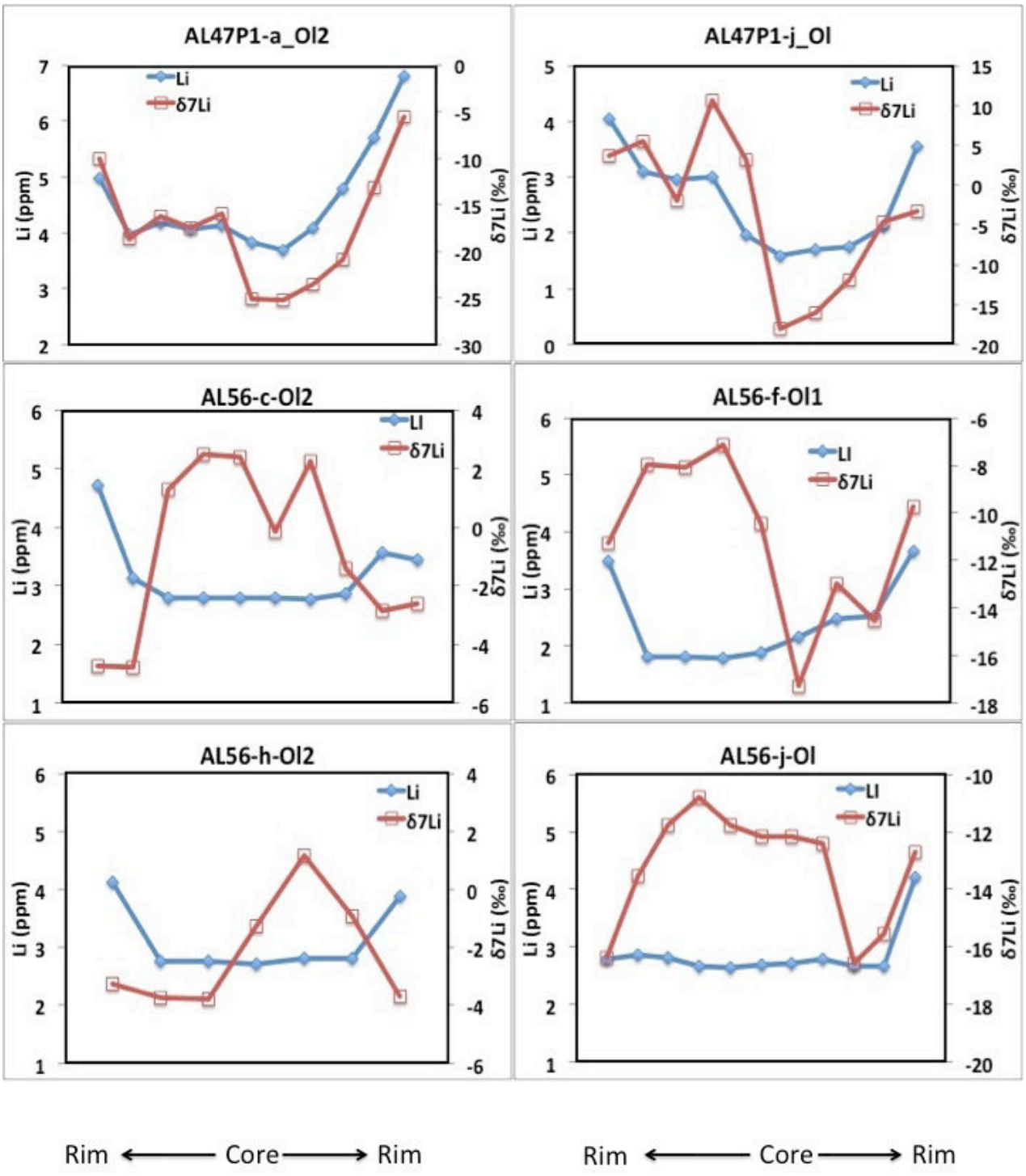

Figure 6-13 (continued).

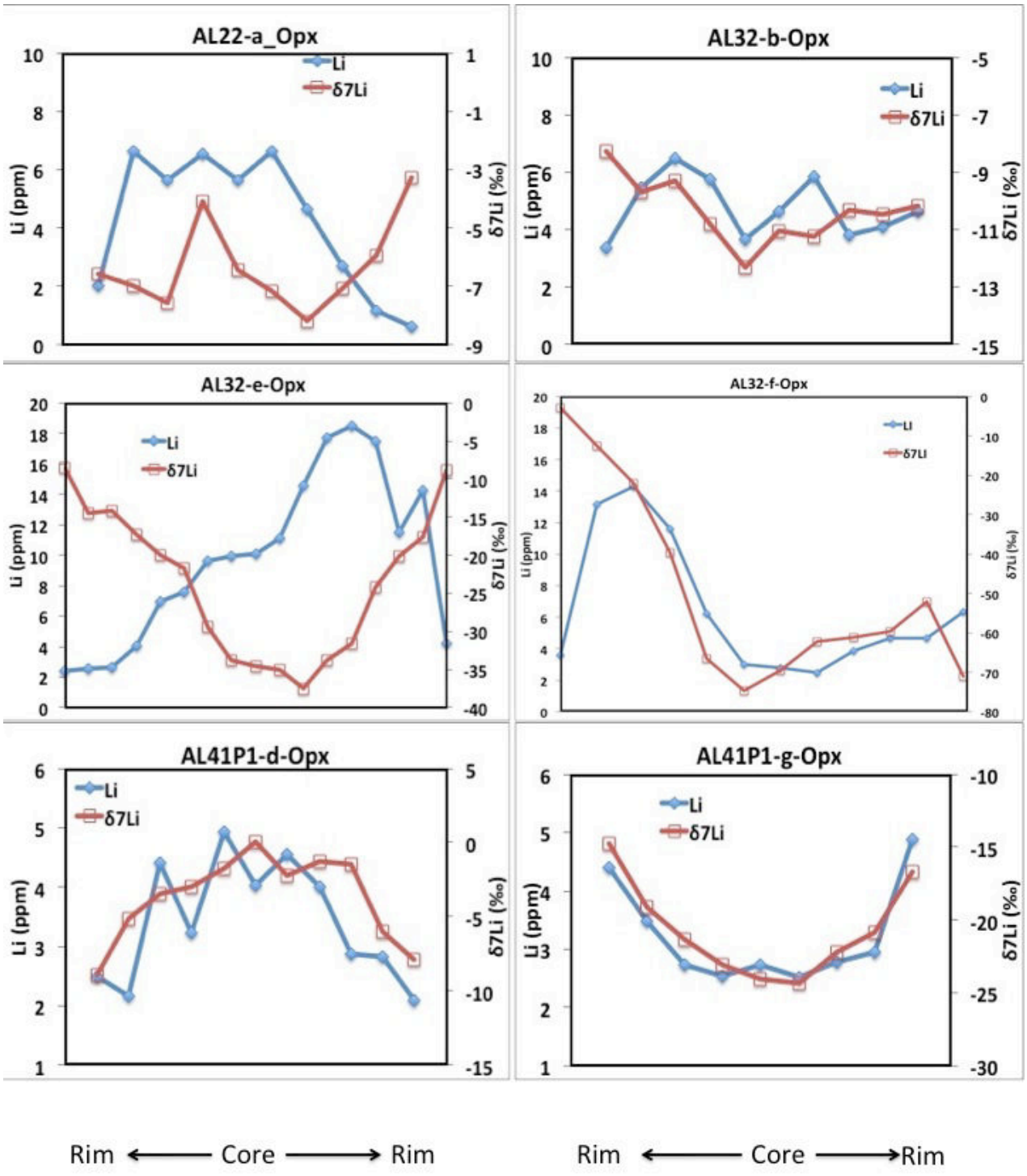

Figure 6-13 (continued).

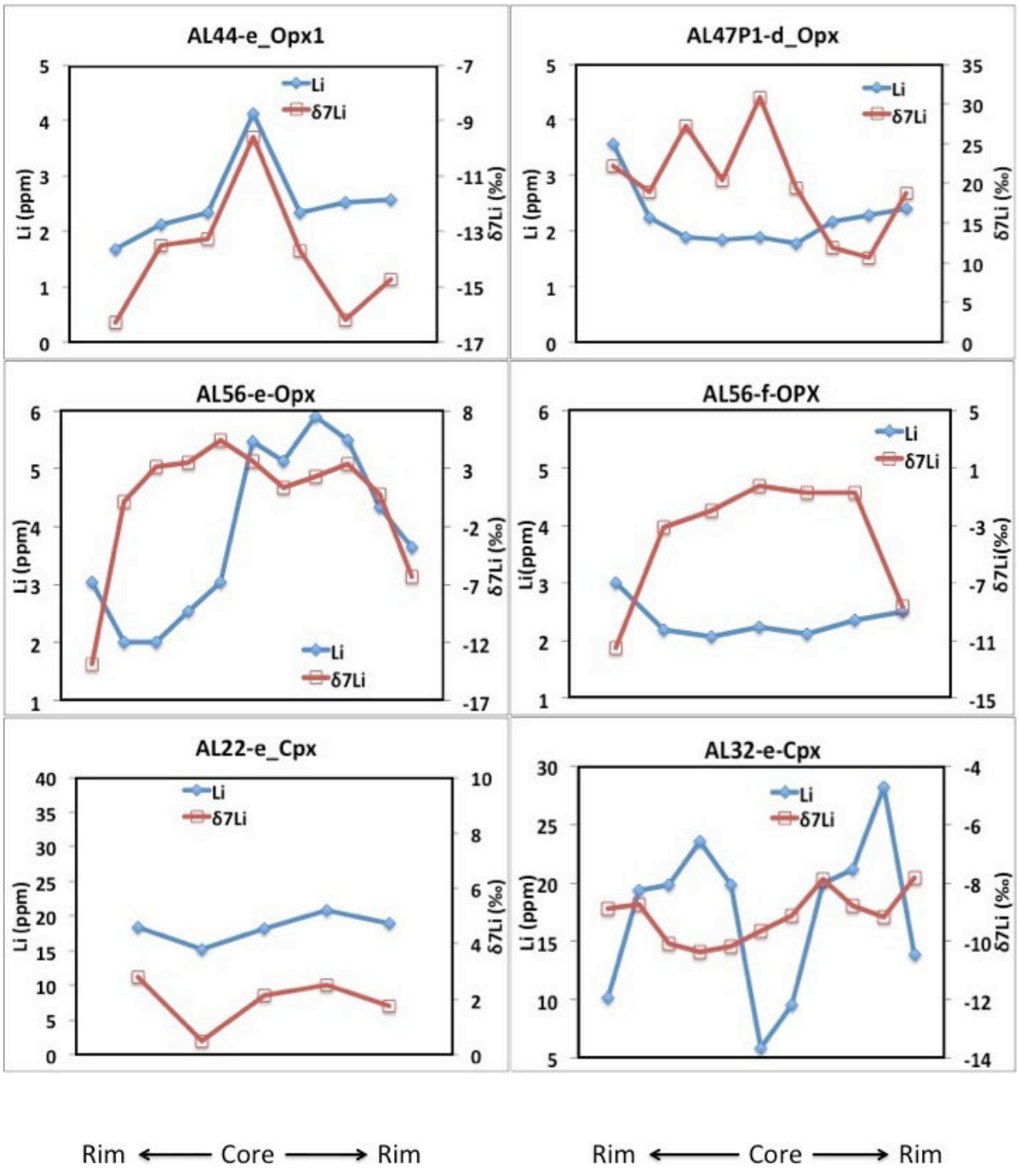

Figure 6-13 (continued).

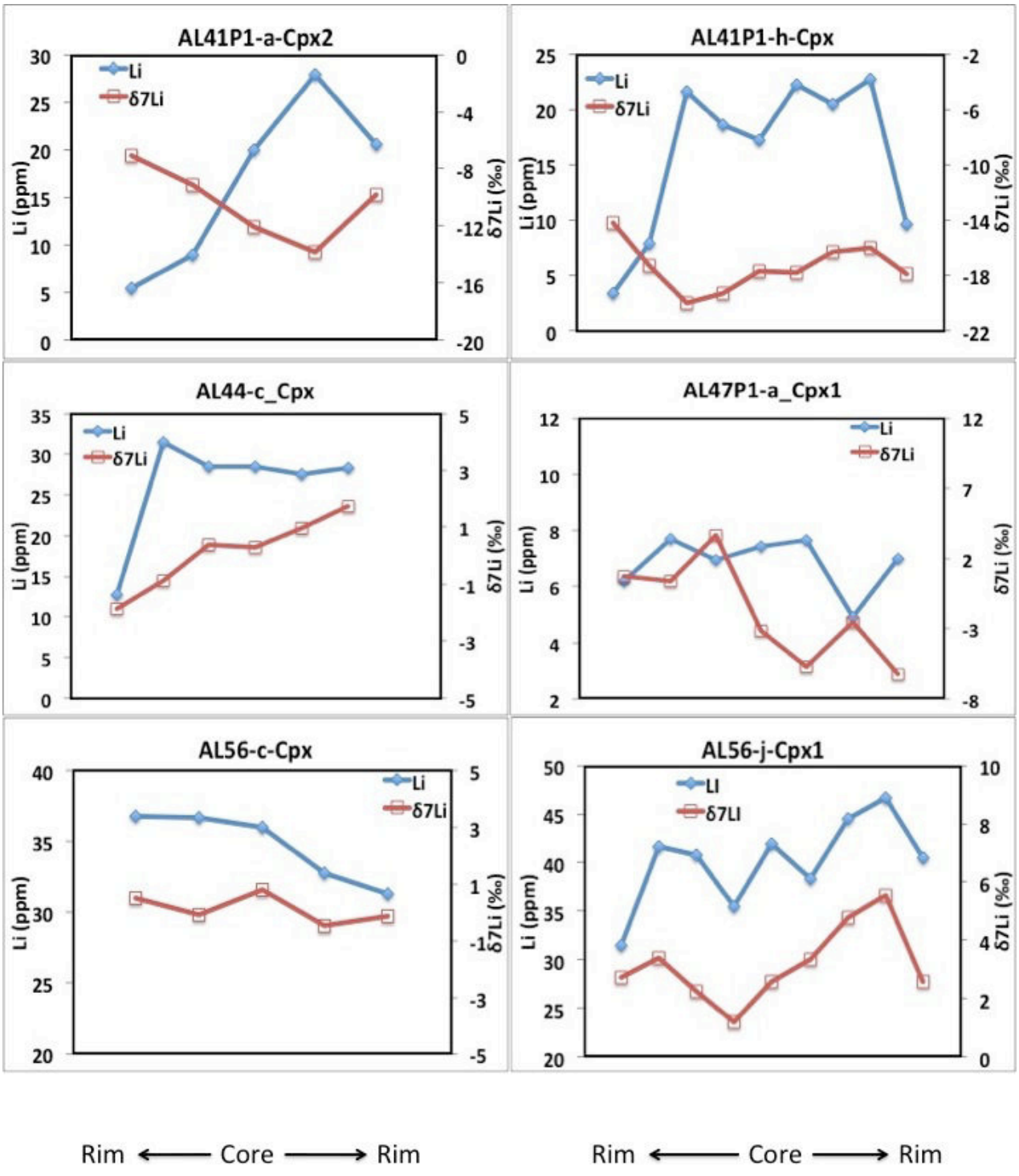

Figure 6-13 (continued).

The higher diffusivity of Li in Cpx than in Ol (e.g., Aulbach and Rudnick, 2009; Jeffcoate et al., 2007; Parkinson et al., 2007) and the smaller grain sizes of Cpx relative to Opx and Ol, account for a faster equilibration of Cpx grains with metasomatic agents, and thus for higher Li concentrations in Cpx during metasomatic

events (Jeffcoate et al., 2007; Rudnick and Ionov, 2007; Xu et al., 2013). In our samples, the extremely high Li content of Cpx therefore reflects a recent diffusive Li uptake (Fig. 6-13). As phenocrysts and microcrystals in the host magma contain 16.5±5.0 ppm lithium, we conclude that the infiltrating melts are residual melts after fractional crystallization of the host magma and should be more enriched in Li due to its incompatibility. The evolved melts then penetrated the xenoliths, providing large amounts of Li to Cpx. Due to the slower Li diffusive rate in Ol, melt infiltration solely increased Li concentrations at the rims (<900μm from the grain boundaries; Fig. 9-3), whereas the cores were unaffected, and preserve the Li concentrations from depth. Li content in Ol cores ranges from 1.3 to 4.4 ppm, representative of the normal mantle to slightly enriched values (Fig. 6-14), possibly indicating a Li addition by a mantle metasomatism prior to entrainment by the host magma. This earlier metasomatic stage is also supported by the lack of correlation between Li contents and Mg# of cores (Fig. 6-14), which is not in accordance with the intermediately incompatible characteristic of Li during partial melting. The irregular distribution of Li across Opx grains further evidence that the samples from Allegre have suffered melt/fluids infiltration not just once.

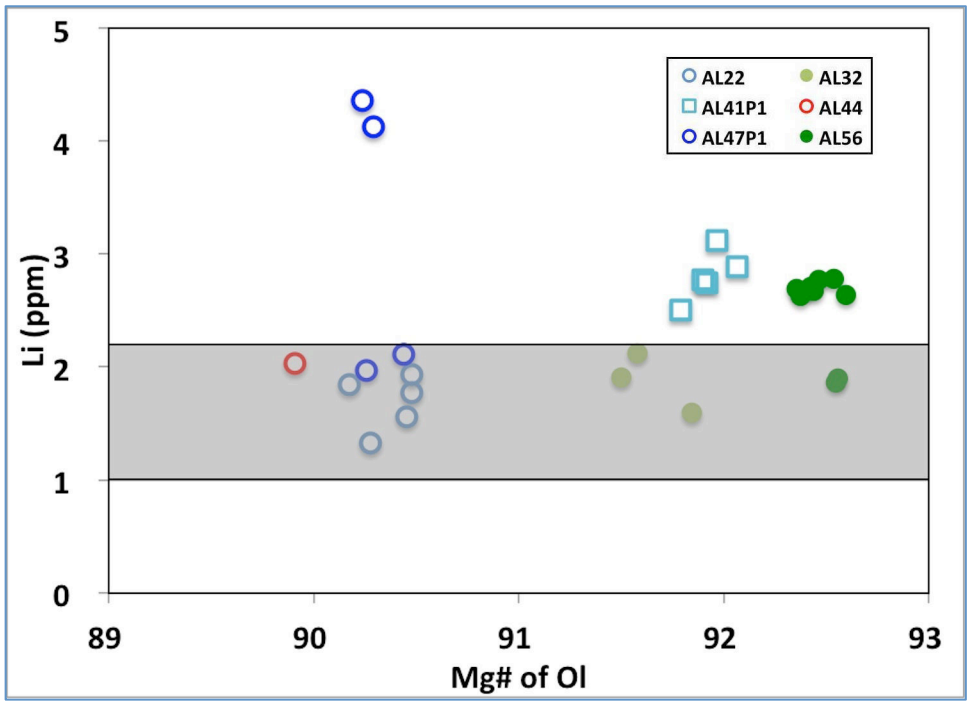

Figure 6-14: The Li concentration plotted against Mg# measured at the same position in Ol cores from Allègre samples. Grains from one single sample are represented by the same symbol. The grey field represents the estimated Li concentrations in olivine from the normal mantle.

The intra-mineral Li content variations observed in our samples are the result of a multi-stage melt exchange, including the involvement of the host magma. Due to the different diffusive rates of Li, the elemental distribution among mineral phases is no longer at equilibrium; here, the Li partition coefficient between Cpx and Ol cannot be used to identify the nature of mantle metasomatic agents.

Beside the identification of various metasomatic events, the fast diffusive rates of Li can be used to bring time constraints on the last melt-rock reaction stage (interactions between xenoliths and host magma during magma ascent and within the lava lake). To estimate the duration of the host magma-xenolith interaction, we use a one-dimensional diffusion model (equation 5) to simulate Li ingress into the marginal zones of Ol grains. Diffusion of Li to a depth of 1mm in Ol requires a few years (3 years at 1100℃; diffusion coefficients from Dohmen et al., 2010). Considering a maximum initial depth of 52km, and average ascent rates of alkali basalts to be 0.2-2m/s (O'Reilly and Griffin, 2011), the maximum duration of xenolith transport to the surface should range from 7 hours to 3 days. The intermediate interval (between 3 days and 3 years) therefore corresponds to the slow cooling of the lava lake.

6.3.1.2 Distinctive Li isotopic offsets among mineral phases induced by asynchronous metasomatic events

Given the large difference of diffusive rates between ^{6}Li and ^{7}Li, with a diffusion coefficient ratio $D_7/D_6=(m_6/m_7)^{\beta}=1.0424$ (m_6 and m_7 are the masses of ^{6}Li and ^{7}Li, respectively; exponent $\beta=0.27$ according to Richter et al., 2014), the Li isotopic composition will be altered during Li exchange by diffusion (e.g., Lundstrom et al., 2005; Wagner and Deloule, 2007). During diffusion, mantle minerals, as the receptors at the end of the diffusive sequence, first become enriched in ^{6}Li owing to its faster diffusion rate, and their isotopic compositions evolve towards negative values, forming a 'trough' in isotopic composition (Fig. 6-15). Inversely, $\delta^{7}Li$ values of the donors, which have lost Li, increase gradually. In receptor minerals, the 'trough' propagates into the interiors of grains until a new equilibrium is achieved (Fig. 6-15), or the system cools below the closure temperature, preserving the disequilibrium state.

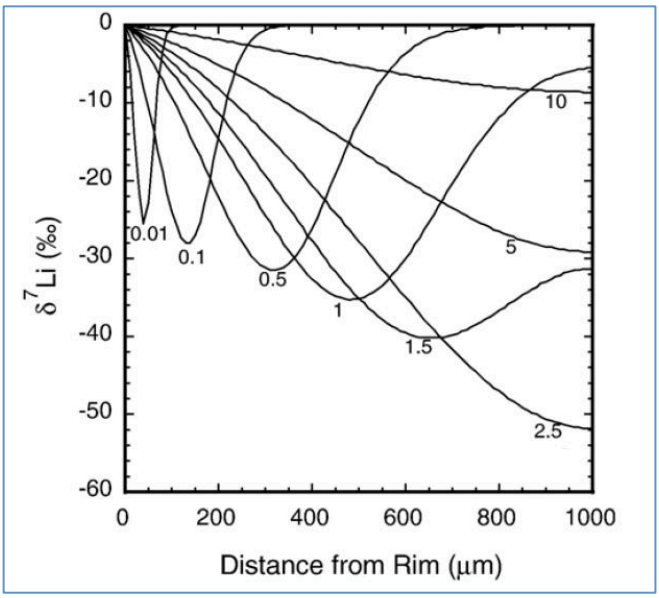

Figure 6-15: Propagation of the δ^7Li tough into a Cpx crystal using the open-system numerical model, adopted from Parkinson et al. (2007). The Li content at the crystal surface is 10 times higher than that of the crytal. δ^7Li values of the crystal surface and interior are the same at the beginning of diffusion (0‰). The numbers beside the curves are the time in years.

Since Cpx have suffered pronounced lithium addition, their isotopic compositions should have been totally or partly reset. In view of some δ^7Li values that plot in the Li isotopic composition range of the upper mantle (Fig. 6-16c), coupled with the lack of obvious Li elemental and isotopic zonation, some Cpx grains must have achieved Li isotopic equilibrium with infiltrated melts/fluids originating from the host magma of similar isotopic composition (3.2±0.6‰) to the upper mantle. Additionally, some Li isotopic imprints generated by an older (mantle) metasomatic event have not been completely erased by this Li uptake (e.g., the negative average δ^7Li values in sample AL41P1 and AL32; Table 5-4). The Li concentration prior to exchange with the host magma, as well as grain size, determines the time needed to reach equilibrium for a whole grain with interstitial melts/fluids (Aulbach and Rudnick, 2009; Gallagher and Elliot, 2009). Thus, the original Li content and δ^7Li signals of (a) potential older metasomatic event(s) prior to entrainment by the host magma have not been totally erased and cumulative effects might account for the large variation of Li content and δ^7Li values currently observed in Cpx among different xenoliths, and even among different grains in a single xenolith (Table 4-5; Fig. 6-13).

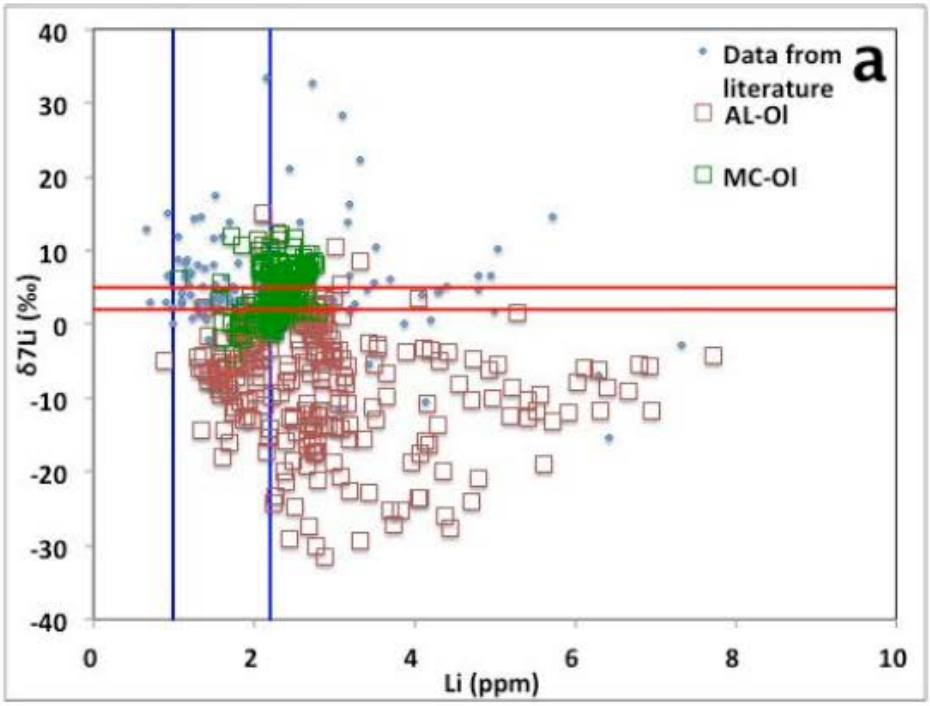
a
Data from literature
AL-Ol
MC-Ol
δ7Li (‰)
Li (ppm)
40
30
20
10
0
-10
-20
-30
-40
0
2
4
6
8
10

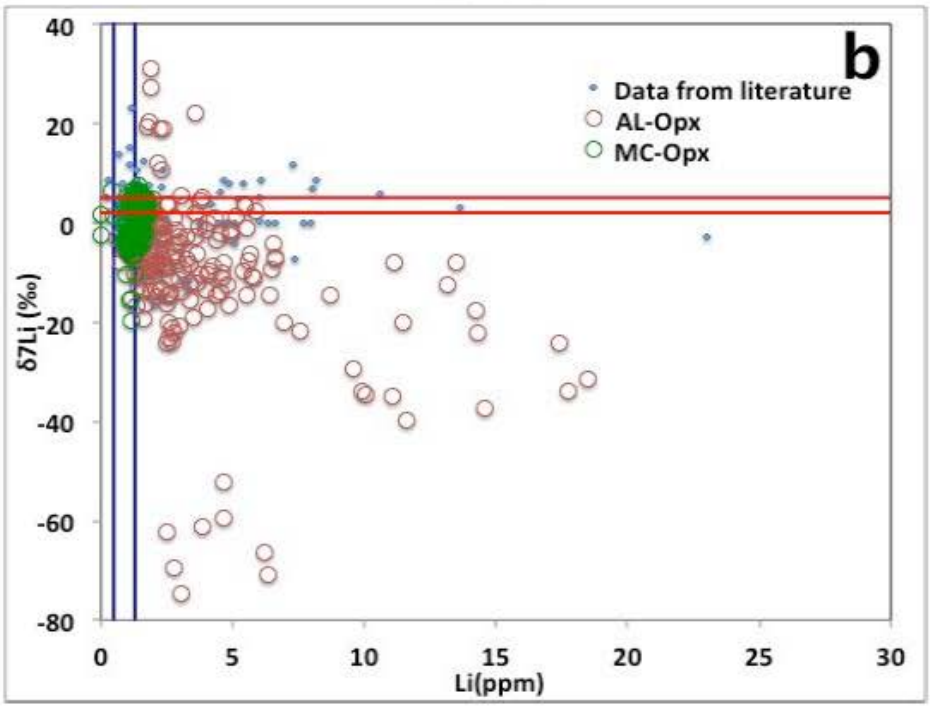
b
Data from literature
AL-Opx
MC-Opx
δ7Li (‰)
Li(ppm)
40
20
0
-20
-40
-60
-80
0
5
10
15
20
25
30

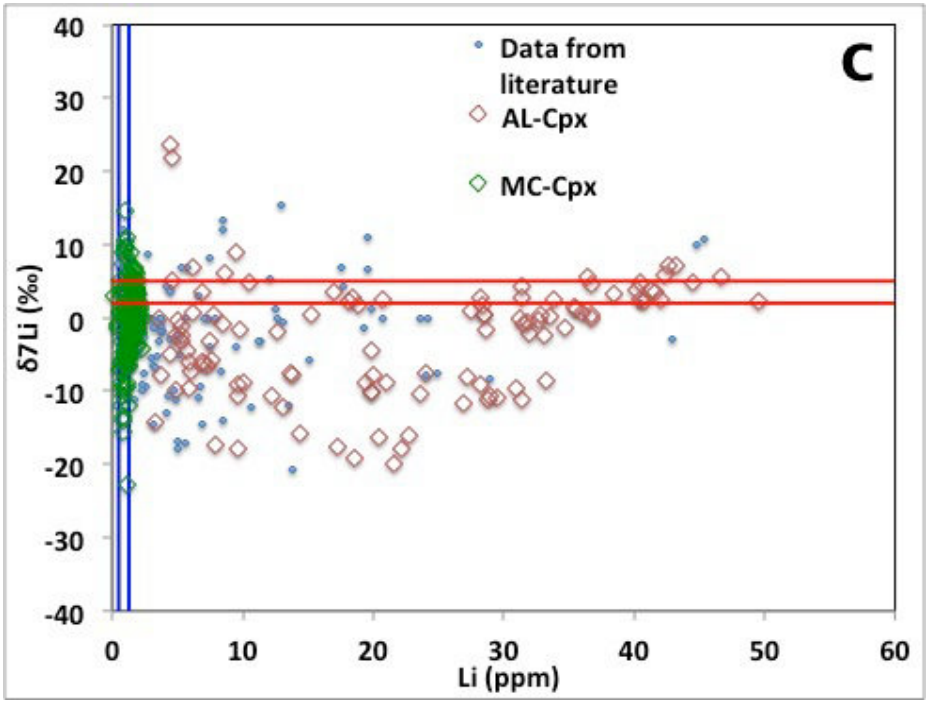

Figure 6-16: Variation of δ^7Li versus Li concentration in Cpx (a), Ol (b) and Opx (c) from Allègre and Mont Coupet samples compared with literature data. In each plot, the values concerning the present study include the whole data set of Ol, Opx and Cpx. The Li concentrations and isotopic compositions of the upper mantle are delineated by red and blue lines, respectively. Small blue filled diamonds represent literature data (Seitz et al., 2004; Rudnick and Ionov, 2007; Wagner and Deloule, 2007; Tang et al., 2007, 2011, 2012; Aulbach et al., 2008; Ionov and Seitz, 2008; Magna et al., 2008; Aulbach and Rudnick, 2009; Kil, 2010; Zhang et al., 2010; Gao et al., 2011; Su et al., 2014).

In Ol grains, enriched rims display lower δ^7Li values than the cores, correlating with increased Li content. However, the cores also display negative δ^7Li values, even when their Li content displays plateaus, which should have preserved the original Li isotopic composition (Fig. 6-13, Fig. 6-17 and Table 4-5). The majority of Ol Li isotopic compositions in Allègre peridotite xenoliths, regardless of the analyzed positions in grains, are therefore lower than the literature data (Fig. 6-16a), with averaged values ranging from -15.9 to -4.6‰ (Table 4-5).

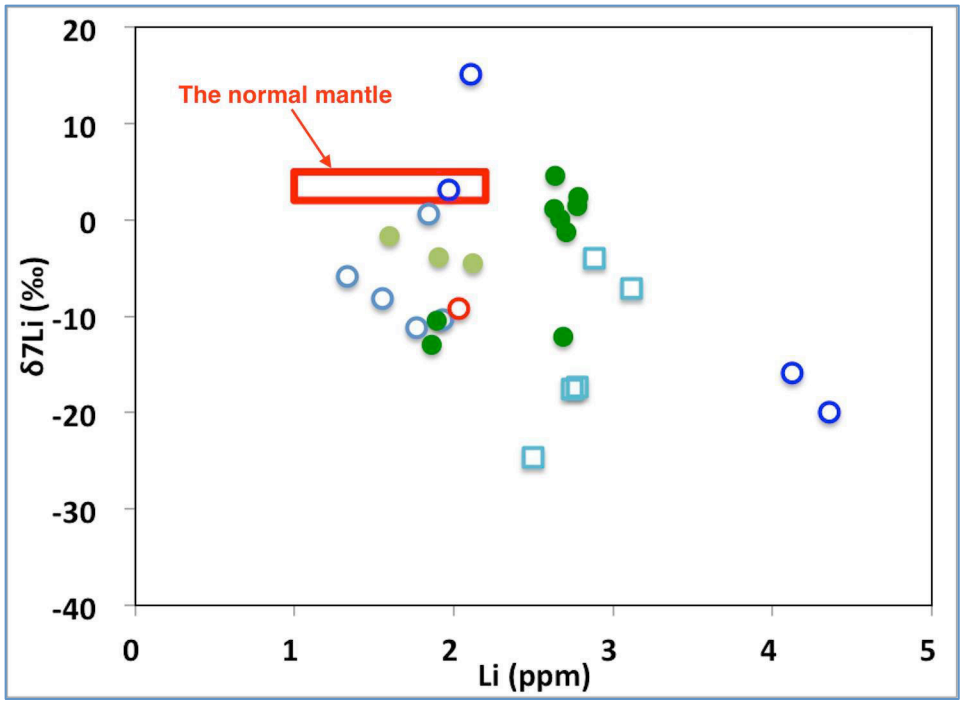

Figure 6-17: δ^7Li against Li concentrations in Ol grain cores of Allègre samples (symbols as in Fig. 6-14).

Note that the δ^7Li profiles presented in this study cannot be totally ascribed to geometric effects (maybe partially) when slicing the thin sections (Parkinson et al., 2007). The freshness of samples, no abnormity in major element compositions and, especially, few peaks corresponding to altered products in the Ol infrared spectra, argues against the view that the low-temperature alteration at the surface may have changed the Li isotopic compositions in cores of Ol grains. Furthermore, in case of Allègre peridotite xenoliths, the negative isotopic compositions in Ol cores cannot result from the kinetic effect of Li diffusive uptake before achieving equilibrium, as it has been invoked for low δ^7Li values observed in Cpx from worldwide peridotites (e.g., Rudnick and Ionov, 2007; Wagner and Deloule, 2007; Xiao et al., 2015). Indeed, in this case, the negative δ^7Li values should be accompanied by increased and inhomogeneous Li concentrations. Even if as shown in diffusion simulation, the slight Li diffusive ingress from a source with δ^7Li of the normal mantle can also induce a deep isotopic trough at the beginning of a diffusive process (Parkinson et al., 2007; Gallagher and Elliot, 2009), it is impossible for the δ^7Li trough to occupy the whole grain given the Li compositional homogenization. In addition, as magma degassing could also provoke pronounced Li isotopic fractionation (as low as -20‰, Vlastélic et al. (2011)), the devolatilization process with decreasing pressures should be

considered to explain the negative δ^7Li values in cores of Ol from currently studied xenoliths hosted in the lava lake. But the problem is that, in this case, the extremely light Li isotopic compositions are indispensably concomitant with a large Li loss (Li content of 0.99 ppm in the devolatilized trachytic pumice studied by Vlastélic et al. (2011)). For Allègre samples, all the cores of Ol grains incorporate similar or higher amount of Li compared with the normal mantle. In conjunction with the high Li concentrations of co-existing Cpx and the Li elemental zonation patterns in Ol, this explanation could also be dismissed.

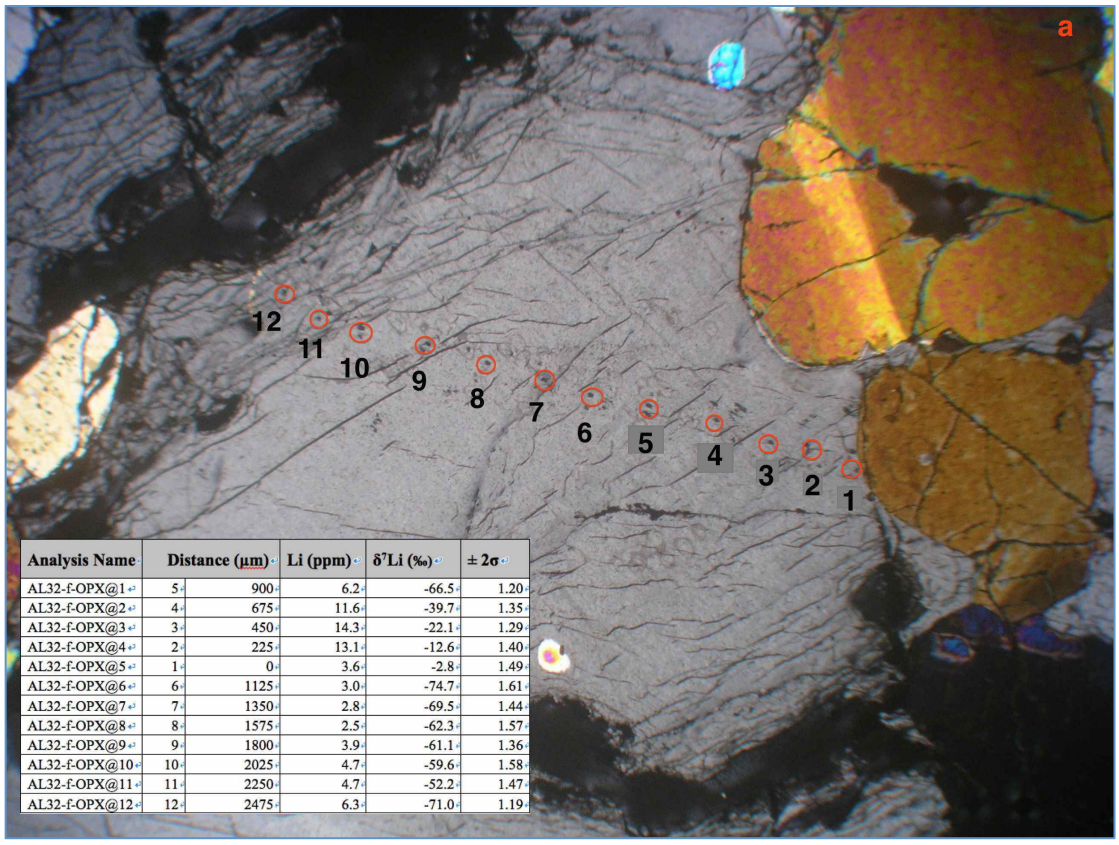

Analysis Name	Distance (μm)		Li (ppm)	δ^7Li (‰)	± 2σ
AL32-f-OPX@1	5	900	6.2	-66.5	1.20
AL32-f-OPX@2	4	675	11.6	-39.7	1.35
AL32-f-OPX@3	3	450	14.3	-22.1	1.29
AL32-f-OPX@4	2	225	13.1	-12.6	1.40
AL32-f-OPX@5	1	0	3.6	-2.8	1.49
AL32-f-OPX@6	6	1125	3.0	-74.7	1.61
AL32-f-OPX@7	7	1350	2.8	-69.5	1.44
AL32-f-OPX@8	8	1575	2.5	-62.3	1.57
AL32-f-OPX@9	9	1800	3.9	-61.1	1.36
AL32-f-OPX@10	10	2025	4.7	-59.6	1.58
AL32-f-OPX@11	11	2250	4.7	-52.2	1.47
AL32-f-OPX@12	12	2475	6.3	-71.0	1.19

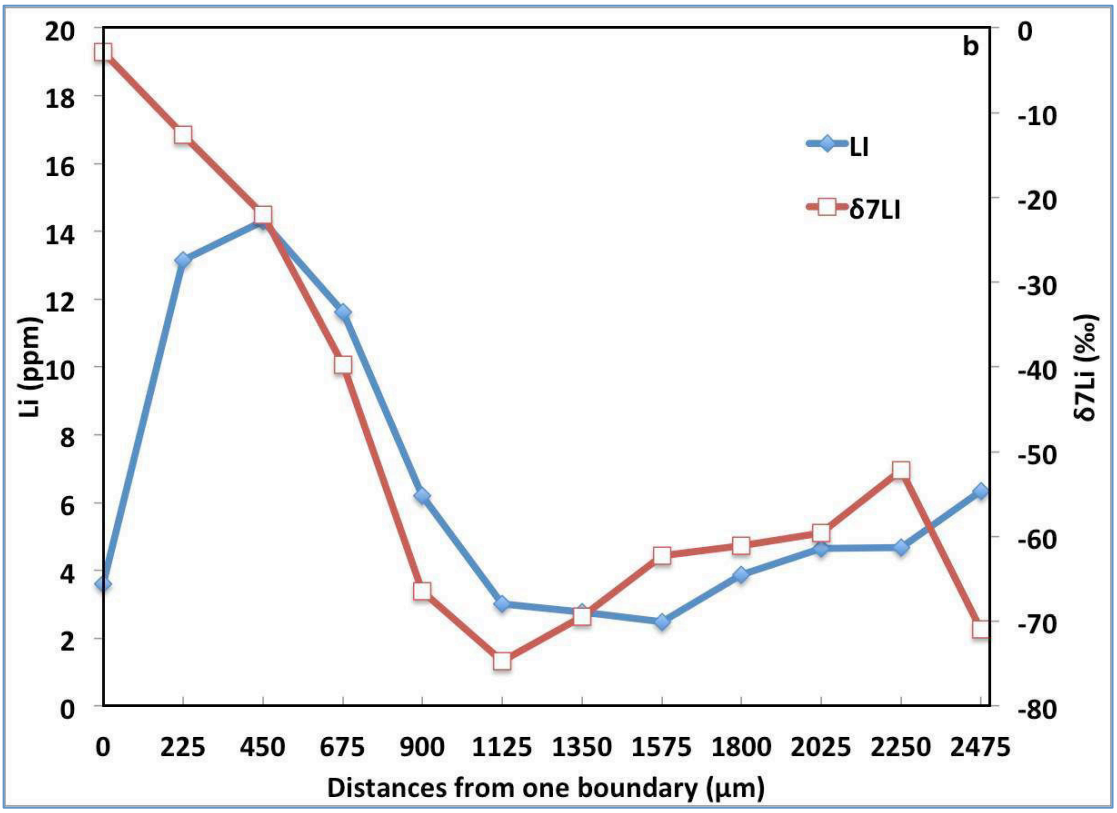

Figure 6-18: A profile measured on one Opx grain in sample AL32 (AL32-f-Opx). (a) The positions of analyzed points in the grain. The result is also shown in the table. (b) A graph showing core-rim variations of Li concentrations and δ^7Li values.

For Opx, the intra-mineral Li isotopic composition variations are much more complicate, but parallel to the characteristics observed in olivine, δ^7Li values of Opx measured points falls in lower part of the graph including the data from worldwide localities (Fig. 6-16b), even though some of these points are situated in the grain cores and have Li concentrations similar to the normal mantle (Fig. 6-13). Especially, a large Opx grain (~3 mm in diameter; Fig. 6-18) has a δ^7Li value as low as -75‰ in the core, with Li concentration of 3 ppm. Towards the rims, Li concentrations increase due to Li diffusive ingress and δ^7Li values also rise to pursue equilibrium with the external percolating melt of heavier Li isotopic compositions. Nevertheless, diffusion ceased before the equilibrium was achieved likely due to the system cooling below the closure temperature for Li diffusion. We consider that it could also be regarded as an evidence for the existence of a low δ^7Li component at depth.

Accordingly, it is likely that the light lithium isotopic compositions at Ol and Opx cores, as well as surviving in some Cpx grains, are the consequence of mantle metasomatism by melts/fluids depleted in ^{7}Li (Fig. 6-17) prior to host magma

entrainment. This process homogenized the lithium concentration and isotopic compositions of the peridotites at the mineral scale prior to entrainment by the host magma.

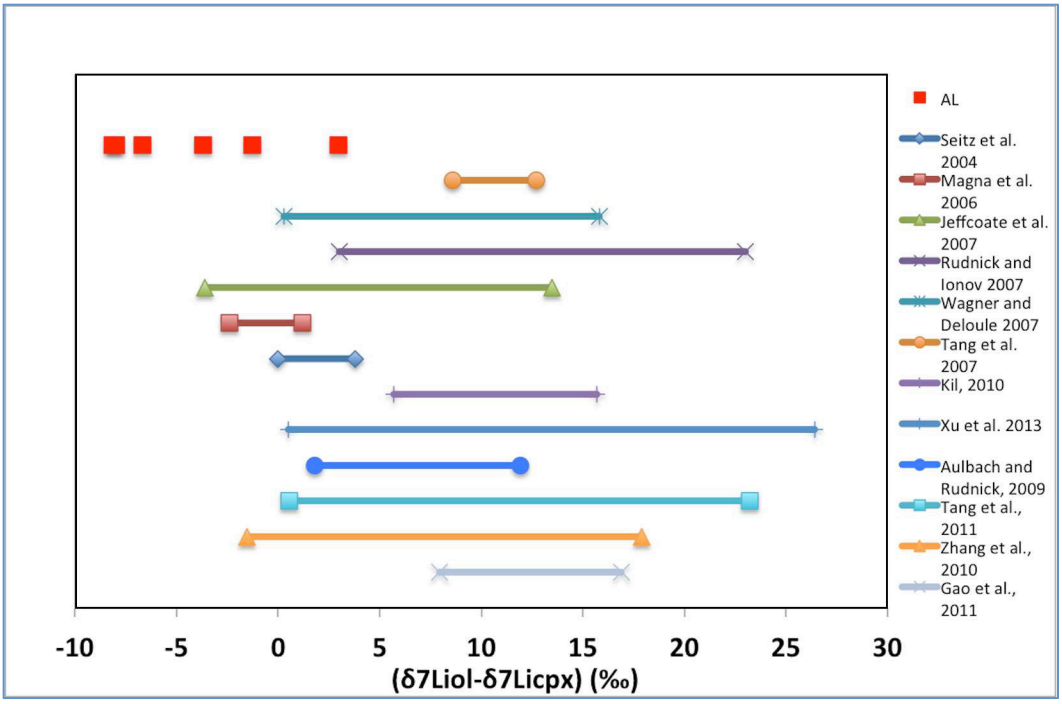

Figure 6-19: Li isotopic discrepancy between Ol and Cpx in samples from Allègre (represented by 'AL') compared with literature data.

As a result, the Li isotopic differences between Ol and Cpx ($\delta^7Li_{Ol}-\delta^7Li_{Cpx}$), are mostly negative in the Allègre xenoliths (Table 6-2)，ranging from -8.8‰ to 0‰, distinct from results of previous studies (Fig. 6-19). An exception is the sample AL32 (2.5‰) due to lower δ^7Li values of its Cpx grains. This clearly indicates that Cpx and Ol have not achieved the Li isotopic equilibrium.

6.3.2 No obvious Li addition but large inter-sample Li isotopic variations in peridotite xenoliths from Mont Coupet

The Li concentration ratios and Li isotopic differences among individual minerals in each sample from Mont Coupet are reported in Table 6-3. The average Li concentrations and isotopic compositions at cores and rims of all the grains for each phase in a single sample are also shown. The measured Li concentrations and isotopic compositions in minerals from Mont Coupet samples are totally different from those measured in minerals from Allègre samples (Fig. 6-16).

Sample	Mineral	Li					δ^7Li (‰)				
		Core (ppm)	Rim (ppm)	$D_{Ol/Cpx}$	$D_{Opx/Cpx}$	$D_{Amp/Cpx}$	Core	Rim	Δ^7Li_{Ol-Cpx}	$\Delta^7Li_{Opx-Cpx}$	$\Delta^7Li_{Amp-Cpx}$
MC34	Ol	2.4	2.2	2	1.1		4.1	2.7	2	-0.6	
	Opx	1.1	1.1				2.4	-1.9			
	Cpx	1.1	1				0.9	-2.7			
MC36	Ol	2.3	2.1	1.4	0.9	0.6	7.9	8.6	5.4	1.1	6.1
	Opx	1.8	1.2				1.5	4.5			
	Cpx	1.9	1.1				2.9	2.4			
	Amp	1	1.1				-3.4	-4.6			
MC38	Ol	2	2	2.6	1.4		-0.3	0.6	9.3	3.7	
	Opx	1.2	1.2				-4.4	-11.7			
	Cpx	0.8	0.9				-9.6	-13.5			
MC43	Ol	2	2.2	1.7	1.1		7.2	5.1	9.7	1.3	
	Opx	1.2	1.2				-3.2	-0.8			
	Cpx	0.8	0.9				-3.2	-4.5			
MC49	Ol	2.5	2.4	1.5	1		7.4	7.2	5.4	2.4	
	Opx	1.7	1.4				3.2	3.3			
	Cpx	1.8	1.4				1.5	0.8			
MC53	Ol	2.2	2.4	2.7	1.3	1.1	4.3	2.5	-0.9	-4.4	11.4
	Opx	1.5	1.2				0.8	-0.9			
	Cpx	0.9	0.9				9.8	-0.7			
	Amp	1	1.1				-6.6	-7.6			

Table 6-3: The average Li concentrations and isotopic compositions at cores and rims, Li concentration ratios and Li isotopic differences (e.g., $\Delta^7Li_{Ol-Cpx}=\delta^7Li_{Ol}-\delta^7Li_{Cpx}$) among individual phases in samples from Mont Coupet.

6.3.2.1 Nearly equilibrated Li partitioning among mineral phases and no concentration zoning in grains

Minerals in peridotite xenoliths from Mont Coupet have Li concentrations ranging between 0.4 to 2.8 ppm, similar to the normal mantle (Fig. 6-20). Meanwhile, Li partitioning among mineral phases is very close to equilibrium (Fig. 6-21; Table 6-3). The averaged Li concentrations of one mineral phase vary a little among individual samples (Table 6-3).

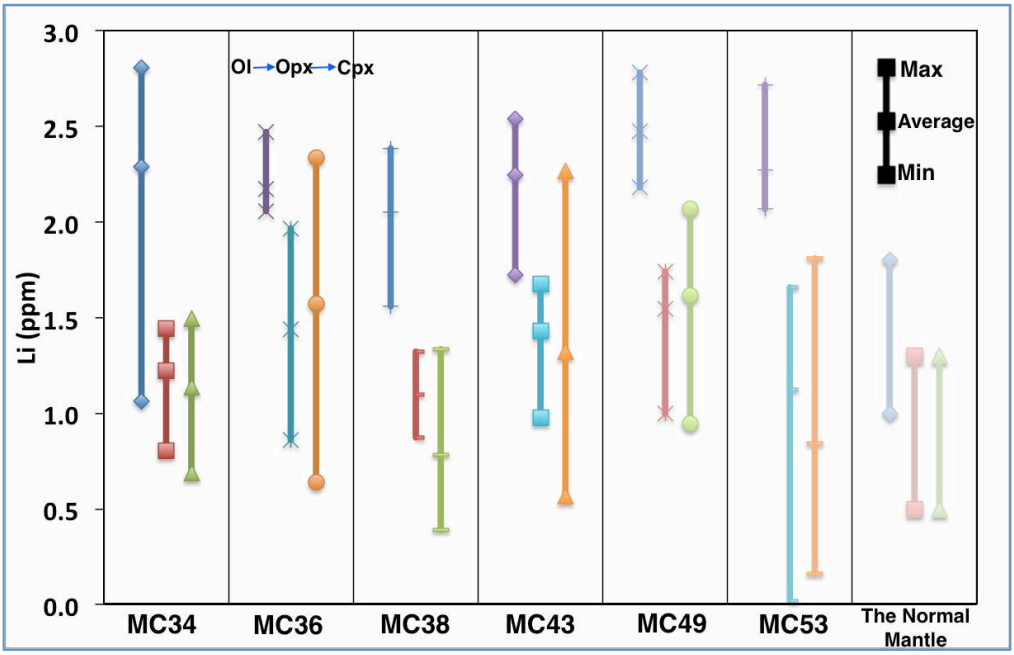

Figure 6-20: Li concentrations in samples from Mont Coupet including the minimum and maximum values compared with the Li concentration ranges estimated for the normal mantle (Seitz and Woodland, 2000; Ottolini et al., 2004).

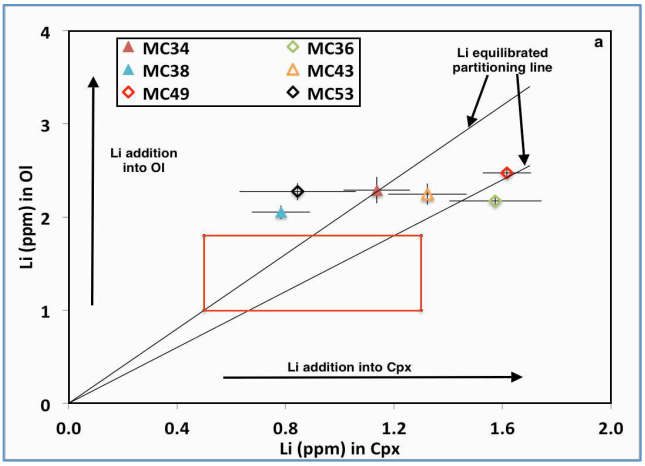

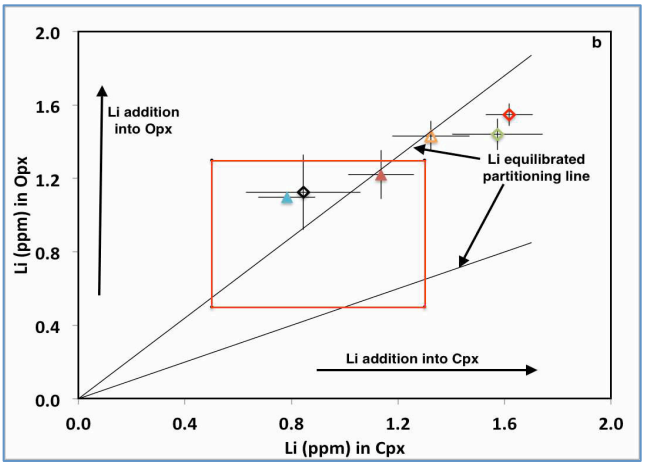

Figure 6-21: Li partitioning between Ol and Cpx (a), between Opx and Cpx (b) in samples from Mont Coupet. The equilibrated lines are plotted according to the equilibrated partition coefficients from Seitz and Woodland (2000), $D_{Ol/Cpx}$=1.5-2.0 and $D_{Opx/Cpx}$=0.5-1.1. The Li content of individual mineral phases in the normal upper mantle is delimitated by a small red square. The metasomatic tendency is according to Seitz and Woodland (2000) and Su et al. (2014).

In the measured profiles, Li concentrations display almost no variations across most of analyzed grains of Ol, Opx, Cpx and Amp (Fig. 6-22). In some grains (mainly Cpx), small decreases towards rims (<1 ppm) are limited within narrow zones close to grain rims; in fact, they are just a little larger than analytical errors.

Since the volcano belongs to the strombolian type, the host magmas of peridotite xenoliths from Mont Coupet should uprise to the earth surface very fast and cool to the ambient temperatures in a very short period. Thus, Li intragranular homogeneous distribution and inter-mineral equilibrated partitioning have not been broken by the host magmas, and the information of Li isotopic systems at mantle depths should be preserved in xenoliths from Mont Coupet.

6.3.2.2 Large isotopic composition variations caused by a recent metasomatism

Relative to almost homogeneous Li distribution from grain cores to rims, the variations of Li isotopic compositions seem much larger across grains of every phase in all the samples. But no regular patterns can be summarized for all the mineral phases (Fig. 6-22) and given the analytical error (±2‰), isotopic variations from grain cores and rims are nearly inexistent. I thus consider that using the δ^7Li value averaged from the results of all the analytical points on one mineral phase to represent the Li isotopic composition of that phase in a sample is acceptable.

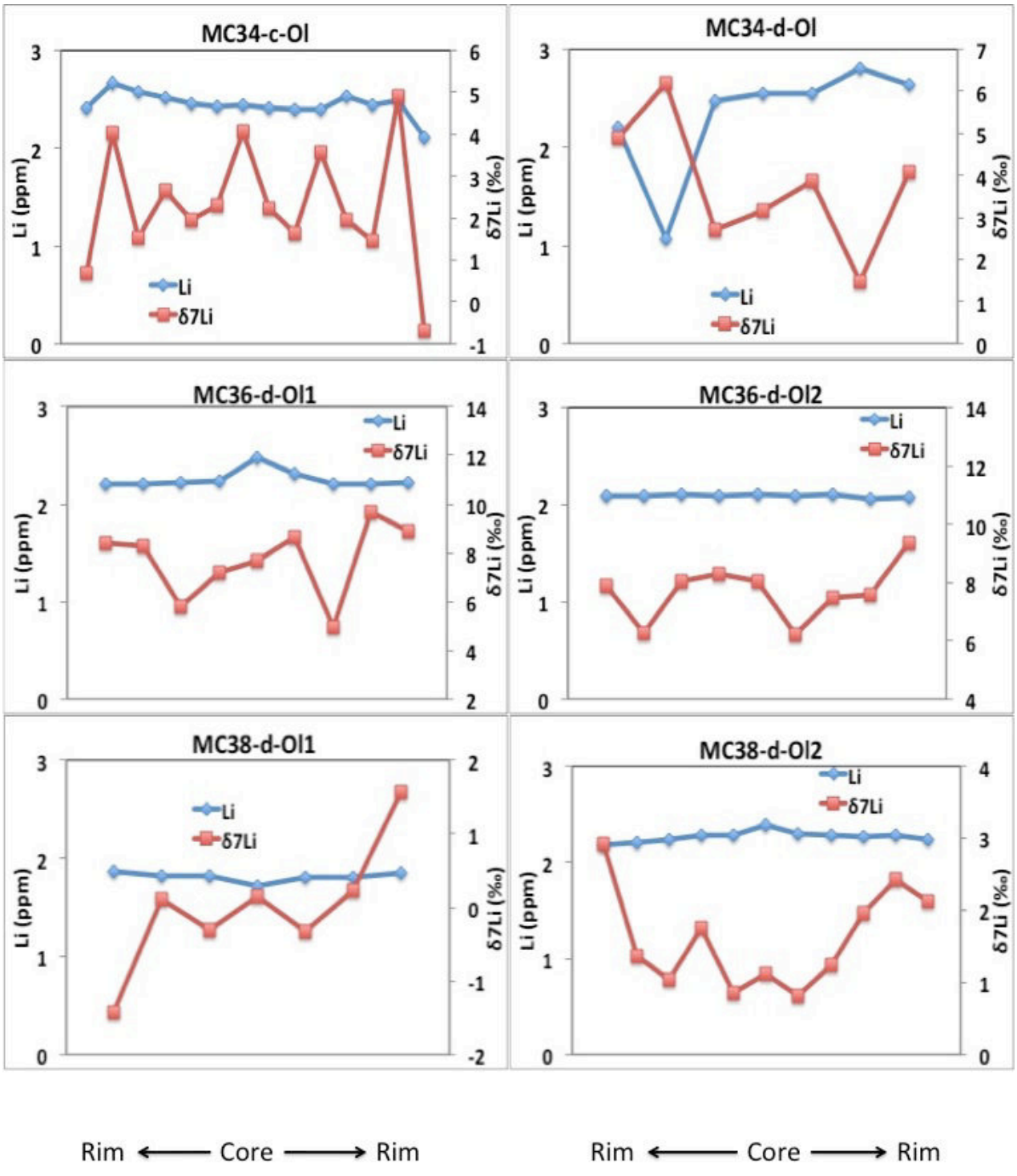

Figure 6-22: Representative Li concentration and δ^7Li profiles of core-rim variations in Ol, Opx, Cpx and Amp grains from Mont Coupet samples.

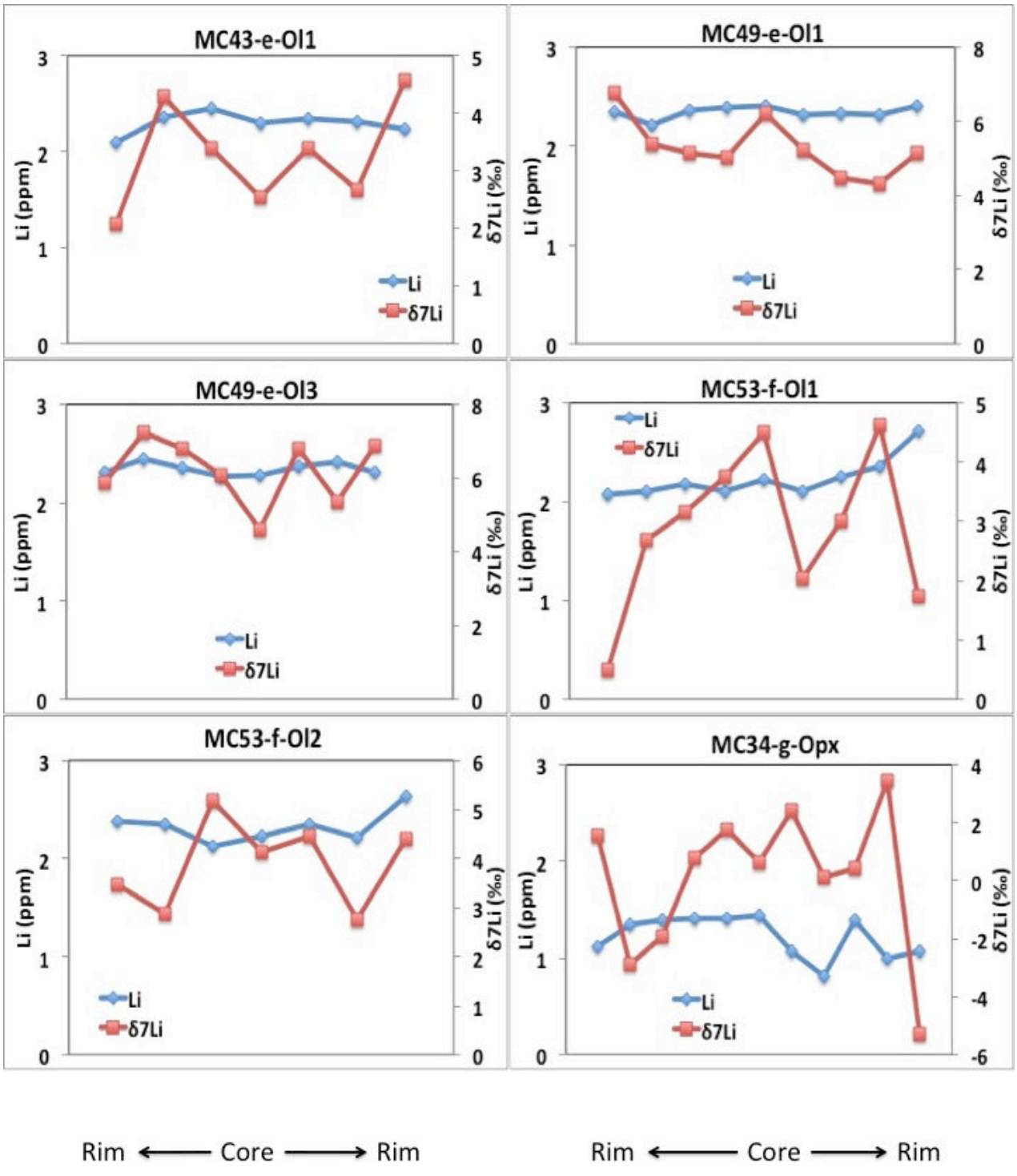

Figure 6-22 (continued)

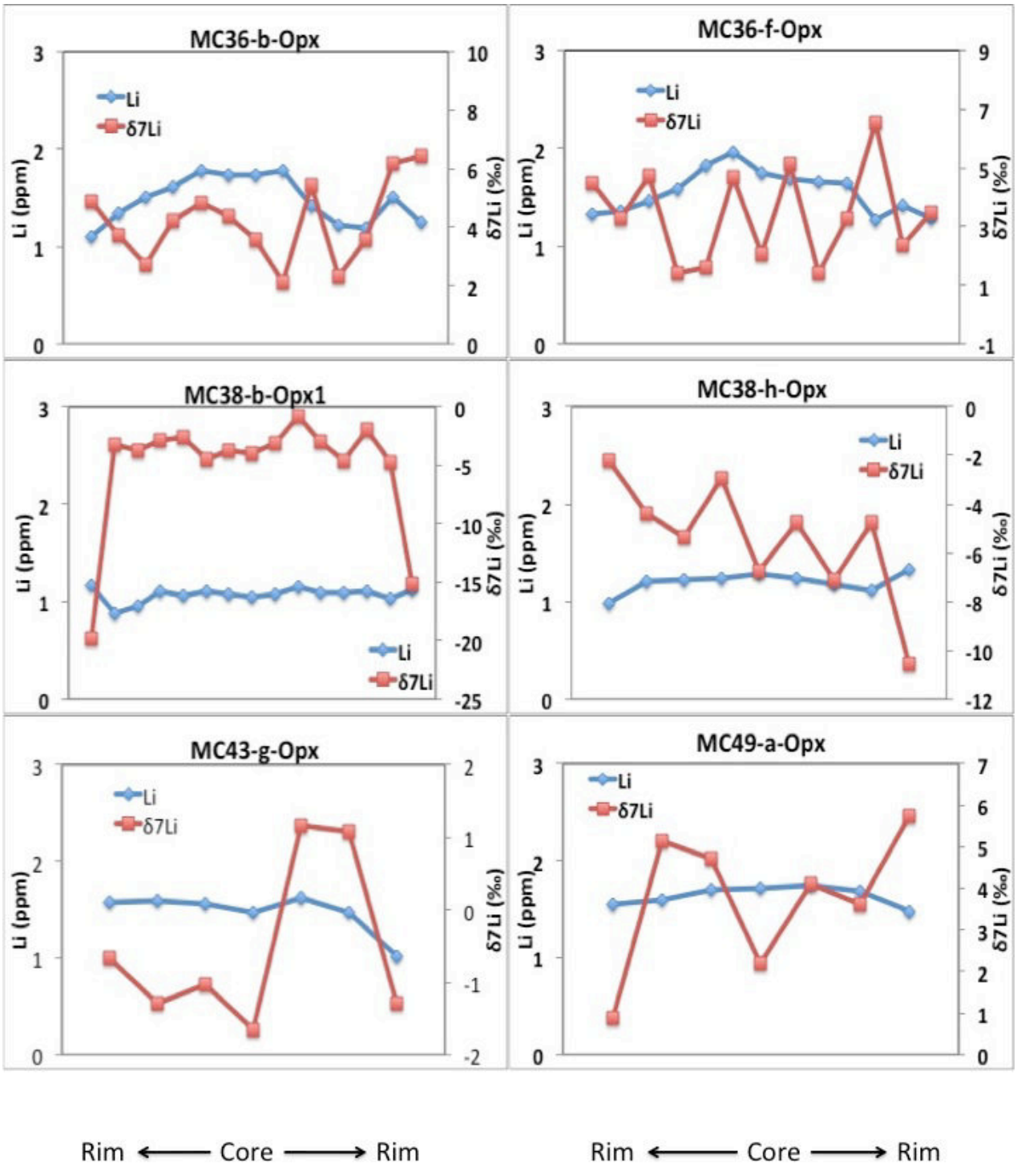

Figure 6-22 (continued)

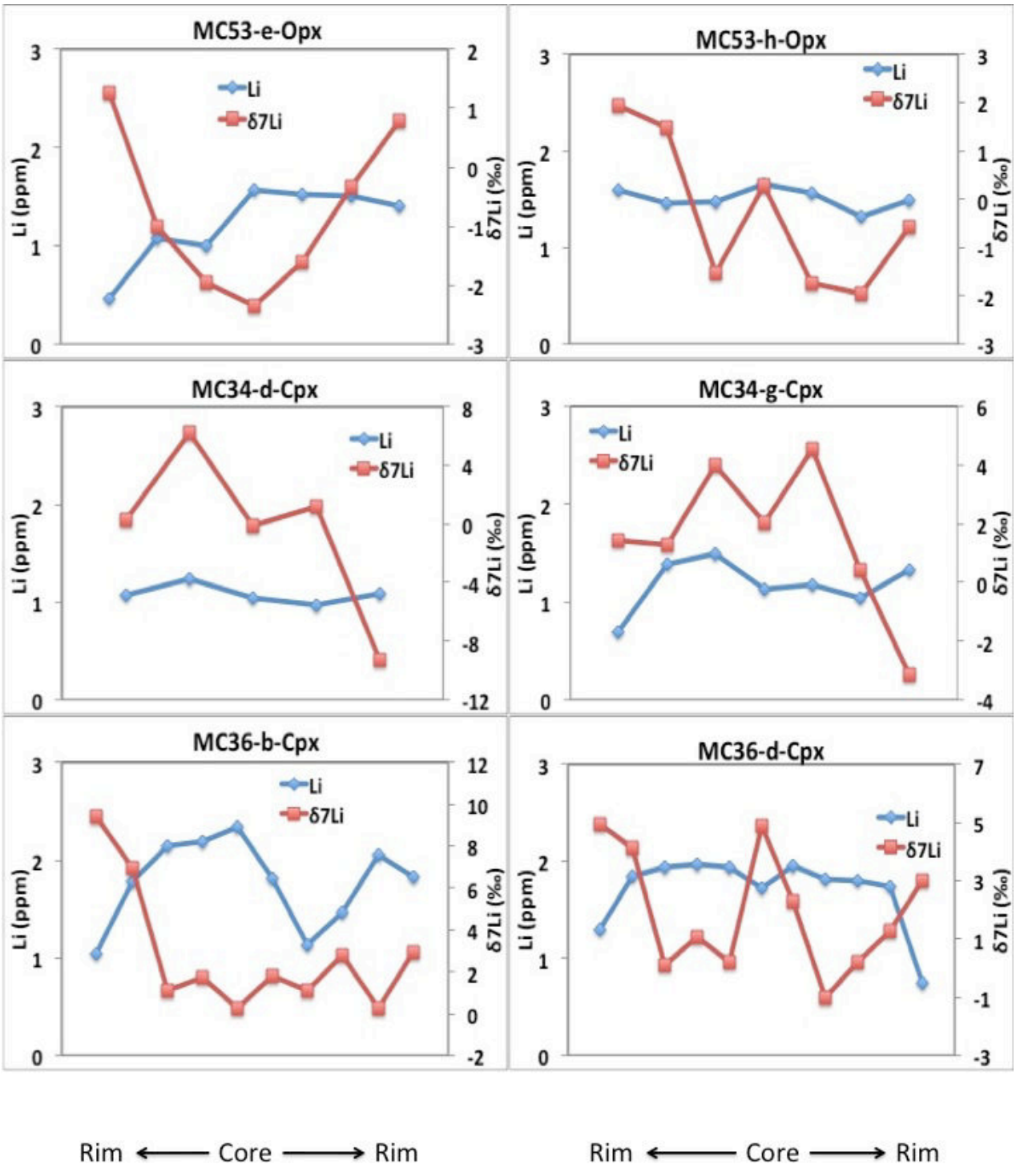

Figure 6-22 (continued)

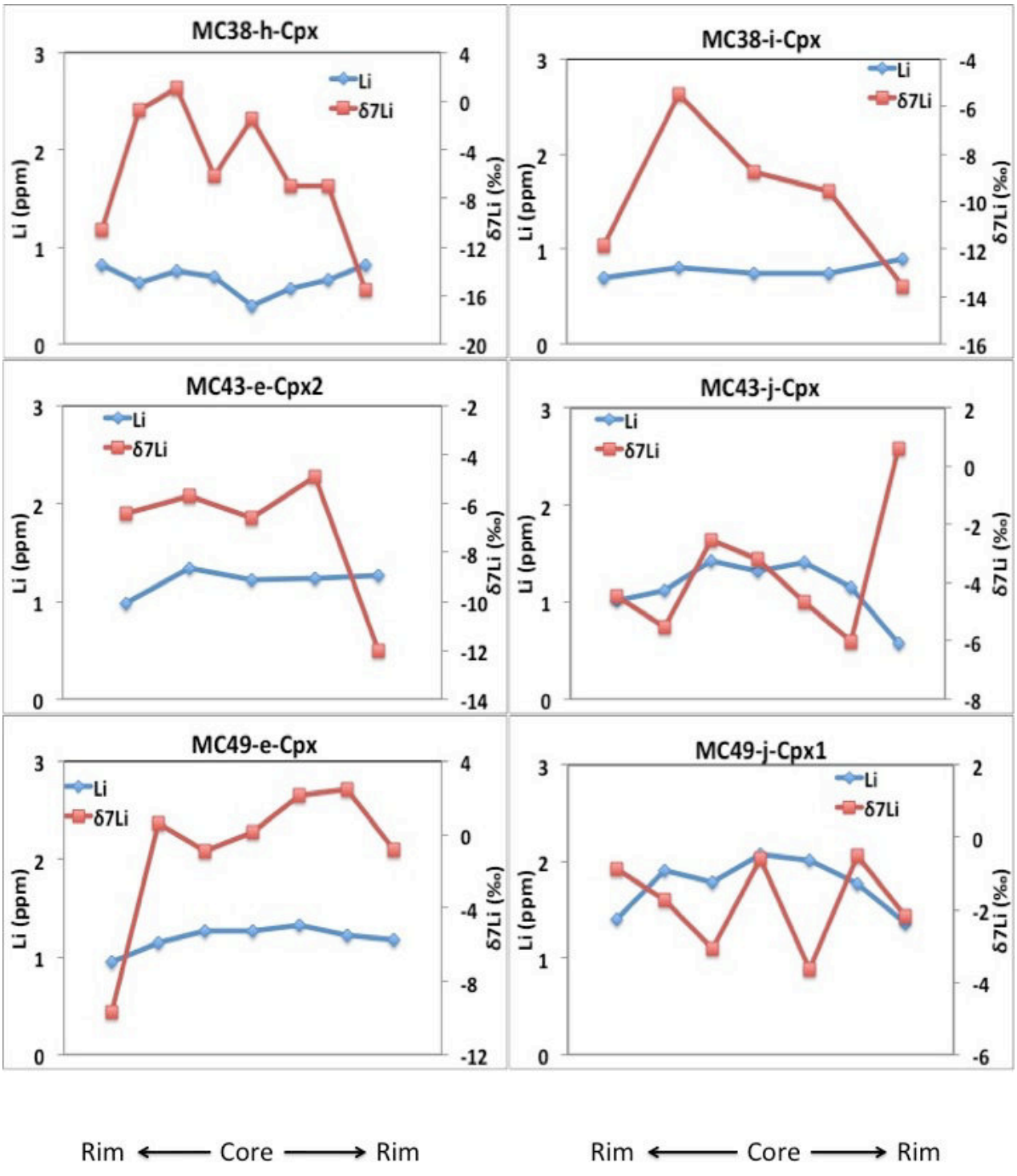

Figure 6-22 (continued)

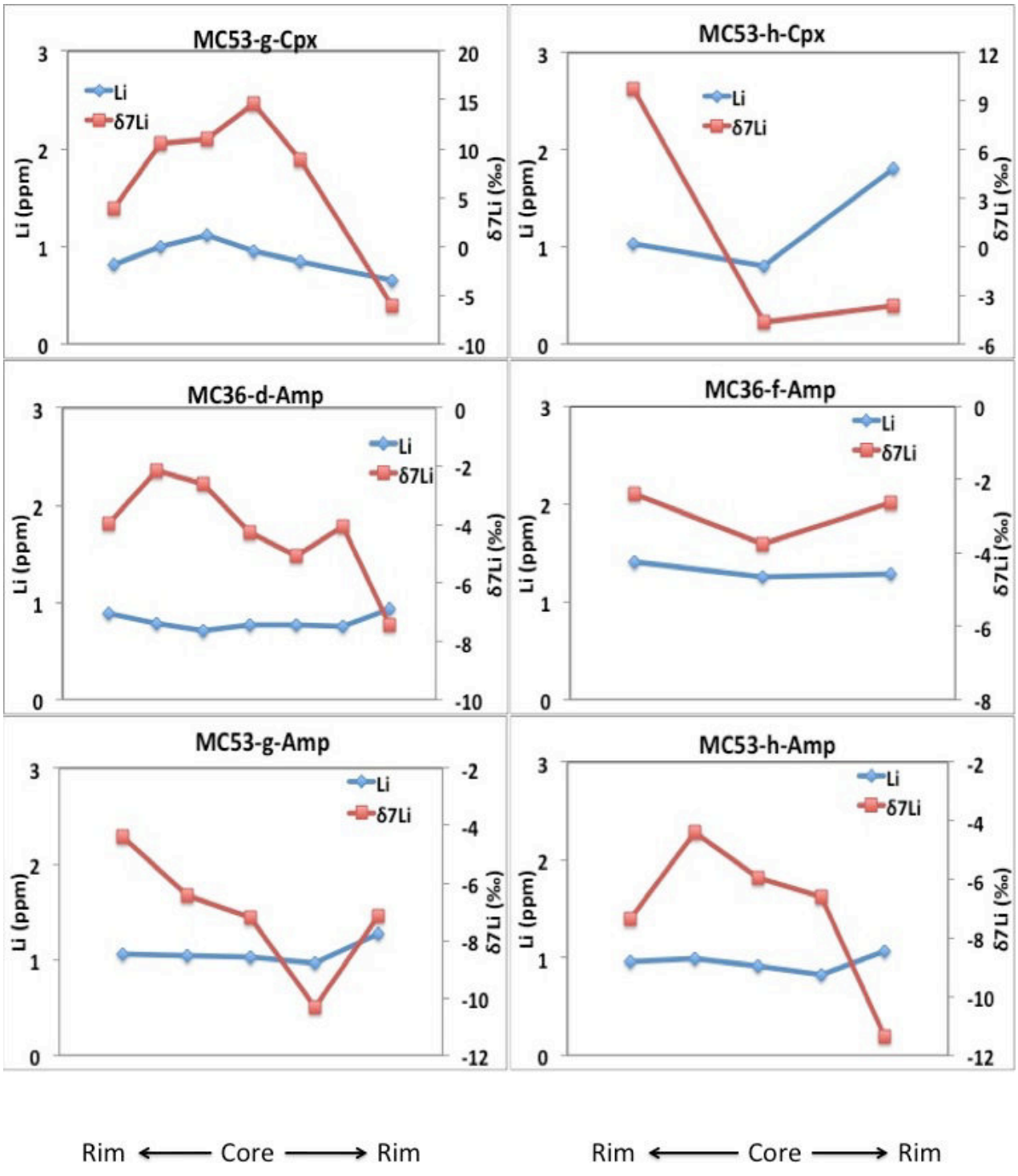

Figure 6-22 (continued)

The Li isotopic compositions of minerals in most of Mont Coupet samples follow the common sequence: Ol>Opx>Cpx, with the exception of hydrous sample MC53, where Li isotopic composition of Cpx is higher than those of coexisting Ol and Opx (Table 6-3). The averaged δ^7Li values of Ol range from +0.5 to +7.7‰, close to the

estimated isotopic compositions of the upper mantle (+2 to +5‰). But the averaged δ^7Li values of Opx and Cpx in some samples are negative. The isotopic differences between Ol and Cpx ($\delta^7Li_{Ol}-\delta^7Li_{Cpx}$) vary from -1.0‰ in Amp-bearing sample MC53 to +9.7‰ in sample MC43. Taking Li equilibrated partitioning among minerals and no signatures of Li diffusive addition into minerals into consideration (Fig. 6-21 and 6-22), these results imply that the isotopic compositions of Cpx in some samples have been affected by an exotic melt with a light isotopic composition, and low or moderate Li content. In light of small or no concentration core-rim variations, Cpx grains in Mont Coupet samples may have achieved Li isotopic equilibrium with the percolating melt in a short time. At the same time, due to the lower diffusive rate of Li in Ol than Cpx, and higher Li content of Ol, the Li isotopic compositions of Ol have not been so largely affected. Since Opx have similar internal crystalline structure to Cpx, it can be supposed that Li has a similar, but lower (given the more common diffusion-induced negative δ^7Li values in Cpx from worldwide mantle xenoliths), diffusive rate in Opx than Cpx, even if up to now there is no experimental determination of Li diffusivity in Opx. However, in some Mont Coupet samples, when the Cpx Li isotopic composition has been modified, the Opx Li isotopic compositions has also been modified by the percolating melt (Table 6-5).

As discussed in the section 6.3.1.2, the disequilibrated Li diffusive uptake can decrease the Li isotopic compositions of host minerals in certain degrees. In xenoliths from Mont Coupet, the lowest Cpx δ^7Li value was measured in sample MC38, which means that Cpx in this sample should contain much more Li than other samples if the light Li isotopic composition is interpreted as the result of nonequilibrium kinetic diffusion. However, in contrary to this assertion, Li concentration of Cpx in sample MC38 is lowest among those of Cpx in all the Mont Coupet samples (Table 4-5; Fig. 6-23a). And, there are no negative co-variations between Cpx δ^7Li values and their Li concentrations when taking all the Mont Coupet samples into consideration (Fig. 6-23a).

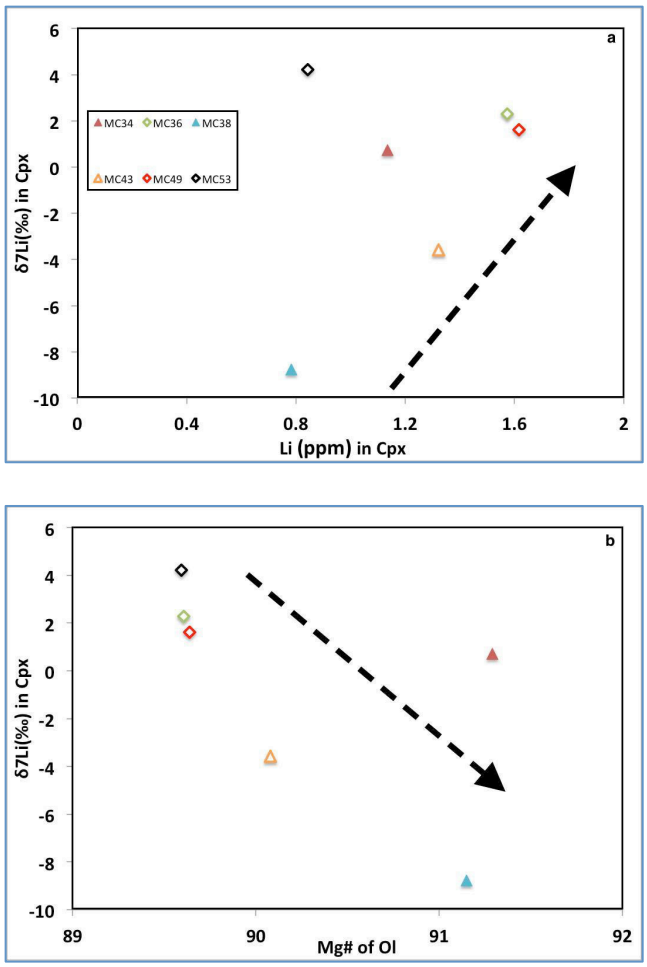

Figure 6-23: Averaged δ^7Li of Cpx versus Li concentrations in Cpx (a) and Mg# of coexisting Ol (b) in samples from Mont Coupet. In graph (a), along the direction of the dashed line, δ^7Li of Cpx increase with increasing Li concentrations, arguing against the view that Li diffusive uptake induces the light Li isotopic compositions. The negative co-relationship between δ^7Li of Cpx and Mg# of Ol (b) is consistent with the phenomenon that harzburgite is susceptible to the melt percolation.

However, Li isotopic compositions in Cpx from Mont Coupet xenoliths indeed display a gradual increase from sample MC38 to MC53 (Fig. 6-23b), with sample MC34 falling out of the intendancy. Here, an interpretation similar to the chromatographic effect described for REE distribution could be invoked to explain the Cpx Li isotopic composition variations among different samples. A small-volume melt with Li concentration similar to the normal mantle and negative δ^7Li value percolated into the lithospheric mantle beneath Mont Coupet. Among the studied xenoliths, the harzburgite MC38 was first passed through and the Li isotopic compositions in its Cpx (also Opx) grains were assimilated in a short time whereas the Ol Li isotopic compositions were influenced in a smaller degree. As the melt left sample MC38 and continued advancing towards other ambient samples, δ^7Li values of Cpx in sample MC38 was no longer changed by the percolating melt. With the melt moving among different parts of the mantle, its light Li isotopic composition was gradually diluted and was eventually turned to show positive δ^7Li values. Thus, the

samples far from the melt channels don't have negative δ^7Li signatures. Considering the high diffusive rate of Li at high temperatures, in a single sample the inter-mineral Li isotopic disequilibrium is a transient state. The preservation of inter-mineral large Li isotopic fractionation currently observed in some samples indicates that the percolation of the melt should occur shortly prior to the entrainment of Mont Coupet peridotite xenoliths by the host magmas.

The δ^7Li values of Amp in samples MC36 and MC53 are both negative and lower than those of coexisting Cpx (Table 4-6; Fig. 6-22). Kinetic disequilibrium induced by Li diffusion from the percolating melt may be responsible for this case. Amp have small grain sizes and low Li concentrations (1 ppm). When Li diffuses from grain boundaries to grain interior, ^{6}Li has higher diffusivity than ^{7}Li and enters the grains faster. A front depleted in ^{7}Li therefore comes into being. If Li diffuses slowly in Amp and the percolating melt leaves the host sample before a diffusive equilibrium achieves between Amp and the melt, the light Li isotopic composition remains in Amp. Nevertheless, no experiment has been performed to estimate the Li diffusivity in Amp. Furthermore, the time needed for Li diffusion to achieve equilibrium between minerals and melts also partly depends on the grain sizes, and the original Li concentrations in minerals, and the natures of melts. The interpretation on Amp negative δ^7Li values in samples MC36 and MC53 therefore needs more experimental data to establish the diffusion model.

6.3.3 Origin of melts with exceptionally light Li isotopic compositions

Considering that only low temperature processes can fractionate Li isotopes to a sufficient degree to generate materials with negative δ^7Li values (e.g., Chan et al., 1992, 2006; Decitre et al., 2002; Liu et al., 2013; Rudnick et al., 2004; Teng et al., 2004; Tomascak et al., 1999, 2004), it is expected that the low δ^7Li component in the mantle derives from a recycled component. Zack et al. (2003) showed that the δ^7Li values of eclogites could be as low as -11‰, quite different from fresh (3.4±1.4‰) or altered (-2‰ to 14‰) MORB. They interpreted these values as a result of isotopic fractionation through Rayleigh distillation during subduction and metamorphic

dehydration of the slab; their interpretation was later supported by experimental observations (Wunder et al., 2006, 2007). After a more comprehensive investigation of Li systematic in orogenic eclogites, Marschall et al. (2007) asserted that devolatilization during subduction would not largely fractionate the Li isotopic compositions between the residual metamorphites and the freed fluids, casting doubt on the role of subducted materials in the delivery of negative δ^7Li components into the deep mantle. Although the study of Agostini et al. (2008) agreed with the contentions of Marschall et al. (2007), they noted that the extensive diffusion-induced fractionation during slab-derived fluids traversing the mantle could also generate large-scale regions of low-δ^7Li. Moreover, the ultimate fate of subducted materials that have entered the deep mantle also depends on the mineralogy and Li isotopic compositions of their protoliths (Adelfadi et al., 2014; Tang et al., 2014). Despite small isotopic fractionations (Marschall et al., 2007), subducted surficial materials with low δ^7Li values have the potential of evolving to residuals of much lower δ^7Li value, creating a distinct negative δ^7Li reservoir in the deep mantle. Recent research on the Himalayan collisional zone carbonatites generated by partial melting of subcontinental lithospheric mantle also obtained light δ^7Li values (-4.5‰ to -0.3‰; Tian et al., 2015), which are attributed to metasomatism by fluids released from subducted oceanic crust or marine sediments.

During the Variscan orogeny, the FMC was part of the Gondwana-Laurussia collision, accompanied by subduction of the Rheic Ocean and oceanic basins (Faure et al., 2009). Hence, the melts/fluids of light Li isotopic compositions that metasomatized the peridotites of the present study may derive from those subducted slabs at depth. Yet, it may be doubted whether the characteristics of materials entering the mantle before the Permian have been kept intact, now that Li has so rapid diffusive rate and the Li compositional heterogeneities in the mantle would be attenuated over time span of 10^8 years (Halama et al., 2008). In contrast, in the light of exalted δ^7Li in HIMU lavas, whose formation has, as a common sense, associated with the subducted altered oceanic crust, compared with non-HIMU lavas, Vlastélic et al. (2009) have proposed that the isotopic disequilibrium could survive diffusion over longer time (more than 1.5Ga for a km-thick altered oceanic crust) than the elemental

disequilibrium, similar to the experimental perspective (Richter et al., 2014). Furthermore, in both mantle xenoliths and mantle-derived lamprophyres from the Bohemian Massif (also belonging to the Variscan orogeny), negative Li isotopic compositions have been reported as a result of mantle metasomatism by subducted crustal materials (Ackerman et al., 2013; Adelfadil et al., 2014). In peridotite xenoliths from the North China Craton, similar anomalous δ^7Li values (as low as -30‰) observed in Ol cores have also been ascribed to metasomatism by melts/fluids from recycled materials related to subducted oceanic crust (Li et al., 2012; Tang et al., 2012, 2014). In addition, the signature of recycled components from the surface is recorded in the D/H ratios of amphiboles in peridotites from the FMC (Deloule et al., 1991). It is therefore likely that subducted materials remain in the mantle beneath the FMC. The asthenospheric upwelling that promoted alkali-volcanism in the Eocene may have produced a high heat flux, inducing slab melting. The melts/fluids of this origin ultimately metasomatized overlying peridotites and introduced the extremely light Li isotopic compositions.

6.3.4 Precedence relationship of the mantle metasomatism and percolation of the negative δ^7Li melt

The metasomatic agents accounting for trace element variations in Cpx and negative Li isotopic compositions preserved in Allègre Ol cores and in Mont Coupet Cpx (or Opx), are not the same due to a few lines of following evidences. On the one hand, the most strongly metasomatized sample from Allègre (AL56 according to Cpx trace element compositions) does not have the lowest δ^7Li values in its Ol cores while sample AL44, in which Cpx display LREE depletion, weak Ti negative anomaly and no Zr-Hf negative anomaly, have the Li isotopic compositions very negative in its Ol cores. The same phenomenon also occurs to the Mont Coupet samples, where sample MC34 displays strong LREE enrichment in its Cpx but the Li isotopic compositions in Cpx (or Opx) are not negative. On the other hand, the melt, which brought the light Li isotopic compositions to the xenoliths from Allègre and Mont Coupet at mantle depths, has been considered to be originally associated with subducted materials after dehydration during subduction. During dehydration of subduction slabs, the released

fluids should take the fluid-mobile elements (LILE and LREE) away but HFSE are normally left in the residuals and taken to the depths with slabs. Thus, the low δ^7Li melts should not have HFSE negative anomalies, in contrast with the trace element compositions in Cpx from Allègre and Mont Coupet.

Given that Ol grains in Allègre samples have equilibrated their Li isotopic compositions with the low-δ^7Li melts/fluids, we can approximate the duration of Li isotopic equilibration using the algorithmic method of Kaliwoda (2008). For a 3 mm Ol grain (common grain size in Allègre xenoliths), ~60 years are needed to fully equilibrate with an ambient melt (diffusion coefficient from Dohmen et al., 2010). Compared with our time constraints based on trace element equilibration (2000 years at 1100℃), the large discrepancy implies that the event responsible for lowering the Li isotopic compositions of Ol cores is likely not contemporaneous with the event that modified the trace element compositions in Cpx. The Li isotopic variation in Ol cores should have been imparted between mantle metasomatism, characterized by LREE enrichment and negative HFSE anomalies, and the host magma-xenolith interaction.

6.4 Water content of minerals in peridotite xenoliths from the French Massif Central

In this section, the water content of the lithospheric mantle under the French Massif Central estimated from peridotite xenoliths will be discussed in detail, including not only the results measured in this study, but also the data from previous studies (Grant et al., 2007b; Sundvall and Stalder, 2011; Schmädicke et al., 2013; Denis et al., 2015). Large part of the discussion is focused on the factors controlling the water content in minerals of peridotite xenoliths.

6.4.1 Assignment of bands in the infrared spectra

Although in the past three decades, many studies have tried to experimentally unravel the H incorporation mechanisms into Opx and identify the OH-stretching band (s) in the infrared spectra of pyroxenes corresponding to each mechanism (Skogby and Rossman, 1991; Rauch and Keppler, 2002; Stalder and Skogby, 2002, 2007; Stalder, 2004; Stalder et al., 2005, 2015; Mierdel et al., 2007; Smyth et al., 2007; Prechtel and Stalder, 2012) or to identify them from theoretical calculations (e.g., Balan et al., 2013), the bands in the infrared spectra collected on Opx from natural samples have never been completely reproduced (Stalder et al., 2015). Some bands in the spectra of Opx synthetized in the Al-doped systems are centered at similar wavenumbers to those in the natural Opx spectra (Rauch and Keppler, 2002; Stalder, 2004; Stalder et al., 2005; Sakurai et al., 2014), but bands at other wavenumbers in the spectra of synthetized pure enstatite or Opx doped with other ions (e.g., Fe, Cr) have not been observed in the natural Opx spectra (e.g., Skogby, 1990; Sundvall and Stalder, 2011). So the bands in the infrared spectra of analyzed Opx in this study are assumed to be dominantly generated by Al-coupled H incorporation.

As for Cpx, Ingrin et al. (1989) have assigned the mechanism responsible for the band at 3640 cm^{-1} as an OH defect with the dipole directing along (101) plane, and other bands at 3535 and 3460 cm^{-1} (bands at 3425 and 3355 cm^{-1} also reported in that study) as substitution defects coupled with trivalent ions (Al^{3+}, Cr^{3+}, and Fe^{3+}) or monovalent ions (e.g., Na^{+}). In a recent experiment to anneal a natural gem-quality

Cr-diopside under high pressure and water-saturated conditions, the peak heights of bands at 3646, 3558, 3525, and 3434 cm^{-1} enlarged in different degrees due to the decrease of the oxygen fugacity (Bromiley et al., 2004), which has been interpreted as H incorporation into M2 site to charge-balance the reduction of Fe^{3+} to Fe^{2+} on M1 site coupled with Na^{+} on M2 site, or into M1 or tetrahedral (T) site coupled with Al^{3+} on T site. H vibration in these positions corresponds to the bands 3646, 3525 and 3434 cm^{-1}, respectively. That means that although the initial incorporation of all H observed in natural Cr-diopsides can't thoroughly be related to Fe^{3+} reduction, it is confirmed that the alteration of ambient oxygen fugacity can obviously change the Cpx storage capacity for H. The band at 3359 cm^{-1}, observed in the infrared spectrum of hydrothermally formed diopside and associated with Ca vacancy (Andrut et al., 2007), doesn't appear in all the Cpx spectra collected in this study.

The O-H bands of Ol infrared spectra collected on natural samples have been reproduced in spectra of synthetic forsterite or Fe-bearing Ol (e.g., Matveev et al., 2001; Lemaire et al., 2004; Berry et al., 2005, 2007b; Mosendelder et al., 2006a, 2006b; Walker et al., 2007; Ingrin et al., 2013). The bands belonging to the Group I occur at wavenumbers 3572 and 3525 cm^{-1}, are present in the Ol spectra of all the analyzed samples in this study and are also the most common (but sometimes not the strongest) in the spectra of worldwide Ol (e.g., Miller et al., 1987; Bell et al. 2004; Matsyuk and Langer, 2004; Matveev et al., 2007; Schmädicke et al., 2013). They have been attributed to H point defects on T site charge-balanced by Ti^{4+} replacing Mg^{2+} on the octahedral site (Berry et al., 2005, 2007a; Walker et al., 2007; Balan et al., 2011). According to the observations and calculations on molecular structures, Ti occupies the T site in substitution of Si in anhydrous forsterite and during hydration, Ti is transferred to the octahedral site and two H atoms enter the T site (Berry et al., 2007a), and the inverse mechanism has been proposed for the diffusive loss of H associated with Ti (Padrón-Navarta et al., 2014). In the band Group II, the bands at 3350 and 3325 cm^{-1}, only present in the Ol spectrum of sample MC34, may be accounted for by H defects in the octahedral site to charge-balance the trivalent ions substituting Mg^{2+} (Berry et al., 2007b; Walker et al., 2007). Due to the low concentrations of trivalent ions in Ol, these bands are not so common in the spectra of

natural mantle Ol and, when occurring, most likely related to Fe^{3+} or Cr^{3+}. The bands at 3225 cm^{-1}, mainly observed in the Ol spectra of Mont Coupet samples, is associated with the substitution of Mg^{2+} by two H, which has been identified not only experimentally (Lemaire et al., 2004; Monsenfelder et al., 2006a; Walker et al., 2007) but also by theoretical calculations (first principles; Balan et al., 2011; Umemoto et al., 2011).

6.4.2 Water partitioning among mineral phases

The water partition coefficients among minerals phases at equilibrium in peridotite have been experimentally estimated or calculated from the partition coefficients between each phase and melts in previous studies (Aubaud et al., 2004, 2008; Grant et al., 2006, 2007a; Hauri et al., 2006b; Tenner et al., 2009, 2012b; Ardia et al., 2012; Férot and Bolfan-Casanova, 2012; Novella et al., 2014; Sakurai et al., 2014). The results show that the partition coefficients between pyroxene (Opx and Cpx) and Ol largely depend on the Al concentrations in pyroxene and the pressure of equilibration (e.g., Ardia et al., 2012; Novella et al., 2014). Thus, the data from experiments performed at low pressure and under Al-bearing conditions should be more appropriate when comparing with natural samples. The results summarized in Warren and Hauri (2014) will be used in this study: $D_{H_2O}^{Ol/Opx}$ =0.11±0.03, and $D_{H_2O}^{Ol/Cpx}$ =0.07±0.02. Concerning the water partitioning between Opx and Cpx, two equations, linking Al concentrations to the H_2O partition coefficients between pyroxene and melts ($D_{H_2O}^{Opx/melt}$, $D_{H_2O}^{Cpx/melt}$), have been established by Novella et al. (2014), who collected a large set of experimental data:

$$D_{H_2O}^{Opx/melt} = 0.0028 * Al_2O_3 \text{ (wt. \%)} + 0.0033 \quad (6)$$

$$D_{H_2O}^{Cpx/melt} = 0.0016 * Al_2O_3 \text{ (wt. \%)} + 0.0078 \quad (7)$$

They will be applied to calculate the H_2O partition coefficients at equilibrium between Cpx and Opx ($D_{H_2O}^{Cpx/Opx} = D_{H_2O}^{Cpx/melt} / D_{H_2O}^{Opx/melt}$) based on Al_2O_3 content in each phase for each analyzed sample (Table 6-4).

Sample	Ratio (Cpx/Opx)	$D_{H_2O}^{Cpx/Opx}$	Ratio (Ol/Opx)	Ratio (Ol/Cpx)
MC34	2.8	1.4	0.009	0.003
MC36	4.5	1.3	0.03	0.007
MC38	1.5	1.2		
MC43	2.4	1.3	0.005	0.002
MC49	2.7	1.4	0.008	0.003
MC53	4.4	1.3	0.022	0.005
AL22	3.9	1.4		
AL41P1	3.3	1.3		
AL44	4.8	1.4	0.059	0.012

Table 6-4: $D_{H_2O}^{Cpx/Opx}$ estimated using Al_2O_3 content in Cpx and Opx, and water concentration ratios between different phases in analyzed samples.

As shown in Table 6-4, the water concentration ratios between Opx and Cpx in the samples from Allègre and Mont Coupet ($C_{H_2O}^{Cpx}/C_{H_2O}^{Opx}$) are higher than $D_{H_2O}^{Cpx/Opx}$ in various degrees. Actually, this obaservation is systematically observed in peridotite xenoliths from worldwide localities (e.g., Warren and Hauri, 2014; Peslier and Bizimis, 2015; Demouchy and Bolfan-Casanova, 2016). The discrepancy may be induced by some deviation of settings in experiments to determine $D_{H_2O}^{Cpx/Opx}$ from environments for natural peridotites; for instance, in high-pressure experiments there is generally aluminiferous garnet generated, but at lower pressures no spinel has emerged in experimental products, which is in contrast with spinel as a constituent mineral in most natural relatively low-pressure peridotites. $C_{H_2O}^{Cpx}/C_{H_2O}^{Opx}$ values of mantle xenoliths in previous studies have been summarized to fall in the range of 2.6±0.9 (Warren and Hauri, 2014; Denis et al., 2015; Hao et al., 2016). But some ratios in xenoliths from Allègre and Mont Coupet are beyond that range (Table 6-4; Fig. 6-24a). Meanwhile, the recent study by Denis et al. (2015) on peridotite xenoliths from Ray Pic, also situated in the FMC, has also got some higher water concentration ratios between co-existing Opx and Cpx when using the method of Bell et al. (1995) to calculate the pyroxene water content. Here, water concentrations of Opx and Cpx in mantle xenoliths from worldwide localities are compiled in a graph and the linear fitting without intercept gives a expression: $C_{H_2O}^{Cpx}=2.07\,C_{H_2O}^{Opx}$ (R^2=0.69; Fig. 6-24b). This ratio is very close to the proposed value in a recent review on water distribution in the lithospheric mantle (2.1; Demouchy and Bolfan-Casanova, 2016). Some higher

water concentration ratios of Opx and Cpx in Allègre and Mont Coupet xenoliths probably point to some metasomatic event (s) subsequent to the partial melting.

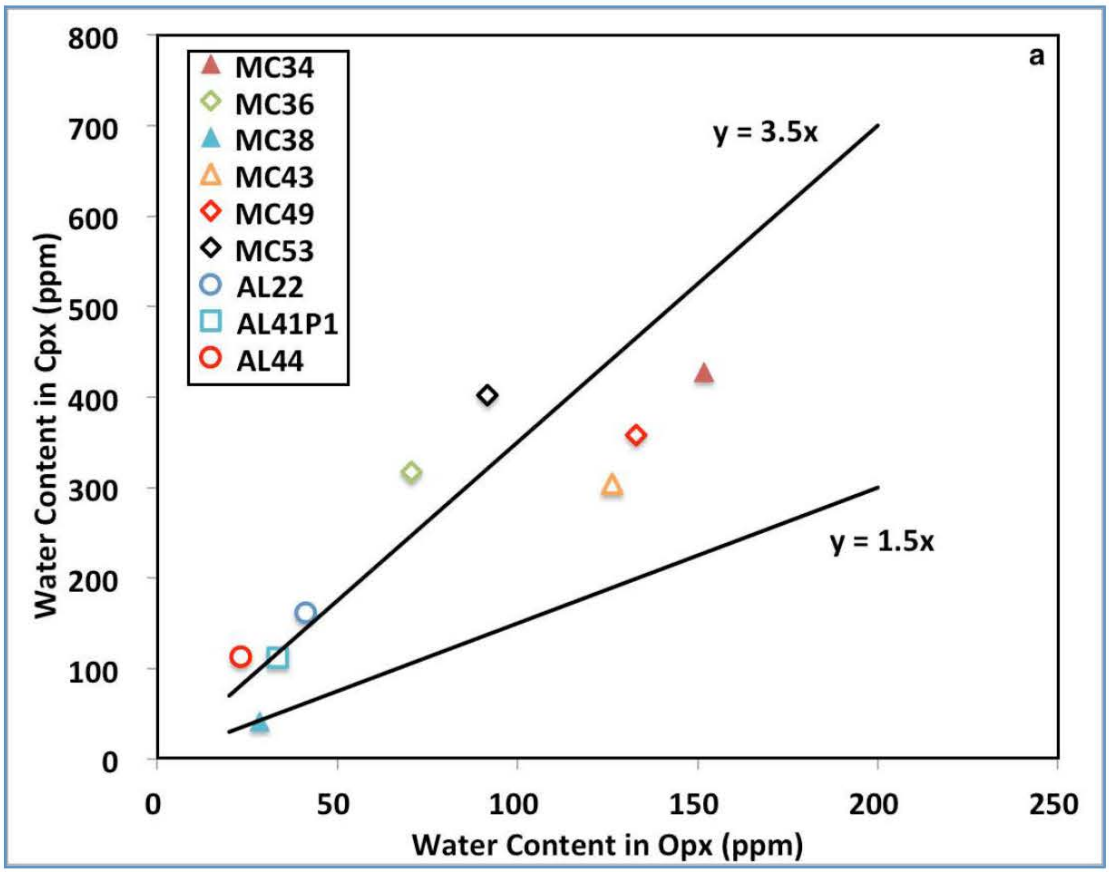

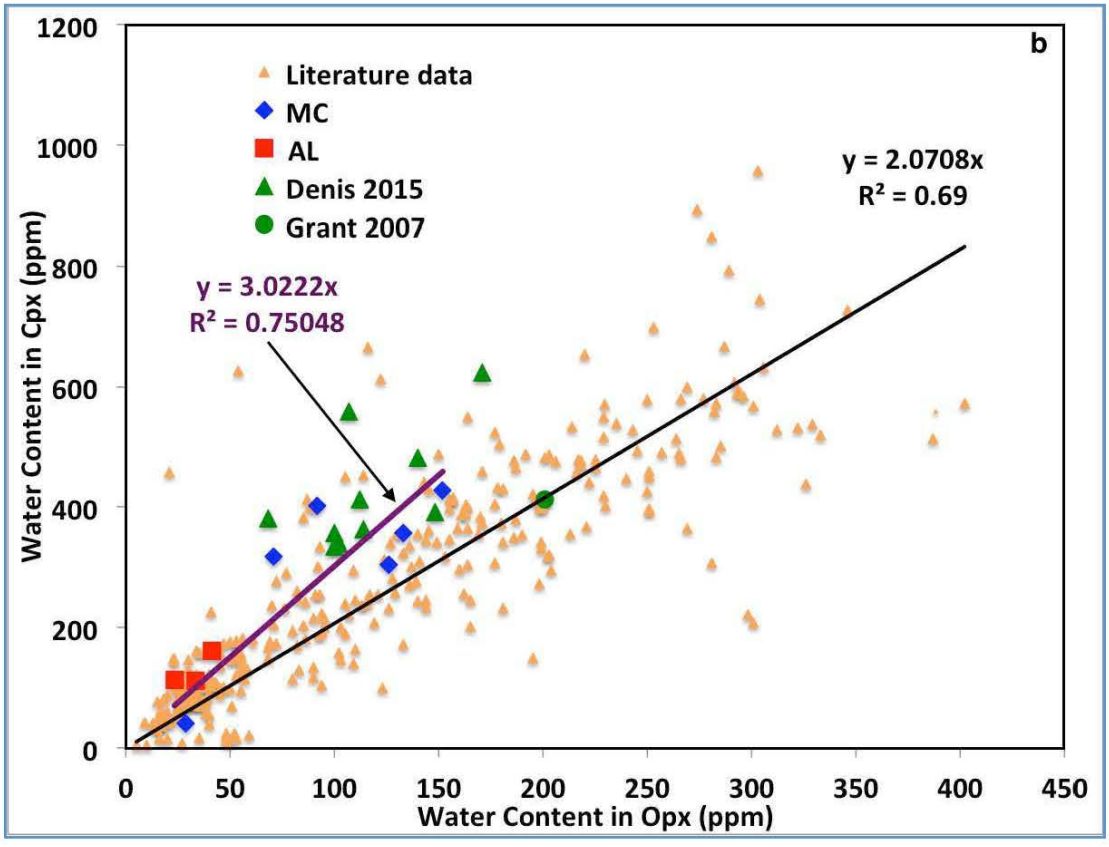

Figure 6-24: Water partitioning between Cpx and Opx in xenoliths from Allègre and Mont Coupet, compared with the $C_{H_2O}^{Cpx}/C_{H_2O}^{Opx}$ range from literature (2.6±0.9; a), and the linear fitting on water concentrations of Opx and Cpx in mantle xenoliths from worldwide localities (b). The purple line in (b) is from linear fitting on the data from the FMC. The literature data in (b) are from Pealier et al. (2002, 2012), Grant et al. (2007b), Falus et al. (2008), Li et al. (2008), Bonadinam et al. (2009), Wang et al. (2010), Xia et al. (2010, 2013), Yu et al. (2011), Hao et al. (2012, 2014), Doucet et al. (2014), Li P. et al. (2014), Warren and Hauri (2014), Denis et al. (2015), Demouchy et al. (2015), and Peslier and Bizimis (2015).

6.4.3 The low water content in minerals from Allègre samples - equilibrated with degassed host magmas

The three Allègre samples analyzed by FTIR are among the samples with high $C_{H_2O}^{Cpx}/C_{H_2O}^{Opx}$. Compared with xenoliths from Mont Coupet and from Ray Pic (Denis et al., 2015), Allègre xenoliths uniformly contain less water in Opx and Cpx, even considering the Ol water concentration in sample AL44 from FTIR and the results obtained by SIMS. The water concentration of whole rocks for Allègre samples has been calculated in combining the modal compositions and FTIR results, assuming the Ol water content to 0 ppm in samples AL22 and AL41P1. The results are very consistent: 10.6, 12.2, and 12.4 ppm in samples AL41P1, AL22, and AL44, respectively. They are much lower than the water content in the MORB source mantle (50-200 ppm). The fractional melting model from Norman (1998) has been used to estimate whether higher degrees of partial melting could have caused a pronounced water depletion in Allègre samples. The source rock is assumed to be a depleted MORB source mantle with water content 150 ppm. A value of 0.1, which has been considered to make the partial melting model best match the measured results (Hao et al., 2014; Denis et al., 2015; Peslier and Bizimis, 2015), is assigned to the water partition coefficient between bulk peridotite and melt. The modeling shows that the three samples AL22, AL41P1 and AL44 fall largely below the modeling curve (Fig. 6-25), which means that the whole rock water content in these samples are too low to be a simple result of partial melting. Moreover, no late stage metasomatism seems to have affected the sample AL44. In this case, the ratio between Ce concentration and water content in Cpx (H_2O/Ce) should be close to the ratio in MORB ratio (~200;

Michael, 1995). But the ratio of 67 in sample AL44 is much lower.

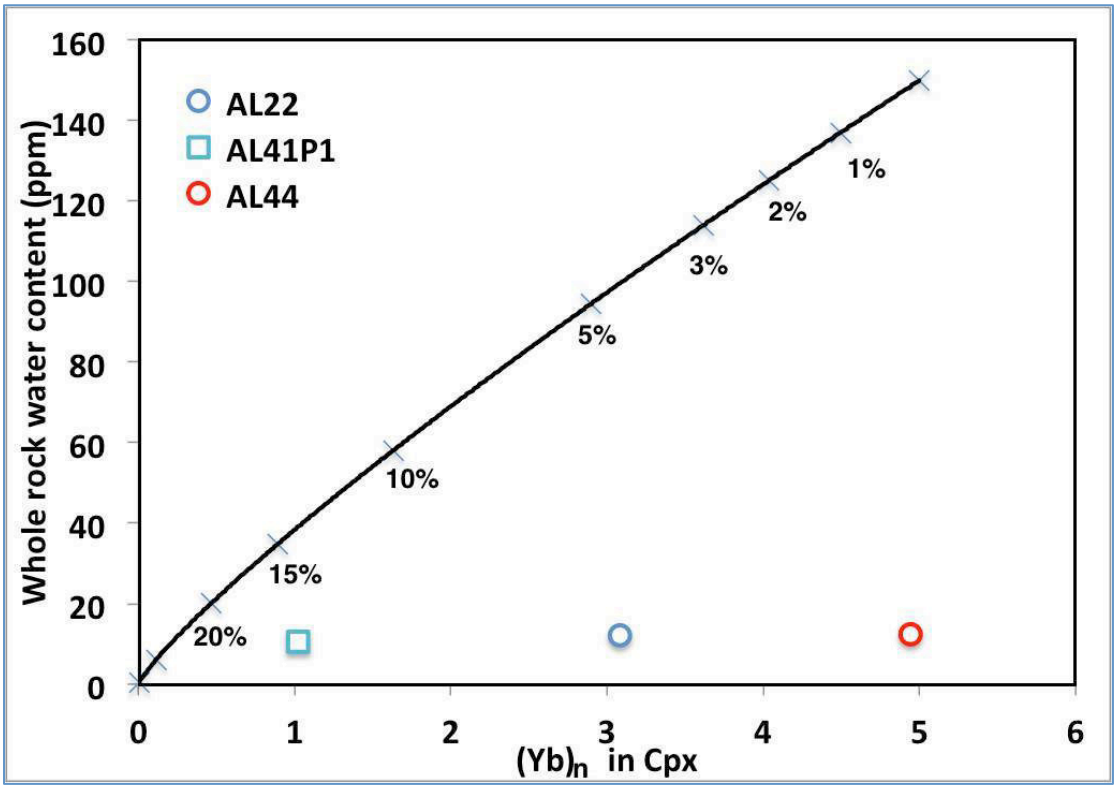

Figure 6-25: The fractional melting modeling results for the whole rock water content in Allègre xenoliths plotted against primitive mantle-normalized Yb content in Cpx. According to the model of Norman (1998), the initial content of Yb are chosen as the primitive mantle compositions from McDonough and Sun (1995). 0.43 is used in the model as the partition coefficient of Yb between Cpx and melts (Hart and Dunn, 1993). The modal composition of Cpx is assumed to be 20%, similar to Norman (1998). The subscript 'n' denotes normalization to primitive mantle compositions (McDonough and Sun, 1995). The initial water content in the whole rock is assumed as 150 ppm and 0.1 is assigned to the partition coefficient between peridotite and basaltic melt (the detail referring to the text).

Additionally, all the infrared spectra collected on Opx grains in Allègre samples, with exception of only one analyzed grain in sample AL44, display no absorption band at 3520 cm^{-1}, totally different from samples from Mont Coupet and even peridotite xenoliths from worldwide localities (e.g., Peslier et al., 2002; Grant et al., 2007; Xia et al., 2010; Sundvall and Stalder, 2011; Doucet et al., 2014; Hao et al., 2016). The band at 3520 cm^{-1} can be considered to be related to a specific H substitution mechanism by which H entered the Opx lattices and diffused out faster, comparable with the observation of Padrón-Navarta et al. (2014), who found that the hydrogen diffusive rate in Ol also relies on the mechanism of hydroxyl incorporation

into Ol lattices. Nevertheless, the band located close to 3520 cm^{-1} is present in the spectra of Al-rich synthesized enstatites, but doesn't exhibit obviously more faster weakening than other bands when samples were annealed in air (Stalder and Skogby, 2007).

In the last section, we have shown that Li isotope system in Allègre xenoliths has been markedly affected by the host magma-xenolith interaction during the slow cooling of the lava lake. Hydrogen has the fastest diffusive rate in mantle minerals at magmatic temperatures (e.g., Kohlstedt and Mackwell, 1998; Hercule and Ingrin, 1999; Stalder and Skogby, 2003; Ingrin and Blanchard, 2006). Meanwhile, the hydrogen solubility in mantle minerals has been experimentally evidenced to decrease with decreasing pressure (e.g., Kohlstedt et al., 1996; Rauch and Keppler, 2002; Férot and Bolfan-Casanova, 2012). And the profiles of hydrogen diffusive loss during xenolith ascent to the surface in host magmas have been observed in previous studies (Demouchy et al., 2006; Peslier and Luhr, 2006; Li et al., 2008; Peslier et al., 2008, 2015; Denis et al., 2013). On the other hand, when the lava lake cooled, water in the lava inevitably degassed to the atmosphere. A water concentration gradient emerged between xenoliths and the degassed host magmas, and hydrogen transferred from xenoliths to the host magmas. Thus, water in Allègre xenoliths should have been lost during cooling of the lava lake, which can be regarded as an explanation for the low water content and the lack of the band at 3520 cm^{-1} in Opx infrared spectra in Allègre samples. In light of no discrepancy in the spectra respectively collected at the cores and rims in most grain, Allègre xenoliths should have achieved hydrogen diffusive equilibrium with the degassed host magma. The slightly higher $C_{H_2O}^{Cpx} / C_{H_2O}^{Opx}$ in Allègre xenoliths may be the consequence of the augmentation of $D_{H_2O}^{Cpx/Opx}$ with decreasing temperatures or pressures, but, as far as I know, no experimental results on water partitioning between Cpx and Opx support this speculation.

From the results of Li isotopes and water in Allègre xenoliths, it can be noted that Li and H have different behaviors in peridotite xenoliths when the host magma cools slowly on the earth surface. Li diffuses from the host magma to xenoliths before the system cools to the closure temperature for Li diffusion rather than degasses due to the sharply decreasing pressure, whereas H in xenoliths transfers to the degassed host

magmas as a result of pressure effect on water solubility in NAMs and water concentration equilibrium between xenoliths and the host magmas.

6.4.4 Mineral water concentration variations in xenoliths from Mont Coupet

6.4.4.1 Preservation of original water content during xenolith ascent

As mentioned in last section, due to the high diffusivity of H at magmatic temperatures and water solubility in NAMs decreasing with diminishing pressures, hydrogen incorporated in lattices of NAMs may be lost during xenolith ascent to the surface. Whether or not the currently obtained water content in xenoliths represents the original value in the mantle sources of xenoliths, has always been a central question encountered by every scholar undertaking researches on water content in mantle xenoliths (e.g., Bell and Rossman, 1992; Ingrin and Skogby, 2000). Although experimentally determined hydrogen diffusivity doesn't vary largely in Ol and pyroxenes (e.g., Ingrin and Blanchard, 20006), the H diffusive loss profiles have been mainly observed in xenolithic Ol but not in coexisting pyroxenes (e.g., Peslier et al., 2002; Peslier and Luhr, 2006; Peslier, 2010) except in Opx in one specific case (Tian et al., the manuscript submitted to Geology). In the two common magma types bearing peridotite xenoliths, alkali basalts and kimberlites, have been estimated of the ascent rates ranging from 0.2 to 2 ms^{-1}, and from 4 to 40 ms^{-1}, respectively (O'Reilly and Griffin, 2010). The large difference in eruption rates of these two magmas has been invoked to account for almost no detectable OH in Ol from peridotite xenoliths entrained by alkali basalts (e.g., Grant et al., 2007b; Yang et al., 2008; Bonadiman et al., 2009; Xia et al., 2010), and relatively higher water content in cores of Ol, generally considered to represent the original water content, from cratonic peridotite xenoliths transported by kimberlites (e.g., Peslier et al., 2008, 2010; Baptiste et al., 2012; Doucet et al., 2014). However, several recent studies on water in peridotite xenoliths transported by basalts have also detected a certain amount of OH in Ol grains and even interpreted it as the original amount prior to entrapment by magmas (Demouchy et al., 2015; Denis et al., 2015).

Firstly, the homogeneous water distribution in pyroxene grains from Mont Coupet

xenoliths has been testified by the absence of variation in spectra collected from grain cores to rims (Fig. 4-14). Large quantities of unpolarized pyroxene spectra from different grains in a single xenolith display moderate variations due to pleochroism rather than real concentration variation. And the water concentration ratios between Opx and Cpx in most samples from Mont Coupet, except two Amp-bearing samples MC36 and MC53, fall in the range restricted by mantle xenoliths from worldwide localities (Table 6-4; Fig. 6-24a). These points indicate that initial water in Opx and Cpx from Mont Coupet xenoliths may have remained intact after entrainment to the earth surface by the host magma.

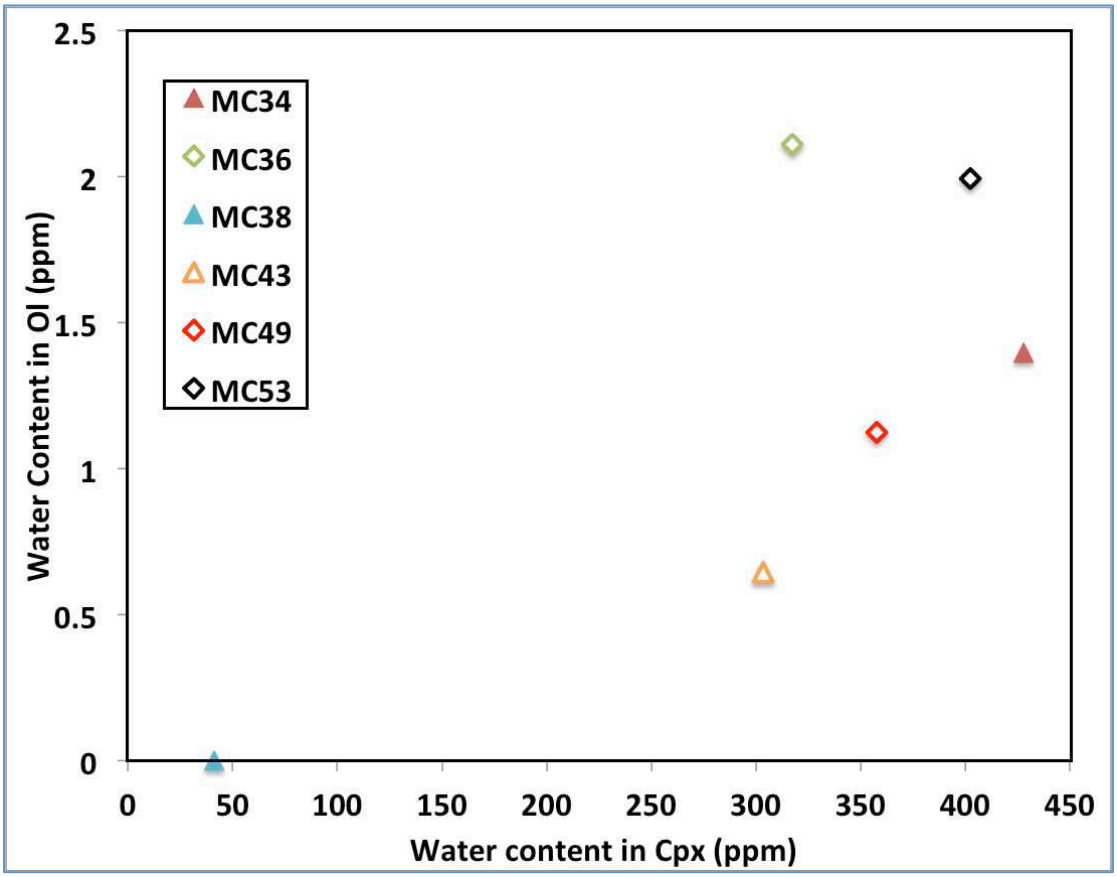

Figure 6-26: Water content in Ol versus water content in Cpx in Mont Coupet xenoliths. The water content in Ol of sample MC38 is assumed as 0 ppm due to no bands observed in the infrared spectra.

Ol in xenoliths from Mont Coupet may have also retained their water content of mantle origin and have not undergone water loss after entrapment by the host magma. Several lines of evidences can support this conclusion. On the one hand, the FTIR profile analyses from core to rim show no variation in spectra across Ol grains (Fig. 4-11). Especially for the profile in one grain from sample MC34, the bandwidth and

peak height of the band at 3225 cm^{-1} don't show any changes. This band has been assigned to the mechanism of two H substituting Mg^{2+}, by which hydrogen incorporated into Ol lattices has been experimentally identified to diffuse the second fastest among the four H incorporation mechanisms, just a little slower than H coupled with trivalent ion substitution, but much faster than H coupled with Ti substitution and H entering Si vacancy (Padrón-Navarta et al., 2014). If hydrogen loss has indeed occurred in Ol, the bands at 3225 cm^{-1} should have displayed profiles from core to rim, or have disappeared, which is in contradiction with observations shown in Fig. 4-11. On the other hand, the water content in Ol from Mont Coupet xenoliths has a roughly positive co-variation with that in co-existing Cpx (Fig. 6-26).

Compared with literature data, Ol in xenoliths from Mont Coupet have been incorporated by rather less hydrogen than Ol in cratonic peridotite xenoliths (e.g., Grant et al., 2007b; Peslier et al., 2008; Doucet et al., 2014), but is consistent with observations from other off-craton mantle xenoliths (e.g., Grant et al., 2007b; Peslier, 2010; Denis et al., 2013). This indicates that Ol in the off-craton lithospheric mantle might indeed have lower water content than Ol from cratonic lithospheric mantle.

6.4.4.2 Processes controlling the water content in peridotite xenoliths from Mont Coupet

For two Amp-bearing samples MC36 and MC53, the water content in Ol, Opx and Cpx doesn't show any remarkably higher values than that in corresponding minerals from other anhydrous samples from Mont Coupet (Table 4-7). In fact, the highest water content of Cpx and Opx is obtained in anhydrous sample MC34. The same observations have been reported in previous studies (Yang et al., 2008; Schmädicke et al., 2013; Denis et al., 2015). Additionally, the whole rock water content in sample MC36 and MC53 is calculated at 41 and 53 ppm (not including water in Amp), respectively, both of which are similar to the water content in the depleted MORB source mantle (50-200 ppm). Thus, the modal mantle metasomatism by aqueous melts/fluids may not have added much water to primary minerals. However, it is noteworthy that these two Amp-bearing samples have higher $C_{H_2O}^{Cpx}/C_{H_2O}^{Opx}$ ratios than the $C_{H_2O}^{Cpx}/C_{H_2O}^{Opx}$ ratio range restricted by mantle xenoliths from worldwide localities

(Table 6-4; Fig. 6-24a).

Among xenoliths from Mont Coupet, Opx and Cpx in sample MC38 contain the least water compared with corresponding minerals in other samples, and Ol infrared spectra from sample MC38 do not display any OH-vibration bands at wavenumbers between 3700-3000 cm^{-1} (Fig. 4-10). According to the major element compositions and Cpx HREE concentrations, sample MC38 should have been depleted strongly by partial melting, with calculated partial melting degree of 16%, the highest among samples from Mont Coupet. Considering H as an incompatible element, the measured extremely low water content in sample MC38 can be accounted for by high-degree partial melting (Fig. 6-27a, b). Although LREE enrichment and HFSE negative anomalies in Cpx of sample MC38 suggest a carbonatite-related metasomatism subsequent to partial melting, the water content result evidences that this metasomatism have not introduced water into the sample simultaneously and even may have affected the relative proportions of H defects in pyroxenes since the spectra of Cpx and Opx are markedly different from those in other samples from Mont Coupet. The band position shift is intrinsically related to the change of OH-streching modes, corresponding to the change of P-T conditions or chemical compositions of host minerals (e.g., Yang et al., 2012; Ingrin et al., 2013), which may have been brought by the percolation of the metasomatic melt. Furthermore, sample MC38 also has the highest calculated spinel $Fe^{3+}/\Sigma Fe$ value (Fig. 6-27c), which can be regarded as an indicator of oxygen fugacity. This is consistent with the experimental observations of Bromiley et al. (2004).

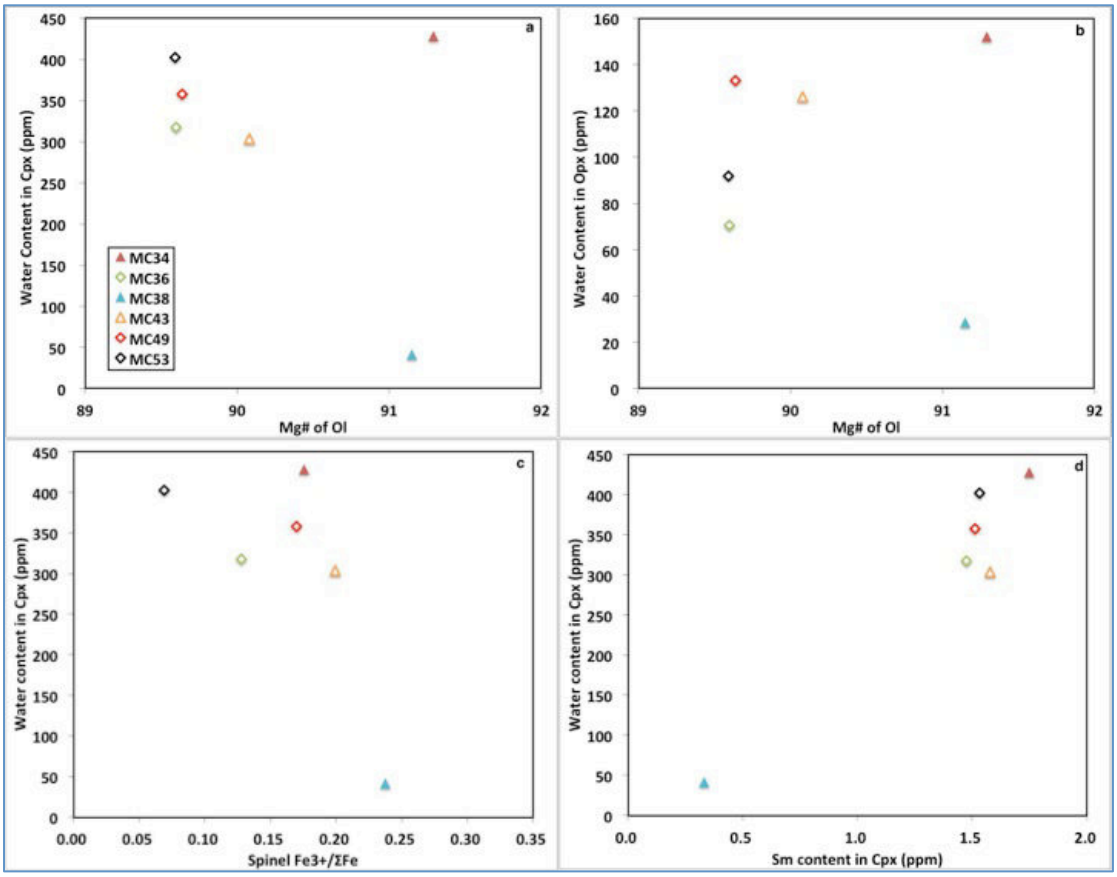

Figure 6-27: Water content in Cpx (a) and in Opx (b) plotted against Ol Mg#; water content in Cpx versus $Fe^{3+}/\Sigma Fe$ values of coexisting Spl (c) and Sm content in Cpx (d) in xenoliths from Mont Coupet.

For sample MC34, where water content in Opx and Cpx is the highest among samples from Mont Coupet, the major element compositions and HREE concentrations also indicate stronger depletion by partial melting compared with samples MC43 and MC49. It severely deviates from the roughly negative co-variation between Cpx or Opx water content and Mg# of Ol for samples from Mont Coupet (Fig. 6-27a, b). The metasomatism, characterized by LREE enrichment in Cpx of sample MC34, might have added some water to sample MC34. According to the modeling for chromatographic effect of a percolating melt, sample MC38 should be situated farther from the melt source than sample MC34. During the metasomatic melt moved from the location of sample MC34 to that of sample MC38, water in the melt might have been lost to the ambient rocks along the melt pathway. Thus, the melt could have lost water but not been able to to increase the water content in sample MC38. This situation is also reflected in the positive co-variation between water content in Cpx and Sm concentrations in Cpx, which seem to have been modified by

the metasomatism just in sample MC34 but not in other Mont Coupet xenoliths (or weakly modified in sample MC38; Fig. 6-27d). In other words, the variations of Sm concentration in Cpx among most Mont Coupet xenoliths (except MC34) mainly depend on the different partial melting degrees.

The whole rock water content in samples MC43 and MC49 falls in the range of water content in depleted MORB source mantle (50-200 ppm), with values of 50 and 88 ppm. Their water content in minerals should just be affected by partial melting, in agreement with LREE depletion in Cpx, which is characteristic of the depleted mantle without late-stage metasomatism.

In summary, partial melting, together with the subsequent carbonatite-related metasomatism, has controlled the water content in samples from Mont Coupet. And the aqueous melts/fluids responsible for presence of Amp in samples MC36 and MC53 have not lead to the increase of water content in these two samples.

6.4.4.3 Relationship between water content and trace element concentrations in Ol

Although H can incorpate into Ol lattice through occupying Mg vancancies charge-balanced by trivalent ions (e.g., Al^{3+} Cr^{3+}, Fe^{3+}), its corresponding bands are only observed in Ol infrared spectra of sample MC34 but not in those of other samples. Here we will not discuss the relationship between concentrations of trivalent ions and concentrations of H responsible for bands at between 3400 and 3300 cm^{-1}.

The maximum content of H, entering Ol associatied with Ti, is calculated from Ti concentrations in Ol according to the expression $Ti^{4+} + 2H^{+} = Mg^{2+} + Si^{4+}$, supposing that all Ti is hydrated and enters in the octahedral site. The calculated water content ranges from 1.39 ppm in sample MC38 to 5.25 ppm in sample MC43, much higher than the measured Ol total water content in each sample, let alone the content of water associated with bands at 3572 and 3525 cm^{-1} (Table 6-5). It implies that a majority of Ti has equivalently substituted Si in the tetrahedral site or in M site to compensate other charge deficient cations rather than to form H defects. It is interesting to note that Ti substituation for Si in the tetrahedral site is energetically more favourable than for Mg in M1 site (Berry et al., 2007a).

Sample	Ti (ppm)	Calculated H_2O (ppm)	Total H_2O (ppm)	H_2O in GI (ppm)
MC34	6	2.2	1.4	0.4
MC36	6.9	2.6	2.1	1.4
MC38	3.7	1.4		
MC43	14	5.3	0.6	0.2
MC49	8.9	3.4	1.1	0.4
MC53	8.3	3.1	2	1.4

Table 6-5: Water content calculated from Ti concentrations in Ol from Mont Coupet. The total H_2O and H_2O in GI represent the Ol total water content measured by FTIR and the measured water content just associated with bands in Group I region, respectively.

6.4.5 Water content in the lithospheric mantle beneath the FMC

Because water in Allègre peridotite xenoliths has been partly lost to the host magma, the results from Allègre samples will be excluded when estimating the water content in the lithospheric mantle beneath the FMC. Combining with data from Grant et al. (2007b) and Denis et al. (2015), mantle xenoliths from the FMC are estimated to contain water ranging from 4.7 to 117 ppm. The data of Denis et al. (2015) have been recalculated using the same calibration methods of this study. The lowest value is from sample MC38 in this study and the highest value belongs to one sample from the volcano Barges (Grant et al., 2007b). As a whole, to deeply investigate water distribution across the lithospheric mantle beneath the FMC is limited by the small amount of samples, especially xenoliths in the northern domain of the FMC (just one in Grant et al. (2007b)). Since the northern and southern mantle domain beneath the FMC has different major and trace element, and Sr-Nd isotopic compositions (e.g., Lenoir et al., 2000; Downes et al., 2003), their water content may also be unlike each other, which requires more data to verify.

Conclusion

In my thesis, major and trace element compositions, Li concentrations, Li isotopic compositions and water distribution in minerals of peridotite xenoliths from Allègre and Mont Coupet have been investigated in detail. The results indicate that rigorous in-situ analysis of Li concentrations and isotopic compositions can distinguish individual metasomatic processes occurring over different timescales, based on the phenomenon that Cpx and Ol retain signatures of different events as a function of the diffusivity of Li in those phases. As a light element is sensitive to melt/fluid activities and changes of ambient conditions, H distribution in mantle minerals can be strongly influenced by different processes, occurring either in the deep mantle or in the slow cooling host magmas. Although both localities are situated in the southern domain of the FMC, distinct signatures of Li isotopes and water distribution reflect different and complicate evolutional histories of the xenoliths from Allègre and Mont Coupet.

For the peridotite xenoliths from Allègre, mineral major element and Cpx HREE compositions reveal that peridotites have been depleted by partial melting and the extraction of basaltic component. The calculated melting degrees range from <1% to 19%. Most Allègre xenoliths fall in the compositional field defined by Downes et al. (2003) for the southern domain on the basis of the Cpx major element compositions, despite their residence in a lava lake and the infiltration of host magmas into some xenoliths.

The Allègre peridotite xenoliths studied here suffered a multi-stage metasomatic process, including interaction with the host-magma (Fig. 7-1). The trace element compositions of Cpx, normalized to the primitive mantle, display characteristic LREE/HREE fractionations and significant HFSE anomalies resulting from melt percolation into a porous peridotite matrix. Thus, we infer that a mantle metasomatism related to carbonatitic melts or melts/fluids originating from sunducting slabs occurred after partial melting.

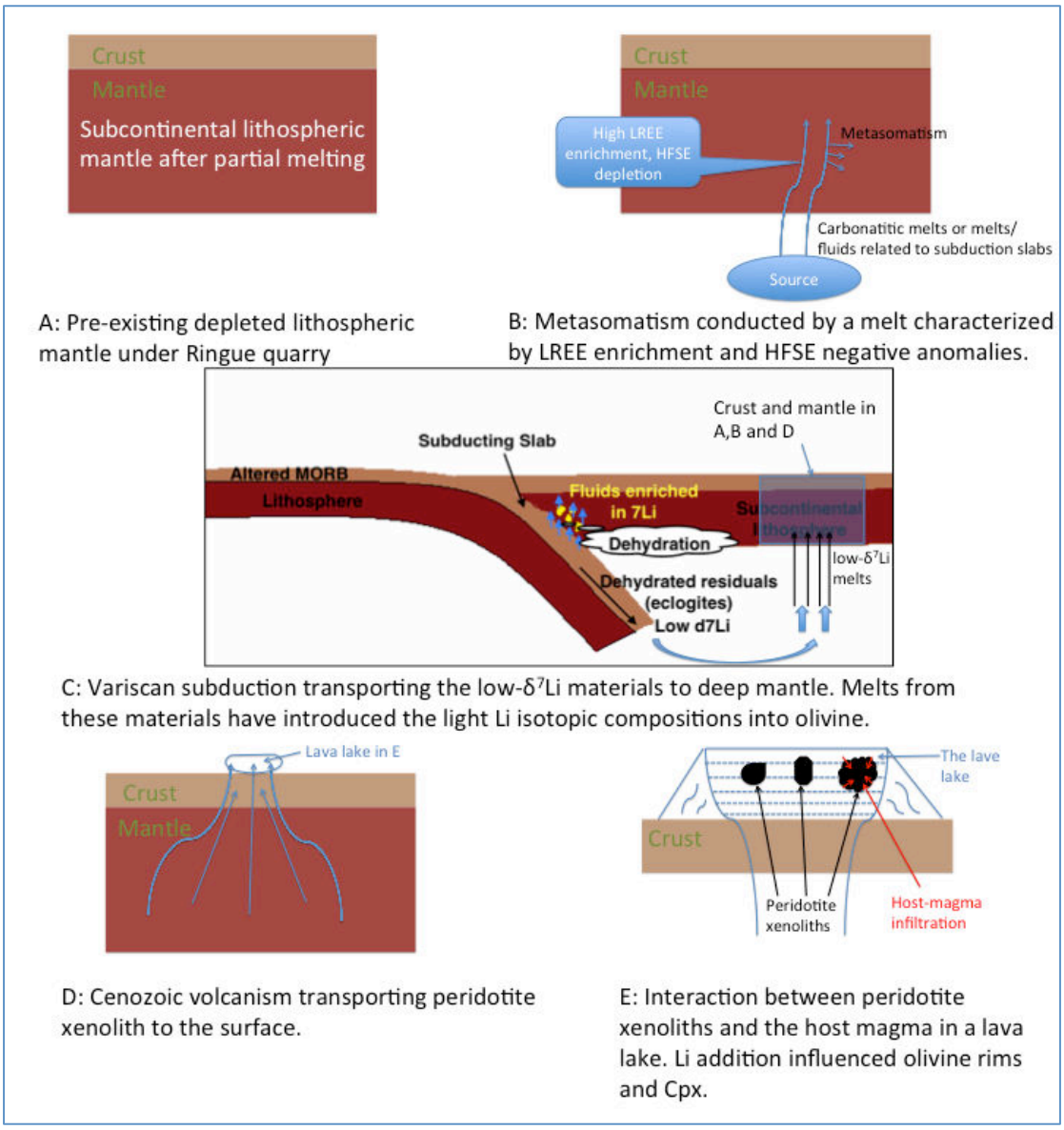

Figure 7-1: A schematic diagram modeling the evolution of peridotite xenoliths from the lithospheric mantle beneath Allègre.

The extremely high Li concentrations in Cpx (compared with the normal mantle), as well as the increased Li concentrations in Ol rims, are a consequence of late-stage Li diffusion from interstitial melts derived from the host magma, whereas Li contents in Ol cores are as high as or higher than those of the normal mantle. Due to Li incorporation from the host magma, and the higher diffusivity of Li in Cpx compared to Ol, the imprints of mantle metasomatism prior to entrainment were erased in some Cpx grains, which exhibit Li isotopic compositions in equilibrium with the host magma (up to 6‰). Most Ol cores in this study have negative δ^7Li values (as low as -25‰). We invoke Li ingress from a low δ^7Li source, probably later than the

carbonatitic mantle metasomatism, to explain the negative Li isotopic compositions of the peridotitic Ol studied herein.

Because hydrogen has very high diffusivity in mantle minerals at magmatic temperatures and because the capacity of NAMs to accommodate hydrogen decreases with decreasing pressure, we concluded that water in Allègre xenoliths has been lost to the degassed host magma during slow cooling in the lava lake. The absence of core-rim variation suggests that xenoliths have achieved water diffusive equilibrium with the host magmas.

For the peridotite xenoliths from Mont Coupet, mineral major element and Cpx HREE compositions point out that xenoliths have also experienced partial melting and melt extraction processes in various degrees, ranging from <1% to 16%. Most samples fall in the compositional field of the southern mantle domain of the FMC, with an exception of sample MC38, which is too depleted and blends into the field of the northern mantle domain.

The Cpx trace element compositions of Mont Coupet xenoliths are characterized by Ti, Nb negative anomalies in all the samples and LREE enrichment relative to HREE in two most depleted samples. It also point to a metasomatism by a carbonatitic melt or a melt/fluid from a subduction slab subsequent to the partial melting event. Compared with Allègre samples, the degrees of LREE enrichment in sample MC34 and MC38 are much weaker. Amp in two Mont Coupet xenoliths (MC36 and MC53) have trace element compositions nearly equilibrated with their coexisting Cpx, except Ba and Nb.

Totally different from Allègre samples, peridotite xenoliths from Mont Coupet have Li concentrations in constituent minerals similar to the estimation for the normal mantle, and display nearly equilibrated inter-mineral Li partitioning and homogeneous intragranular Li distribution in every mineral phase. Meanwhile, we have not observed extremely light Li isotopic compositions in Ol cores. The negative δ^7Li values of Cpx and Opx in some samples should have been induced by an exchange with a small-volume melt with Li concentration similar to the normal mantle and light Li isotopic compositions. The preservation of inter-mineral large Li

isotopic fractionation currently observed in these samples indicates that the percolation of the melt should have occurred shortly prior to the entrainment of Mont Coupet xenoliths by the host magmas.

Peridotite xenoliths from Mont Coupet have retained their original water content from the mantle depths. Partial melting has controlled the water content in most samples from Mont Coupet. However, the subsequent metasomatism characterized by LREE enrichment and HFSE ngative anomalies have re-hydrated the sample MC34, which has the highest water content among the Mont Coupet samples. But the aqueous melts/fluids responsible for presence of Amp in samples MC36 and MC53 have not lead to the increase of water content in these two samples.

The metasomatic agent responsible for the light Li isotopic compositions in samples from both localities can be linked to recycled oceanic crust, which is capable of carrying components with negative δ^7Li values to the deep mantle during subduction.

References

Abdelfadil, K. M., Romer, R. L., Glodny, J., 2014. Mantle wedge metasomatism revealed by Li isotopes in orogenic lamprophyres. *Lithos*, *196*, 14-26.

Ackerman, L., ŠpaČek, P., Magna, T., Ulrych, J., Svojtka, M., Hegner, E., Balogh, K., 2013. Alkaline and carbonate-rich melt metasomatism and melting of subcontinental lithospheric mantle: evidence from mantle xenoliths, NE Bavaria, Bohemian Massif. *Journal of Petrology*, egt059.

Adam J., Green, T., 2001. Experimentally determined partition coefficients for minor and trace elements in peridotite minerals and carbonatitic melt, and their relevance to natural carbonatites. *European Journal of Mineralogy*, *13*(5), 815-827.

Agostini, S., Ryan, J. G., Tonarini, S., Innocenti, F., 2008. Drying and dying of a subducted slab: coupled Li and B isotope variations in Western Anatolia Cenozoic Volcanism. *Earth and Planetary Science Letters*, *272*(1), 139-147.

Aines, R. D., Rossman, G. R., 1984. Water in minerals? A peak in the infrared. *Journal of Geophysical Research: Solid Earth*, *89*(B6), 4059-4071.

Alard, O., Lorand, J. P., Reisberg, L., Bodinier, J. L., Dautria, J. M., O'reilly, S. Y., 2011. Volatile-rich metasomatism in Montferrier xenoliths (Southern France): implications for the abundances of chalcophile and highly siderophile elements in the subcontinental mantle. *Journal of Petrology*, *52*(10), 2009-2045.

Andrut, M., Wildner, M., Ingrin, J., Beran, A., 2007. Mechanisms of OH defect incorporation in naturally occurring, hydrothermally formed diopside and jadeite. *Physics and Chemistry of Minerals*, *34*(8), 543-549.

Arai, S., 1994. Characterization of spinel peridotites by olivine-spinel compositional relationships: review and interpretation. *Chemical geology*, *113*(3), 191-204.

Ardia, P., Hirschmann, M. M., Withers, A. C., Tenner, T. J., 2012. H_2O storage capacity of olivine at 5–8GPa and consequences for dehydration partial melting of the upper mantle. *Earth and Planetary Science Letters*, *345*, 104-116.

Asimow, P. D., Langmuir, C. H., 2003. The importance of water to oceanic mantle melting regimes. *Nature*, *421*(6925), 815-820.

Aubaud, C., Hauri, E. H., Hirschmann, M. M., 2004. Hydrogen partition coefficients between nominally anhydrous minerals and basaltic melts. *Geophysical Research Letters*, *31*(20).

Aubaud, C., Hirschmann, M. M., Withers, A. C., Hervig, R. L., 2008. Hydrogen partitioning between melt, clinopyroxene, and garnet at 3 GPa in a hydrous MORB with 6 wt.% H2O. *Contributions to Mineralogy and Petrology*, *156*(5), 607-625.

Aulbach, S., Rudnick, R. L., McDonough, W. F., 2008. Li-Sr-Nd isotope signatures of the plume and cratonic lithospheric mantle beneath the margin of the rifted Tanzanian craton (Labait). *Contributions to mineralogy and Petrology*, *155*(1), 79-92.

Aulbach, S., Rudnick, R. L., 2009. Origins of non-equilibrium lithium isotopic fractionation in xenolithic peridotite minerals: examples from Tanzania. *Chemical Geology*, *258*(1), 17-27.

Bai, Q., Kohlstedt, D. L., 1992. Substantial hydrogen solubility in olivine and implications for water storage in the mantle. *Nature*, *357*(6380), 672-674.

Bai, Q., Kohlstedt, D. L., 1993. Effects of chemical environment on the solubility and incorporation mechanism for hydrogen in olivine. *Physics and Chemistry of Minerals*, *19*(7), 460-471.

Balan, E., Blanchard, M., Yi, H., Ingrin, J., 2013. Theoretical study of OH-defects in pure enstatite. *Physics and Chemistry of Minerals*, *40*(1), 41-50.

Balan, E., Ingrin, J., Delattre, S., Kovács, I., Blanchard, M., 2011. Theoretical infrared spectrum of OH-defects in forsterite. *European Journal of Mineralogy*, *23*(3), 285-292.

Bali, E., Bolfan-Casanova, N., Koga, K. T., 2008. Pressure and temperature dependence of H solubility in forsterite: an implication to water activity in the Earth interior. *Earth and Planetary Science Letters*, *268*(3), 354-363.

Baptiste, V., Tommasi, A., Demouchy, S., 2012. Deformation and hydration of the lithospheric mantle beneath the Kaapvaal craton, South Africa. *Lithos*, *149*, 31-50.

Beck, P., Barrat, J. A., Chaussidon, M., Gillet, P., Bohn, M., 2004. Li isotopic variations in single pyroxenes from the Northwest Africa 480 shergottite (NWA 480): a record of degassing of Martian magmas?. *Geochimica et Cosmochimica Acta*, *68*(13), 2925-2933.

Behr, H. J., Engel, W., Franke, W., Giese, P., Weber, K., 1984. The Variscan belt in Central Europe: main structures, geodynamic implications, open questions. *Tectonophysics*, *109*(1), 15-40.

Bell, D. R., Rossman, G. R., 1992. Water in Earth's mantle: the role of nominally anhydrous minerals. *Science*, *255*(5050), 1391.

Bell, D. R., Ihinger, P. D., Rossman, G. R., 1995. Quantitative analysis of trace OH in garnet and pyroxenes. *American Mineralogist*, *80*(5-6), 465-474.

Bell, D. R., Rossman, G. R., Maldener, J., Endisch, D., Rauch, F., 2003. Hydroxide in olivine: a quantitative determination of the absolute amount and calibration of the IR spectrum. *Journal of Geophysical Research: Solid Earth*, *108*(B2).

Bell, D. R., Rossman, G. R., Moore, R. O., 2004. Abundance and partitioning of OH in a high-pressure magmatic system: megacrysts from the Monastery kimberlite, South Africa. *Journal of petrology*, *45*(8), 1539-1564.

Bell, D. R., Hervig, R. L., Buseck, P. R., Aulbach, S., 2009. Lithium isotope analysis of olivine by SIMS: Calibration of a matrix effect and application to magmatic phenocrysts. *Chemical Geology*, *258*(1), 5-16.

Berger, J., Féménias, O., Coussaert, N., Demaiffe, D., 2005. Magmatic garnet-bearing mafic xenoliths (Puy Beaunit, French Massif Central) PT path from crystallisation to exhumation. *European journal of mineralogy*, *17*(5), 687-701.

Berger, J., Féménias, O., Coussaert, N., Mercier, J. C. C., Demaiffe, D., 2007. Cumulating processes at the crust-mantle transition zone inferred from Permian mafic-ultramafic xenoliths (Puy Beaunit, France). *Contributions to Mineralogy and Petrology*, *153*(5), 557-575.

Berry, A. J., Hermann, J., O'Neill, H. S., Foran, G. J., 2005. Fingerprinting the water site in mantle olivine. *Geology*, *33*(11), 869-872.

Berry, A. J., Walker, A. M., Hermann, J., O'Neill, H. S. C., Foran, G. J., Gale, J. D., 2007a. Titanium substitution mechanisms in forsterite. *Chemical Geology*, *242*(1), 176-186.

Berry, A. J., O'Neill, H. S. C., Hermann, J., Scott, D. R., 2007b. The infrared signature of water associated with trivalent cations in olivine. *Earth and Planetary Science Letters*, *261*(1), 134-142.

Bizimis, M., Peslier, A. H., 2015. Water in Hawaiian garnet pyroxenites: Implications for water heterogeneity in the mantle. *Chemical Geology*, *397*, 61-75.

Blundy, J., Dalton, J., 2000. Experimental comparison of trace element partitioning between clinopyroxene and melt in carbonate and silicate systems, and implications for mantle metasomatism. *Contributions to Mineralogy and Petrology*, *139*(3), 356-371.

Bodinier, J. L., Vasseur, G., Vernieres, J., Dupuy, C., Fabries, J., 1990. Mechanisms of mantle metasomatism: geochemical evidence from the Lherz orogenic peridotite. *Journal of Petrology*, *31*(3),

597-628.

Bodinier, J. L., Godard, M. (2003). Orogenic, ophiolitic, and abyssal peridotites. *Treatise on geochemistry*, *2*, 568.

Bodnar, R. J., Azbej, T., Becker, S. P., Cannatelli, C., Fall, A., Severs, M. J., 2013. Whole Earth geohydrologic cycle, from the clouds to the core: The distribution of water in the dynamic Earth system. *Geological Society of America Special Papers*, *500*, 431-461.

Bolfan-Casanova, N., Keppler, H., Rubie, D. C., 2000. Water partitioning between nominally anhydrous minerals in the MgO–SiO 2–H 2 O system up to 24 GPa: implications for the distribution of water in the Earth's mantle. *Earth and Planetary Science Letters*, *182*(3), 209-221.

Bolfan-Casanova, N., 2005. Water in the Earth's mantle. *Mineralogical Magazine*, *69*(3), 229-257.

Bonadiman, C., Beccaluva, L., Coltorti, M., Siena, F., 2005. Kimberlite-like metasomatism and 'garnet signature'in spinel-peridotite xenoliths from Sal, Cape Verde Archipelago: relics of a subcontinental mantle domain within the Atlantic Oceanic lithosphere?. *Journal of Petrology*, *46*(12), 2465-2493.

Bonadiman, C., Coltorti, M., Beccaluva, L., Siena, F., 2008,. Mantle metasomatism vs. host magma interaction: the ongoing controversy. In *Geophysical Research Abstracts* (Vol. 10).

Bonadiman, C., Hao, Y., Coltorti, M., Dallai, L., Faccini, B., Huang, Y., Xia, Q., 2009. Water contents of pyroxenes in intraplate lithospheric mantle. *European Journal of Mineralogy*, *21*(3), 637-647.

Bouman, C., Elliott, T., Vroon, P. Z., 2004. Lithium inputs to subduction zones. *Chemical Geology*, *212*(1), 59-79.

Bouvier, A. S., Métrich, N., Deloule, E., 2010. Light elements, volatiles, and stable isotopes in basaltic melt inclusions from Grenada, Lesser Antilles: Inferences for magma genesis. *Geochemistry, Geophysics, Geosystems*, *11*(9).

Boyd, F. R., 1989. Compositional distinction between oceanic and cratonic lithosphere. *Earth and Planetary Science Letters*, *96*(1), 15-26.

Brenan, J. M., Neroda, E., Lundstrom, C. C., Shaw, H. F., Ryerson, F. J., Phinney, D. L., 1998a. Behaviour of boron, beryllium, and lithium during melting and crystallization: constraints from mineral-melt partitioning experiments. *Geochimica et Cosmochimica Acta*, *62*(12), 2129-2141.

Brenan, J. M., Ryerson, F. J., Shaw, H. F., 1998b. The role of aqueous fluids in the slab-to-mantle transfer of boron, beryllium, and lithium during subduction: experiments and models. *Geochimica et Cosmochimica Acta*, *62*(19), 3337-3347.

Brey, G. P., Köhler, T., 1990. Geothermobarometry in four-phase lherzolites II. New thermobarometers, and practical assessment of existing thermobarometers. *Journal of Petrology*, *31*(6), 1353-1378.

Bromiley, G. D., Keppler, H., McCammon, C., Bromiley, F. A., Jacobsen, S. D., 2004. Hydrogen solubility and speciation in natural, gem-quality chromian diopside. *American Mineralogist*, *89*(7), 941-949.

Brooker, R. A., James, R. H., Blundy, J. D., 2004. Trace elements and Li isotope systematics in Zabargad peridotites: evidence of ancient subduction processes in the Red Sea mantle. *Chemical Geology*, *212*(1), 179-204.

Carlson, R. W., Pearson, D. G., James, D. E., 2005. Physical, chemical, and chronological characteristics of continental mantle. *Reviews of Geophysics*, *43*(1).

Carpenter, R. L., Edgar, A. D., Thibault, Y., 2002. Origin of spongy textures in clinopyroxene and spinel from mantle xenoliths, Hessian Depression, Germany. *Mineralogy and Petrology*, *74*(2-4), 149-162.

Carpenter Woods, S., Mackwell, S., Dyar, A., 2000. Hydrogen in diopside: diffusion profiles. *American Mineralogist*, *85*(4), 480-487.

Chacko, T., Cole, D. R., Horita, J., 2001. Equilibrium oxygen, hydrogen and carbon isotope fractionation factors applicable to geologic systems. *Reviews in mineralogy and geochemistry*, *43*(1), 1-81.

Chan, L. H., Edmond, J. M., 1988. Variation of lithium isotope composition in the marine environment: a preliminary report. *Geochimica et Cosmochimica Acta*, *52*(6), 1711-1717.

Chan, L. H., Edmond, J. M., Thompson, G., Gillis, K., 1992. Lithium isotopic composition of submarine basalts: implications for the lithium cycle in the oceans. *Earth and Planetary Science Letters*, *108*(1), 151-160.

Chan, L. H., Gieskes, J. M., Chen-Feng, Y., Edmond, J. M., 1994. Lithium isotope geochemistry of sediments and hydrothermal fluids of the Guaymas Basin, Gulf of California. *Geochimica et Cosmochimica Acta*, *58*(20), 4443-4454.

Chan, L. H., Kastner, M., 2000. Lithium isotopic compositions of pore fluids and sediments in the

Chen, Y., Provost, A., Schiano, P., Cluzel, N., 2011. The rate of water loss from olivine-hosted melt inclusions. *Contributions to Mineralogy and Petrology*, *162*(3), 625-636.

Chen, Y., Provost, A., Schiano, P., Cluzel, N., 2013. Magma ascent rate and initial water concentration inferred from diffusive water loss from olivine-hosted melt inclusions. *Contributions to Mineralogy and Petrology*, *165*(3), 525-541.

Costa Rica subduction zone: implications for fluid processes and sediment contribution to the arc volcanoes. *Earth and Planetary Science Letters*, *183*(1), 275-290.

Chan, L. H., Leeman, W. P., You, C. F., 2002a. Lithium isotopic composition of Central American volcanic arc lavas: implications for modification of subarc mantle by slab-derived fluids: correction. *Chemical Geology*, *182*(2), 293-300.

Chan, L. H., Alt, J. C., Teagle, D. A., 2002b. Lithium and lithium isotope profiles through the upper oceanic crust: a study of seawater–basalt exchange at ODP Sites 504B and 896A. *Earth and Planetary Science Letters*, *201*(1), 187-201.

Chan, L. H., Frey, F. A., 2003. Lithium isotope geochemistry of the Hawaiian plume: results from the Hawaii Scientific Drilling Project and Koolau volcano. *Geochemistry, Geophysics, Geosystems*, *4*(3).

Chan, L. H., Leeman, W. P., Plank, T., 2006. Lithium isotopic composition of marine sediments. *Geochemistry, Geophysics, Geosystems*, *7*(6).

Chan, L. H., Lassiter, J. C., Hauri, E. H., Hart, S. R., Blusztajn, J., 2009. Lithium isotope systematics of lavas from the Cook–Austral Islands: constraints on the origin of HIMU mantle. *Earth and Planetary Science Letters*, *277*(3), 433-442.

Chazot, G., Menzies, M. A., Harte, B., 1996. Determination of partition coefficients between apatite, clinopyroxene, amphibole, and melt in natural spinel lherzolites from Yemen: implications for wet melting of the lithospheric mantle. *Geochimica et Cosmochimica Acta*, *60*(3), 423-437.

Chen, J., Inoue, T., Weidner, D. J., Wu, Y., Vaughan, M. T., 1998. Strength and water weakening of mantle minerals, olivine, wadsleyite and ringwoodite. *Geophysical Research Letters*, *25*(4), 575-578.

Coltorti, M., Bonadiman, C., Hinton, R. W., Siena, F., Upton, B. G. J., 1999. Carbonatite metasomatism of the oceanic upper mantle: evidence from clinopyroxenes and glasses in ultramafic xenoliths of Grande Comore, Indian Ocean. *Journal of Petrology*, *40*(1), 133-165.

Coltorti, M., Beccaluva, L., Bonadiman, C., Salvini, L., Siena, F., 2000. Glasses in mantle xenoliths as geochemical indicators of metasomatic agents. *Earth and planetary science letters*, *183*(1), 303-320.

Coltorti, M., Bonadiman, C., Faccini, B., Grégoire, M., O'Reilly, S. Y., Powell, W., 2007. Amphiboles from suprasubduction and intraplate lithospheric mantle. *Lithos*, *99*(1), 68-84.

Coogan, L. A., Kasemann, S. A., Chakraborty, S., 2005. Rates of hydrothermal cooling of new oceanic upper crust derived from lithium-geospeedometry. *Earth and Planetary Science Letters*, *240*(2), 415-424.

Cormier, L., Gaskell, P. H., Calas, G., Zhao, J., Soper, A. K. (1998). Environment around Li in the LiAlSiO 4 ionic conductor glass: A neutron-scattering and reverse Monte Carlo study. *Physical Review B*, *57*(14), R8067.

Costa, F., Chakraborty, S., 2008. The effect of water on Si and O diffusion rates in olivine and implications for transport properties and processes in the upper mantle. *Physics of the Earth and Planetary Interiors*, *166*(1), 11-29.

Dautria, J. M., Liotard, J. M., Bosch, D., Alard, O., 2010. 160Ma of sporadic basaltic activity on the Languedoc volcanic line (Southern France): A peculiar case of lithosphere–asthenosphere interplay. *Lithos*, *120*(1), 202-222.

Decitre, S., Deloule, E., Reisberg, L., James, R., Agrinier, P., Mével, C., 2002. Behavior of Li and its isotopes during serpentinization of oceanic peridotites. *Geochemistry, Geophysics, Geosystems*, *3*(1), 1-20.

De Hoog, J. C., Gall, L., Cornell, D. H., 2010. Trace-element geochemistry of mantle olivine and application to mantle petrogenesis and geothermobarometry. *Chemical Geology*, *270*(1), 196-215.

Dellinger, M., Gaillardet, J., Bouchez, J., Calmels, D., Louvat, P., Dosseto, A., Gorge, C., Alanoca, L., Maurice, L., 2015. Riverine Li isotope fractionation in the Amazon River basin controlled by the weathering regimes. *Geochimica et Cosmochimica Acta*, *164*, 71-93.

Deloule, E., Albarede, F., Sheppard, S. M., 1991. Hydrogen isotope heterogeneities in the mantle from ion probe analysis of amphiboles from ultramafic rocks. *Earth and Planetary Science Letters*, *105*(4), 543-553.

Deloule, E., Chaussidon, M., Allé, P., 1992. Instrumental limitations for isotope measurements with a Caméca® ims-3f ion microprobe: Example of H, B, S and Sr. *Chemical Geology: Isotope Geoscience section*, *101*(1), 187-192.

Demouchy, S., Mackwell, S., 2003. Water diffusion in synthetic iron-free forsterite. *Physics and Chemistry of Minerals*, *30*(8), 486-494.

Demouchy, S., Jacobsen, S. D., Gaillard, F., Stern, C. R., 2006. Rapid magma ascent recorded by water diffusion profiles in mantle olivine. *Geology*, *34*(6), 429-432.

Demouchy, S., Mackwell, S. J., Kohlstedt, D. L., 2007. Influence of hydrogen on Fe–Mg interdiffusion in (Mg, Fe) O and implications for Earth's lower mantle. *Contributions to Mineralogy and Petrology*, *154*(3), 279-289.

Demouchy, S., Ishikawa, A., Tommasi, A., Alard, O., Keshav, S., 2015. Characterization of hydration in the mantle lithosphere: Peridotite xenoliths from the Ontong Java Plateau as an example. *Lithos*, *212*, 189-201.

Demouchy, S., Bolfan-Casanova, N., 2016. Distribution and transport of hydrogen in the lithospheric mantle: A review. *Lithos*, *240*, 402-425.

Denis, C. M., Demouchy, S., Shaw, C. S., 2013. Evidence of dehydration in peridotites from Eifel Volcanic Field and estimates of the rate of magma ascent. *Journal of Volcanology and Geothermal Research*, *258*, 85-99.

Denis, C. M., Alard, O., Demouchy, S., 2015. Water content and hydrogen behaviour during metasomatism in the uppermost mantle beneath Ray Pic volcano (Massif Central, France). *Lithos*, *236*, 256-274.

Dixon, J. E., Leist, L., Langmuir, C., Schilling, J. G., 2002. Recycled dehydrated lithosphere observed in plume-influenced mid-ocean-ridge basalt. *Nature*, *420*(6914), 385-389.

Dixon, J. E., Dixon, T. H., Bell, D. R., Malservisi, R., 2004. Lateral variation in upper mantle viscosity: role of water. *Earth and Planetary Science Letters*, *222*(2), 451-467.

Dohmen, R., Kasemann, S. A., Coogan, L., & Chakraborty, S. (2010). Diffusion of Li in olivine. Part I: experimental observations and a multi species diffusion model. *Geochimica et Cosmochimica Acta*, *74*(1), 274-292.

Doucet, L. S., Peslier, A. H., Ionov, D. A., Brandon, A. D., Golovin, A. V., Goncharov, A. G., Ashchepkov, I. V., 2014. High water contents in the Siberian cratonic mantle linked to metasomatism: An FTIR study of Udachnaya peridotite xenoliths. *Geochimica et Cosmochimica Acta*, *137*, 159-187.

Downes, H., 1987. Relationship between geochemistry and textural type in spinel lherzolites, Massif Central and Languedoc, France. *Mantle Xenoliths*, *125*, 133.

Downes, H., Dupuy, C., 1987. Textural, isotopic and REE variations in spinel peridotite xenoliths, Massif Central, France. *Earth and Planetary Science Letters*, *82*(1), 121-135.

Downes, H., Reichow, M. K., Mason, P. R. D., Beard, A. D., Thirlwall, M. F., 2003. Mantle domains in the lithosphere beneath the French Massif Central: trace element and isotopic evidence from mantle clinopyroxenes. *Chemical Geology*, *200*(1), 71-87.

Downes, H., Macdonald, R. A. Y., Upton, B. G., Cox, K. G., Bodinier, J. L., Mason, P. R., James, D., Hill, P. G., Hearn, B. C., 2004. Ultramafic xenoliths from the Bearpaw Mountains, Montana, USA: Evidence for multiple metasomatic events in the lithospheric mantle beneath the Wyoming craton. *Journal of Petrology*, *45*(8), 1631-1662.

Downes, H., de Vries, C., Wittig, N., 2015. Hf–Zr anomalies in clinopyroxene from mantle xenoliths from France and Poland: implications for Lu–Hf dating of spinel peridotite lithospheric mantle. *International Journal of Earth Sciences*, *104*(1), 89-102.

Elliott, T., Jeffcoate, A., Bouman, C., 2004. The terrestrial Li isotope cycle: light-weight constraints on mantle convection. *Earth and Planetary Science Letters*, *220*(3), 231-245.

Elliott, T., Thomas, A., Jeffcoate, A., Niu, Y., 2006. Lithium isotope evidence for subduction-enriched mantle in the source of mid-ocean-ridge basalts. *Nature*, *443*(7111), 565-568.

Falus, G., Tommasi, A., Ingrin, J., Szabó, C., 2008. Deformation and seismic anisotropy of the lithospheric mantle in the southeastern Carpathians inferred from the study of mantle xenoliths. *Earth and Planetary Science Letters*, *272*(1), 50-64.

Faure, M., Lardeaux, J. M., Ledru, P., 2009. A review of the pre-Permian geology of the Variscan French Massif Central. *Comptes Rendus Geoscience*, *341*(2), 202-213.

Féménias, O., Coussaert, N., Bingen, B., Whitehouse, M., Mercier, J. C. C., Demaiffe, D., 2003. A Permian underplating event in late-to post-orogenic tectonic setting. Evidence from the mafic–ultramafic layered xenoliths from Beaunit (French Massif Central). *Chemical Geology*, *199*(3), 293-315.

Féménias, O., Ohnenstetter, D., Coussaert, N., Berger, J., Demaiffe, D., 2005. Origin of micro-layering in a deep magma chamber: Evidence from two ultramafic–mafic layered xenoliths from Puy Beaunit (French Massif Central). *Lithos*, *83*(3), 347-370.

Féménias, O., Ohnenstetter, D., Coussaert, N., Berger, J., Demaiffe, D., 2005. Origin of micro-layering in a deep magma chamber: Evidence from two ultramafic–mafic layered xenoliths from Puy Beaunit (French Massif Central). *Lithos*, *83*(3), 347-370.

Férot, A., Bolfan-Casanova, N., 2012. Water storage capacity in olivine and pyroxene to 14GPa: Implications for the water content of the Earth's upper mantle and nature of seismic discontinuities. *Earth and Planetary Science Letters*, *349*, 218-230.

Fichtner, A., Villaseñor, A., 2015. Crust and upper mantle of the western Mediterranean–Constraints from full-waveform inversion. *Earth and Planetary Science Letters*, *428*, 52-62.

Fitzsimons, I. C. W., Harte, B., Clark, R. M., 2000. SIMS stable isotope measurement: counting statistics and analytical precision. *Mineralogical Magazine*, *64*(1), 59-83.

Flesch, G. D., Anderson, A. R., Svec, H. J., 1973. A secondary isotopic standard for 6 Li/7 Li determinations. *International Journal of Mass Spectrometry and Ion Physics*, *12*(3), 265-272.

Foley, S. F., Prelevic, D., Rehfeldt, T., Jacob, D. E., 2013. Minor and trace elements in olivines as probes into early igneous and mantle melting processes. *Earth and Planetary Science Letters*, *363*, 181-191.

France, L., Chazot, G., Kornprobst, J., Dallai, L., Vannucci, R., Grégoire, M., Bertrand, H., Boivin, P., 2015. Mantle refertilization and magmatism in old orogenic regions: The role of late-orogenic pyroxenites. *Lithos*, *232*, 49-75.

Frey, F. A., Green, D. H., 1974. The mineralogy, geochemistry and origin of Iherzolite inclusions in Victorian basanites. *Geochimica et cosmochimica acta*, *38*(7), 1023-1059.

Frey, F. A., Prinz, M., 1978. Ultramafic inclusions from San Carlos, Arizona: petrologic and geochemical data bearing on their petrogenesis. *Earth and Planetary Science Letters*, *38*(1), 129-176.

Füri, E., Deloule, E., Gurenko, A., Marty, B., 2014. New evidence for chondritic lunar water from combined D/H and noble gas analyses of single Apollo 17 volcanic glasses. *Icarus*, *229*, 109-120.

Gaetani, G. A., Grove, T. L., 1998. The influence of water on melting of mantle peridotite. *Contributions to Mineralogy and Petrology*, *131*(4), 323-346.

Gallagher, K., Elliott, T., 2009. Fractionation of lithium isotopes in magmatic systems as a natural consequence of cooling. *Earth and Planetary Science Letters*, *278*(3), 286-296.

Gao, Y., Snow, J. E., Casey, J. F., Yu, J., 2011. Cooling-induced fractionation of mantle Li isotopes from the ultraslow-spreading Gakkel Ridge. *Earth and Planetary Science Letters*, *301*(1), 231-240.

Goes, S., Spakman, W., Bijwaard, H., 1999. A lower mantle source for central European volcanism. *Science*, *286*(5446), 1928-1931.

Gose, J., Schmädicke, E., Beran, A., 2009. Water in enstatite from Mid-Atlantic Ridge peridotite: Evidence for the water content of suboceanic mantle?. *Geology*, *37*(6), 543-546.

Gose, J., Schmädicke, E., Stalder, R., 2011. Water in mantle orthopyroxene–no visible change in defect water during serpentinization. *European Journal of Mineralogy*, *23*(4), 529-536.

Gorring, M. L., Kay, S. M., 2000. Carbonatite metasomatized peridotite xenoliths from southern Patagonia: implications for lithospheric processes and Neogene plateau magmatism. *Contributions to Mineralogy and Petrology*, *140*(1), 55-72.

Granet, M., Wilson, M., Achauer, U., 1995. Imaging a mantle plume beneath the French Massif Central. *Earth and Planetary Science Letters*, *136*(3), 281-296.

Grant, K. J., Kohn, S. C., Brooker, R. A., 2006. Solubility and partitioning of water in synthetic forsterite and enstatite in the system MgO–SiO2–H2O±Al2O3. *Contributions to Mineralogy and Petrology*, *151*(6), 651-664.

Grant, K. J., Kohn, S. C., Brooker, R. A., 2007a. The partitioning of water between olivine, orthopyroxene and melt synthesised in the system albite–forsterite–H 2 O. *Earth and Planetary Science Letters*, *260*(1), 227-241.

Grant, K., Ingrin, J., Lorand, J. P., Dumas, P., 2007b. Water partitioning between mantle minerals from peridotite xenoliths. *Contributions to Mineralogy and Petrology*, *154*(1), 15-34.

Grant, K. J., Wood, B. J. (2010). Experimental study of the incorporation of Li, Sc, Al and other trace elements into olivine. *Geochimica et Cosmochimica Acta*, *74*(8), 2412-2428.

Green, D. H., Hibberson, W. O., Kovács, I., Rosenthal, A., 2010. Water and its influence on the lithosphere-asthenosphere boundary. *Nature*, *467*(7314), 448-451.

Green, D. H., Hibberson, W. O., Rosenthal, A., Kovács, I., Yaxley, G. M., Falloon, T. J., Brink, F., 2014. Experimental study of the influence of water on melting and phase assemblages in the upper mantle. *Journal of Petrology*, *55*(10), 2067-2096.

Grégoire, M., Langlade, J. A., Delpech, G., Dantas, C., Ceuleneer, G., 2009. Nature and evolution of the lithospheric mantle beneath the passive margin of East Oman: evidence from mantle xenoliths sampled by Cenozoic alkaline lavas. *Lithos*, *112*(3), 203-216.

Guzmics, T., Kodolányi, J., Kovács, I., Szabó, C., Bali, E., Ntaflos, T., 2008. Primary carbonatite melt inclusions in apatite and in K-feldspar of clinopyroxene-rich mantle xenoliths hosted in lamprophyre dikes (Hungary). *Mineralogy and Petrology*, *94*(3-4), 225-242.

Halama, R., McDonough, W. F., Rudnick, R. L., Bell, K., 2008. Tracking the lithium isotopic evolution of the mantle using carbonatites. *Earth and Planetary Science Letters*, *265*(3), 726-742.

Hao, Y., Xia, Q., Liu, S., Feng, M., Zhang, Y., 2012. Recognizing juvenile and relict lithospheric mantle beneath the North China Craton: combined analysis of H 2 O, major and trace elements and Sr–Nd isotope compositions of clinopyroxenes. *Lithos*, *149*, 136-145.

Hao, Y., Xia, Q., Li, Q., Chen, H., Feng, M., 2014. Partial melting control of water contents in the Cenozoic lithospheric mantle of the Cathaysia block of South China. *Chemical Geology*, *380*, 7-19.

Hao, Y. T., Xia, Q. K., Jia, Z. B., Zhao, Q. C., Li, P., Feng, M., Liu, S. C., 2016. Regional heterogeneity in the water content of the Cenozoic lithospheric mantle of Eastern China. *Journal of Geophysical Research: Solid Earth*.

Hart, S. R., Dunn, T., 1993. Experimental cpx/melt partitioning of 24 trace elements. *Contributions to Mineralogy and Petrology*, *113*(1), 1-8.

Harvey, J., Gannoun, A., Burton, K. W., Schiano, P., Rogers, N. W., Alard, O., 2010. Unravelling the effects of melt depletion and secondary infiltration on mantle Re–Os isotopes beneath the French Massif Central. *Geochimica et Cosmochimica Acta*, *74*(1), 293-320.

Hauri, E. H., Shaw, A. M., Wang, J., Dixon, J. E., King, P. L., Mandeville, C., 2006a. Matrix effects in hydrogen isotope analysis of silicate glasses by SIMS. *Chemical geology*, *235*(3), 352-365.

Hauri, E. H., Gaetani, G. A., Green, T. H., 2006b. Partitioning of water during melting of the Earth's upper mantle at H 2 O-undersaturated conditions. *Earth and Planetary Science Letters*, *248*(3), 715-734.

Hellebrand, E., Snow, J. E., Dick, H. J., Hofmann, A. W., 2001. Coupled major and trace elements as indicators of the extent of melting in mid-ocean-ridge peridotites. *Nature*, *410*(6829), 677-681.

Herzberg, C., 2004. Geodynamic information in peridotite petrology. *Journal of Petrology*, *45*(12), 2507-2530.

Hercule, S., Ingrin, J., 1999. Hydrogen in diopside: Diffusion, kinetics of extraction-incorporation, and solubility. *American Mineralogist*, *84*(10), 1577-1587.

Hier-Majumder, S., Mei, S., Kohlstedt, D. L., 2005a. Water weakening of clinopyroxenite in diffusion creep. *Journal of Geophysical Research: Solid Earth*, *110*(B7).
Hier-Majumder, S., Anderson, I. M., Kohlstedt, D. L., 2005b. Influence of protons on Fe-Mg interdiffusion in olivine. *Journal of Geophysical Research: Solid Earth*, *110*(B2).
Hinton, R. W., 1995. Ion microprobe analysis in geology. In *Microprobe techniques in the Earth Sciences* (pp. 235-289). Springer US.
Hirschmann, M. M., 2006. Water, melting, and the deep Earth H2O cycle. *Annu. Rev. Earth Planet. Sci.*, *34*, 629-653.
Hirschmann, M. M., Tenner, T., Aubaud, C., Withers, A. C., 2009. Dehydration melting of nominally anhydrous mantle: The primacy of partitioning. *Physics of the Earth and Planetary Interiors*, *176*(1), 54-68.
Hirth, G., Kohlstedt, D. L., 1996. Water in the oceanic upper mantle: implications for rheology, melt extraction and the evolution of the lithosphere. *Earth and Planetary Science Letters*, *144*(1), 93-108.
Hoernle, K. A. J., Zhang, Y. S., Graham, D., 1995. Seismic and geochemical evidence for large-scale mantle upwelling beneath the eastern Atlantic and western and central Europe.
Huang, X., Xu, Y., Karato, S. I., 2005. Water content in the transition zone from electrical conductivity of wadsleyite and ringwoodite. *Nature*, *434*(7034), 746-749.
Huh, Y., Chan, L. H., Zhang, L., Edmond, J. M. (1998). Lithium and its isotopes in major world rivers: implications for weathering and the oceanic budget. *Geochimica et Cosmochimica Acta*, *62*(12), 2039-2051.
Huh, Y., Chan, L. H., Edmond, J. M., 2001. Lithium isotopes as a probe of weathering processes: Orinoco River. *Earth and Planetary Science Letters*, *194*(1), 189-199.
Hui, H., Peslier, A. H., Rudnick, R. L., Simonetti, A., Neal, C. R., 2015. Plume-cratonic lithosphere interaction recorded by water and other trace elements in peridotite xenoliths from the Labait volcano, Tanzania. *Geochemistry, Geophysics, Geosystems*, *16*(6), 1687-1710.
Ingrin, J., Latrous, K., Doukhan, J. C., Doukhan, N., 1989. Water in diopside: an electron microscopy and infrared spectroscopy study. *European Journal of Mineralogy*, 327-342.
Ingrin, J., Hercule, S., Charton, T., 1995. Diffusion of hydrogen in diopside: results of dehydration experiments. *Journal of Geophysical Research: Solid Earth*, *100*(B8), 15489-15499.
Ingrin, J., Skogby, H., 2000. Hydrogen in nominally anhydrous upper-mantle minerals concentration levels and implications. *European Journal of Mineralogy*, *12*(3), 543-570.
Ingrin, J., Blanchard, M., 2006. Diffusion of hydrogen in minerals. *Reviews in mineralogy and geochemistry*, *62*(1), 291-320.
Ingrin, J., Liu, J., Depecker, C., Kohn, S. C., Balan, E., Grant, K. J., 2013. Low-temperature evolution of OH bands in synthetic forsterite, implication for the nature of H defects at high pressure. *Physics and Chemistry of Minerals*, *40*(6), 499-510.
Inoue, T., Wada, T., Sasaki, R., Yurimoto, H., 2010. Water partitioning in the Earth's mantle. *Physics of the Earth and Planetary Interiors*, *183*(1), 245-251.
Ionov, D. A., Dupuy, C., O'Reilly, S. Y., Kopylova, M. G., Genshaft, Y. S., 1993. Carbonated peridotite xenoliths from Spitsbergen: implications for trace element signature of mantle carbonate metasomatism. *Earth and Planetary Science Letters*, *119*(3), 283-297.
Ionov, D. A., O'Reilly, S. Y., Ashchepkov, I. V., 1995. Feldspar-bearing lherzolite xenoliths in alkali basalts from Hamar-Daban, southern Baikal region, Russia. *Contributions to Mineralogy and Petrology*, *122*(1-2), 174-190.

Ionov, D. A., Griffin, W. L., O'Reilly, S. Y., 1997. Volatile-bearing minerals and lithophile trace elements in the upper mantle. *Chemical Geology*, *141*(3), 153-184.

Ionov, D. A., Bodinier, J. L., Mukasa, S. B., Zanetti, A., 2002. Mechanisms and sources of mantle metasomatism: major and trace element compositions of peridotite xenoliths from Spitsbergen in the context of numerical modelling. *Journal of Petrology*, *43*(12), 2219-2259.

Ionov, D. A., Seitz, H. M., 2008. Lithium abundances and isotopic compositions in mantle xenoliths from subduction and intra-plate settings: mantle sources vs. eruption histories. *Earth and Planetary Science Letters*, *266*(3), 316-331.

Jagoutz, E., Palme, H., Baddenhausen, H., Blum, K., Cendales, M., Dreibus, G., Spettel, B., Lorenz, V., Wänke, H., 1979. The abundances of major, minor and trace elements in the earth's mantle as derived from primitive ultramafic nodules. In *Lunar and Planetary Science Conference Proceedings* (Vol. 10, pp. 2031-2050).

James, R. H., Palmer, M. R., 2000. The lithium isotope composition of international rock standards. *Chemical Geology*, *166*(3), 319-326.

Jamtveit, B., Brooker, R., Brooks, K., Larsen, L. M., Pedersen, T., 2001. The water content of olivines from the North Atlantic Volcanic Province. *Earth and Planetary Science Letters*, *186*(3), 401-415.

Jeffcoate, A. B., Elliott, T., Kasemann, S. A., Ionov, D., Cooper, K., Brooker, R., 2007. Li isotope fractionation in peridotites and mafic melts. *Geochimica et Cosmochimica Acta*, *71*(1), 202-218.

Johnson, K. T., 1998. Experimental determination of partition coefficients for rare earth and high-field-strength elements between clinopyroxene, garnet, and basaltic melt at high pressures. *Contributions to Mineralogy and Petrology*, *133*(1-2), 60-68.

Jung, H., Karato, S. I., 2001. Water-induced fabric transitions in olivine. *Science*, *293*(5534), 1460-1463.

Juvigne, E. (1992). Studies on the age of 2 volcanic lacustrine craters of Auvergne (France). *COMPTES RENDUS DE L ACADEMIE DES SCIENCES SERIE II*, *314*(4), 401-404.

Kaeser, B., Kalt, A., Ludwig, T., 2007. Li, Be, and B abundances in minerals of peridotite xenoliths from Marsabit (Kenya): Disequilibrium processes and implications for subduction zone signatures. *Geochemistry, Geophysics, Geosystems*, *8*(9).

Kaliwoda, M., Ludwig, T., Altherr, R., 2008. A new SIMS study of Li, Be, B and δ 7 Li in mantle xenoliths from Harrat Uwayrid (Saudi Arabia). *Lithos*, *106*(3), 261-279.

Karato, S. I., Paterson, M. S., FitzGerald, J. D., 1986. Rheology of synthetic olivine aggregates: influence of grain size and water. *Journal of Geophysical Research: Solid Earth*, *91*(B8), 8151-8176.

Karato, S. I., 1990. The role of hydrogen in the electrical conductivity of the upper mantle. *Nature*, *347*, 272.

Karato, S. I., Wu, P., 1993. Rheology of the upper mantle- A synthesis. *Science*, *260*(5109), 771-778.

Karato, S. I., Jung, H., 1998. Water, partial melting and the origin of the seismic low velocity and high attenuation zone in the upper mantle. *Earth and Planetary Science Letters*, *157*(3), 193-207.

Karato, S. I., Jung, H., Katayama, I., Skemer, P., 2008. Geodynamic significance of seismic anisotropy of the upper mantle: new insights from laboratory studies. *Annu. Rev. Earth Planet. Sci.*, *36*, 59-95.

Karato, S. I., 2010a. Rheology of the Earth's mantle: A historical review. *Gondwana Research*, *18*(1), 17-45.

Karato, S. I., 2010b. Rheology of the deep upper mantle and its implications for the preservation of the continental roots: A review. *Tectonophysics*, *481*(1), 82-98.

Karato, S. I., Olugboji, T., Park, J., 2015. Mechanisms and geologic significance of the mid-lithosphere discontinuity in the continents. *Nature Geoscience*, *8*(7), 509-514.

Kelley, K. A., Plank, T., Newman, S., Stolper, E. M., Grove, T. L., Parman, S., Hauri, E. H., 2010. Mantle melting as a function of water content beneath the Mariana Arc. *Journal of Petrology*, egq036.

Kil, Y., 2010. Lithium isotopic disequilibrium of minerals in the spinel lherzolite xenoliths from Boeun, Korea. *Journal of Geochemical Exploration*, *107*(1), 56-62.

Klemme, S., Van der Laan, S. R., Foley, S. F., Günther, D., 1995. Experimentally determined trace and minor element partitioning between clinopyroxene and carbonatite melt under upper mantle conditions. *Earth and Planetary Science Letters*, *133*(3), 439-448.

Kobayashi, K., Tanaka, R., Moriguti, T., Shimizu, K., Nakamura, E., 2004. Lithium, boron, and lead isotope systematics of glass inclusions in olivines from Hawaiian lavas: evidence for recycled components in the Hawaiian plume. *Chemical Geology*, *212*(1), 143-161.

Koga, K., Hauri, E., Hirschmann, M., Bell, D., 2003. Hydrogen concentration analyses using SIMS and FTIR: comparison and calibration for nominally anhydrous minerals. *Geochemistry, Geophysics, Geosystems*, *4*(2).

Köhler, T. P., Brey, G., 1990. Calcium exchange between olivine and clinopyroxene calibrated as a geothermobarometer for natural peridotites from 2 to 60 kb with applications. *Geochimica et Cosmochimica Acta*, *54*(9), 2375-2388.

Kohlstedt, D. L., Keppler, H., Rubie, D. C., 1996. Solubility of water in the α, β and γ phases of (Mg, Fe) 2SiO4. *Contributions to Mineralogy and Petrology*, *123*(4), 345-357.

Kohlstedt, D. L., Mackwell, S. J., 1998. Diffusion of hydrogen and intrinsic point defects in olivine. *Zeitschrift für physikalische Chemie*, *207*(Part_1_2), 147-162.

Košler, J., Magna, T., Mlčoch, B., Mixa, P., Nývlt, D., Holub, F. V., 2009. Combined Sr, Nd, Pb and Li isotope geochemistry of alkaline lavas from northern James Ross Island (Antarctic Peninsula) and implications for back-arc magma formation. *Chemical Geology*, *258*(3), 207-218.

Kovács, I., O'Neill, H. S. C., Hermann, J., Hauri, H., 2010. Site-specific infrared OH absorption coefficients for water substitution into olivine. *American Mineralogist*, *95*(2-3), 292-299.

Lardeaux, J. M., Ledru, P., Daniel, I., Duchene, S., 2001. The Variscan French Massif Central—a new addition to the ultra-high pressure metamorphic 'club': exhumation processes and geodynamic consequences. *Tectonophysics*, *332*(1), 143-167.

LaTourrette, T. Z., Burnett, D. S., 1992. Experimental determination of U and Th partitioning between clinopyroxene and natural and synthetic basaltic liquid. *Earth and Planetary Science Letters*, *110*(1), 227-244.

LaTourrette, T., Hervig, R. L., Holloway, J. R., 1995. Trace element partitioning between amphibole, phlogopite, and basanite melt. *Earth and Planetary Science Letters*, *135*(1), 13-30.

Leake, B. E., Woolley, A. R., Arps, C. E., Birch, W. D., Gilbert, M. C., Grice, J. D., ..., Linthout, K., 1997. Nomenclature of amphiboles; report of the subcommittee on amphiboles of the International Mineralogical Association, Commission on New Minerals and Mineral Names. *The Canadian Mineralogist*, *35*(1), 219-246.

Lee, C. T., Rudnick, R. L., 1999. Compositionally stratified cratonic lithosphere: petrology and geochemistry of peridotite xenoliths from the Labait volcano, Tanzania. In *Proceedings of the VIIth International Kimberlite Conference* (Vol. 1, pp. 503-521).

Lemaire, C., Kohn, S. C., Brooker, R. A., 2004. The effect of silica activity on the incorporation mechanisms of water in synthetic forsterite: a polarised infrared spectroscopic study. *Contributions to Mineralogy and Petrology*, *147*(1), 48-57.

Lenoir, X., Garrido, C. J., Bodinier, J. L., Dautria, J. M., 2000. Contrasting lithospheric mantle domains beneath the Massif Central (France) revealed by geochemistry of peridotite xenoliths. *Earth and Planetary Science Letters*, *181*(3), 359-375.

Le Roux, V., Bodinier, J. L., Tommasi, A., Alard, O., Dautria, J. M., Vauchez, A., Riches, A. J. V., 2007. The Lherz spinel lherzolite: refertilized rather than pristine mantle. *Earth and Planetary Science Letters*, *259*(3), 599-612.

Li, P., Xia, Q, K., Deloule, E., 2012. Anomalous lithium isotopic compositions of the Cenozoic lithospheric mantle beneath Penglai, Shandong Province: the ion probe analyses of peridotite xenoliths. *Geological Journal of China Universities*, *18*(1), 62-73.

Li, Z. X. A., Lee, C. T. A., Peslier, A. H., Lenardic, A., Mackwell, S. J., 2008. Water contents in mantle xenoliths from the Colorado Plateau and vicinity: Implications for the mantle rheology and hydration-induced thinning of continental lithosphere. *Journal of Geophysical Research: Solid Earth*, *113*(B9).

Libowitzky, E., Rossman, G. R., 1997. An IR absorption calibration for water in minerals. *American Mineralogist*, *82*(11-12), 1111-1115.

Liu, X. M., Rudnick, R. L., McDonough, W. F., Cummings, M. L., 2013. Influence of chemical weathering on the composition of the continental crust: insights from Li and Nd isotopes in bauxite profiles developed on Columbia River Basalts. *Geochimica et Cosmochimica Acta*, *115*, 73-91.

Lorand, J. P., Alard, O., 2001. Platinum-group element abundances in the upper mantle: new constraints from in situ and whole-rock analyses of Massif Central xenoliths (France). *Geochimica et Cosmochimica Acta*, *65*(16), 2789-2806.

Lorand, J. P., Alard, O., Luguet, A., Keays, R. R., 2003. Sulfur and selenium systematics of the subcontinental lithospheric mantle: inferences from the Massif Central xenolith suite (France). *Geochimica et Cosmochimica Acta*, *67*(21), 4137-4151.

Lundstrom, C. C., Chaussidon, M., Hsui, A. T., Kelemen, P., Zimmerman, M., 2005. Observations of Li isotopic variations in the Trinity Ophiolite: evidence for isotopic fractionation by diffusion during mantle melting. *Geochimica et Cosmochimica Acta*, *69*(3), 735-751.

Mackwell, S. J., Kohlstedt, D. L., Paterson, M. S., 1985. The role of water in the deformation of olivine single crystals. *Journal of Geophysical Research: Solid Earth*, *90*(B13), 11319-11333.

Mackwell, S. J., Kohlstedt, D. L., 1990. Diffusion of hydrogen in olivine: implications for water in the mantle. *Journal of Geophysical Research: Solid Earth*, *95*(B4), 5079-5088.

Magna, T., Wiechert, U., Halliday, A. N., 2006. New constraints on the lithium isotope compositions of the Moon and terrestrial planets. *Earth and Planetary Science Letters*, *243*(3), 336-353.

Magna, T., Ionov, D. A., Oberli, F., Wiechert, U., 2008. Links between mantle metasomatism and lithium isotopes: Evidence from glass-bearing and cryptically metasomatized xenoliths from Mongolia. *Earth and Planetary Science Letters*, *276*(1), 214-222.

Manthilake, M. A. G. M., Miyajima, N., Heidelbach, F., Soustelle, V., Frost, D. J., 2013. The effect of aluminum and water on the development of deformation fabrics of orthopyroxene. *Contributions to Mineralogy and Petrology*, *165*(3), 495-505.

Marschall, H. R., von Strandmann, P. A. P., Seitz, H. M., Elliott, T., Niu, Y., 2007. The lithium isotopic composition of orogenic eclogites and deep subducted slabs. *Earth and Planetary Science*

Letters, *262*(3), 563-580.
Marschall, H. R., Altherr, R., Gméling, K., Kasztovszky, Z., 2009. Lithium, boron and chlorine as tracers for metasomatism in high-pressure metamorphic rocks: a case study from Syros (Greece). *Mineralogy and Petrology*, *95*(3-4), 291-302.
Marty, B., 2012. The origins and concentrations of water, carbon, nitrogen and noble gases on Earth. *Earth and Planetary Science Letters*, *313*, 56-66.
Matsyuk, S. S., Langer, K., 2004. Hydroxyl in olivines from mantle xenoliths in kimberlites of the Siberian platform. *Contributions to Mineralogy and Petrology*, *147*(4), 413-437.
Matte, P., 1986. Tectonics and plate tectonics model for the Variscan belt of Europe. *Tectonophysics*, *126*(2), 329-374.
Matte, P., 1991. Accretionary history and crustal evolution of the Variscan belt in Western Europe. *Tectonophysics*, *196*(3), 309-337.
Matveev, S., O'neill, H. S. C., Ballhaus, C., Taylor, W. R., Green, D. H., 2001. Effect of silica activity on OH– IR spectra of olivine: implications for low-aSiO2 mantle metasomatism. *Journal of Petrology*, *42*(4), 721-729.
Matveev, S., Stachel, T., 2007. FTIR spectroscopy of OH in olivine: a new tool in kimberlite exploration. *Geochimica et Cosmochimica Acta*, *71*(22), 5528-5543.
McDonough, W. F., Frey, F. A., 1989. Rare earth elements in upper mantle rocks. *Reviews in Mineralogy and Geochemistry*, *21*(1), 100-145.
McDonough, W. F., Sun, S. S., 1995. The composition of the Earth. *Chemical geology*, *120*(3), 223-253.
Mei, S., Kohlstedt, D. L., 2000a. Influence of water on plastic deformation of olivine aggregates: 1. Diffusion creep regime. *Journal of Geophysical Research: Solid Earth*, *105*(B9), 21457-21469.
Mei, S., Kohlstedt, D. L., 2000b. Influence of water on plastic deformation of olivine aggregates: 2. Dislocation creep regime. *Journal of Geophysical Research: Solid Earth*, *105*(B9), 21471-21481.
Menzies, M. A. (1983). Mantle ultramafic xenoliths in alkaline magmas: evidence for mantle heterogeneity modified by magmatic activity. *Continental basalts and mantle xenoliths*, 92-110.
Menzies, M., Hawkesworth, C., 1987. Mantle metasomatism.
Mercier, J. C., Nicolas, A., 1975. Textures and fabrics of upper-mantle peridotites as illustrated by xenoliths from basalts. *Journal of Petrology*, *16*(2), 454-487.
Merle, O., Michon, L., Camus, G., de Goer, A., 1998. L'extension oligocène sur la transversale septentrionale du rift du Massif Central. *Bulletin de la Société Géologique de France*, *169*(5), 615-626.
Michael, P. J., 1988. The concentration, behavior and storage of H 2 O in the suboceanic upper mantle: Implications for mantle metasomatism. *Geochimica et Cosmochimica Acta*, *52*(2), 555-566.
Michael, P., 1995. Regionally distinctive sources of depleted MORB: evidence from trace elements and H_2O. *Earth and Planetary Science Letters*, *131*(3), 301-320.
Michon, L., Merle, O., 2001. The evolution of the Massif Central Rift; spatio-temporal distribution of the volcanism. *Bulletin de la Société géologique de France*, *172*(2), 201-211.
Mierdel, K., Keppler, H., 2004. The temperature dependence of water solubility in enstatite. *Contributions to Mineralogy and Petrology*, *148*(3), 305-311.
Mierdel, K., Keppler, H., Smyth, J. R., Langenhorst, F., 2007. Water solubility in aluminous orthopyroxene and the origin of Earth's asthenosphere. *Science*, *315*(5810), 364-368.
Miller, G. H., Rossman, G. R., Harlow, G. E., 1987. The natural occurrence of hydroxide in olivine. *Physics and chemistry of minerals*, *14*(5), 461-472.

Millot, R., Vigier, N., Gaillardet, J., 2010. Behaviour of lithium and its isotopes during weathering in the Mackenzie Basin, Canada. *Geochimica et Cosmochimica Acta*, *74*(14), 3897-3912.
Moriguti, T., Nakamura, E., 1998a. High-yield lithium separation and the precise isotopic analysis for natural rock and aqueous samples. *Chemical Geology*, *145*(1), 91-104.
Moriguti, T., Nakamura, E., 1998b. Across-arc variation of Li isotopes in lavas and implications for crust/mantle recycling at subduction zones. *Earth and planetary science letters*, *163*(1), 167-174.
Mosenfelder, J. L., Deligne, N. I., Asimow, P. D., Rossman, G. R., 2006a. Hydrogen incorporation in olivine from 2–12 GPa. *American Mineralogist*, *91*(2-3), 285-294.
Mosenfelder, J. L., Sharp, T. G., Asimow, P. D., Rossman, G. R., 2006. Hydrogen incorporation in natural mantle olivines. *Earth's Deep Water Cycle*, 45-56.
Mosenfelder, J. L., Rossman, G. R., 2013a. Analysis of hydrogen and fluorine in pyroxenes: I. Orthopyroxene. *American Mineralogist*, *98*(5-6), 1026-1041.
Mosenfelder, J. L., Rossman, G. R., 2013. Analysis of hydrogen and fluorine in pyroxenes: II. Clinopyroxene. *American Mineralogist*, *98*(5-6), 1042-1054.
Mottl, M. J., Glazer, B. T., Kaiser, R. I., Meech, K. J., 2007. Water and astrobiology. *Chemie der Erde-Geochemistry*, *67*(4), 253-282.
Mundl, A., Ntaflos, T., Ackerman, L., Bizimis, M., Bjerg, E. A., Wegner, W., Hauzenberger, C. A., 2015. Geochemical and Os–Hf–Nd–Sr Isotopic Characterization of North Patagonian Mantle Xenoliths: Implications for Extensive Melt Extraction and Percolation Processes. *Journal of Petrology*, egv048.
Nance, R. D., Gutiérrez-Alonso, G., Keppie, J. D., Linnemann, U., Murphy, J. B., Quesada, C., Strachan, R. A., Woodcock, N. H., 2010. Evolution of the Rheic ocean. *Gondwana Research*, *17*(2), 194-222.
Navon, O., Stolper, E., 1987. Geochemical consequences of melt percolation: the upper mantle as a chromatographic column. *The Journal of Geology*, 285-307.
Nestola, F., Smyth, J. R., 2016. Diamonds and water in the deep Earth: a new scenario. *International Geology Review*, *58*(3), 263-276.
Nicolas, A., Lucazeau, F., Bayer, R., 1987. Peridotite xenoliths in Massif Central basalts, France: textural and geophysical evidence for asthenospheric diapirism. *Mantle xenoliths*, 563-574.
Nishi, M., Irifune, T., Tsuchiya, J., Tange, Y., Nishihara, Y., Fujino, K., Higo, Y., 2014. Stability of hydrous silicate at high pressures and water transport to the deep lower mantle. *Nature Geoscience*, *7*(3), 224-227.
Nishio, Y., Nakai, S. I., Yamamoto, J., Sumino, H., Matsumoto, T., Prikhod'ko, V. S., Arai, S., 2004. Lithium isotopic systematics of the mantle-derived ultramafic xenoliths: implications for EM1 origin. *Earth and Planetary Science Letters*, *217*(3), 245-261.
Nishio, Y., Nakai, S. I., Kogiso, T., Barsczus, H. G., 2005. Lithium, strontium, and neodymium isotopic compositions of oceanic island basalts in the Polynesian region: constraints on a Polynesian HIMU origin. *Geochemical Journal*, *39*(1), 91-103.
Nixon, P. H., 1987. Mantle xenoliths.
Norman, M. D., 1998. Melting and metasomatism in the continental lithosphere: laser ablation ICPMS analysis of minerals in spinel lherzolites from eastern Australia. *Contributions to Mineralogy and Petrology*, *130*(3-4), 240-255.
Norry, M. J., Hawkesworth, C. J., 1983. *Continental basalts and mantle xenoliths*. Shiva.

Novella, D., Frost, D. J., Hauri, E. H., Bureau, H., Raepsaet, C., Roberge, M., 2014. The distribution of H_2O between silicate melt and nominally anhydrous peridotite and the onset of hydrous melting in the deep upper mantle. *Earth and Planetary Science Letters*, *400*, 1-13.

Ohira, I., Ohtani, E., Sakai, T., Miyahara, M., Hirao, N., Ohishi, Y., Nishijima, M., 2014. Stability of a hydrous δ-phase, AlOOH–MgSiO 2 (OH) 2, and a mechanism for water transport into the base of lower mantle. *Earth and Planetary Science Letters*, *401*, 12-17.

O'Leary, J. A., Gaetani, G. A., Hauri, E. H., 2010. The effect of tetrahedral Al 3+ on the partitioning of water between clinopyroxene and silicate melt. *Earth and Planetary Science Letters*, *297*(1), 111-120.

O'Reilly, S. Y., Griffin, W. L., 2011. Rates of magma ascent: constraints from mantle-derived xenoliths. In *Timescales of Magmatic Processes* (pp. 116-124). John Wiley and Sons, Ltd.

Otsuka, K., Karato, S. I., 2015. The influence of ferric iron and hydrogen on Fe–Mg interdiffusion in ferropericlase ((Mg, Fe) O) in the lower mantle. *Physics and Chemistry of Minerals*, *42*(4), 261-273.

Ottolini, L., Le Fèvre, B., Vannucci, R., 2004. Direct assessment of mantle boron and lithium contents and distribution by SIMS analyses of peridotite minerals. *Earth and Planetary Science Letters*, *228*(1), 19-36.

Ottolini, L., Laporte, D., Raffone, N., Devidal, J. L., Le Fèvre, B., 2009. New experimental determination of Li and B partition coefficients during upper mantle partial melting. *Contributions to Mineralogy and Petrology*, *157*(3), 313-325.

Padrón-Navarta, J. A., Hermann, J., O'Neill, H. S. C., 2014. Site-specific hydrogen diffusion rates in forsterite. *Earth and Planetary Science Letters*, *392*, 100-112.

Paquin, J., Altherr, R., 2002. Subduction-related lithium metasomatism during exhumation of the Alpe Arami ultrahigh-pressure garnet peridotite (Central Alps, Switzerland). *Contributions to Mineralogy and Petrology*, *143*(5), 623-640.

Paquin, J., Altherr, R., Ludwig, T., 2004. Li–Be–B systematics in the ultrahigh-pressure garnet peridotite from Alpe Arami (Central Swiss Alps): implications for slab-to-mantle wedge transfer. *Earth and Planetary Science Letters*, *218*(3), 507-519.

Parkinson, I. J., Hammond, S. J., James, R. H., Rogers, N. W., 2007. High-temperature lithium isotope fractionation: insights from lithium isotope diffusion in magmatic systems. *Earth and Planetary Science Letters*, *257*(3), 609-621.

Paterson, M. S., 1982. The determination of hydroxyl by infrared absorption in quartz, silicate glasses, and similar materials. *Bulletin de la Societe Francaise de Mineralogie*, *105*, 20-29.

Pearson, D. G., Canil, D., Shirey, S. B., 2003. Mantle samples included in volcanic rocks: xenoliths and diamonds. *Treatise on geochemistry*, *2*, 171-275.

Penniston-Dorland, S. C., Sorensen, S. S., Ash, R. D., Khadke, S. V., 2010. Lithium isotopes as a tracer of fluids in a subduction zone mélange: Franciscan Complex, CA. *Earth and Planetary Science Letters*, *292*(1), 181-190.

Penniston-Dorland, S. C., Bebout, G. E., von Strandmann, P. A. P., Elliott, T., Sorensen, S. S., 2012. Lithium and its isotopes as tracers of subduction zone fluids and metasomatic processes: Evidence from the Catalina Schist, California, USA. *Geochimica et Cosmochimica Acta*, *77*, 530-545.

Peslier, A. H., Luhr, J. F., 2006. Hydrogen loss from olivines in mantle xenoliths from Simcoe (USA) and Mexico: mafic alkalic magma ascent rates and water budget of the sub-continental lithosphere. *Earth and Planetary Science Letters*, *242*(3), 302-319.

Peslier, A. H., Woodland, A. B., Wolff, J. A., 2008. Fast kimberlite ascent rates estimated from hydrogen diffusion profiles in xenolithic mantle olivines from southern Africa. *Geochimica et Cosmochimica Acta*, *72*(11), 2711-2722.

Peslier, A. H., 2010. A review of water contents of nominally anhydrous natural minerals in the mantles of Earth, Mars and the Moon. *Journal of Volcanology and Geothermal Research*, *197*(1), 239-258.

Peslier, A. H., Woodland, A. B., Bell, D. R., Lazarov, M., 2010. Olivine water contents in the continental lithosphere and the longevity of cratons. *Nature*, *467*(7311), 78-81.

Peslier, A. H., Woodland, A. B., Bell, D. R., Lazarov, M., Lapen, T. J., 2012. Metasomatic control of water contents in the Kaapvaal cratonic mantle. *Geochimica et Cosmochimica Acta*, *97*, 213-246.

Peslier, A. H., Bizimis, M., 2015. Water in Hawaiian peridotite minerals: A case for a dry metasomatized oceanic mantle lithosphere. *Geochemistry, Geophysics, Geosystems*, *16*(4), 1211-1232.

Peslier, A. H., Bizimis, M., Matney, M., 2015. Water disequilibrium in olivines from Hawaiian peridotites: Recent metasomatism, H diffusion and magma ascent rates. *Geochimica et Cosmochimica Acta*, *154*, 98-117.

Pezzali, I., France, L., Chazot, G., Vannucci, R., 2015. Analogues of exhumed pyroxenite layers in the Alboran domain sampled as xenoliths by Middle Atlas Cenozoic volcanism. *Lithos*.

Pilet, S., Baker, M. B., Stolper, E. M., 2008. Metasomatized lithosphere and the origin of alkaline lavas. *Science*, *320*(5878), 916-919.

Pin, C., 1990. Variscan oceans: ages, origins and geodynamic implications inferred from geochemical and radiometric data. *Tectonophysics*, *177*(1), 215-227.

Pistiner, J. S., Henderson, G. M., 2003. Lithium-isotope fractionation during continental weathering processes. *Earth and Planetary Science Letters*, *214*(1), 327-339.

Prechtel, F., Stalder, R., 2012. OH-defects in Al-and Cr-doped synthetic enstatites and defect geobarometry on natural orthopyroxenes from the Earth's mantle. *European Journal of Mineralogy*, *24*(3), 471-481.

Rauch, M., Keppler, H., 2002. Water solubility in orthopyroxene. *Contributions to Mineralogy and Petrology*, *143*(5), 525-536.

Richter, F. M., Davis, A. M., DePaolo, D. J., Watson, E. B., 2003. Isotope fractionation by chemical diffusion between molten basalt and rhyolite. *Geochimica et Cosmochimica Acta*, *67*(20), 3905-3923.

Richter, F., Watson, B., Chaussidon, M., Mendybaev, R., Ruscitto, D., 2014. Lithium isotope fractionation by diffusion in minerals. Part 1: Pyroxenes. *Geochimica et Cosmochimica Acta*, *126*, 352-370.

Rivalenti, G., Mazzucchelli, M., Zanetti, A., Vannucci, R., Bollinger, C., Hémond, C., Bertotto, G. W., 2007. Xenoliths from Cerro de los Chenques (Patagonia): an example of slab-related metasomatism in the backarc lithospheric mantle. *Lithos*, *99*(1), 45-67.

Rossman, G. R., 1996. Studies of OH in nominally anhydrous minerals. *Physics and Chemistry of Minerals*, *23*(4-5), 299-304.

Rudnick, R. L., McDonough, W. F., Chappell, B. W., 1993. Carbonatite metasomatism in the northern Tanzanian mantle: petrographic and geochemical characteristics. *Earth and Planetary Science Letters*, *114*(4), 463-475.

Rudnick, R. L., 1995. Making continental crust. *Nature*, *378*(6557), 571-577.

Rudnick, R. L., Gao, S., Ling, W. L., Liu, Y. S., McDonough, W. F., 2004. Petrology and geochemistry of spinel peridotite xenoliths from Hannuoba and Qixia, North China craton. *Lithos*, *77*(1), 609-637.

Rudnick, R. L., Tomascak, P. B., Njo, H. B., Gardner, L. R., 2004. Extreme lithium isotopic fractionation during continental weathering revealed in saprolites from South Carolina. *Chemical Geology*, *212*(1), 45-57.

Rudnick, R. L., Ionov, D. A., 2007. Lithium elemental and isotopic disequilibrium in minerals from peridotite xenoliths from far-east Russia: product of recent melt/fluid–rock reaction. *Earth and Planetary Science Letters*, *256*(1), 278-293.

Ryan, J. G., Langmuir, C. H., 1987. The systematics of lithium abundances in young volcanic rocks. *Geochimica et Cosmochimica Acta*, *51*(6), 1727-1741.

Ryan, J. G., Kyle, P. R., 2004. Lithium abundance and lithium isotope variations in mantle sources: insights from intraplate volcanic rocks from Ross Island and Marie Byrd Land (Antarctica) and other oceanic islands. *Chemical Geology*, *212*(1), 125-142.

Ryu, J. S., Vigier, N., Lee, S. W., Lee, K. S., Chadwick, O. A., 2014. Variation of lithium isotope geochemistry during basalt weathering and secondary mineral transformations in Hawaii. *Geochimica et Cosmochimica Acta*, *145*, 103-115.

Saal, A. E., Hauri, E. H., Langmuir, C. H., Perfit, M. R., 2002. Vapour undersaturation in primitive mid-ocean-ridge basalt and the volatile content of Earth's upper mantle. *Nature*, *419*(6906), 451-455.

Sakurai, M., Tsujino, N., Sakuma, H., Kawamura, K., Takahashi, E., 2014. Effects of Al content on water partitioning between orthopyroxene and olivine: Implications for lithosphere–asthenosphere boundary. *Earth and Planetary Science Letters*, *400*, 284-291.

Scambelluri, M., Hermann, J., Morten, L., Rampone, E., 2006. Melt-versus fluid-induced metasomatism in spinel to garnet wedge peridotites (Ulten Zone, Eastern Italian Alps): clues from trace element and Li abundances. *Contributions to Mineralogy and Petrology*, *151*(4), 372-394.

Schmädicke, E., Gose, J., Witt-Eickschen, G., Brätz, H., 2013. Olivine from spinel peridotite xenoliths: Hydroxyl incorporation and mineral composition. *American Mineralogist*, *98*(10), 1870-1880.

Seitz, H. M., Woodland, A. B., 2000. The distribution of lithium in peridotitic and pyroxenitic mantle lithologies—an indicator of magmatic and metasomatic processes. *Chemical Geology*, *166*(1), 47-64.

Seitz, H. M., Brey, G. P., Lahaye, Y., Durali, S., Weyer, S., 2004. Lithium isotopic signatures of peridotite xenoliths and isotopic fractionation at high temperature between olivine and pyroxenes. *Chemical Geology*, *212*(1), 163-177.

Shaw, C. S., Heidelbach, F., Dingwell, D. B., 2006. The origin of reaction textures in mantle peridotite xenoliths from Sal Island, Cape Verde: the case for "metasomatism" by the host lava. *Contributions to Mineralogy and Petrology*, *151*(6), 681-697.

Shaw, C. S., Dingwell, D. B., 2008. Experimental peridotite–melt reaction at one atmosphere: a textural and chemical study. *Contributions to Mineralogy and Petrology*, *155*(2), 199-214.

Skogby H., Rossman G. R., 1989. OH– in pyroxene: an experimentalstudy of incorporation mechanisms and stability. *American Mineralogist*, 74, 1059–1069.

Skogby, H., Bell, D. R., Rossman, G. R., 1990. Hydroxide in pyroxene: variations in the natural environment. *American Mineralogist*, *75*(7-8), 764-774.

Skogby, H., Rossman, G. R., 1991. The intensity of amphibole OH bands in the infrared absorption spectrum. *Physics and Chemistry of Minerals*, *18*(1), 64-68.

Skogby, H., 1994. OH incorporation in synthetic clinopyroxene. *American Mineralogist*, *79*, 240-249.

Sneeringer, M., Hart, S. R., Shimizu, N., 1984. Strontium and samarium diffusion in diopside. *Geochimica et Cosmochimica Acta*, *48*(8), 1589-1608.

Smyth, J. R., Frost, D. J., Nestola, F., Holl, C. M., Bromiley, G., 2006. Olivine hydration in the deep upper mantle: effects of temperature and silica activity. *Geophysical Research Letters*, *33*(15).

Smyth, J. R., Mierdel, K., Keppler, H., Langenhorst, F., Dubrovinsky, L., Nestola, F., 2007. Crystal chemistry of hydration in aluminous orthopyroxene. *American Mineralogist*, *92*(5-6), 973-976.

Sobolev, S. V., Zeyen, H., Stoll, G., Werling, F., Altherr, R., Fuchs, K., 1996. Upper mantle temperatures from teleseismic tomography of French Massif Central including effects of composition, mineral reactions, anharmonicity, anelasticity and partial melt. *Earth and Planetary Science Letters*, *139*(1), 147-163.

Sobolev, S. V., Zeyen, H., Granet, M., Achauer, U., Bauer, C., Werling, F., Altherr, R., Fuchs, K., 1997. Upper mantle temperatures and lithosphere-asthenosphere system beneath the French Massif Central constrained by seismic, gravity, petrologic and thermal observations. *Tectonophysics*, *275*(1), 143-164.

Stalder, R., Skogby, H., 2002. Hydrogen incorporation in enstatite. *European Journal of Mineralogy*, *14*(6), 1139-1144.

Stalder, R., Skogby, H., 2003. Hydrogen diffusion in natural and synthetic orthopyroxene. *Physics and Chemistry of Minerals*, *30*(1), 12-19.

Stalder, R., 2004. Influence of Fe, Cr and Al on hydrogen incorporation in orthopyroxene. *European Journal of Mineralogy*, *16*(5), 703-711.

Stalder, R., Klemme, S., Ludwig, T., Skogby, H., 2005. Hydrogen incorporation in orthopyroxene: interaction of different trivalent cations. *Contributions to Mineralogy and Petrology*, *150*(5), 473-485.

Stalder, R., Skogby, H., 2007. Dehydration mechanisms in synthetic Fe-bearing enstatite. *European journal of mineralogy*, *19*(2), 201-216.

Stalder, R., Karimova, A., Konzett, J., 2015. OH-defects in multiple-doped orthoenstatite at 4–8 GPa: filling the gap between pure and natural systems. *Contributions to Mineralogy and Petrology*, *169*(4), 1-10.

Su, B. X., Zhang, H. F., Sakyi, P. A., Yang, Y. H., Ying, J. F., Tang, Y. J., Qin, K. ZH., Xiao, Y., Zhao, X. M., Mao, Q., Ma, Y. G., 2011. The origin of spongy texture in minerals of mantle xenoliths from the Western Qinling, central China. *Contributions to Mineralogy and Petrology*, *161*(3), 465-482.

Su, B. X., Zhang, H. F., Deloule, E., Sakyi, P. A., Xiao, Y., Tang, Y. J., Hu, Y., Ying, J. F., Liu, P. P., 2012. Extremely high Li and low δ 7 Li signatures in the lithospheric mantle. *Chemical Geology*, *292*, 149-157.

Su, B. X., Zhang, H. F., Deloule, E., Vigier, N., Hu, Y., Tang, Y. J., Xiao, Y., Sakyi, P. A., 2014. Distinguishing silicate and carbonatite mantle metasomatism by using lithium and its isotopes. *Chemical Geology*, *381*, 67-77.

Su, B. X., Gu, X. Y., Deloule, E., Zhang, H. F., Li, Q. L., Li, X. H., Vigier, N., Tang, Y. J., Tang, G. Q., Liu, Y., Pang, K. N., Brewer, A., Mao, Q., Ma, Y. G., 2015. Potential Orthopyroxene, Clinopyroxene and Olivine Reference Materials for In Situ Lithium Isotope Determination. *Geostandards and Geoanalytical Research*.

Sundvall, R., Skogby, H., Stalder, R., 2009. Hydrogen diffusion in synthetic Fe-free diopside. *European journal of mineralogy*, *21*(5), 963-970.

Sundvall, R., Stalder, R., 2011. Water in upper mantle pyroxene megacrysts and xenocrysts: A survey study. *American Mineralogist*, *96*(8-9), 1215-1227.

Takazawa, E., Frey, F. A., Shimizu, N., Obata, M., Bodinier, J. L., 1992. Geochemical evidence for melt migration and reaction in the upper mantle. *Nature*, *359*(6390), 55-58.

Tang, Y. J., Zhang, H. F., Nakamura, E., Moriguti, T., Kobayashi, K., Ying, J. F., 2007. Lithium isotopic systematics of peridotite xenoliths from Hannuoba, North China Craton: implications for melt–rock interaction in the considerably thinned lithospheric mantle. *Geochimica et Cosmochimica Acta*, *71*(17), 4327-4341.

Tang, Y. J., Zhang, H. F., Ying, J. F., 2010. A brief review of isotopically light Li–a feature of the enriched mantle?. *International Geology Review*, *52*(9), 964-976.

Tang, Y. J., Zhang, H. F., Nakamura, E., Ying, J. F., 2011. Multistage melt/fluid-peridotite interactions in the refertilized lithospheric mantle beneath the North China Craton: constraints from the Li–Sr–Nd isotopic disequilibrium between minerals of peridotite xenoliths. *Contributions to Mineralogy and Petrology*, *161*(6), 845-861.

Tang, Y. J., Zhang, H. F., Deloule, E., Su, B. X., Ying, J. F., Xiao, Y., Hu, Y., 2012. Slab-derived lithium isotopic signatures in mantle xenoliths from northeastern North China Craton. *Lithos*, *149*, 79-90.

Tang, Y. J., Zhang, H. F., Deloule, E., Su, B. X., Ying, J. F., Santosh, M., Xiao, Y., 2014. Abnormal lithium isotope composition from the ancient lithospheric mantle beneath the North China Craton. *Scientific reports*, *4*.

Teng, F. Z., McDonough, W. F., Rudnick, R. L., Dalpé, C., Tomascak, P. B., Chappell, B. W., Gao, S., 2004. Lithium isotopic composition and concentration of the upper continental crust. *Geochimica et Cosmochimica Acta*, *68*(20), 4167-4178.

Teng, F. Z., McDonough, W. F., Rudnick, R. L., Walker, R. J., 2006. Diffusion-driven extreme lithium isotopic fractionation in country rocks of the Tin Mountain pegmatite. *Earth and Planetary Science Letters*, *243*(3), 701-710.

Teng, F. Z., Rudnick, R. L., McDonough, W. F., Gao, S., Tomascak, P. B., Liu, Y., 2008. Lithium isotopic composition and concentration of the deep continental crust. *Chemical Geology*, *255*(1), 47-59.

Tenner, T. J., Hirschmann, M. M., Withers, A. C., Hervig, R. L., 2009. Hydrogen partitioning between nominally anhydrous upper mantle minerals and melt between 3 and 5 GPa and applications to hydrous peridotite partial melting. *Chemical Geology*, *262*(1), 42-56.

Tenner, T. J., Hirschmann, M. M., Humayun, M., 2012a. The effect of H_2O on partial melting of garnet peridotite at 3.5 GPa. *Geochemistry, Geophysics, Geosystems*, *13*(3).

Tenner, T. J., Hirschmann, M. M., Withers, A. C., Ardia, P., 2012b. H_2O storage capacity of olivine and low-Ca pyroxene from 10 to 13 GPa: consequences for dehydration melting above the transition zone. *Contributions to Mineralogy and Petrology*, *163*(2), 297-316.

Tian, S., Hou, Z., Su, A., Qiu, L., Mo, X., Hou, K., Zhao, Y., Hu, W., Yang, Z., 2015. The anomalous lithium isotopic signature of Himalayan collisional zone carbonatites in western Sichuan, SW China: Enriched mantle source and petrogenesis. *Geochimica et Cosmochimica Acta*, *159*, 42-60.

Tomascak, P. B., Tera, F., Helz, R. T., Walker, R. J., 1999. The absence of lithium isotope fractionation during basalt differentiation: new measurements by multicollector sector ICP-MS. *Geochimica et Cosmochimica Acta*, *63*(6), 907-910.

Tomascak, P. B., Widom, E., Benton, L. D., Goldstein, S. L., Ryan, J. G., 2002. The control of lithium budgets in island arcs. *Earth and Planetary Science Letters*, *196*(3), 227-238.

Tomascak, P. B., 2004. Developments in the understanding and application of lithium isotopes in the earth and planetary sciences. *Reviews in Mineralogy and Geochemistry*, *55*(1), 153-195.

Tomascak, P. B., Langmuir, C. H., le Roux, P. J., Shirey, S. B., 2008. Lithium isotopes in global mid-ocean ridge basalts. *Geochimica et Cosmochimica Acta*, *72*(6), 1626-1637.

Touron, S., 2005. *Geochemical Fingerprints of Mantle Metasomatism Beneath the Massif Central, France* (Doctoral dissertation, Macquarie University (Division of Environmental & Life Sciences, Department of Earth and Planetary Sciences)).

Touron, S., Renac, C., O'Reilly, S. Y., Cottin, J. Y., Griffin, W. L., 2008. Characterization of the metasomatic agent in mantle xenoliths from Deves, Massif Central (France) using coupled in situ trace-element and O, Sr and Nd isotopic compositions. *Geological Society, London, Special Publications*, *293*(1), 177-196.

Uenver-Thiele, L., Woodland, A. B., Downes, H., Altherr, R., 2014. Oxidation state of the lithospheric mantle below the Massif Central, France. *Journal of Petrology*, *55*(12), 2457-2480.

McDonough, W. F., Sun, S. S., 1995. The composition of the Earth. *Chemical geology*, *120*(3), 223-253.

Umemoto, K., Wentzcovitch, R. M., Hirschmann, M. M., Kohlstedt, D. L., Withers, A. C., 2011. first-principles investigation of hydrous defects and IR frequencies in forsterite: The case for Si vacancies. *American Mineralogist*, *96*(10), 1475-1479.

Vannucci, R., Piccardo, G. B., Rivalenti, G., Zanetti, A., Rampone, E., Ottolini, L., Oberti, R., Mazzucchelli, M., Bottazzi, P., 1995. Origin of LREE-depleted amphiboles in the subcontinental mantle. *Geochimica et Cosmochimica Acta*, *59*(9), 1763-1771.

Vasseur, G., Vernieres, J., Bodiner, J. L., 1991. Modelling of trace element transfer between mantle melt and heterogranular peridotite matrix. *Journal of Petrology*, (2), 41-54.

Vlastélic, I., Koga, K., Chauvel, C., Jacques, G., Télouk, P., 2009. Survival of lithium isotopic heterogeneities in the mantle supported by HIMU-lavas from Rurutu Island, Austral Chain. *Earth and Planetary Science Letters*, *286*(3), 456-466.

Von Strandmann, P. A. P., Elliott, T., Marschall, H. R., Coath, C., Lai, Y. J., Jeffcoate, A. B., Ionov, D. A., 2011. Variations of Li and Mg isotope ratios in bulk chondrites and mantle xenoliths. *Geochimica et Cosmochimica Acta*, *75*(18), 5247-5268.

Wagner, C., Mokhtari, A., Deloule, E., Chabaux, F., 2003. Carbonatite and alkaline magmatism in Taourirt (Morocco): petrological, geochemical and Sr–Nd isotope characteristics. *Journal of Petrology*, *44*(5), 937-965.

Wagner, C., Deloule, E., 2007. Behaviour of Li and its isotopes during metasomatism of French Massif Central lherzolites. *Geochimica et Cosmochimica Acta*, *71*(17), 4279-4296.

Wagner, C., Pascal, M. L., Fialin, M., 2013. Conflicting interpretations of petrogenetic processes recorded by reaction textures in peridotite xenoliths. In *EGU General Assembly Conference Abstracts* (Vol. 15, p. 3423).

Walker, A. M., Hermann, J., Berry, A. J., O'Neill, H. S. C., 2007. Three water sites in upper mantle olivine and the role of titanium in the water weakening mechanism. *Journal of Geophysical Research: Solid Earth*, *112*(B5).

Walter, M. J., 2014. Melt extraction and compositional variability in mantle lithosphere. *Treatise on geochemistry (2nd edition)*, *2*, 393-419.

Wang, Z., Hiraga, T., Kohlstedt, D. L., 2004. Effect of H+ on Fe–Mg interdiffusion in olivine,(Fe, Mg) 2SiO4. *Applied physics letters*, *85*(2), 209-211.

Wang, D., Mookherjee, M., Xu, Y., Karato, S. I., 2006. The effect of water on the electrical conductivity of olivine. *Nature*, *443*(7114), 977-980.

Wanner, C., Sonnenthal, E. L., Liu, X. M., 2014. Seawater δ 7 Li: A direct proxy for global CO 2 consumption by continental silicate weathering?. *Chemical Geology*, *381*, 154-167.

Warren, J. M., Hauri, E. H., 2014. Pyroxenes as tracers of mantle water variations. *Journal of Geophysical Research: Solid Earth*, *119*(3), 1851-1881.

Wells, P. R., 1977. Pyroxene thermometry in simple and complex systems. *Contributions to mineralogy and Petrology*, *62*(2), 129-139.

Wenger, M., Armbruster, T. (1991). Crystal chemistry of lithium: oxygen coordination and bonding. *European Journal of Mineralogy*, 387-400.

Werling, F., Altherr, R., 1997. Thermal evolution of the lithosphere beneath the French Massif Central as deduced from geothermobarometry on mantle xenoliths. *Tectonophysics*, *275*(1), 119-141.

Wilson, M., Downes, H., 1991. Tertiary—Quaternary extension-related alkaline magmatism in western and central Europe. *Journal of Petrology*, *32*(4), 811-849.

Withers, A. C., Hirschmann, M. M., Tenner, T. J., 2011. The effect of Fe on olivine H2O storage capacity: Consequences for H2O in the martian mantle. *American Mineralogist*, *96*(7), 1039-1053.

Wittig, N., Baker, J. A., Downes, H., 2006. Dating the mantle roots of young continental crust. *Geology*, *34*(4), 237-240.

Wittig, N., Baker, J. A., Downes, H., 2007. U–Th–Pb and Lu–Hf isotopic constraints on the evolution of sub-continental lithospheric mantle, French Massif Central. *Geochimica et Cosmochimica Acta*, *71*(5), 1290-1311.

Woo, Y., Yang, K., Kil, Y., Yun, S. H., Arai, S., 2014. Silica-and LREE-enriched spinel peridotite xenoliths from the Quaternary intraplate alkali basalt, Jeju Island, South Korea: Old subarc fragments?. *Lithos*, *208*, 312-323.

Wood, B. J., Banno, S., 1973. Garnet-orthopyroxene and orthopyroxene-clinopyroxene relationships in simple and complex systems. *Contributions to mineralogy and petrology*, *42*(2), 109-124.

Woodland, A. B., Seitz, H. M., Yaxley, G. M., 2004. Varying behaviour of Li in metasomatised spinel peridotite xenoliths from western Victoria, Australia. *Lithos*, *75*(1), 55-66.

Workman, R. K., Hart, S. R., 2005. Major and trace element composition of the depleted MORB mantle (DMM). *Earth and Planetary Science Letters*, *231*(1), 53-72.

Wunder, B., Meixner, A., Romer, R. L., Heinrich, W., 2006. Temperature-dependent isotopic fractionation of lithium between clinopyroxene and high-pressure hydrous fluids. *Contributions to Mineralogy and Petrology*, *151*(1), 112-120.

Wunder, B., Meixner, A., Romer, R. L., Feenstra, A., Schettler, G., Heinrich, W., 2007. Lithium isotope fractionation between Li-bearing staurolite, Li-mica and aqueous fluids: an experimental study. *Chemical Geology*, *238*(3), 277-290.

Xia, Q. K., Hao, Y., Li, P., Deloule, E., Coltorti, M., Dallai, L., Yang X. Z., Feng, M., 2010. Low water content of the Cenozoic lithospheric mantle beneath the eastern part of the North China Craton. *Journal of Geophysical Research: Solid Earth*, *115*(B7).

Xia, Q. K., Hao, Y. T., Liu, S. C., Gu, X. Y., Feng, M., 2013. Water contents of the Cenozoic lithospheric mantle beneath the western part of the North China Craton: Peridotite xenolith constraints. *Gondwana Research*, *23*(1), 108-118.

Xiao, Y., Zhang, H. F., Deloule, E., Su, B. X., Tang, Y. J., Sakyi, P. A., Hu, Y., Ying, J. F., 2015. Large Lithium Isotopic Variations in Minerals from Peridotite Xenoliths from the Eastern North China Craton. *The Journal of Geology*, *123*(1), 79-94.

Xu, R., Liu, Y., Tong, X., Hu, Z., Zong, K., Gao, S., 2013. In-situ trace elements and Li and Sr isotopes in peridotite xenoliths from Kuandian, North China Craton: insights into Pacific slab subduction-related mantle modification. *Chemical Geology*, *354*, 107-123.

Xu, X., O'REILLY, S. Y., Griffin, W. L., Zhou, X., 2000. Genesis of young lithospheric mantle in southeastern China: an LAM–ICPMS trace element study. *Journal of Petrology*, *41*(1), 111-148.

Xu, Y. G., Menzies, M. A., Bodinier, J. L., Bedini, R. M., Vroon, P., Mercier, J. C., 1998. Melt percolation and reaction atop a plume: evidence from the poikiloblastic peridotite xenoliths from Borée (Massif Central, France). *Contributions to Mineralogy and Petrology*, *132*(1), 65-84.

Yakob, J. L., Feineman, M. D., Deane, J. A., Eggler, D. H., Penniston-Dorland, S. C., 2012. Lithium partitioning between olivine and diopside at upper mantle conditions: An experimental study. *Earth and Planetary Science Letters*, *329*, 11-21.

Yang, X. Z., Xia, Q. K., Deloule, E., Dallai, L., Fan, Q. C., Feng, M., 2008. Water in minerals of the continental lithospheric mantle and overlying lower crust: a comparative study of peridotite and granulite xenoliths from the North China Craton. *Chemical Geology*, *256*(1), 33-45.

Yang, Y., Xia, Q. K., Feng, M., Liu, S. C., 2012. OH in natural orthopyroxene: an in situ FTIR investigation at varying temperatures. *Physics and Chemistry of Minerals*, *39*(5), 413-418.

Yaxley, G. M., Green, D. H., Kamenetsky, V., 1998. Carbonatite metasomatism in the southeastern Australian lithosphere. *Journal of Petrology*, *39*(11-12), 1917-1930.

Yoshikawa, M., Kawamoto, T., Shibata, T., Yamamoto, J., 2010. Geochemical and Sr–Nd isotopic characteristics and pressure–temperature estimates of mantle xenoliths from the French Massif Central: evidence for melting and multiple metasomatism by silicate-rich carbonatite and asthenospheric melts. *Geological Society, London, Special Publications*, *337*(1), 153-175.

Yoshino, T., Matsuzaki, T., Yamashita, S., Katsura, T., 2006. Hydrous olivine unable to account for conductivity anomaly at the top of the asthenosphere. *Nature*, *443*(7114), 973-976.

Yoshino, T., Katsura, T., 2013. Electrical conductivity of mantle minerals: role of water in conductivity anomalies. *Annual review of earth and planetary sciences*, *41*, 605-628.

You, C. F., Chan, L. H. (1996). Precise determination of lithium isotopic composition in low concentration natural samples. *Geochimica et Cosmochimica Acta*, *60*(5), 909-915.

Yu, Y., Xu, X. S., Griffin, W. L., O'Reilly, S. Y., Xia, Q. K., 2011. H_2O contents and their modification in the Cenozoic subcontinental lithospheric mantle beneath the Cathaysia block, SE China. *Lithos*, *126*(3), 182-197.

Zack, T., Tomascak, P. B., Rudnick, R. L., Dalpé, C., McDonough, W. F., 2003. Extremely light Li in orogenic eclogites: the role of isotope fractionation during dehydration in subducted oceanic crust. *Earth and Planetary Science Letters*, *208*(3), 279-290.

Zanetti, A., Mazzucchelli, M., Rivalenti, G., Vannucci, R., 1999. The Finero phlogopite-peridotite massif: an example of subduction-related metasomatism. *Contributions to Mineralogy and Petrology*, *134*(2-3), 107-122.

Zangana, N. A., Downes, H., Thirlwall, M. F., Hegner, E., 1997. Relationship between deformation, equilibration temperatures, REE and radiogenic isotopes in mantle xenoliths (Ray Pic, Massif Central, France): an example of plume-lithosphere interaction?. *Contributions to Mineralogy and Petrology*, *127*(1-2), 187-203.

Zangana, N. A., Downes, H., Thirlwall, M. F., Marriner, G. F., Bea, F., 1999. Geochemical variation in peridotite xenoliths and their constituent clinopyroxenes from Ray Pic (French Massif Central): implications for the composition of the shallow lithospheric mantle. *Chemical Geology*, *153*(1), 11-35.

Zeyen, H., Novak, O., Landes, M., Prodehl, C., Driad, L., Hirn, A., 1997. Refraction-seismic investigations of the northern Massif Central (France). *Tectonophysics*, *275*(1), 99-117.

Zhang, B., Matsuzaki, T., Wu, X., 2013. Water solubility in orthopyroxene: Dependence on temperature and Al content. *Chinese Science Bulletin*, *58*(32), 3895-3902.

Zhang, F., Wright, K., 2012. Coupled (Li+, Al3+) substitutions in hydrous forsterite. *American Mineralogist*, *97*(2-3), 425-429.

Zhang, H. F., Deloule, E., Tang, Y. J., Ying, J. F., 2010. Melt/rock interaction in remains of refertilized Archean lithospheric mantle in Jiaodong Peninsula, North China Craton: Li isotopic evidence. *Contributions to Mineralogy and Petrology*, *160*(2), 261-277.

Zhao, Y. H., Ginsberg, S. B., Kohlstedt, D. L., 2004. Solubility of hydrogen in olivine: dependence on temperature and iron content. *Contributions to Mineralogy and Petrology*, *147*(2), 155-161.

Ziegler, P. A., 1992. European Cenozoic rift system. *Tectonophysics*, *208*(1), 91-111.

Zinner, E., Fahey, A. J., McKeegan, K. D., 1986. Characterization of electron multipliers by charge distributions. In *Secondary Ion Mass Spectrometry SIMS V* (pp. 170-172). Springer Berlin Heidelberg.

Appendix

Vol. 39 — N° 3 09 15 P. 357 – 369

GEOSTANDARDS and GEOANALYTICAL RESEARCH

Potential Orthopyroxene, Clinopyroxene and Olivine Reference Materials for *In Situ* Lithium Isotope Determination

Ben-Xun **Su** (1)*, Xiao-Yan **Gu** (2), Etienne **Deloule** (2), Hong-Fu **Zhang** (1), Qiu-Li **Li** (1), Xian-Hua **Li** (1), Nathalie **Vigier** (3), Yan-Jie **Tang** (1), Guo-Qiang **Tang** (1), Yu **Liu** (1), Kwan-Nang **Pang** (4), Aaron **Brewer** (5), Qian **Mao** (1) and Yu-Guang **Ma** (1)

(1) State Key Laboratory of Lithospheric Evolution, Institute of Geology and Geophysics, Chinese Academy of Sciences, PO Box 9825, Beijing, 100029, China
(2) Centre de Recherches Pétrographiques et Géochimiques, UMR 5873 CNRS - Université de Lorraine, BP20, Vandoeuvre-lès-Nancy Cedex, 54501, France
(3) Laboratoire d'Océanographie de Villefranche, OOV, CNRS, UPMC, Villefranche sur Mer, France
(4) Department of Geosciences, National Taiwan University, Taipei, Taiwan
(5) Isotope Laboratory, Department of Earth and Space Sciences, University of Washington, Seattle, WA, 98195, USA
* Corresponding author. e-mail: subenxun@mail.igcas.ac.cn

Over 1400 electron probe and 700 ion probe microanalyses were performed on eleven mineral separates to evaluate their potential as reference materials for *in situ* Li isotopic determination. Our results suggest the homogenous distributions of major elements, Li and its isotopes for each sample. Hence, these samples are suitable to be used as reference materials for *in situ* measurements of Li abundance and Li isotopes by secondary ion mass spectrometry (SIMS) or laser ablation-inductively coupled plasma-mass spectrometry (LA-ICP-MS). These samples have the advantage of mitigating probable matrix effects during calibration owing to the wide range of compositions. The effect of composition on the δ^7Li of olivine measured by SIMS is a linear function of composition, with δ^7Li increasing by 1.0‰ for each mole per cent decrease in forsterite component.

Keywords: lithium isotopes, mineral reference materials, ion probe, *in situ* determination.

***Plus de 1400 micro-analyses à la sonde électronique et plus de 700 à la sonde ionique ont été réalisées sur onze échantillons de minéraux séparés afin d'évaluer leur potentiel comme matériel de référence pour la détermination in situ* de la composition isotopique du Li. Nos résultats suggèrent que les distributions des éléments majeurs, du Li et de ses isotopes pour chaque échantillon sont homogènes. Par conséquent, ces échantillons sont aptes à être utilisés comme matériaux de référence pour les mesures *in situ* de l'abondance du Li et des isotopes du Li par spectrométrie de masse à ionisation secondaire (SIMS) ou par spectrométrie de masse à plasma inductif couplée à l'ablation laser (LA-ICP-MS). Ces échantillons ont l'avantage d'atténuer les probables effets de matrice pendant l'étalonnage et ceci en raison de la large gamme de compositions. L'effet de la composition sur le δLi^7 de l'olivine mesurée par SIMS est une fonction linéaire de la composition, avec une augmentation de ce δLi^7 de 1,0 ‰ pour chaque pour cent de diminution molaire du composant forstérite.**

Mots-clés : isotopes du lithium, minéraux de référence, sonde ionique, détermination in situ.

Received 05 Apr 14 – Accepted 16 Sep 14

Olivine, orthopyroxene and clinopyroxene are major constituents of the mantle and mantle-derived magmas. Recent studies indicate that the concentration and isotopic composition of Li in these minerals are important tracers for mantle melting, fluid–rock interaction, crustal recycling and fractional crystallisation (Seitz and Woodland 2000, Richter *et al.* 2003, Tomascak 2004, Jeffcoate *et al.* 2007, Rudnick and Ionov 2007, Tang *et al.* 2007, Bouvier *et al.* 2008, 2010, Halama *et al.* 2008, Bell *et al.* 2009, Gallagher and Elliott 2009, Hamelin *et al.* 2009). In particular, large Li isotopic fractionation at small scales observed in mantle minerals provides detailed insights into mantle processes

doi: 10.1111/j.1751-908X.2014.00313.x
© 2014 The Authors. Geostandards and Geoanalytical Research © 2014 International Association of Geoanalysts

(Decitre *et al.* 2002, Wagner and Deloule 2007, Zhang *et al.* 2010, Su *et al.* 2012a, 2014a, b, Tang *et al.* 2014) and requires microanalysis as opposed to bulk analyses, as well as sufficient measurement precision and accuracy to make assessments of these processes. However, limited data at the intra- and intergrain scales restrict our insight into the geochemical behaviour of Li isotopes during a variety of geological processes. Fortunately, the technical developments of secondary ion mass spectrometry (SIMS) and laser ablation-multiple collector-inductively coupled plasma-mass spectrometry (LA-MC-ICP-MS) make it possible to conduct *in situ* determination of Li isotopes (Decitre *et al.* 2002, Xu *et al.* 2013). Nonetheless, its application has been hampered by the rarity of reference materials with sufficient homogeneity due to the mobile nature of Li (Chan *et al.* 1992, Beck *et al.* 2004, 2006, Coogan *et al.* 2005, Lundstrom *et al.* 2005, Teng *et al.* 2006, Magna *et al.* 2008, Dohmen *et al.* 2010, Richter *et al.* 2014). In addition, the probable matrix effect during calibration of the instruments represents another problem (Kasemann *et al.* 2005, Jeffcoate *et al.* 2007, Bell *et al.* 2009), which needs to be overcome by analysing a series of reference materials with large compositional variations.

Samples

To define new mineral reference materials, we conducted extensive Li isotopic measurements on a variety of ultramafic rocks. Among them, five samples of olivine, three samples of orthopyroxene and three samples of clinopyroxene displayed homogeneous distributions of Li and its isotopes and were thus suitable to be used as reference materials for calibration and measurement by SIMS and LA-MC-ICP-MS. Samples with prefixes '06-JY' are minerals separated from mantle xenoliths entrained in Cenozoic basalts at Jingyu, north China. The sample 09XDTC1-24OL is olivine separated from a dunite of the Xiadong intrusion, an Alaskan-type complex in eastern Tianshan, NW China. Petrographic descriptions of the samples are available in Su *et al.* (2012b) and Tang *et al.* (2012). Additionally, tens to hundreds of grams of each sample were separated and certain hand specimens were leftover. These samples are available upon request to the corresponding author.

Analytical methods

The mineral separates were mounted in epoxy resin and polished to expose the interior of the crystals for analysis. The internal structure of the crystals was examined using back-scattered electron images to select suitable positions for analysis. In order to ensure homogeneity of the crystals, compositional profiles were obtained by a large number of major element determinations using a JEOL JXA-8100 electron probe microanalyser (EPMA) at the Institute of Geology and Geophysics, Chinese Academy of Sciences (IGGCAS), Beijing, China. Operating conditions were as follows: an accelerating voltage of 15 kV, a beam current of 10 nA, a beam diameter of 5 μm and counting time of 10 to 30 s. The ZAF procedure was applied for matrix corrections.

The Li isotopic measurements were carried out in four sessions using a Cameca IMS-1280 SIMS at IGGCAS, Beijing, China (sessions 1 and 2) and using a Cameca IMS-1270 SIMS at CRPG, Nancy, France (sessions 3 and 4) following the method established by Decitre *et al.* (2002). The O^- primary ion beam was accelerated at 13 kV, with an intensity of about 15–30 nA. The elliptical spot area was approximately 20 × 30 μm. Positive secondary ions were measured on an ion multiplier in pulse counting mode, with a mass resolution ($M/\Delta M$) of 1500 and an energy slit open at 40 eV without any energy offset. A 180-s presputtering without raster was applied before analysis. The secondary ion beam position in the contrast aperture, as well as the magnetic field and the energy offset, was automatically centred before each measurement. Thirty cycles were measured with counting times of 12, 4 and 4 s for ^6Li, background at the 6.5 mass, and ^7Li, respectively. The working conditions of the IMS-1280 and IMS-1270 instruments were slightly different and are described elsewhere (Li *et al.* 2011, 2012, Su *et al.* 2012a). The measured raw δ^7Li_m (‰) values are expressed as δ^7Li ($[(^7Li/^6Li)_{sample}/(^7Li/^6Li)_{L\text{-}SVEC} - 1] \times 1000$) relative to the reference material L-SVEC ($^7Li/^6Li = 12.0192$; Flesch *et al.* 1973, Decitre *et al.* 2002).

Concentrations of Li of the mineral separates were measured by solution ICP-MS at the IGGCAS, Beijing, China, and isotopic compositions were measured by solution MC-ICP-MS at the CRPG, Nancy, France. The samples were dissolved in a 3:1 mixture of concentrated HF-HNO_3 in Teflon bombs and then purified in cation exchange columns. Analyses were performed on 2–3% HNO_3 solutions with Li concentrations of 30 ng ml^{-1}, typically yielding a current intensity of 1.5 to 2 × 10^{-11} A for the ^7Li ion (using 10^{11} Ω resistors). The analytical protocol involved the acquisition of fifteen ratios with a 16-s integration time per ratio, which yielded a within-run precision of ~ 0.15‰. Samples were bracketed by the L-SVEC reference material to correct for instrumental mass fractionation. The measured $^7Li/^6Li$ ratio of a given sample was normalised to the mean $^7Li/^6Li$ of the two RMs analysed immediately before and after it. The analytical procedures are described in detail by Millot *et al.* (2004) and Vigier *et al.* (2008). Each sample was analysed only once due to the small amount available for isotope determinations and low Li levels. We measured several types of reference materials during the various Li measurement

 © 2014 The Authors. Geostandards and Geoanalytical Research © 2014 International Association of Geoanalysts

Table 1.
Mean composition and range of major elements in the minerals analysed using EPMA at IGGCAS

Sample/No.		SiO_2	TiO_2	Al_2O_3	Cr_2O_3	FeO	MnO	MgO	CaO	Na_2O	K_2O	NiO	Total	Mg#
06JY06OPX	Mean	56.4	0.16	3.84	0.42	6.43	0.15	32.5	0.80	0.07	0.01	0.09	100.9	90.1
138	Range	55.5–57.1	0.06–0.26	3.65–4.16	0.31–0.53	6.19–6.63	0.07–0.21	31.9–33.2	0.72–0.92	0.00–0.13	0.00–0.05	0.00–0.17	99.7–101.5	89.8–90.4
06JY31OPX	Mean	57.1	0.09	3.34	0.53	5.94	0.14	32.6	0.93	0.11	0.01	0.10	100.9	90.8
76	Range	56.2–57.7	0.00–0.21	3.06–3.80	0.43–0.65	5.82–6.16	0.09–0.20	32.0–33.3	0.76–1.13	0.00–0.22	0.00–0.04	0.01–0.16	99.5–101.5	90.6–91.1
06JY34OPX	Mean	57.6	0.09	2.86	0.54	5.22	0.13	33.6	0.68	0.14	0.01	0.10	101.0	92.1
98	Range	56.3–58.2	0.00–0.16	2.66–3.35	0.40–0.75	5.01–5.41	0.08–0.18	33.0–34.3	0.58–0.80	0.06 ~0.25	0.00–0.06	0.04–0.17	99.2–101.5	91.8–92.3
06JY06CPX	Mean	52.4	0.59	0.77	5.09	3.04	0.09	15.3	20.8	1.08	0.01	0.04	99.2	90.0
126	Range	51.7–53.3	0.41–0.75	0.55–1.07	4.80–5.51	2.91–3.26	0.00–0.15	14.9–15.7	20.3–21.3	0.92–1.28	0.00–0.05	0.00–0.12	98.5–100.3	89.3–90.5
06JY29CPX	Mean	53.6	0.18	1.18	4.33	2.44	0.08	15.5	20.4	1.39	0.01	0.05	99.2	91.9
104	Range	52.9–54.5	0.03–0.28	1.04–1.28	4.11–4.63	2.25–2.59	0.01–0.14	14.8–16.0	19.9–20.7	1.10–1.57	0.00–0.04	0.00–0.11	98.4–100.2	91.5–92.6
06JY31CPX	Mean	53.6	0.29	4.38	1.22	2.83	0.09	16.2	20.5	1.17	0.01	0.05	100.4	91.1
168	Range	52.6–54.6	0.17–0.46	4.28–4.77	1.00–1.36	2.63–3.26	0.02–0.15	15.6–16.9	19.5–21.1	0.98–1.34	0.00–0.05	0.00–0.15	98.7–101.4	90.1–91.8
06JY06OL	Mean	41.5	0.02	0.01	0.02	10.1	0.15	48.3	0.08	0.02	0.01	0.35	100.6	89.6
95	Range	40.4–42.2	0.00–0.08	0.00–0.07	0.00–0.11	9.75–10.4	0.08–0.22	47.6–48.8	0.03–0.11	0.00–0.08	0.00–0.04	0.28–0.43	99.4–101.5	89.3–90.0
06JY29OL	Mean	41.9	0.02	0.01	0.02	8.57	0.13	49.5	0.08	0.01	0.01	0.38	100.6	91.2
158	Range	40.6–42.8	0.00–0.08	0.00–0.06	0.00–0.10	8.34–8.81	0.04–0.21	48.6–50.2	0.03–0.13	0.00–0.08	0.00–0.06	0.30–0.47	98.5–101.5	90.9–91.5
06JY31OL	Mean	42.2	0.02	0.02	0.04	9.35	0.13	48.3	0.11	0.01	0.01	0.38	100.6	90.3
93	Range	41.0–43.1	0.00–0.11	0.00–0.08	0.00–0.12	9.11–9.63	0.07–0.20	47.4–49.3	0.06–0.16	0.00–0.08	0.00–0.04	0.28–0.48	98.6–101.5	90.0–90.6
06JY34OL	Mean	41.8	0.02	0.01	0.02	8.30	0.13	49.7	0.06	0.01	0.01	0.38	100.4	91.5
127	Range	40.8–42.6	0.00–0.10	0.00–0.05	0.00–0.08	8.08–8.50	0.05–0.19	48.7–50.4	0.02–0.10	0.00–0.09	0.00–0.05	0.29–0.46	99.0–101.5	91.3–91.8
09XDTC1-24OL	Mean	42.2	0.02	0.01	0.00	5.69	0.13	51.0	0.01	0.01	0.01	0.34	99.4	94.2
95	Range	41.6–42.7	0.00–0.09	0.00–0.07	0.00–0.03	4.99–6.03	0.06–0.20	50.1–52.1	0.00–0.04	0.00–0.07	0.00–0.04	0.22–0.43	98.5–100.3	93.8–95.0

Note: Mg# = 100 × Mg/(Mg + Fe).

© 2014 The Authors. Geostandards and Geoanalytical Research © 2014 International Association of Geoanalysts

GEOSTANDARDS and GEOANALYTICAL RESEARCH

© 2014 The Authors. Geostandards and Geoanalytical Research © 2014 International Association of Geoanalysts

GEOSTANDARDS and GEOANALYTICAL RESEARCH

Table 2.
Summary of raw data of Li measurements for the orthopyroxene, clinopyroxene and olivine conducted at IGGCAS and CRPG

Sample	Mineral	Session 1 at IGGCAS (1 –5 Feb 2012)				Session 2 at IGGCAS (2 –11 Jan 2014)			
		δ^7Li_m (‰)	Mean ± 1*s*	[^{7}Li] (cps/nA)	Mean ± 1*s*	δ^7Li_m (‰)	Mean ± 1*s*	[^{7}Li] (cps/nA)	Mean ± 1*s*
06JY06OPX	Opx	34.7–38.5	36.6 ± 1.0	66451–75621	69579 ± 581	37.7–41.3	39.4 ± 0.9	63486–75777	68272 ± 629
06JY31OPX	Opx	30.0–33.8	32.0 ± 1.1	52007–65006	58538 ± 360				
06JY34OPX	Opx	32.4–36.5	34.3 ± 1.3	41915–55812	49836 ± 416	36.2–40.3	38.5 ± 1.1	26067–46073	37904 ± 241
06JY06CPX	Cpx	32.2–35.2	33.7 ± 0.8	33900–62996	47928 ± 185				
06JY29CPX	Cpx	26.7–31.8	29.4 ± 1.4	31317–43970	36364 ± 90	32.9–36.1	34.7 ± 0.9	44436–55247	49082 ± 469
06JY31CPX	Cpx	28.9–33.7	31.4 ± 1.3	28469–46416	36694 ± 59				
06JY06OL	Ol	30.4–33.0	31.6 ± 0.7	106334–115148	110865 ±774	33.6–37.2	35.3 ± 0.9	112306–137061	121745 ± 1532
06JY29OL	Ol	24.2–26.8	25.5 ± 0.7	86927–94490	91116 ± 601	26.8–30.2	28.0 ± 1.1	39565–54937	49192 ± 339
06JY31OL	Ol	25.9–29.6	27.3 ± 0.8	92571–101609	96888 ± 497				
06JY34OL	Ol	24.7–28.6	26.9 ± 0.8	72824–79941	76973 ± 466	31.0–34.2	32.7 ± 0.8	89607–99061	93339 ± 1175
09XDTC1-24OL	Ol	27.5–31.6	29.5 ± 1.4	64536–132536	89162 ± 435	33.8–38.6	35.7 ± 1.6	57461–167190	97255 ± 1194
Sample	**Mineral**	**Session 3 at CRPG (10 –11 Sep 2013)**				**Session 4 at CRPG (18 Sep 2013)**			
		δ^7Li_m (‰)	Mean ± 1*s*	[^{7}Li] (cps/nA)	Mean ± 1*s*	δ^7Li_m (‰)	Mean ± 1*s*	[^{7}Li] (cps/nA)	Mean ± 1*s*
06JY06OPX	Opx	41.0–44.0	42.9 ± 1.0	2508–2774	2649 ± 71	36.9–42.9	38.8 ± 2.3	2505–2620	2570 ± 37
06JY31OPX	Opx	37.9–41.9	40.1 ± 1.1	2089–2206	2140 ± 30	34.3–37.9	35.6 ± 1.6	1158–2220	2169 ± 49
06JY34OPX	Opx	34.3–41.9	38.7 ± 1.8	1749–1979	1827 ± 54				
06JY06CPX	Cpx	36.1–43.4	40.6 ± 0.9	1836–2037	1934 ± 46				
06JY29CPX	Cpx	34.5–38.7	35.9 ± 1.3	1399–1720	1546 ± 82				
06JY31CPX	Cpx	36.6–42.0	38.7 ± 1.6	1440–1627	1537 ± 47	33.0–36.5	35.0 ± 1.8	1683–1744	1712 ± 18
06JY06OL	Ol	36.3–38.4	37.2 ± 0.7	4663–4793	4727 ± 34	32.4–35.1	34.0 ± 1.2	4524–4848	4727 ± 100
06JY29OL	Ol	29.9–33.5	32.2 ± 0.9	3649–3830	3731 ± 52				
06JY31OL	Ol	33.6–36.4	34.9 ± 0.8	4057–4240	4161 ± 49	31.0–32.4	31.9 ± 0.6	4382–4582	4479 ± 61
06JY34OL	Ol	30.1–36.6	33.7 ± 1.1	1816–3079	2737 ± 254				
09XDTC1-24OL	Ol								

sessions including pure Li RMs (Li^7N and Li^6N; Carignan *et al.* 2007), seawater (SW), granite (JG-2) and basalt (BHVO; Balter and Vigier 2014). The analyses of these RMs yielded δ^7Li = 30.3 ± 0.6 (all uncertainties for the RMs here are quoted as 2*s*; *n* = 15) for Li^7N; δ^7Li = -8.4 ± 0.8 (*n* = 8) for Li^6N; δ^7Li = 30.6 ± 0.04 (*n* = 1) for SW; δ^7Li = -1.12 ± 0.3 (*n* = 2) for JG-2; and δ^7Li = 4.2 ± 0.8 (*n* = 3) for BHVO.

Results

The mean values and ranges of the major element compositions of olivine, orthopyroxene and clinopyroxene are listed in Table 1 (see Table S1 for the full data set). The δ^7Li values and $^7Li^+$ count rates measured by SIMS are summarised in Table 2 (see Tables S2–S5 for the full data set). Concentrations and isotopic compositions of Li measured by solution ICP-MS and MC-ICP-MS, respectively, are listed in Table 3. The grains appear homogeneous, as evidenced from the lack of compositional zoning and inclusions under backscattered electron microscopy (Figure 1).

06JY06OPX

Sample 06JY06OPX (orthopyroxene) was shown to have an Al_2O_3 content in the range 3.65–4.16% m/m with a mean of 3.84% m/m, a CaO content from 0.72 to 0.92% m/m with a mean of 0.42% m/m and a Mg# (100 × Mg/(Mg + Fe)) of 89.8–90.4 with a mean of 90.1 (Figure 2, Table 1). Thirty-two analyses were conducted on the sample in session 1 using a primary ion current of 20–22 nA. Measured δ^7Li_m values ranged from 34.7 to 38.5‰, forming a Gaussian distribution pattern with a mean δ^7Li_m of 36.6 ± 1.0‰ (Figure 3). The $^7Li^+$ count rates were between 66451 and 75621 cps/nA with a mean of 69579 ± 581 cps/nA (Table 2). In session 2, thirty-two analyses yielded a δ^7Li_m range of 37.7–41.3‰ with a mean value of 39.4 ± 0.9‰, and a $^7Li^+$ count rate of 63486–75777 cps/nA with a mean value of 68272 ± 629 cps/nA (Figure 3, Table 2). Six analyses were conducted in session 3 and five in session 4, giving measured δ^7Li_m values varying from 41.0 to 44.0‰ and from 36.9 to 42.9‰, respectively. The Li concentration and isotopic ratio of the sample measured by ICP-MS and MC-ICP-MS were 1.37 ± 0.16 μg g^{-1} and 3.69 ± 0.03‰ (Table 3).

06JY31OPX

Sample 06JY31OPX (orthopyroxene) was shown to have an Al_2O_3 content of 3.06–3.80% m/m with a mean of 3.34% m/m, a CaO content of 0.76–1.13% m/m (mean = 0.93% m/m) and a Mg# range of 90.6–91.1

Table 3.
Lithium concentration and isotopic results for the orthopyroxene, clinopyroxene and olivine samples measured using ICP-MS at IGGCAS, China, and MC-ICP-MS at CRPG, France, respectively

Sample	Opx					Cpx					Ol				
	Mg#	Li (μg g^{-1})	2*s*	δ^7Li	2*s*	Mg#	Li (μg g^{-1})	2*s*	δ^7Li	2*s*	Mg#	Li (μg g^{-1})	2*s*	δ^7Li	2*s*
06JY06	90.1	1.37	0.16	3.69	0.03	90.0	1.23	0.04	1.34	0.04	89.6	2.23	0.24	5.34	0.29
06JY29						91.9	1.03	0.24	-2.56	0.53	91.2	1.73	0.12	3.09	0.13
06JY31	90.8	1.33	0.24	-0.19	0.21	91.1	1.16	0.02	-2.37	0.45	90.3	2.70	0.60	4.51	0.33
06JY34	92.1	1.07	0.10	-0.77	0.25						91.5	1.46	0.08	3.33	0.16
09XDTC1-24											94.2	1.49	0.06	8.91	0.21

© 2014 The Authors. Geostandards and Geoanalytical Research © 2014 International Association of Geoanalysts

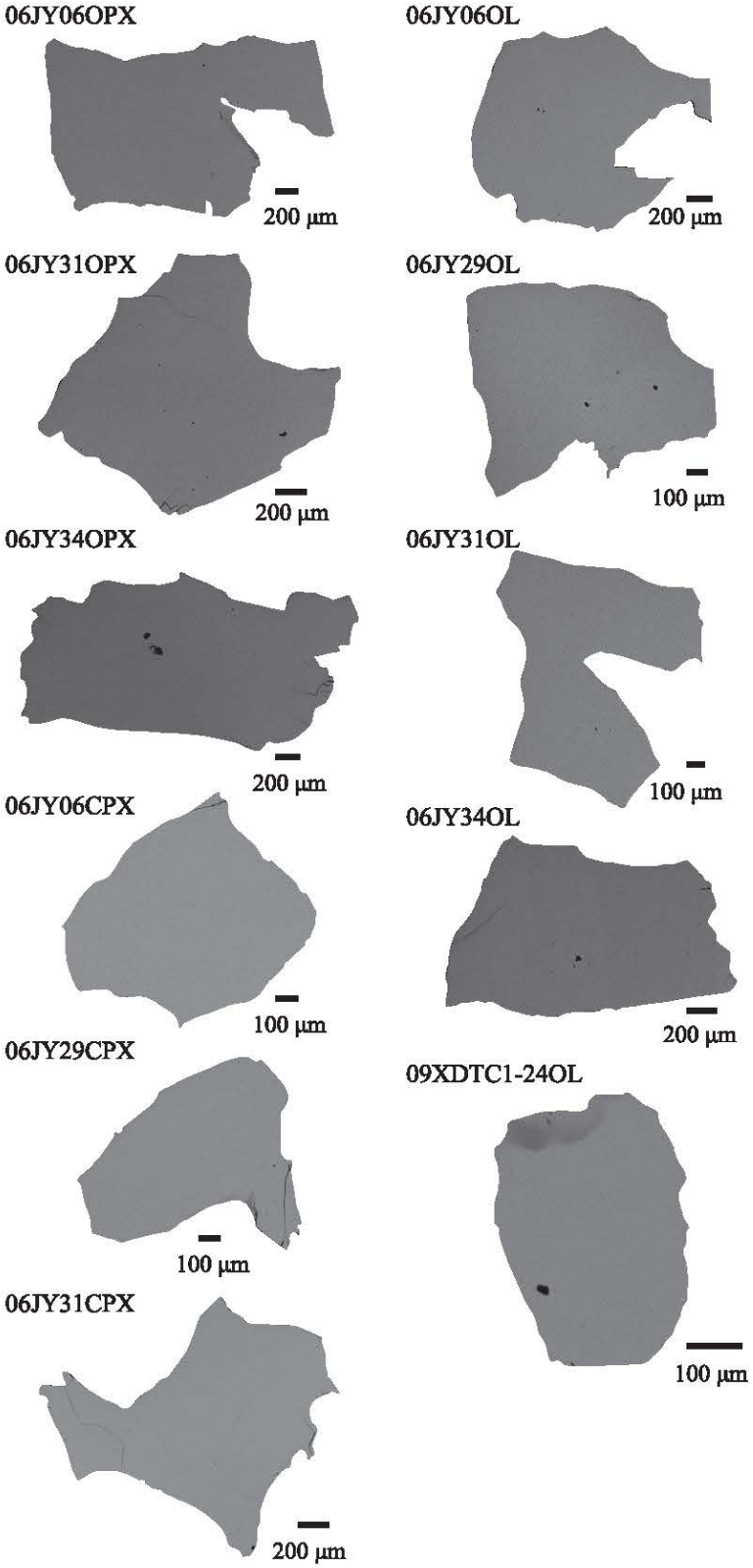

Figure 1. Back-scattered images of representative orthopyroxene, clinopyroxene and olivine grains.

with a mean of 90.8 (Figure 2, Table 1). Thirty-eight measurements were conducted in session 1 with a primary ion current of ~ 20 nA, yielding a restricted δ^7Li_m range of 30.0–33.8‰ and a $^7Li^+$ count rate of 52007–65006 cps/nA. Six measurements were conducted in session 3 and four in session 4 both with a primary ion current of 12–13 nA, which gave δ^7Li_m values of 37.9–41.9 and 34.3–37.9‰, respectively. The Li concentration and isotopic ratio of the sample measured by ICP-MS and MC-ICP-MS were 1.33 ± 0.24 μg g^{-1} and -0.19 ± 0.21‰ (Table 3).

© 2014 The Authors. Geostandards and Geoanalytical Research © 2014 International Association of Geoanalysts

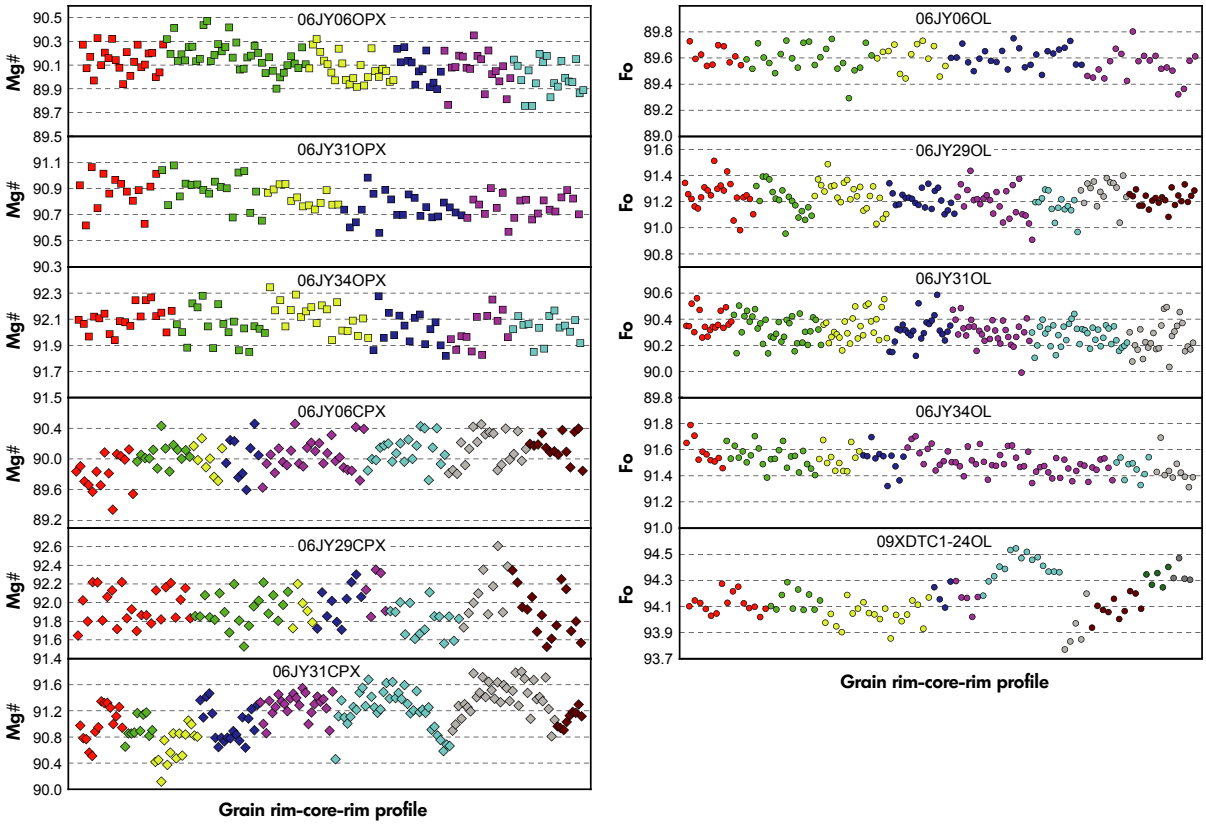

Figure 2. Major element compositions of orthopyroxene, clinopyroxene and olivine. Different grains of an individual sample are marked in a different colour.

06JY34OPX

Sample 06JY34OPX (orthopyroxene) showed narrow compositional variations of 2.66–3.35% m/m Al_2O_3, 0.58–0.80% m/m CaO and 91.8–92.3 Mg# (Figure 2, Table 1). Thirty-three, forty-five and eight analyses were made on the sample in sessions 1, 2 and 3, respectively, with primary ion currents between 10 and 22 nA. Overall, the measured δ^7Li_m values for 06JY34OPX ranged from 32.4 to 41.9‰ in three separate sessions under different instrumental conditions. Analytical uncertainties of the δ^7Li_m values in each single session were between 1.1 and 1.8‰ (Figure 3). The $^7Li^+$ count rates in the three sessions were between 41915 and 55812 cps/nA, 26067 and 46073 cps/nA, and 1749 and 1979 cps/nA, respectively (Table 2). Solution ICP-MS and MC-ICP-MS analyses on the sample gave a Li concentration of 1.07 ± 0.10 µg g^{-1} and δ^7Li of -0.77 ± 0.25‰ (Table 3).

06JY06CPX

Sample 06JY06CPX (clinopyroxene) was characterised by low Al_2O_3 (0.55–1.07% m/m) and Na_2O (0.92–1.28% m/m) and high TiO_2 (0.41–0.75% m/m) and Cr_2O_3 (4.80–5.51% m/m) with a Mg# range of 89.3–90.5 (Figure 2, Table 1). The thirty-eight δ^7Li_m values measured in session 1 ranged from 32.2 to 35.2‰ with a mean of 33.7 ± 0.8‰ (Figure 4), and the $^7Li^+$ count rates ranged from 33900 to 62996 cps/nA with a mean value of 47928 ± 185 cps/nA (Table 2). In session 3, twelve measurements yielded a δ^7Li_m range of 36.1–43.4‰ with a mean value of 40.6 ± 0.9‰ and a $^7Li^+$ count rate between 1836 and 2037 cps/nA (mean value of 1934 ± 46 cps/nA). Solution ICP-MS and MC-ICP-MS analyses of the sample gave a Li concentration of 1.23 ± 0.04 µg g^{-1} and a δ^7Li value of 1.34 ± 0.04‰ (Table 3).

06JY29CPX

Sample 06JY29CPX (clinopyroxene) contained 0.03–0.28% m/m TiO_2, 1.04–1.28% m/m Al_2O_3, 4.11–4.63% m/m Cr_2O_3 and 1.10–1.57% m/m Na_2O, with a Mg# of 91.5–92.6 (Figure 2, Table 1). Three sessions of analysis were conducted on the sample with different primary ion currents (19–21 nA in session 1, 24–25 nA in session 2 and

© 2014 The Authors. Geostandards and Geoanalytical Research © 2014 International Association of Geoanalysts

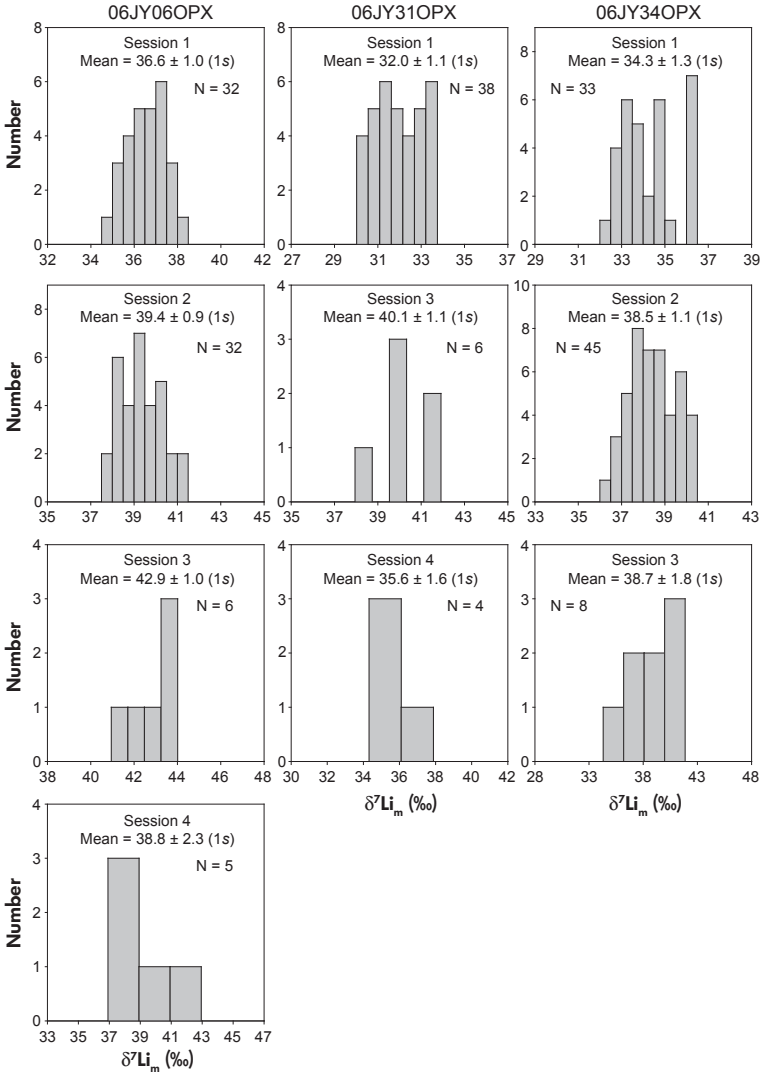

Figure 3. Histograms of the measured raw δ^7Li_m values for orthopyroxene samples 06JY06OPX, 06JY31OPX and 06JY34OPX.

~ 14 nA in session 3, Tables S2–S4). The measured δ^7Li_m values ranged from 26.7 to 31.8, 32.9 to 36.1 and 34.5 to 38.7‰ in sessions 1, 2 and 3, respectively (Figure 4), while their corresponding $^7Li^+$ count rates were 31317–43970, 44436–55247 and 1399–1720 cps/nA (Table 2). The Li concentration and isotopic ratio of the sample measured by ICP-MS and MC-ICP-MS were 1.03 ± 0.24 μg g^{-1} and -2.56 ± 0.53‰ (Table 3).

06JY31CPX

Sample 06JY31CPX (clinopyroxene) was characterised by high Al_2O_3 (4.28–4.77% m/m) and low Cr_2O_3 (1.00–1.36% m/m) contents. Its TiO_2 and Na_2O contents and Mg# values ranged from 0.17 to 0.46, 0.98 to 1.34 and 90.1 to 91.8% m/m, respectively (Table 1, Figure 2). Although a few crystals were slightly zoned in terms of Mg# profile, these did not show spatial zoning of other analytes such as Al_2O_3, TiO_2 or Na_2O (now shown in Figure 2; see data in Table S1). The forty-five measurements conducted on the sample in session 1 yielded a δ^7Li_m range of 28.9–33.7‰ with a mean value of 31.4 ± 1.3‰ and a $^7Li^+$ count rate between 28469 and 46416 cps/nA (mean of 36694 ± 59 cps/nA; Figure 4, Table 2). Six measurements were conducted in session 3 and four in session 4, yielding δ^7Li_m variations of 36.6–42.0 and 33.0–36.5‰, respectively (Figure 4, Table 2). Solution ICP-MS and MC-ICP-MS analyses on the sample gave a Li concentration of 1.16 ± 0.02 μg g^{-1} and a δ^7Li of -2.37 ± 0.45‰ (Table 3).

06JY06OL

Sample 06JY06OL (olivine) had a restricted Mg# of 89.3–90.0 with a mean value of 89.6 (Figure 2). Forty, thirty-nine, eight and four measurements were conducted in the four sessions, respectively, each under different instrumental conditions. Overall, the measured δ^7Li_m values in each single

© 2014 The Authors. Geostandards and Geoanalytical Research © 2014 International Association of Geoanalysts

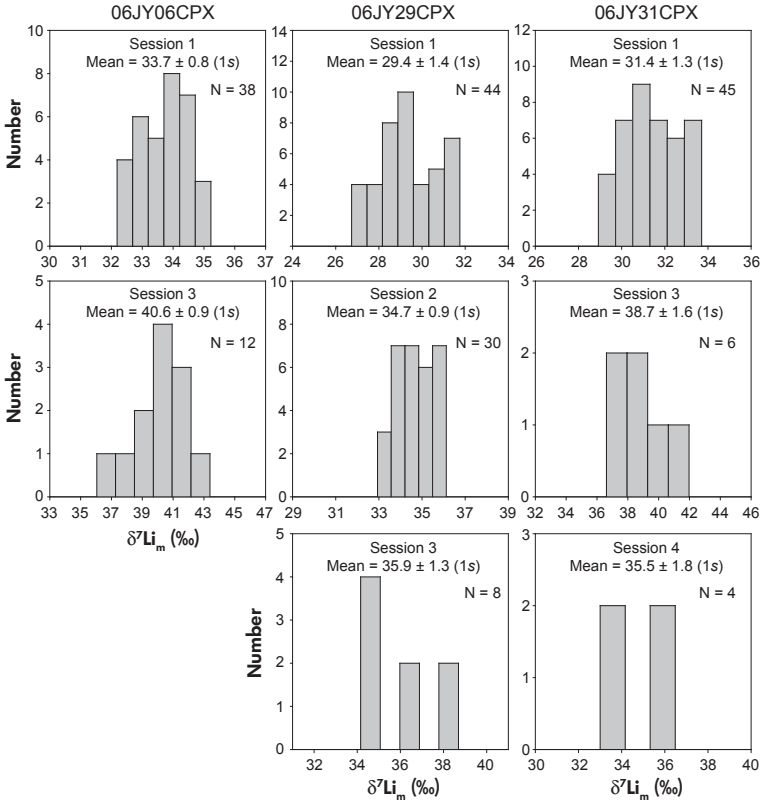

Figure 4. Histograms of the measured raw δ^7Li_m values for clinopyroxene samples 06JY06CPX, 06JY29CPX and 06JY31CPX.

session had a restricted range (Figure 5), and analytical uncertainties of the δ^7Li_m values were between 0.7 and 1.2‰ (Table 2). The $^7Li^+$ count rates in sessions 1 and 2 were between 106334 and 137061 cps/nA, and the third and fourth sessions gave a $^7Li^+$ count rate range of 4524–4848 cps/nA (Table 2). The sample contained 2.23 ± 0.24 μg g^{-1} Li and a δ^7Li of 5.34 ± 0.29‰, as measured by ICP-MS and MC-ICP-MS, respectively (Table 3).

06JY29OL

Sample 06JY29OL (olivine) was determined to have a Mg# ranging from 90.9 to 91.5 with a mean value of 91.2 (Table 1). Three analytical sessions were conducted on the sample. The forty-one analyses in session 1 yielded a δ^7Li_m range of 24.2–26.8‰ with a mean value of 25.5 ± 0.7‰ and a $^7Li^+$ count rate range from 86927 to 94490 cps/nA with a mean value of 91116 ± 601 (Figure 5, Table 2). The fourteen measurements of δ^7Li_m in session 2 were in the range 26.8–30.2‰ (mean value 28.0 ± 1.1‰), and the $^7Li^+$ count rate in the same session varied from 39565 to 54937 cps/nA (mean value 49192 ± 339 cps/nA). In session 3, eight analyses gave δ^7Li_m between 29.9 and 33.5 (mean value 32.2 ± 0.9‰), and the $^7Li^+$ count rates were between 3649 and 3830 cps/nA with a mean of 3731 ± 52 cps/nA. The Li concentration and δ^7Li value measured by ICP-MS and MC-ICP-MS were 1.73 ± 0.12 μg g^{-1} and 3.09 ± 0.13‰ (Table 3).

06JY31OL

Sample 06JY31OL (olivine) had a narrow Mg# range of 90.0–90.6 (Figure 2, Table 1). Three SIMS sessions were conducted on the sample with different primary ion currents of 19–20 nA, ~ 14 nA and ~ 13 nA (Tables S2, S4 and S5). Overall, the analyses in each single session yielded restricted δ^7Li_m values and $^7Li^+$ count rate ranges (Figure 5, Table 2). The mean values of δ^7Li_m and $^7Li^+$ count rate in three sessions were 27.3 ± 0.8‰ and 96888 ± 497 cps/nA, 34.9 ± 0.8‰ and 4161 ± 49 cps/nA, and 31.9 ± 0.6‰ and 4479 ± 61 cps/nA, respectively (Figure 5, Table 2). The Li content of the sample was 2.70 ± 0.60 μg g^{-1} and its δ^7Li values was determined as 4.51 ± 0.33‰, measured by ICP-MS and MC-ICP-MS, respectively (Table 3).

06JY34OL

Sample 06JY34OL (olivine) had a Mg# range of 91.3–91.8 with a mean value of 91.5 (Figure 2, Table 1). Thirty-six, thirty and twelve SIMS measurements were conducted in sessions 1, 2 and 3, respectively. The measured δ^7Li_m values in each single session formed a Gaussian distribution

© 2014 The Authors. Geostandards and Geoanalytical Research © 2014 International Association of Geoanalysts

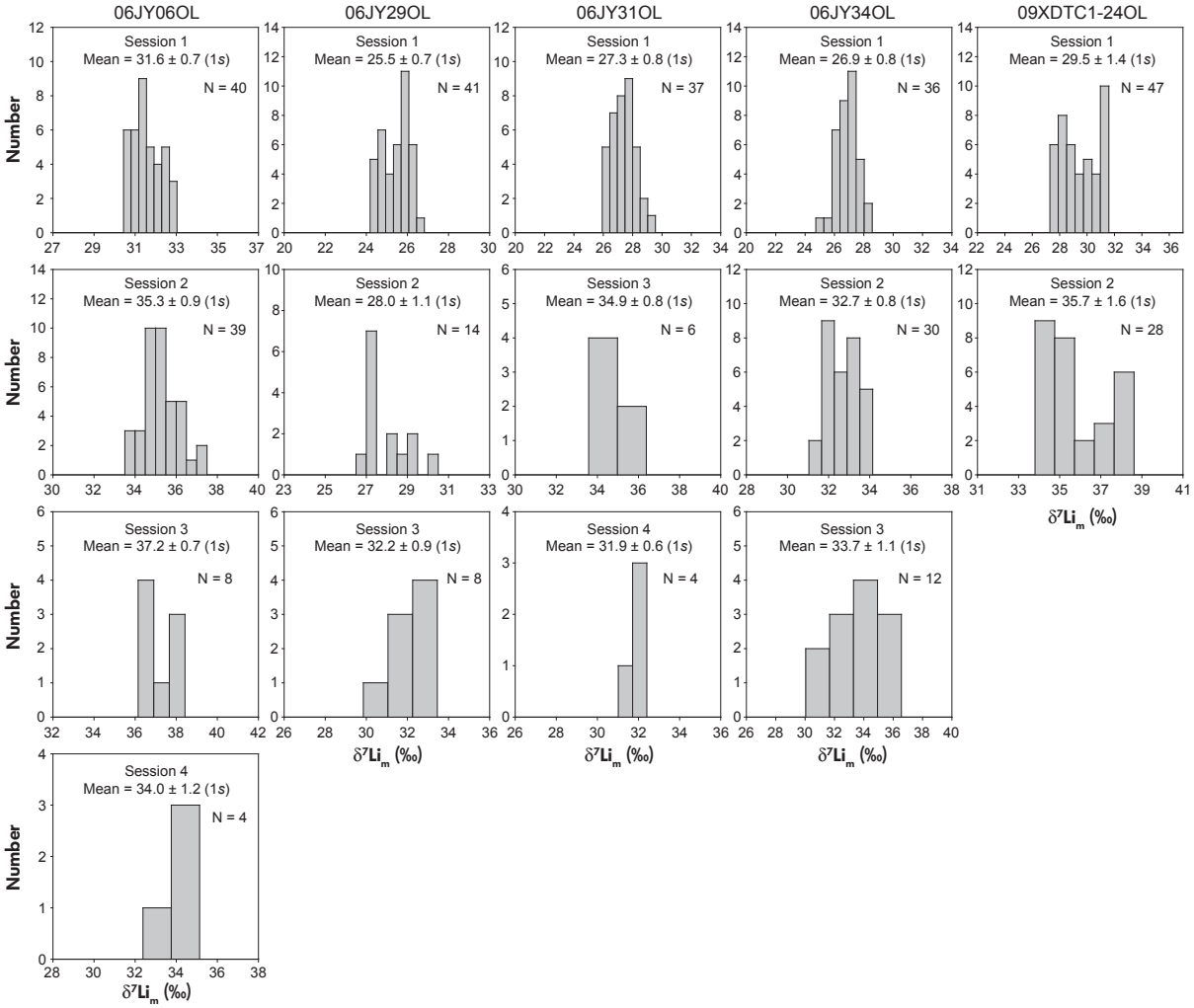

Figure 5. Histograms of the measured raw δ^7Li_m values for olivine samples 06JY06OL, 06JY29OL, 06JY31OL, 06JY34OL and 09XDTC1-24OL.

pattern with mean values of 26.9 ± 0.8, 32.7 ± 0.8 and 33.7 ± 1.1‰ (Figure 5). The $^7Li^+$ count rates were in the ranges 72824–79941, 89607–99061 and 1816–3079 cps/nA in the first, second and third sessions, respectively (Table 2). The Li concentration and δ^7Li value of the sample measured by ICP-MS and MC-ICP-MS were 1.46 ± 0.08 μg g^{-1} and 3.33 ± 0.16‰ (Table 3).

09XDTC1-24OL

Sample 09XDTC1-24OL (olivine) was characterised as having a very high Mg# of 93.8–95.0, with a mean value of 94.2 (Figure 2, Table 1). Forty-seven SIMS measurements were conducted on the sample in session 1 and twenty-eight in session 2. The measured δ^7Li_m values in session 1 ranged from 27.5 to 31.6‰ with a mean of 29.5 ± 1.4‰, and the $^7Li^+$ count rates in this session varied from 64536 to 132536 cps/nA with a mean of 89162 ± 435 cps/nA (Figure 5, Table 2). In session 2, the δ^7Li_m values and $^7Li^+$ count rates were 33.8–38.6‰ and 57461–167190 cps/nA, respectively. The ICP-MS and MC-ICP-MS analyses on the sample gave a Li concentration of 1.49 ± 0.06 μg g^{-1} and a δ^7Li value of 8.91 ± 0.21‰ (Table 3).

Discussion and concluding remarks

Eleven mineral separates including olivine, orthopyroxene and clinopyroxene were shown by extensive EPMA data to have low within-sample variations in terms of major elements. Five samples of olivine had Fo contents ranging from 89.3 to 94.2 with homogeneous compositions in individual samples (Table 1, Figure 2). There were considerable intersample variations for the three samples of orthopyroxene (~ 2.66–4.16% m/m Al_2O_3 and

 © 2014 The Authors. Geostandards and Geoanalytical Research © 2014 International Association of Geoanalysts

Mg# = 89.8–92.3) and the three samples of clinopyroxene (~ 0.55–4.77% m/m Al_2O_3, ~ 1.00–5.51% m/m Cr_2O_3, ~ 0.92–1.57% m/m Na_2O and Mg# = 89.3–92.6). The SIMS data demonstrate the homogeneity of the measured δ^7Li_m value and the constancy of the $^7Li^+$ count rate, although some data did not show Gaussian distribution patterns, most likely due to the low number of analyses. The δ^7Li_m values of the olivine, orthopyroxene and clinopyroxene samples in each of the four sessions generally varied within 4, 4 and 5‰, respectively (Figure 3, Table 2), while the narrow ranges of the $^7Li^+$ count rate indicate that Li concentrations of these minerals are homogeneous. This study demonstrates that analysed samples can be used as working references for *in situ* determination of Li concentration and isotope composition using SIMS and LA-MC-ICP-MS.

The lithium contents measured in our samples are in the range typical of depleted mantle peridotite (Tang *et al.* 2007, 2014, Su *et al.* 2014a), but the concentration ratios between the different phases (olivine–clinopyroxene, olivine–orthopyroxene and clinopyroxene–orthopyroxene) are not at equilibrium (Table 3; Seitz and Woodland 2000), even where in most cases, olivine is the main Li carrier. The nonequilibrium of Li contents could be related to a late-stage process whereby these peridotite minerals experienced Li exchange with melt or fluid shortly before or coincident with their entrainment into the host basalt (Rudnick and Ionov 2007, Tang *et al.* 2012). However, the measured δ^7Li values of the olivine span a small range from +3 to +9‰, which is well within that of the upper mantle range (Tang *et al.* 2007, Su *et al.* 2014a, b). We note that the olivine displayed higher δ^7Li values than the orthopyroxene, and the orthopyroxene higher values than the clinopyroxene, as expected from descriptions in the literature (Jeffcoate *et al.* 2007, Wagner and Deloule 2007). As a whole, our samples are therefore representative of mantle peridotite.

The SIMS data from sessions 1 and 3 were used for consideration of instrumental mass fractionation (IMF) as a function of mineral species and chemical composition. The compositional dependence of IMF (matrix effect) is illustrated by plotting for each sample the difference between the average δ^7Li determined by SIMS and the bulk solution δ^7Li by MC-ICP-MS (Figure 6). Due to the narrow compositional ranges (Mg# = 90–92) of only three samples of both orthopyroxene and clinopyroxene, the correlation parameters between Mg# and δ^7Li_{SIMS}–$\delta^7Li_{MC\text{-}ICP\text{-}MS}$ for clinopyroxene are very small, while contrasting tendencies for orthopyroxene were presented in the two sessions. Although an empirical conclusion cannot be reached, it appears that

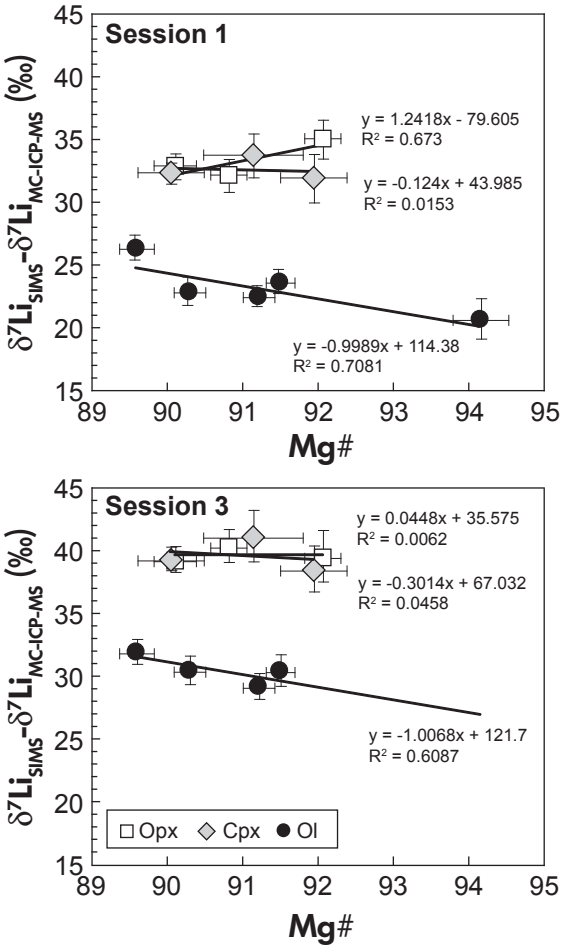

Figure 6. Variation of the instrumental mass fractionation (IMF) as a function of Mg# (100 × Mg/(Mg + Fe)) composition for orthopyroxene, clinopyroxene and olivine, determined on the secondary ion mass spectrometry (SIMS) at IGGCAS. The IMF was calculated as the difference between the average δ^7Li measured by SIMS and that determined by MC-ICP-MS. Errors were propagated from both MC-ICP-MS and SIMS analyses. The line and its equation represent a conventional *y* on *x* linear regression.

our uncertainties do not reveal any IMF as a function of composition induced by Mg# among the studied clinopyroxene samples. For olivine, both plots show a clear tendency for δ^7Li to increase with decreasing Fo content (Figure 6). Linear regression of the data yielded a 1.0‰ matrix effect per Fo unit, which is slightly lower than the result (1.3‰) of Bell *et al.* (2009). However, it should be noted that the analyses of Bell *et al.* (2009) were performed using Cameca IMS 3f and 6f ion microprobes at Arizona State University, with different instrumental conditions that may explain this discrepancy. Olivine composition must, therefore,

© 2014 The Authors. Geostandards and Geoanalytical Research © 2014 International Association of Geoanalysts

be known precisely for accurate Li isotope determination by SIMS.

Acknowledgements

This work was financially supported by the National Natural Science Foundation of China (Grants 41173009, 41173011 and 91214203), the Strategic Priority Research Programme (B) of the Chinese Academy of Sciences (Grant No. XDB03010203), and Hong Kong Scholars Programme (No. XJ2012048).

References

Balter V. and Vigier N. (2014)
Natural variations of lithium isotopes in a mammalian model. **Metallomics**, **6**, 582–586.

Beck P., Barrat J.A., Chaussidon M., Gillet P. and Bohn M. (2004)
Lithium isotopes in the northwest Africa 480 shergottite (NWA 480): A record of degassing of Martian magmas? **Geochimica et Cosmochimica Acta**, **68**, 2925–2933.

Beck P., Chaussidon M., Barrat J.A., Gillet P. and Bohn M. (2006)
Diffusion induced Li isotopic fractionation during the cooling of magmatic rocks: The case of pyroxene phenocrysts from nakhlite meteorites. **Geochimica et Cosmochimica Acta**, **70**, 4813–4825.

Bell D.R., Hervig R.L., Buseck P.R. and Aulbach S. (2009)
Lithium isotope analysis of olivine by SIMS: Calibration of a matrix effect and application to magmatic phenocrysts. **Chemical Geology**, **258**, 5–16.

Bouvier A.S., Métrich N. and Deloule E. (2008)
Slab-derived fluids in magma sources of St. Vincent (Lesser Antilles Arc): Volatile and light element imprints. **Journal of Petrology**, **49**, 1427–1448.

Bouvier A.S., Métrich N. and Deloule E. (2010)
Volatiles, light elements and stable isotopes in Grenada magmas (Lesser Antilles). Do melt inclusions record a pressure column melting of mantle? **Geochemistry, Geophysics, Geosystems**, 2010GC003051.

Carignan J., Vigier N. and Millot R. (2007)
Three secondary reference materials for Li isotope measurements: Li^{7}-N, Li^{6}-N and LiCl-N solutions. **Geostandards and Geoanalytical Research**, **31**, 7–12.

Chan L.H., Edmond J.M., Thompson G. and Gillis K. (1992)
Lithium isotopic composition of submarine basalts: Implications for the lithium cycle in the oceans. **Earth and Planetary Science Letters**, **108**, 151–160.

Coogan L.A., Kasemann S.A. and Chakraborty S. (2005)
Rates of hydrothermal cooling of new oceanic crust derived from lithium-geospeedometry. **Earth and Planetary Science Letters**, **240**, 415–424.

Decitre S., Deloule E., Reisberg L., James R., Agrinier P. and Mével C. (2002)
Behavior of Li and its isotopes during serpentinization of oceanic peridotites. **Geochemistry, Geophysics, Geosystems**, **3**, 1–20.

Dohmen R., Kasemann S.A., Coogan L.A. and Chakraborty S. (2010)
Diffusion of Li in olivine. Part 1: Experimental observations and a multiple species diffusion model. **Geochimica et Cosmochimica Acta**, **74**, 274–292.

Flesch G.D., Anderson A.R.J. and Svec H.J. (1973)
A secondary isotopic standard for $^{6}Li/^{7}Li$ determinations. **International Journal of Mass Spectrometry and Ion Physics**, **12**, 265–272.

Gallagher K. and Elliott T. (2009)
Fractionation of lithium isotopes in magmatic systems as a natural consequence of cooling. **Earth and Planetary Science Letters**, **278**, 286–296.

Halama R., McDonough W.F., Rudnick R.L. and Bell K. (2008)
Tracking the lithium isotopic evolution of the mantle using carbonatites. **Earth and Planetary Science Letters**, **265**, 726–742.

Hamelin C., Seitz H.M., Barrat J.A., Dosso L., Maury R.C. and Chaussidon M. (2009)
A low δ^{7}Li lower crustal component: Evidence from an alkalic intraplate volcanic series (Chaîne des Puys, French Massif Central). **Chemical Geology**, **266**, 205–217.

Jeffcoate A.B., Elliott T., Kasemann S.A., Ionov D., Cooper K. and Brooker R. (2007)
Li isotope fractionation in peridotites and mafic melts. **Geochimica et Cosmochimica Acta**, **71**, 202–218.

Kasemann S.A., Jeffcoate A.B. and Elliott T. (2005)
Lithium isotope composition of basalt glass reference material. **Analytical Chemistry**, **77**, 5251–5257.

Li X.H., Li Q.L., Liu Y. and Tang G.Q. (2011)
Further characterisation of M257 zircon standard: A working reference for SIMS analysis of Li isotopes. **Journal of Analytical Atomic Spectrometry**, **26**, 352–358.

Li P., Xia Q.K. and Deloule E. (2012)
Anomalous lithium isotopic compositions of the Cenozoic lithospheric mantle beneath Penglai, Shandong Province: The ion probe analyses of peridotite xenoliths. **Geological Journal of China Universities**, **18**, 62–73.

Lundstrom C.C., Chaussidon M., Hsui A.T., Kelemen P. and Zimmerman M. (2005)
Observations of Li isotopic variations in the Trinity Ophiolite: Evidence for isotopic fractionation by diffusion during mantle melting. **Geochimica et Cosmochimica Acta**, **69**, 735–751.

Magna T., Ionov D.A., Oberli F. and Wiechert U. (2008)
Links between mantle metasomatism and lithium isotopes: Evidence from glass-bearing and cryptically metasomatized xenoliths from Mongolia. **Earth and Planetary Science Letters**, **276**, 214–222.

 © 2014 The Authors. Geostandards and Geoanalytical Research © 2014 International Association of Geoanalysts

references

Millot R., Guerrot C. and Vigier N. (2004)
Accurate and high-precision isotopic measurements of lithium isotopes in two reference materials by MC-ICP-MS. Geostandards and Geoanalytical Research, 28, 153–160.

Richter F.M., Davis A.M., DePaolo D.J. and Watson E.B. (2003)
Isotope fractionation by chemical diffusion between molten basalt and rhyolite. Geochimica et Cosmochimica Acta, 67, 3905–3923.

Richter F.M., Watson B., Chaussidon M., Mendybaev R. and Ruscitto D. (2014)
Lithium isotope fractionation by diffusion in minerals. Part 1: Pyroxenes. Geochimica et Cosmochimica Acta, 126, 352–370.

Rudnick R.L. and Ionov D.A. (2007)
Lithium elemental and isotopic disequilibrium in minerals from peridotite xenoliths from far east Russia: Product of recent melt/fluid-rock reaction. Earth and Planetary Science Letters, 256, 278–293.

Seitz H.M. and Woodland A.B. (2000)
The distribution of lithium in peridotitic and pyroxenitic mantle lithologies – an indicator of magmatic and metasomatic processes. Chemical Geology, 166, 47–64.

Su B.X., Zhang H.F., Deloule E., Sakyi P.A., Xiao Y., Tang Y.J., Hu Y., Ying J.F. and Liu P.P. (2012a)
Extremely high Li and low δ^7Li signatures in the lithospheric mantle. Chemical Geology, 292–293, 149–157.

Su B.X., Qin K.Z., Sakyi P.A., Malaviarachchi S.P.K., Liu P.P., Tang D.M., Xiao Q.H., Sun H., Ma Y.G. and Mao Q. (2012b)
Occurrence of an Alaskan-type complex in the Middle Tianshan Massif, Central Asian Orogenic Belt: Inferences from petrological and mineralogical studies. International Geology Review, 54, 249–269.

Su B.X., Zhang H.F., Deloule E., Vigier N. and Sakyi P.A. (2014a)
Lithium elemental and isotopic variations in rock-melt interaction. Chemie der Erde/Geochemistry, doi:10.1016/j.chemer.2014.04.005.

Su B.X., Zhang H.F., Deloule E., Vigier N., Hu Y., Tang Y.J., Xiao Y. and Sakyi P.A. (2014b)
Distinguishing silicate and carbonatite mantle metasomatism by using lithium and its isotopes. Chemical Geology, 381, 67–77.

Tang Y.J., Zhang H.F., Nakamura E., Moriguti T., Kobayashi K. and Ying J.F. (2007)
Lithium isotopic systematics of peridotite xenoliths from Hannuoba, North China Craton: Implications for melt-rock interaction in the considerably thinned lithospheric mantle. Geochimica et Cosmochimica Acta, 71, 4327–4341.

Tang Y.J., Zhang H.F., Deloule E., Su B.X., Ying J.F., Xiao Y. and Hu Y. (2012)
Slab-derived lithium isotopic signatures in mantle xenoliths from northeastern North China Craton. Lithos, 149, 79–90.

Tang Y.J., Zhang H.F., Deloule E., Su B.X., Ying J.F., Santosh M. and Xiao Y. (2014)
Abnormal lithium isotope composition from the ancient lithospheric mantle beneath the North China Craton. Scientific Reports, 4, 4274.

Teng F.Z., McDonough W.F., Rudnick R.L. and Walker R.J. (2006)
Diffusion-driven extreme lithium isotopic fractionation in country rocks of the Tin Mountain pegmatite. Earth and Planetary Science Letters, 243, 701–710.

Tomascak P.B. (2004)
Developments in the understanding and application of lithium isotopes in Earth and planetary sciences. Reviews in Mineralogy and Geochemistry, 55, 153–195.

Vigier N., Decarreau A., Millot R., Carignan J., Petit S. and France-Lanord C. (2008)
Quantifying Li isotope fractionation during smectite formation and implications for the Li cycle. Geochimica et Cosmochimica Acta, 72, 780–792.

Wagner C. and Deloule E. (2007)
Behaviour of Li and its isotopes during metasomatism of French Massif Central lherzolites. Geochimica et Cosmochimica Acta, 71, 4279–4296.

Xu R., Liu Y., Tong X., Hu Z., Zong K. and Gao S. (2013)
In situ trace elements and Li and Sr isotopes in peridotite xenoliths from Kuandian, North China Craton: Insights into Pacific slab subduction-related mantle modification. Chemical Geology, 354, 107–123.

Zhang H.F., Deloule E., Tang Y.J. and Ying J.F. (2010)
Melt/rock interaction in remains of refertilized Archean lithospheric mantle in Jiaodong Peninsula, North China Craton: Li isotopic evidence. Contributions to Mineralogy and Petrology, 160, 261–277.

Supporting information

The following supplementary information may be found in the online version of this article:

Tables S1–S5. Complete analytical data set.

This material is available as part of the online article from: http://onlinelibrary.wiley.com/doi/10.1111/j.1751-908X.2014.00313.x/abstract (This link will take you to the article abstract).

© 2014 The Authors. Geostandards and Geoanalytical Research © 2014 International Association of Geoanalysts

Multi-stage metasomatism revealed by trace element and Li isotope distributions in minerals of peridotite xenoliths from Allègre volcano (French Massif Central)

Xiaoyan GU [a], Etienne DELOULE [a], Lydéric FRANCE [a], Jannick INGRIN [b],

[a] CRPG, UMR CNRS 5873 - Université de Lorraine, 54501 Vandoeuvre les Nancy, France

[b] UMET, UMR CNRS 8207, Université de Lille1, Bât. C6, 59655 Villeneuve d'Ascq, France

Keywords: Mantle metasomatism; Xenolith-host magma interaction; Li isotope; Low δ^7Li value; Peridotite xenolith; French Massif Central.

COMMENTS FROM EDITORS AND REVIEWERS

Dear Dr. Gu,
Reviewers have now commented your paper. You will see that both reviewers are supportive of publication pending major and moderate revision. Comments are clearly reported in two constructive reviews: please carefully address all queries in the revised manuscript text and in a point by point rebuttal letter.

In more detail, the critical reviewer 1 provides several scientific and editorial comments. From an editorial point of view, the reviewer suggests you:
(1) to improve and rewrite the abstract;
(2) to improve the petrographic description of rocks for identifying possible metasomatic phases that may shed light on the type and nature of metasomatic processes and agents;
(3) to shorten, focus and clarify the discussion section;
(4) to cut the number of references. The maximum number of references for a regular Lithos submission is around 80. Please reduce the number to a maximum of 90-100 references.

From a scientific point of view, reviewer 1 is unconvinced that the trace element metasomatic signature of the studied rocks can be unequivocally attributed to carbonatite metasomatism. Silicate melts can induce similar variations. Therefore, it is suggested to seek for diagnostic minerals, and to provide more detailed textural and petrographic descriptions of rocks. Reviewer 1 also suggest to compare direct bulk-rock Li analyses with mass balance estimates of bulk Li contents, to define if some intragranular phase may host excess Li that is not accounted for by major rock-forming minerals.

If you think you can address the reviewers' comments, please submit the revised manuscript within 60 days. Clearly show in a marked manuscript the changes done to the text; discuss these changes and the eventual disagreement with the revisers in the accompanying letter.

With kind regards

Marco Scambelluri
Lithos editor

General comments from Reviewer 1:

I revised the paper entitled: "*Multi-stage metasomatism revealed by trace element and Li isotope distributions in minerals of peridotite xenoliths from Allègre volcano (French Massif Central)"*. This manuscript details the descriptions of some peridotite xenoliths in the southern domain of the French Massif Central. The study based on in-situ measurements of trace elements in clinopyroxenes by using LA-ICP-MS, and lithium concentrations and isotopic compositions in pyroxenes and olivines.

-The manuscript is interested and introduces exceptionally high Li concentrations in Cpx. The trace elements and lithium isotope are used to indicate the stages of metasomatism or multi-stage metasomatism. They can be used to distinguish the partial melting stage and subsequent metasomatic events. The scientific contents and data are also of high standard, but some sections in discussion are not of high standard and need more modifications. I suggest re-writing the abstract and putting the interested data. Your abstract is slightly similar to abstract that was published in Goldschmidit 2014. Your abstract should be mature enough. The authors referred to modal compositional modification of peridotites, try to focus on metasomatic minerals used as evidence of modal metasomatism; I think that plagioclase is one evidence of refertilization and metasomatism in your paper…….etc.

-Petrographic part isn't in a good shape. I know you focus on geochemistry, but try to re-write the petrographic part too.

Discussion is length, and is sometimes not easy to understand. The title of some sections in Discussion is not match with the text content. For example: section: ***7.1 Depletion controlled by partial melting***; this title should be changed and the text should be modified. Discussion sections should include parts for tectonic setting and origin of peridotites. The tectonic setting can be determined by mineral chemistry. You can draw one figure (a, b) including spinelCr# - Olv Fo for tectonic setting (Arai, 1994) and SpinelCr#-spinel Mg# (Dick and Bullen, 19984); also, for CpxNa2O versus SpinelCr#

diagram (see comment #29).

-the authors depend on the negative HFSE associated with enrichment of LREE as evidence of carbonatite metasomatism; this is also for silicate metasomatism. The carbonatite metasomatism is characterized by appearance of some minerals such as Clinopyroxene, phlogopite, apatite and k-feldspar (Guzmics et al., 2008 MP). These minerals are the products of metasomatic reactions between ultramafic mantle and carbonatite melt initially infiltrating the mantle rock (Guzmics et al., 2008 MP). Do you check the other secondary minerals or metasomatized minerals to support your suggestion?

The authors used around 154 references; try to reduce the references to be 90 or less, try to exclude conference references, thesis references and book references and used the update and the pioneering works. There are too many citations that destroy the personality of the authors. What is your idea or your personality?

Abbreviation, you can use Cpx and Opx as abbreviations to long word orthopyroxene and clinopyroxene but all minerals (short word) are named by the full names: Spl, spinel; ol: olivine….etc. Please, don't use abbrivaition for ol, spl, and others.

Another important point is the determination of Li in bulk rock. The authors determined the Li in-situ analyses in olivine and pyroxenes. If you determined the Li as bulk and calculate Li based on a mass-balance calculation for minerals (modal% of minerals from point counting and concentration of Li in minerals); then compare the calculated Li from mass balance and Li contents from bulk-rock analyses; the results can be used to indicate if Li can be concentrated on the grain boundaries or not? Also, you can compare Li as bulk with Li in minerals.

The authors should take care of figures. Some parts of the MS must be modified based on the comments below. This paper can be accepted after "***Major Revision***". Please, check the following detail comments to modify your paper.

Reviewed by Mohamed Zaki Khedr

Comments from Reviewer 2:

The manuscript presents a characterization of Li elemental/isotope systematics in a suite of mantle xenoliths from the Massif Central, paralleled by petrography and geochemical data. This coherent suite is thus well dedicated to the major aim of the manuscript, i.e. to provide possible link between partial melting/metasomatic overprints and Li systematics. The manuscript is clearly written, well structured, fully referenced; the conclusions are sound and provided with reasonable discussion, not only for the intrinsic suite studied by the authors but also with possible relation to other settings where mantle xenoliths are found, here mostly focused to Cenozoic alkaline volcanism in western and central Europe. I do not hold any major reservations and have only minor comments, which are below.
Reviewed by Tomas Magna

Multi-stage metasomatism revealed by trace element and Li isotope distributions in minerals of peridotite xenoliths from Allègre volcano (French Massif Central)

Xiaoyan GU [a], Etienne DELOULE [a], Lydéric FRANCE [a], Jannick INGRIN [b],

[a] CRPG, UMR CNRS 5873 - Université de Lorraine, 54501 Vandoeuvre les Nancy, France

[b] UMET, UMR CNRS 8207, Université de Lille1, Bât. C6, 59655 Villeneuve d'Ascq, France

Keywords: Mantle metasomatism; Xenolith-host magma interaction; Li content; δ^7Li; Peridotite xenolith; French Massif Central.

Abstract

The modal, chemical, and isotopic compositions of mantle peridotite are largely modified by metasomatic impregnations, which may affect them repeatedly. Xenoliths are commonly used to characterize those metasomatic processes along with the structure, and chemical and isotopic compositions of mantle domains. Nevertheless, the original mantle signatures borne by mantle xenoliths are potentially skewed by the interactions occurring between the host magma and the xenolith itself. Here we attempt to identify to which degree the original Li contents and isotopic compositions, as well as other trace element contents from mantle xenoliths, can be modified by interactions with the host magma. Peridotite xenoliths that have suffered extensive interactions with the host magma were sampled in the solidified lava lake of Allègre, in the South of the French Massif Central in order to decipher the signature related to the xenolith-host melt interaction, and to further unravel the evolution of the sub-continental lithospheric mantle. *In-situ* measurements were conducted for trace element composition in clinopyroxene (Cpx) by LA-ICP-MS, and for lithium content and isotopic composition in pyroxene and olivine (Ol) by SIMS. Negative HFSE anomalies (Ti/Eu ratio as low as 437) and markedly high LREE/HREE ratios ($(La/Yb)_N$ as high as 79) are characteristic of a mantle metasomatism in depth. Lithium isotopic systematic indicate that at least two different metasomatic events affected the peridotite. Exceptionally high Li contents, up to 50 ppm, in Cpx and slightly Li enrichment of Ol rims are ascribed to a diffusive Li influx with a positive δ^7Li value (+3.2‰) from the host magma. On the other hand, Ol cores preserved an extremely light Li isotopic compositions (δ^7Li as low as -25‰) with high Li content (up to

4.4 ppm) compared to normal mantle. This points out a metasomatic event occurring before the xenoliths entrainment to the surface. The negative δ^7Li signature of this early metasomatism can be related to the fluids released during the subduction that occurred during the Variscan orogeny. It can be shown from the trace element distribution in the minerals that the HFSE and REE signatures in Cpx and the negative δ^7Li signature in Ol cores were not acquired simultaneously. Therefore at least three successive metasomatic evens affected the Allegre peridotite, revealed through the use of detailed *in-situ* Li isotopic analyses to trace melt-rock interactions.

1. Introduction

Mantle xenoliths are transported to the surface by rapidly upwelling magmas (alkali basalts or kimberlites), and have traditionally been considered to be capable of retaining intrinsic signatures of the lithospheric mantle at the time of entrainment. Peridotite xenoliths thus provide insight into the composition (mineralogical and geochemical) and evolution of the upper mantle. Although peridotite xenoliths retain their in-depth major element compositions after various degrees of partial melting (Herzberg, 2004; Walter, 2003), most have subsequently been modified by melt/fluid percolations (i.e., mantle metasomatism; Bodinier et al., 1990; Menzies and Hawkesworth, 1987; Rudnick et al., 1993).

Metasomatism typically induces significant variations in whole-rock and mineral trace element compositions (cryptic metasomatism), sometimes accompanied by mineralogical changes and the emergence of additional minerals, including amphibole, phlogopite, or apatite (modal metasomatism). The chemical signatures of metasomatism can be used to determine the metasomatic agents (commonly, carbonatite melts, silicate melts, and CO_2/H_2O enriched fluids), but, in some cases, trace element compositions should be used in parallel with other tools, such as lithium isotopes, to decipher the origin of metasomatic melts/fluids (Su et al., 2014, and references therein). In addition to mantle metasomatism, percolation of the host magma into xenoliths may obscure some of the initial information and distort lithospheric mantle signatures (Shaw et al., 2006). Thus, discriminating between mantle metasomatism and host magma-xenolith interaction is necessary for a better understanding of the evolution of the lithospheric mantle at depth.

Lithium is uniquely suitable for the quantification of melt/fluid-rock interactions since Li is

fluid-mobile and intermediately incompatible during partial melting and melt-rock reactions (Brenan et al., 1998; Ottilini et al., 2009; Ryan and Langmuir, 1987). The Li isotopic composition of melts and minerals, expressed as:

$$\delta^7Li = [(^7Li/^6Li)_{sample}/(^7Li/^6Li)_{L\text{-}SVEC}\text{-}1]\times 1000, \quad (1)$$

where $(^7Li/^6Li)_{L\text{-}SVEC}$=12.0192 (Flesh et al., 1973), is a powerful tool since the large mass difference between ^6Li and ^7Li (≈16%) results in significant isotopic fractionation during various geochemical processes (see Tomascak, 2004 for a review). The experimentally determined diffusivity of Li under mantle conditions is several orders of magnitude higher than that of other incompatible metal elements (Coogan et al., 2005; Dohmen et al., 2010), with ^6Li diffusing much faster than ^7Li in minerals (Ritcher et al., 2014). Consequently, Li has been used to quantify melt/fluid-rock interactions including metasomatism (e.g., Decitre et al., 2002; Lundstrom et al., 2005; Su et al., 2014), low-T weathering processes (e.g., Ryu et al., 2014), and material recycling in subduction-related settings (e.g., Elliott et al., 2004, 2006).

In the context of mantle-metasomatized peridotites, several researchers have claimed that Li would be selectively enriched either in olivine (Ol) during carbonatite-related mantle metasomatism or in clinopyroxene (Cpx) during silicate-related mantle metasomatism, making the partitioning of Li an indicator of the metasomatic agent (Ottolini et al., 2004; Seitz and Woodland, 2000; Su et al., 2014; Tang et al., 2007; Wagner and Deloule, 2007). The equilibrium Li partitioning can also be rapidly modified by the host magma during entrainment of xenoliths (Rudnick and Ionov, 2007). In order to use Li partitioning as a tracer

92 of mantle metasomatism in xenoliths, the extent of different metasomatic stages must first be
93 deciphered.
94 In peridotite xenoliths, negative δ^7Li values concomitant with high Li concentrations are
95 commonly observed in Cpx and are ascribed to the kinetic fractionation of Li induced by
96 diffusive uptake from infiltrating metasomatic melts/fluids (e.g., Jeffcoate et al., 20007;
97 Rudnick and Ionov, 2007). Due to the lower diffusivity of Li in its structure relative to Cpx,
98 Ol is capable of preserving earlier Li concentrations and isotopic compositions more
99 representative of the lithospheric mantle (Aulbach and Rudnick, 2009). Up to present, the
100 longevity of Li isotopic heterogeneities in the mantle (e.g., Halama et al., 2008; Vlastéli et al.,
101 2009) and the role of processes occurring during slab subduction in producing and delivering
102 low-δ^7Li materials into the deep mantle remain issues to be further explored (e.g., Zack et al.,
103 2003; Marschall et al., 2007). However, light lithium isotopic compositions, observed in
104 peridotites (Li et al., 2012; Nishio et al., 2004; Tang et al., 2014) and magmatites of mantle
105 origin (Agostini et al., 2008; Abdelfadil et al., 2014; Tian et al., 2015), have been regarded as
106 a signature of subduction related materials.
107 In this study, in order to fully understand the host magma-xenolith interactions, we have
108 selected xenoliths sampled from a solidified lava lake in which such interactions are expected
109 to have left strong chemical imprints. We use *in-situ* measurements of Cpx trace element
110 compositions and Li isotope distributions in Ol and pyroxenes from mantle peridotites to
111 distinguish the signatures of host magma-xenolith interactions and mantle metasomatism
112 suffered by the lithospheric mantle underneath the French Massif Central (FMC).
113

2. Geological background

The FMC (part of the Variscan belt in Western Europe) has been affected by alkaline volcanism since the early Cenozoic (Michon and Merle, 2001); the most recent volcanism occurred in the Chaîne des Puys ~6,900 yr ago (Juvigne, 1992). The entire volcanism has been subdivided into three magmatic phases: the pre-lift, rift-related, and major magmatic events (Michon and Merle, 2001). The last event lasted from Miocene till recently and produced a few large magmatic provinces (Fig. 1). Its occurrence has been related to a mantle diapir. Seismic tomography has revealed low-velocity anomalies beneath the FMC, which have been ascribed to either a mantle plume (Goes et al., 1999; Granet et al., 1995) or thermal anomalies not rooted in the lower mantle (Fichtner and Villaseñor, 2015). Additionally, the magmatism has recently been proposed to be likely enhanced by the presence of fertile lithologies (pyroxenites and/or amphibolites) in the FMC mantle (France et al., 2015). Anyway, the resulted extensive alkali-basaltic volcanism around the FMC transported numerous peridotite xenoliths to the surface (e.g., Lenoir et al., 2000).

Peridotite xenoliths studied herein were sampled at the Ringue quarry in Allègre, situated in the southern FMC domain (Fig. 1). The quarry samples a solidified lava lake that filled a maar ~3 Ma. The large-scale prismatic jointing is nicely exposed in the quarry.

3. The lithospheric mantle beneath the FMC

Lenoir et al. (2000) integrated textural observations with bulk rock major and trace element compositions of peridotite xenoliths widely distributed in the FMC (25 volcanic centers) and identified two distinct lithospheric mantle domains to the North and South of a boundary at

~45°30'N (Fig. 1). The northern domain is more refractory, with Sr-Nd isotopic compositions largely overlapping the compositional field of the European Asthenospheric Reservoir, while the southern domain is more fertile, with MORB-like Sr-Nd isotopic compositions (Downes et al., 2003; Granet et al., 1995; Lenoir et al., 2000). Both domains have been metasomatized to different degrees, with LREE enrichment more pronounced in the northern domain (Downes et al., 2003; Lenoir et al., 2000). The southern domain subducted underneath the northern domain during the Variscan orogeny (Lenoir et al., 2000). The metasomatic agents recorded in peridotites and pyroxenites from the FMC have been tentatively attributed to a deep, recycled, and enriched component, possibly related to Variscan subduction (Downes and Dupuy, 1987; Touron et al., 2008; Yoshikawa et al., 2010). *In-situ* measurements of amphibole D/H ratios in peridotites from the FMC support the existence of these subducted materials (Deloule et al., 1991).

4. Analytical methods

4.1 Sample preparation

25 peridotite xenoliths with diameters ranging from <1 to 15 cm were collected. The outer basaltic shells were sawed off to retain the cores, free of visible intrusive veins and post-serpentinization alteration. After careful investigation under a binocular microscope, thin sections were polished for xenoliths with larger grains and more transparent crystals. Then detailed petrographical observations were performed on each thin section and nine samples were selected for electron micro-probe analysis. The rules for this selection are based on different features under the microscope, e.g., modal compositions, textures, no visible veins

158 connecting with host magmas, the colors of spinel. After EPMA, a representative subset of six
159 samples, covering the total major element composition range, was used for trace element, Li
160 isotope measurements.

161 **4.2 Electron micro-probe analysis (EPMA)**

162 Major element compositions of constituent minerals were analyzed on carbon-coated thin
163 sections using a Cameca SX100 electron microprobe at the Service Commun de Microscopies
164 Electroniques et de Microanalyses X (SCMEM), University of Lorraine (France). The
165 operating conditions were set at an accelerating voltage of 20 kV and a beam current of 20 nA
166 with a focused beam. Alkaline elements are analyzed first to minimize errors due to element
167 migration; counting times were 10 s on peak and 5 s for backgrounds. For all other elements,
168 counting times were 20 s on peak and 10 s for backgrounds. A minimum of three grains was
169 analyzed for each mineral phase in a single thin section; at least two points were analyzed on
170 the cores and rims of each crystal (no fewer than four points per crystal).

171 **4.3 Laser ablation inductively coupled plasma mass spectrometry (LA-ICP-MS)**

172 Cpx trace element compositions were determined using LA-ICP-MS at the GeoResources
173 Laboratory, University of Lorraine (France). Double-polished thick sections (~0.15 mm thick)
174 or thin sections from EMPA were ablated *in-situ* using a nanosecond excimer laser (GEOLAS
175 Pro; 193 nm wavelength) with a spot size of 44 μm at 5 Hz with an energy density of 10 J/cm^2
176 per pulse. The ablation products were transported in a helium flow, mixed with argon gas, and
177 then analyzed with an Agilent 7500 ICP-MS. A complete analysis comprises 30 s for
178 background acquisition and 50 s for sample acquisition. The raw intensities of ions were
179 recorded as a function of time. SiO_2 contents obtained from EMPA were used as an internal

standard; NIST 612 and 614 (Jochum et al., 2011), analyzed at the beginning and end of the analytical session, were used as external standards. The precision of our data is mostly less than 5% at the confidence limit 95%.

4.4 Secondary ion mass spectrometry (SIMS)

Li concentrations and isotopic compositions were measured with Cameca IMS1270 and 1280 ion microprobes at the Centre de Recherches Pétrographiques et Géochimiques (CRPG; France); thin sections were gold-coated before SIMS analysis. At least three points (the number of analyses depending on grain size) were measured from core to rim on each grain, in areas devoid of cracks and inclusions.

To sputter the secondary positive ions ($^{7}Li^{+}$ and $^{6}Li^{+}$), primary $^{16}O^{-}$ beams were used at intensities ranging from 8 to 15 nA, with diameters of 20-40 μm, slightly varying among individual analytical sessions. The 10 kV secondary positive ions were counted without energy offset at a mass resolution of 1100 (M/ΔM) to separate the ^{6}LiH from ^{7}Li, in mono-collection mode. Counting rates for ^{7}Li ranged from 2×10^{4} to 2×10^{5} cps, varying with the Li content of samples and the primary beam intensities. Following a 120 s pre-sputtering, twenty-five to forty cycles were accumulated with counting times of 4 s, 12 s and 4 s for the background at mass 5.7, ^{6}Li and ^{7}Li, respectively. Prior to every analytical session, the deadtime of the counting system was calculated according to Deloule et al. (1992). A series of standard minerals, described in detail in Su et al. (2015), was used to calibrate instrumental mass fractionation, defined as $\Delta_i = \delta^{7}Li_{SIMS}-\delta^{7}Li_{known}$ (Decitre et al., 2002). These reference minerals are from mantle xenoliths, with Mg# comparable to the corresponding mineral phases in our samples. Throughout every analytical session, the standards were analyzed to

monitor the fluctuation of Δ_i with temporal variations of instrumental parameters, including the primary beam intensity (Fitzsimons et al., 2000). Unlike previous studies using an IMS 3f ion probe (e.g., Decitre et al., 2002), reference pyroxenes and Ol do not produce the same Δ_i; pyroxenes and Ol have co-variations of -0.39 and -0.52 δ unit per Mg#, respectively (Fig. 2a). Thus, due to the narrow and similar range of Mg# in our samples relative to the standards, no large inaccuracy (±1‰) is introduced when applying an averaged Δ_i of individual standard minerals to calculate the δ^7Li values of the corresponding sample minerals. The absence of significant compositional variation across the analyzed grains, as well as the limited compositional range of our samples, dictate that variations in our results are not the consequence of matrix effects.

The lithium ionization yield (Li ion counts / [primary beam intensity * Li concentration measured by ICP-MS]) was determined on the reference minerals (Fig. 2b), and Li concentrations were calculated by dividing the measured ^{7}Li intensity by the average ion yield of the standards. The estimated precision of this procedure is better than 20%.

5. Petrological descriptions

The peridotite xenoliths studied herein are fresh samples displaying clean minerals that are free of any surface alteration feature. They can be divided into two groups, spinel-bearing lherzolite (Cpx up to 12%) and spinel-bearing harzburgite (Fig. 3). No hydrous minerals or other accessory minerals characteristic of modal metasomatism (e.g., apatite) were observed.

According to the classification of Mercier and Nicolas (1975), our samples have been divided into three textural classes: protogranular, porphyroclastic and equigranular textures

(Table 1). The protogranular texture, the most common in our samples (~60% of the studied samples), is regarded as an original texture that evolved (through plastic flow and recrystallization) to porphyroclastic, and further to equigranular textures (Downes and Dupuy, 1987; Mercier and Nicolas, 1975). In protogranular samples (Fig. 4a), coarse grains of Ol and orthopyroxene (Opx) are of similar sizes (1.5-2.5 mm). Some Ol grains display kink-banded texture and the boundaries of some Opx grains are curvilinear. Cpx is either clustered with spinel (Spl) as a characteristic feature of this textural type (Downes et al., 2003; Lenoir et al., 2000), mainly in sample AL56 (Fig. 4b), or dispersed interstitially with similar-sized or larger coexisting Ol and Opx. Cpx and Spl have usually smaller grain sizes (<1 mm) than Ol and Opx. Spl commonly exhibits a vermicular from. In porphyroclastic samples (Fig. 4c; ~25% of the studied samples), Ol and Opx porphyroclasts (up to 3.5 mm across) are embedded in granulablasts comprising smaller (<1 mm) Ol, Opx, Cpx and Spl. The rare equigranular samples (~15% of the studied samples) comprise uniform small grains (<1 mm) displaying triple junctions. Rare interactions with the host magma (possibly once it had pooled in the lava lake) are recorded as, in some samples, both small microlitic veins that crosscut some minerals and glass pools.

Sample AL47P1 displays spongy-textured rims of various widths (<50 μm to 300 μm; Fig. 4d), most commonly around Cpx and Spl; these rims comprise fined-grained Cpx, plagioclase, Opx, Ol, and Spl, ± glass (Fig. 4e, f). Although no consensus has been achieved on the origin of such spongy textures in peridotite xenoliths (Carpenter et al., 2002; Shaw and Dingwell, 2008; Shaw et al., 2006; Su et al., 2011), the interpretation of decompression-induced partial melting (Su et al., 2011) will be adopted in the present study; infiltrating host melts may also

participate in the formation of spongy textures (Carpenter et al., 2002).

6. Results

6.1 Major element compositions of minerals

Nine representative samples (Table 1) displaying protogranular (7 samples, including sample AL47P1) or porphyroclastic textures (2 samples), and devoid of microlitic veins, were selected for mineral major element analysis (Table 2). No significant core-to-rim variation was observed in any sample except AL47P1.

Ol forsterite (Fo) contents (or Mg# = 100×molarMg/(Mg+Fe)) vary from 89.2 to 92.4 (Table 2), nearly encompassing the range of Fo contents in off-craton peridotites worldwide, and overlapping the Fo range of cratonic peridotites (Rudnick et al., 2004). NiO and MnO contents range from 0.33 to 0.38 wt.%, and from 0.12 to 0.15 wt.%, respectively. No large inter-grain variation has been observed in individual samples (for example, the standard deviation of MgO contents within every sample is less than 0.56).

Opx Mg# varies from 89.7 to 92.9, similar to the Fo range, and thus indicating a chemical equilibrium between Ol and Opx after partial melting (Ottolini et al., 2004). Al_2O_3 and TiO_2 contents vary from 1.72 to 3.91 wt.%, and from 0.02 to 0.09 wt.%, respectively; both show a rough negative correlation with Mg#, whereas there is no evident covariation of CaO and Na_2O with Mg# in Opx (Table 2). Our measured TiO_2 contents (0.02 to 0.09 wt.%) are slightly lower than in other peridotites worldwide; similar low TiO_2 contents have been reported in peridotites metasomatized by subduction-related melts (e.g., Zanetti et al., 1999).

Cpx is Cr-diopside with Cr_2O_3 contents and Mg# ranging from 0.55 to 1.58 wt.%, and from

88.9 to 92.6, respectively. No compositional differences were observed between Cpx clustered with Spl and those scattered interstitially. Al_2O_3 and CaO contents in Cpx range from 3.28 to 6.89 wt.% and from 20.21 to 22.68 wt.%, respectively; both have negative correlation with Mg# of Ol (Fig. 5c and e). There is no significant major element compositional variation among Cpx grains in a single thin section, but a small difference between cores and rims of Cpx should be treated with caution.

Spl Cr# (=100×molarCr/(Cr+Al)) varies from 7.28 to 58.39. There is no significant composition difference between Spl clustered with Cpx and those scattering randomly in interstitial positions. Spl Cr# of Allègre xenoliths falls in the Cr# range of Spl from subcontinental peridotite xenoliths (Arai, 1994; Fig. 5b). In addition, Spl in sample AL56 contain exceptionally high TiO_2 (0.69 wt.%), even when compared with the comprehensive dataset of Spl from the upper mantle of the FMC (Uenver-Thiele et al., 2014).

In sample AL47P1, Cpx and Spl exhibiting spongy-textured rims have major element variations only in narrow zones approaching the spongy rims. MgO, Cr_2O_3 and SiO_2 are enriched toward the Cpx rims while Na_2O, CaO, Al_2O_3 and TiO_2 are depleted. It is consistent with the interpretation of the formation of the spongy texture; the basaltic components were extracted into the interstitial melt during decompression-induced partial melting while the compatible elements resided in Cpx. In other domains, no significant core-to-rim variation is observed.

6.2 Cpx trace element compositions

Cpx trace element compositions are reported in Table 3. In every sample, more than 7 grains were analyzed at the cores, and the rims of some large grains (1 to 4 grains;

290 Supplementary Table 1) were analyzed to monitor core-to-rim trace element homogeneity.
291 Cpx rims are enriched in Sr, La, and Ce only in sample AL47P1 (Supplementary Table 1).
292 Otherwise, no significant variation was observed among different grains in any given sample;
293 thus, we shall use the average contents of individual samples in the following discussion.

294 The chondrite-normalized rare earth element (REE) distribution patterns vary greatly
295 among the six analyzed samples (Fig. 7a). Cpx in sample AL44 is highly depleted in light
296 REE (LREE) relative to middle REE (MREE), and has a nearly flat transition from MREE to
297 heavy REE (HREE) ($(La/Yb)_N$=0.1; $(Sm/Yb)_N$=0.8, the subscript 'N' represents
298 normalization to chrondrite; McDonough and Sun, 1995). In contrast, REE distributions of
299 Cpx in samples AL22 and AL47P1 are spoon-shaped, with steep inflections from Nd to La,
300 and nearly flat from MREE to HREE ($(La/Sm)_N$=3.9 and 11.8, respectively; $(Sm/Yb)_N$=0.9
301 and 0.8, respectively). Cpx from samples AL32 and AL41P1 are enriched in LREE compared
302 to HREE, and chondrite-normalized element contents decrease continuously from La to Lu
303 ($(La/Yb)_N$=79 and 46.7, respectively; $(Sm/Yb)_N$=6.4 and 3.7, respectively). The REE
304 distribution pattern of Cpx in sample AL56 is distinct due to higher contents of most elements
305 except La and Ce (ΣREE=211.1ppm). Moreover, in this sample, the chondrite-normalized
306 concentrations are depleted in LREE compared to MREE, and decrease nearly linearly from
307 Nd to Lu.

308 Extended trace element compositions of Cpx (Table 3) exhibit negative High Field
309 Strength Elements (HFSE; Nb, Zr, Hf, and Ti in this study) anomalies when element
310 abundances are normalized to the primitive mantle (McDonough and Sun, 1995; Fig. 7b). All
311 samples exhibit strong negative Nb anomalies. The magnitudes of negative Ti anomalies

312 ($Ti^*=2\times Ti_n/(Eu_n+Gd_n)$; the subscript 'n' represents normalization to the primitive mantle)
313 gradually decrease from sample AL56 ($Ti^*=0.06$) to sample AL47P1 ($Ti^*=0.83$). Samples
314 AL32, AL41P1 and AL56 exhibit strong negative Zr and Hf anomalies; sample AL47P1
315 displays small negative Zr and Hf anomalies, and samples AL22 and AL44 do not show
316 anomalies (Table 3). Due to high LREE contents, Cpx from samples AL32 and AL56 display
317 negative Sr_n anomalies compared to adjacent elements (Ce_n and Sm_n), in contrast to absent or
318 weak positive anomalies in other samples. In all the Allègre samples, Th and U are enriched
319 to different degrees (Th_n and U_n values as high as 19.5 and 27.9, respectively, in sample
320 AL22; Fig. 7b)

321 **6.3 Lithium concentrations and isotopic compositions**

322 Li concentrations and isotopic compositions are reported in Table 4 and Supplementary
323 Table 2. Li content in Ol cover a range of 0.9 to 7.7 ppm, with averages of individual samples
324 varying from 1.7 to 4.0 ppm. Ol cores have lower or similar Li contents compared with their
325 rims (Supplementary Fig. 1; Table 4), ranging from 1.3 to 4.4 ppm and from 1.4 to 7.7 ppm,
326 respectively; increased Li contents at rims occur within 900μm of the grain boundary. Li
327 contents in Opx range from 0.6 to 18.5 ppm, and, in most cases, are higher than those in
328 coexisting Ol. The compositional zonation in Opx is variable; cores of some grains contain
329 much more Li than their corresponding rims, whereas other grains show the opposite pattern
330 (Supplementary Fig. 1). Cpx contain much more Li than coexisting Ol and exhibit much
331 larger variations, from 3.4 to 49.5 ppm, with averages of individual samples varying from 7.3
332 to 34.6 ppm. Cpx Li concentrations in sample AL47P1 are lower than Cpx in other samples.

333 Lithium isotopic compositions also display large variations. Ol δ^7Li values range from -32

334 to +15‰ with averages ranging from -9.6 to -4.6‰; Opx values range from -74.7 to +30.9‰
335 with averages from -25.1 to +20.1‰; Cpx values range from -11.6 to +23.7‰ with averages
336 from -7.6 to +1.8‰ (Table 4 and Supplementary Table 2). Despite their regular Li
337 concentration zonations, Ol don't exhibit regular δ^7Li profiles; most samples have slightly
338 higher average δ^7Li values in cores than in rims (Table 4). The δ^7Li distributions in Opx
339 grains are more complicated. Their patterns can be divided into three groups (Supplementary
340 Fig. 1): 1) δ^7Li values decrease from core to rim; 2) δ^7Li values increase systematically from
341 core to rim; and 3) the δ^7Li profiles across the grains are irregularly sinuous. In Cpx grains,
342 no large core-rim δ^7Li variations have been observed. The averaged δ^7Li values of Ol and
343 Opx in each sample, as well as those of Cpx in some samples, fall outside the Li isotopic
344 composition of the upper mantle (+2 to +5‰; Table 4), which is estimated on the basis of
345 data from oceanic basalts (Chan et al., 1992; Tomascak et al., 2008), equilibrated fertile
346 peridotites (Jeffcoate et al., 2007; Magna et al., 2006; Pogge von Strandmann et al., 2011;
347 Seitz et al., 2004), and mantle derived carbonatites (Halama et al., 2008).
348 To identify whether the host magma had influenced xenoliths with respect to Li
349 concentration and isotopic composition, we carefully winnowed some phenocrysts and
350 microcrystals of Cpx for SIMS analysis; the average Li concentration and δ^7Li values of these
351 Cpx are 16.5±5ppm and 3.2±0.6‰, respectively. Since no per mil-level Li isotopic
352 fractionation occurs during crystal-melt differentiation at magmatic temperatures (Tomascak
353 et al., 1999), the δ^7Li value can be regarded as the Li isotopic composition of the host magma
354 (and even the residual melts after differential crystallization). From Li concentration of Cpx
355 crystals, Li concentration in the host magma can be estimated as no lower than 36 ppm

356 (T=800°C; the partition coefficient between Cpx and melt calculated from Caciagli et al.
357 (2011)).
358
359 ## 7. Thermobarometry
360 The two-pyroxene thermometer, from Brey and Köhler (1990; henceforth expressed as
361 T_{BK}), has been used to calculate the equilibrium temperatures. This method was used in
362 previous studies to estimate the equilibrium temperatures of peridotite xenoliths from the
363 FMC (Werling and Altherr, 1997; Yoshikawa et al., 2010; Zagana et al., 1997), allowing for
364 direct comparison to the results from other localities in the FMC. The calculated equilibrium
365 temperatures of Allègre xenoliths range from 840℃ to 1077℃ (Table 1), falling within the
366 range proposed by Werling and Altherr (1997; 721 to 1190℃). We do not observe the
367 relationship between equilibrium temperatures and textural types, as described by Zagana et
368 al. (1997).
369 Based on Ca-in-olivine geobarometer (Köhler and Brey, 1990), we calculate equilibrium
370 pressures ranging from 9.3 to 14.8kbar (Table 1), with the exception of AL43, for which a
371 5.4kbar pressure is obtained. This low value may result from Ca disequilibrium between Ol
372 and Cpx, and this value is discarded in the following discussion. Given a lithospheric density
373 of 2.85 g/cm^3 (Yoshikawa et al., 2010), our samples originate from depths of 31.6 to 52km,
374 upper mantle depths, considering the depth of the Moho to be at 28 to 30km (Michon and
375 Merle, 2001; Werling and Altherr, 1997).
376
377 ## 8. Discussion

8.1 The continental depleted mantle after partial melting in various degrees

Partial melting of peridotites is one of the fundamental processes controlling mantle evolution. The common fertility indexes of peridotites, including the modal compositions of Cpx, the Fo contents in Ol, and Cr# of Spl, vary at different scales corresponding to distinct degrees of partial melting. As shown in Fig. 5a, the modal abundance of Cpx (1% to 10%) in xenoliths from Allègre systematically decreases with increasing Fo content (89.2 to 92.4), indicating an incremental degree of melting. Additionally, the positive correlation between Cr# of Spl (7.3 to 58.4) and Fo content is consistent with the olivine-spinel mantle array (Arai, 1994) and all the samples from Allègre fall in the zone defined by sub-continental peridotites worldwide (Fig. 5b; Arai, 1994; Khedr et al., 2013).

Most of our samples fall in the field of the Massif Central southern domain determined by Downes et al. (2003) based on Cpx major element compositions (Fig. 5f and 5g). Al_2O_3, TiO_2 and CaO content show a roughly negative relationship with Fo content (Fig. 5c, 5d and 5e), due to extraction of basaltic components during partial melting. Mildly incompatible elements in Cpx (HREE + Y) are mainly unaffected by later metasomatic events and record the partial melting event, along with Fo and Cr# of Spl (Fig. 6c and d). In contrast, LREE contents (Fig. 6a) seem to be affected by later metasomatic events, and do not display such correlations with Fo and Cr# of Spl. Only the HREE content of sample AL56 falls outside the trends of Cpx modal proportions, Fo content, and Cr# of Spl; AL56 was therefore enriched by a metasomatic stage (Fig. 6c and d). In all other samples, the correlation between Cpx HREE content, Fo content of Ol, and Cr# of Spl indicate that Cpx is cogenetic with Ol, and thus suffered the partial melting event.

Hellebrand et al. (2001) have established a relationship linking Cr# of Spl in residual peridotites to the extent of partial melting. Using their equation, the degrees of partial melting of Allègre samples were calculated to range from 1 to 19% (Table 1). No estimate could be made on sample AL27P2, for which the Spl Cr# of 7.28 is lower than the literature data (Touron et al., 2008; Werling and Altherr, 1997; Xu et al., 1998; Yoshikawa et al., 2010) and falls outside the calibrated range of the equation. The fractional melting model of Norman (1998), based on HREE contents, has also been used to estimate the degree of partial melting in samples for which the REE concentrations of Cpx have been measured (Fig. 8); the results are consistent with those calculated according to Hellebrand et al. (2001; Fig. 8), with the exception of sample AL56, in which the metasomatism is strongest and even HREE were enriched (Fig. 6c and d; a deeper discussion seeing in next section).

8.2 Multi-stage metasomatism revealed by trace element and Li signatures

8.2.1 Mantle metasomatism evidenced by trace element compositions

Cpx in un-metasomatized peridotites, merely undergoing partial melting, should be depleted in incompatible elements (e.g., LREE, LILE, HFSE…) depending on the element partition coefficients; LREE are thus more depleted than HREE in residual peridotites. The trace element pattern of AL44 illustrates this tendency (Fig. 7a), whereas the trace element distribution patterns in Cpx from other samples deviate from this trend to different degrees, indicating that they have been modified by subsequent percolation of exotic melts or fluids (metasomatism). A series of fractionated REE patterns has been ascribed to the chromatographic effects during melt percolation into a porous matrix (Bodinier et al., 1990; Ionov et al., 2002; Mundl et al., 2015). The incipient percolating melt is presumed to be

highly enriched in LREE relative to MREE and HREE (Ionov et al., 2002; Mundl et al., 2015). Elemental redistribution between peridotite minerals and the percolating melt depends mainly on the mineral-melt partition coefficient of a given element. Once the melt enters the host peridotite suite, the melt reacts first with peridotites closest to the melt conduit, where the peridotite minerals are quickly enriched in HREE (less incompatible than LREE) and the melt becomes relatively depleted in LREE. Sample AL56 corresponds to the host peridotite at this stage (Fig. 7a) as the upward convex REE pattern is consistent with previous modeling results (Xu et al., 1998; Ionov et al., 2002; Mundl et al., 2015). Through progressive percolation, the HREE-depleted melt (thus relatively LREE-enriched), no longer exchanging HREE with the host peridotites farther from the melt source, then introduces a strong LREE enrichment in the host peridotites. Among our studied samples, AL32 and AL41P1 display the highest $LREE_N/MREE_N$ or $LREE_N/HREE_N$ ratios (Table 3; Fig. 7a) and can be assigned to this stage. As percolation continues, LREE continue to migrate from the melt to the host peridotites until the LREE/HREE fractionation diminishes. The progression from AL47P1 (La_N/Yb_N=9.4), to AL22 (La_N/Yb_N=3.9) and to AL44 (La_N/Yb_N=0.1) mirrors this process. Strongly metasomatized samples should record higher equilibrium temperatures due to their proximity to the melt source (Denis et al., 2015); indeed, samples AL56 and AL32 return equilibrium temperatures of 1077 and 1071℃, respectively. LREE enrichment of metasomatized Cpx in our samples is accompanied by different degrees of negative HFSE anomalies (Fig. 7b).

Experiments under mantle conditions have shown that HFSE partition coefficients between carbonatitic melts and Cpx are much higher than those between silicate melts and Cpx (Adam and Green, 2001; Blundy and Dalton, 2000; Klemme et al., 1995). As Cpx present in the

carbonatitic melt source controls the trace element budget of those melts, they will be relatively depleted in HFSE, which will be recorded in the trace element distribution patterns of peridotites metasomatized by them. In natural peridotite samples, carbonatitic metasomatism is commonly associated with low Ti/Eu (usually<1500; Coltorti et al., 1999; Fig. 9a) and elevated Zr/Hf (>37) in Cpx (e.g., Coltorti et al., 1999; Ionov et al., 1993; Rudnick et al., 1993; Yaxley et al., 1998), values consistent with our data. Sample AL56 have the lowest Ti/Eu ratio (437) among the Allègre samples, but its $(La/Yb)_N$ ratio is not the highest one (Fig. 9a). This sample was most strongly metasomatized and the metasomatic melt has also added HREE to Cpx. With respect to the Zr/Hf ratios of Cpx in Allègre samples, the highest value occurs in sample AL22 (52) rather than sample AL56 (33), the most metasomatized in term of REE addition and lowest Ti/Eu ratio in its Cpx. But Zr negative anomalies are indeed present in some strongly metasomatized samples (Fig. 9b). A recent study of peridotites entrained by Ray Pic volcano (also belonging to the FMC southern domain) observed negative HFSE anomalies in Cpx from the most strongly metasomatized samples (Denis et al., 2015). HFSE anomalies associated with LREE enrichments have also been recognized as a signature of carbonate-rich metasomatic silicate melts (e.g., Ionov et al., 2002). Nevertheless, the carbonatite-related metasomatism usually generated additional accessory minerals concomitant with geochemical signatures (e.g., apatite in Rudnick et al. (1993); feldspar in Guzmics et al. (2008)). After detailed petrographical investigation, no secondary mineral has been observed in all the Allègre samples. Moreover, in light of their mobility in aqueous fluids, negative HFSE anomalies were classically attributed to subduction settings, where mantle domains have been enriched in fluid-mobile elements (like LILE) and

466 depleted in fluid-immobile elements (HFSE; e.g., Zanetti et al., 1999; Rivalent et al., 2007).
467 From the currently obtained evidences, it is not cogent to unequivocally attribute mantle
468 metasomatism suffered by the Allègre xenoliths to either carbonatitic melts or melts/fluids
469 derived from a subducting slab.

470 As Cpx grains in sample AL56 do not show trace element zoning from core to rim, we
471 interpret that the trace element compositions of Cpx in that sample have equilibrated with the
472 reactive melt. To assess the origin of the melt responsible for the trace element characteristics
473 of our samples, the trace element composition of melts in equilibrium with Cpx in sample
474 AL56 were calculated based on the equation: $C_{melt}=C_{mineral}/D_p$, where C_{melt} and $C_{mineral}$ denote
475 the concentrations of elements in the melt and Cpx, respectively, and D_p represents the
476 experimentally measured partition coefficients of trace elements between Cpx and either a
477 silicate melt (from Hart and Dunn, 1993, and Johnson, 1998) or a carbonatite melt (from
478 Klemme et al., 1995). As shown in Fig. 10, the calculated trace element patterns of reactive
479 melts, using two sets of partition coefficients, are characterized by marked LREE and U-Th
480 enrichment and pronounced HFSE (Zr, Hf, and Ti) negative anomalies, and do not match the
481 trace element patterns of representative alkaline basalts in the FMC (Wilson and Downes,
482 1991).

483 **8.2.2 Inter-mineral lithium concentration disequilibrium and intra-granular**
484 **inhomogeneous Li distribution**

485 Using fertile equilibrated peridotites, unaffected by metasomatic processes, as
486 representative of the normal mantle, the Li partitioning sequence among mantle minerals is
487 recognized as Ol>Cpx≥Opx, with Li contents of 1.0-2.2 ppm for Ol, and 0.5-1.3 ppm for

488 pyroxene (Ottolini et al., 2004; Seitz and Woodland, 2000; Fig. 11). Since Spl and garnet
489 contain even less Li (Jeffcoate et al., 2007; Seitz and Woodland, 2000) and their modal
490 abundance in peridotite is commonly very low, those minerals are usually not considered..

491 The minerals in Allègre samples have incorporated additional Li (relative to the normal
492 mantle), with concentrations up to 50 ppm in Cpx of AL56 (Fig. 11); the lone exception in
493 our dataset is Cpx in AL47P1 (from 4.5 to 10.5 ppm), which probably lost Li to the melt
494 during the formation of their spongy rims. Strong Li distribution disequilibria among mineral
495 phases are concomitant with this Li addition (Fig. 12). The Li concentration ratios between Ol
496 and Cpx ($D_{Li}^{Ol/Cpx}$) range from 0.08 to 0.54, much lower than the partition coefficient at
497 equilibrium (Fig. 12a; 1.5~2.0, Seitz and Woodland, 2000; 1.74, Ottolini et al., 2009).
498 Preferential Li enrichment in either Ol or Cpx has been attributed to the type of interacting
499 melt at mantle depth (Seitz and Woodland, 2000; Su et al., 2014). Silicate melts preferentially
500 enrich Cpx in Li (e.g., Aulbach and Rudnick, 2009; Rudnick and Ionov, 2007; Seitz and
501 Woodland, 2000; Tang et al., 2007; Wagner and Deloule, 2007), whereas carbonatitic melts
502 preferentially enrich Ol (Ottolini et al., 2004). From this, the large Li enrichment in Allègre
503 peridotite Cpx seems to result form contamination by silicate melts. Nevertheless, the
504 xenoliths cooled slowly in a solidified lava lake, and petrographic features are indeed
505 indicative of host magma percolation into xenoliths. Consequently, the Li distributions in the
506 xenoliths could have been modified in the lava lake due to the rapid diffusive rate of Li, and it
507 is important to identify the respective effects of late infiltration of the host magma, and earlier
508 mantle metasomatism, on the final Li distribution in our samples.

509 The Li concentration profiles indicate that the Li addition not only induced inter-mineral

disequilibria, but also disrupted the intra-granular Li elemental homogeneity (Fig. 11 and Supplementary Fig. 1). Cpx cores show high Li concentrations (up to 40 ppm) similar to Cpx rims, within error. Li distribution in Ol grains is more variable; some grains have constant Li contents from cores to rims, while, in other grains, Li contents rise suddenly just near grain boundaries.

The higher diffusivity of Li in Cpx than in Ol (e.g., Aulbach and Rudnick, 2009; Jeffcoate et al., 2007; Parkinson et al., 2007) and the smaller grain sizes of Cpx relative to Opx and Ol, account for higher Li concentrations in Cpx as a result of metasomatic events (Jeffcoate et al., 2007; Rudnick and Ionov, 2007). In our samples, the extremely high Li contents of Cpx reflect a recent diffusive Li uptake. As Li concentration in the host magma cannot be lower that 36 ppm, we consider that infiltrating melts from the host magma are residual melts after fractional crystallization of the host magma, enriched in Li due to its incompatibility. Thus, they are capable of providing large amounts of Li to Cpx. Due to the slower Li diffusive rate in Ol, melt infiltration solely increased Li concentrations at the rims (<900μm from the grain boundaries), whereas the cores were unaffected, and preserve the Li concentrations from depth. Li contents in Ol cores range from 1.3 to 4.4 ppm, representative of normal mantle to slightly enriched values (Fig. 13a), indicating a mantle metasomatism prior to entrainment by the host magma. This earlier metasomatic stage is supported by the lack of correlation between Li contents and Mg# of cores (Fig. 13a), which is not in accordance with the intermediately incompatible characteristic of Li during partial melting. Combining with some evidences of host magma infiltration from petrographic observations and the host magma as a lava lake on the earth surface, the high Li concentrations in Cpx and steep Li concentration

increase at the rims of olivine grains can be attributed to Li uptake from infiltrating melts derived from the host magma.

The intra-mineral Li compositional variation observed in our samples is the result of a multi-stage melt exchange, including the involvement of the host magma. Due to the different diffusive rates of Li in different phases, the elemental distribution among mineral phases is no longer in equilibrium; here, the Li partition coefficient between Cpx and Ol cannot be used to identify the nature of mantle metasomatic agents.

8.2.3 Distinctive Li isotopic offsets between Cpx and Ol induced by asynchronous metasomatic events

Given the large difference of diffusive rates between ^{6}Li and ^{7}Li, with a diffusion coefficient ratio $D_7/D_6=(m_6/m_7)^{\beta}=1.0424$ (m_6 and m_7 are the masses of ^{6}Li and ^{7}Li, respectively; exponent $\beta=0.27$ according to Richter et al., 2014), the Li isotopic composition will be altered during Li exchange by diffusion (e.g., Lundstrom et al., 2005; Wagner and Deloule, 2007). During diffusion, mantle minerals, as the receptors at the end of the diffusive sequence, first become enriched in ^{6}Li owing to its faster diffusion rate, and their isotopic compositions evolve towards negative values, forming a 'trough' in isotopic composition. Inversely, $\delta^{7}Li$ values of the donors, which have lost Li, increase gradually. In receptor minerals, the 'trough' propagates into the interiors of grains until a new equilibrium is achieved, or the system cools below the closure temperature, preserving the disequilibrium state.

Since Cpx have suffered pronounced lithium addition, their isotopic compositions should have been totally or partly reset. In view of some $\delta^{7}Li$ values that plot in the Li isotopic

554 composition range of the upper mantle (Fig. 14a), coupled with the lack of obvious Li
555 elemental and isotopic zonation, some Cpx grains must have achieved Li isotopic equilibrium
556 with infiltrated melts/fluids originating from the host magma of similar isotopic composition
557 (3.2±0.6‰) to the upper mantle. Additionally, some Li isotopic imprints generated by an
558 older (mantle) metasomatic event have not been completely attenuated by this Li uptake (e.g.,
559 the negative δ^7Li values in sample AL41P1 and AL32; Table 4). The Li concentration prior to
560 exchange with the host magma, as well as grain size, determines the time needed to reach
561 equilibrium for a whole grain with interstitial melts/fluids (Aulbach and Rudnick, 2009;
562 Gallagher and Elliot, 2009). Thus, the original Li content and δ^7Li signals of (an) older
563 metasomatic event(s) prior to entrainment by the host magma have not been totally erased and
564 cumulative effects might account for the large variation of Li content and δ^7Li values
565 currently observed in Cpx among different xenoliths, and even among different grains in a
566 single xenolith (Table 4; Supplementary Fig. 1).

567 In Ol grains, enriched rims display lower δ^7Li values than the cores, correlating with
568 increased Li content. However, the cores also display negative δ^7Li values, even when their Li
569 content plateaus, which should have preserved the original Li isotopic composition
570 (Supplementary Fig. 1, Fig. 13b and Table 4). Thus, the majority of Ol Li isotopic
571 compositions in Allègre peridotite xenoliths, regardless of the analyzed positions in grains,
572 are lower than the literature data (Fig. 14b). Note that the δ^7Li profiles presented in this study
573 should not reflect geometric effects when slicing the thin sections (Parkinson et al., 2007).
574 Accordingly, it is likely that the light lithium isotopic compositions at Ol cores, as well as in
575 some Cpx grains, are the consequence of mantle metasomatism by melts/fluids depleted in ^{7}Li

576 (Fig. 13b) prior to host magma entrainment. The roughly negative relationship between Li
577 concentrations and δ^7Li in Ol cores (Fig. 14b) indicates that Li was added from a source of
578 negative Li isotopic composition. This Li addition process homogenized the lithium
579 concentration and isotopic compositions of the peridotites at the mineral scale prior to
580 entrainment by the host magma.

581 As a result, the Li isotopic difference between Ol and Cpx ($\delta^7Li_{Ol} - \delta^7Li_{Cpx}$), are mostly
582 negative in the Allègre samples (Table 4)，ranging from -8.8‰ to 0‰, distinct from results of
583 previous studies. The exception is the sample AL32 (2.5‰) due to lower δ^7Li values of its
584 Cpx grains. This clearly shows that Cpx and Ol have not achieved the Li isotopic equilibrium.

585 **8.2.4 Origin of exceptionally light Li isotopic compositions in Ol cores**

586 Considering that only low-T processes can fractionate Li isotopes to a sufficient degree to
587 generate materials with negative δ^7Li values (e.g., Chan et al., 1992, 2006; Decitre et al., 2002;
588 Rudnick et al., 2004; Teng et al., 2004; Tomascak et al., 1999, 2004), it is expected that the
589 low-δ^7Li component in the mantle derives from a recycled component. Zack et al. (2003)
590 showed that the δ^7Li values of eclogites could be as low as -11‰, quite different from fresh
591 (3.4±1.4‰; Tomascak et al., 2008) or altered (-2‰ to 14‰; Chan et al., 1992) MORB. They
592 interpreted these values as a result of isotopic fractionation through Rayleigh distillation
593 during subduction and metamorphic dehydration of the protoliths; their interpretations were
594 later supported by experimental observations (Wunder et al., 2006). After a more
595 comprehensive investigation, Marschall et al. (2007) asserted that devolatilization during
596 subduction would not largely fractionate the Li isotopic compositions between the residual
597 metamorphites and the released fluids (≤ 3‰), casting doubt on the role of subducted

598 materials in the delivery of low-δ^7Li components into the deep mantle. Nevertheless, the
599 ultimate fate of subducted materials that have entered the deep mantle also depends on the
600 mineralogy and Li isotopic compositions of their protoliths (Adelfadi et al., 2014; Tang et al.,
601 2014). Despite small isotopic fractionations (Marschall et al., 2007), subducted surficial
602 materials with low δ^7Li values have the potential of evolving to residuals of much lower δ^7Li
603 value, creating a distinct low-δ^7Li reservoir in the deep mantle. Recent research on the
604 Himalayan collisional zone carbonatites generated by partial melting of subcontinental
605 lithospheric mantle also obtained light δ^7Li values (-4.5‰ to -0.3‰; Tian et al., 2015), which
606 are attributed to metasomatism by fluids released from subducted oceanic crust or marine
607 sediments.

608 During the Variscan orogeny, the FMC was part of the Gondwana-Laurussia collision,
609 accompanied by subduction of the Rheic Ocean and oceanic basins (Faure et al., 2009).
610 Hence, the melts/fluids of light Li isotopic compositions that metasomatized the peridotites of
611 the present study may derive from those subducted slabs at depth. In both mantle xenoliths
612 and mantle-derived lamprophyres from the Bohemian Massif (also belonging to the Variscan
613 orogeny), negative Li isotopic compositions have been reported as a result of mantle
614 metasomatism by subducted crustal materials (Ackerman et al., 2013; Adelfadil et al., 2014).
615 In addition, the signature of recycled components from the surface is recorded in the D/H
616 ratios of amphiboles in peridotites from the FMC (Deloule et al., 1991). In peridotite
617 xenoliths from the North China Craton, similar anomalous δ^7Li values (as low as -30‰)
618 observed in Ol cores have also been ascribed to metasomatism by melts/fluids from recycled
619 materials related to subducted oceanic crust (Li et al., 2012; Tang et al., 2014). It is therefore

likely that subducted materials remain in the mantle beneath the FMC. The asthenospheric upwelling that promoted alkali-volcanism in the Eocene may have produced a high heat flux, inducing slab melting. The melts/fluids of this origin ultimately metasomatized overlying peridotites and introduced the extremely light Li isotopic compositions.

8.2.5 Precedence relationship between different metasomatic processes

The metasomatic agents accounting for trace element variations in Cpx and negative Li isotopic compositions preserved in Allègre Ol cores, are not the same due to a few lines of following evidences. On the one hand, the most strongly metasomatized sample from Allègre (AL56 according to Cpx trace element compositions) does not have the lowest δ^7Li values in its Ol cores. Whereas sample AL44, in which Cpx display LREE depletion, weak Ti negative anomaly and no Zr-Hf negative anomaly, have the Li isotopic compositions very negative in its Ol cores. On the other hand, the melt, which brought the light Li isotopic compositions to the xenoliths from Allègre, has been originally associated with subducted materials after dehydration during subduction. During dehydration of subduction slabs, the released fluids should take the fluid-mobile elements (LILE and LREE) away but HFSE are normally left in the residuals and taken to the depths with slabs. Thus, the low δ^7Li melts should not have HFSE negative anomalies, in contrast with the trace element compositions in Cpx from Allègre.

To constrain the time needed for Cpx trace element compositions to equilibrate with a metasomatic melt, we apply a one-dimensional diffusion model simulating Sr concentrations, assuming that Sr diffuses from percolating melts of constant Sr concentration to Cpx grains acting as semi-infinite reservoirs:

$$\frac{C - C_s}{C_0 - C_s} = erf\left(\frac{x}{2\sqrt{Dt}}\right) \quad (2)$$

where C is the Sr concentration at any given distance x and time t after the onset of Sr diffusion, C_0 is the initial Sr concentration in the mineral core, C_s is the Sr concentration at the mineral boundary, D is the diffusion coefficient (Sr diffusion coefficient from Sneeringer et al., 1984), and *erf* is the error function. We assume that the Sr concentration of the average depleted MORB mantle (DMM; Workman and Hart, 2005) represents the initial concentration in pre-existing Cpx; the Sr concentration in the melt is constant (calculated above based on sample AL56). The model results imply that, to thoroughly equilibrate a 2mm-diameter Cpx grain in sample AL56, the percolating melt spent approximately 2.4Ma at 850℃ or 200 years at 1100℃.

To estimate the duration of host magma-xenolith interaction, we use a one-dimensional diffusion model (equation 2) to simulate Li uptake into the marginal zones of Ol grains. Diffusion of Li to a depth of 1mm in Ol requires a few years (3 years at 1100℃; diffusion coefficients from Dohmen et al., 2010). Considering a maximum initial depth of 52km, and average ascent rates of alkali basalts to be 0.2-2 m/s (O'Reilly and Griffin, 2011), the maximum duration of xenolith transport to the surface should range from 7 hours to 3 days. The intermediate interval (between 3 days and 3 years) perhaps corresponds to the slow cooling of the lava lake.

Given that Ol grains have equilibrated their Li isotopic compositions with the low-δ^7Li melts/fluids, we can approximate the duration of Li isotopic equilibration using the algorithmic method of Kaliwoda (2008). For a 3mm Ol grain (common grain size in Allègre xenoliths), ~60 years are needed to fully equilibrate with an ambient melt (diffusion

664 coefficient from Dohmen et al., 2010). Compared with our time constraints based on trace
665 element equilibration (2000 years at 1100℃), the large discrepancy implies that the event
666 responsible for lowering the Li isotopic compositions of Ol cores is likely not
667 contemporaneous with the event that modified the trace element compositions in Cpx. This
668 agrees with the observation that the most strongly metasomatized sample (AL56 according to
669 Cpx trace element compositions) does not have the lowest δ^7Li values in its Ol cores. The Li
670 isotopic variation in Ol cores should have been imparted between the mantle metasomatism,
671 characterized by LREE enrichment and negative HFSE anomalies, and the host
672 magma-xenolith interaction (Fig. 15).
673

674 ## Conclusion

675 We have shown that rigorous in-situ analysis of Li concentrations and isotopic
676 compositions can distinguish individual metasomatic processes occurring over different
677 timescales, based on the phenomenon that Cpx and Ol retain signatures of different events as
678 a function of the diffusivity of Li in those phases.
679 Major element compositions of minerals reveal that Allègre peridotite xenoliths originated
680 as residue after partial melting of the mantle and extraction of basaltic components. The
681 xenoliths fall in the compositional field proposed by Lenoir et al. (2000) and Downes et al.
682 (2003) for the southern domain, despite their long residence time in a lava lake and
683 infiltration of the host magma into some xenoliths.
684 The peridotite xenoliths studied here suffered a multi-stage metasomatic process, including
685 interaction with the host-magma (Fig. 15). The trace element compositions of Cpx,

686 normalized to the primitive mantle, are characterized by high LREE/HREE ratios and
687 significant negative HFSE anomalies resulting from melt percolation into a porous peridotite
688 matrix. This observation enriches the previous knowledge of the lithospheric mantle beneath
689 the FMC. The negative HFSE anomalies have been proposed to be mainly present in the
690 northern mantle domain (Lenoir et al., 2000; Wittig et al., 2007).

691 The extremely high Li concentrations in Cpx (compared with the normal mantle), as well
692 as the increased Li concentrations in Ol rims, are a consequence of late-stage Li diffusion
693 from interstitial melts derived from the host magma, whereas Li contents in Ol cores are as
694 high as, or slightly higher than, those of the normal mantle. Due to Li incorporation from the
695 host magma, and the higher diffusivity of Li in Cpx compared to Ol, the imprints of mantle
696 metasomatism prior to entrainment were erased in some Cpx grains, which exhibit Li isotopic
697 compositions in equilibrium with the host magma (up to 6‰). Most Ol cores in this study
698 have negative δ^7Li values (as low as -25‰). We invoke Li uptake from a low δ^7Li source,
699 probably later than the mantle metasomatism characterized by LREE enrichment and negative
700 HFSE anomalies, to explain the negative Li isotopic compositions of the peridotitic Ol
701 studied herein. This metasomatic agent of low δ^7Li values is originally related to the recycled
702 oceanic crust, which is capable of carrying components with negative δ^7Li values to the deep
703 mantle during subduction. The metasomatic events, accounting for trace element variations in
704 Cpx and negative Li isotopic compositions preserved in Allègre Ol cores, occurred in
705 different periods.

706

707 **Acknowledgements**

This research was supported by the INSU SYSTER program and the State Scholarship Fund of China. We thank Olivier ROUER for access to EMP analysis, Marie-Christine BOIRON and Chantal PEIFFERT for help in analyzing trace elements using LA-ICPMS. GU X.Y. also appreciates Marc CHAUSSIDON, Andrey GURENKO for direction in using SIMS at CRPG. Special gratitude is expressed to Nordine BOUDEN for assistance in guaranteeing the operation of IMS 1270 when GU X.Y. used it. We are grateful to Christiane WAGNER and Michel GRÉGOIRE for discussions. Pei LI have also helped GU X.Y. a lot understand the Li isotope results and improve the Li diffusion modeling.

References

Abdelfadil, K. M., Romer, R. L., Glodny, J., 2014. Mantle wedge metasomatism revealed by Li isotopes in orogenic lamprophyres. *Lithos*, *196*, 14-26.

Ackerman, L., ŠpaČek, P., Magna, T., Ulrych, J., Svojtka, M., Hegner, E., Balogh, K., 2013. Alkaline and carbonate-rich melt metasomatism and melting of subcontinental lithospheric mantle: evidence from mantle xenoliths, NE Bavaria, Bohemian Massif. *Journal of Petrology*, egt059.

Adam J., Green, T., 2001. Experimentally determined partition coefficients for minor and trace elements in peridotite minerals and carbonatitic melt, and their relevance to natural carbonatites. *European Journal of Mineralogy*, *13*(5), 815-827.

Agostini, S., Ryan, J. G., Tonarini, S., Innocenti, F., 2008. Drying and dying of a subducted slab: coupled Li and B isotope variations in Western Anatolia Cenozoic Volcanism. *Earth and Planetary Science Letters*, *272*(1), 139-147.

Arai, S., 1994. Characterization of spinel peridotites by olivine-spinel compositional relationships: review and interpretation. *Chemical geology*, *113*(3), 191-204.

Aulbach, S., Rudnick, R. L., 2009. Origins of non-equilibrium lithium isotopic fractionation in xenolithic peridotite minerals: examples from Tanzania. *Chemical Geology*, *258*(1), 17-27.

Bell, D. R., Hervig, R. L., Buseck, P. R., Aulbach, S., 2009. Lithium isotope analysis of olivine by SIMS: Calibration of a matrix effect and application to magmatic phenocrysts. *Chemical Geology*, *258*(1), 5-16.

Blundy, J., Dalton, J., 2000. Experimental comparison of trace element partitioning between clinopyroxene and melt in carbonate and silicate systems, and implications for mantle metasomatism. *Contributions to Mineralogy and Petrology*, *139*(3), 356-371.

Bodinier, J. L., Vasseur, G., Vernieres, J., Dupuy, C., Fabries, J., 1990. Mechanisms of mantle metasomatism: geochemical evidence from the Lherz orogenic peridotite. *Journal of Petrology*, *31*(3), 597-628.

Brenan, J. M., Ryerson, F. J., Shaw, H. F., 1998. The role of aqueous fluids in the slab-to-mantle transfer of boron, beryllium, and lithium during subduction: experiments and models. *Geochimica et Cosmochimica Acta*, *62*(19), 3337-3347.

Brey, G. P., Köhler, T., 1990. Geothermobarometry in four-phase lherzolites II. New thermobarometers, and practical assessment of existing thermobarometers. *Journal of Petrology*, *31*(6), 1353-1378.

Carpenter, R. L., Edgar, A. D., Thibault, Y., 2002. Origin of spongy textures in clinopyroxene and spinel from mantle xenoliths, Hessian Depression, Germany. *Mineralogy and Petrology*, *74*(2-4), 149-162.

Chan, L. H., Edmond, J. M., Thompson, G., Gillis, K., 1992. Lithium isotopic composition of submarine basalts: implications for the lithium cycle in the oceans. *Earth and Planetary Science Letters*, *108*(1), 151-160.

Chan, L. H., Leeman, W. P., Plank, T., 2006. Lithium isotopic composition of marine sediments. *Geochemistry, Geophysics, Geosystems*, *7*(6).

Coltorti, M., Bonadiman, C., Hinton, R. W., Siena, F., Upton, B. G. J., 1999. Carbonatite metasomatism of the oceanic upper mantle: evidence from clinopyroxenes and glasses in ultramafic xenoliths of Grande Comore, Indian Ocean. *Journal of Petrology*, *40*(1), 133-165.

Coogan, L. A., Kasemann, S. A., Chakraborty, S., 2005. Rates of hydrothermal cooling of new oceanic upper crust derived from lithium-geospeedometry. *Earth and Planetary Science Letters*, *240*(2), 415-424.

Decitre, S., Deloule, E., Reisberg, L., James, R., Agrinier, P., Mével, C., 2002. Behavior of Li and its isotopes during serpentinization of oceanic peridotites. *Geochemistry, Geophysics, Geosystems*, *3*(1), 1-20.

Deloule, E., Albarede, F., Sheppard, S. M., 1991. Hydrogen isotope heterogeneities in the mantle from ion probe analysis of amphiboles from ultramafic rocks. *Earth and Planetary Science Letters*, *105*(4), 543-553.

Deloule, E., Chaussidon, M., Allé, P., 1992. Instrumental limitations for isotope measurements with a Caméca®

761 ims-3f ion microprobe: Example of H, B, S and Sr. *Chemical Geology: Isotope Geoscience section*, *101*(1),
762 187-192.
763 Denis, C. M., Alard, O., Demouchy, S., 2015. Water content and hydrogen behaviour during metasomatism in
764 the uppermost mantle beneath Ray Pic volcano (Massif Central, France). *Lithos*, *236*, 256-274.
765 Dohmen, R., Kasemann, S. A., Coogan, L., Chakraborty, S., 2010. Diffusion of Li in olivine. Part I:
766 experimental observations and a multi species diffusion model. *Geochimica et Cosmochimica Acta*, *74*(1),
767 274-292.
768 Downes, H., Dupuy, C., 1987. Textural, isotopic and REE variations in spinel peridotite xenoliths, Massif
769 Central, France. *Earth and Planetary Science Letters*, *82*(1), 121-135.
770 Downes, H., Reichow, M. K., Mason, P. R. D., Beard, A. D., Thirlwall, M. F., 2003. Mantle domains in the
771 lithosphere beneath the French Massif Central: trace element and isotopic evidence from mantle clinopyroxenes.
772 *Chemical Geology*, *200*(1), 71-87.
773 Elliott, T., Jeffcoate, A., Bouman, C., 2004. The terrestrial Li isotope cycle: light-weight constraints on mantle
774 convection. *Earth and Planetary Science Letters*, *220*(3), 231-245.
775 Elliott, T., Thomas, A., Jeffcoate, A., Niu, Y., 2006. Lithium isotope evidence for subduction-enriched mantle in
776 the source of mid-ocean-ridge basalts. *Nature*, *443*(7111), 565-568.
777 Faure, M., Lardeaux, J. M., Ledru, P., 2009. A review of the pre-Permian geology of the Variscan French Massif
778 Central. *Comptes Rendus Geoscience*, *341*(2), 202-213.
779 Fichtner, A., Villaseñor, A., 2015. Crust and upper mantle of the western Mediterranean–Constraints from
780 full-waveform inversion. *Earth and Planetary Science Letters*, *428*, 52-62.
781 Fitzsimons, I. C. W., Harte, B., Clark, R. M., 2000. SIMS stable isotope measurement: counting statistics and
782 analytical precision. *Mineralogical Magazine*, *64*(1), 59-83.
783 Flesch, G. D., Anderson, A. R., Svec, H. J., 1973. A secondary isotopic standard for 6 Li/7 Li determinations.
784 *International Journal of Mass Spectrometry and Ion Physics*, *12*(3), 265-272.
785 Gallagher, K., Elliott, T., 2009. Fractionation of lithium isotopes in magmatic systems as a natural consequence
786 of cooling. *Earth and Planetary Science Letters*, *278*(3), 286-296.
787 Goes, S., Spakman, W., Bijwaard, H., 1999. A lower mantle source for central European volcanism. *Science*,
788 *286*(5446), 1928-1931.
789 Granet, M., Wilson, M., Achauer, U., 1995. Imaging a mantle plume beneath the French Massif Central. *Earth*
790 *and Planetary Science Letters*, *136*(3), 281-296.
791 Halama, R., McDonough, W. F., Rudnick, R. L., Bell, K., 2008. Tracking the lithium isotopic evolution of the
792 mantle using carbonatites. *Earth and Planetary Science Letters*, *265*(3), 726-742.
793 Hart, S. R., Dunn, T., 1993. Experimental cpx/melt partitioning of 24 trace elements. *Contributions to*
794 *Mineralogy and Petrology*, *113*(1), 1-8.
795 Hellebrand, E., Snow, J. E., Dick, H. J., Hofmann, A. W., 2001. Coupled major and trace elements as indicators
796 of the extent of melting in mid-ocean-ridge peridotites. *Nature*, *410*(6829), 677-681.
797 Herzberg, C., 2004. Geodynamic information in peridotite petrology. *Journal of Petrology*, *45*(12), 2507-2530.
798 Ionov, D. A., Dupuy, C., O'Reilly, S. Y., Kopylova, M. G., Genshaft, Y. S., 1993. Carbonated peridotite
799 xenoliths from Spitsbergen: implications for trace element signature of mantle carbonate metasomatism. *Earth*
800 *and Planetary Science Letters*, *119*(3), 283-297.
801 Ionov, D. A., Bodinier, J. L., Mukasa, S. B., Zanetti, A., 2002. Mechanisms and sources of mantle metasomatism:
802 major and trace element compositions of peridotite xenoliths from Spitsbergen in the context of numerical
803 modelling. *Journal of Petrology*, *43*(12), 2219-2259.

Ionov, D. A., Seitz, H. M., 2008. Lithium abundances and isotopic compositions in mantle xenoliths from subduction and intra-plate settings: mantle sources vs. eruption histories. *Earth and Planetary Science Letters*, *266*(3), 316-331.

Jeffcoate, A. B., Elliott, T., Kasemann, S. A., Ionov, D., Cooper, K., Brooker, R., 2007. Li isotope fractionation in peridotites and mafic melts. *Geochimica et Cosmochimica Acta*, *71*(1), 202-218.

Jochum, K. P., Weis, U., Stoll, B., Kuzmin, D., Yang, Q., Raczek, I., Jacob, D., Stracke, A., Birbaum, K., Frick, I. A., Günther, D., Enzweiler, J., 2011. Determination of reference values for NIST SRM 610–617 glasses following ISO guidelines. *Geostandards and Geoanalytical Research*, *35*(4), 397-429.

Johnson, K. T., 1998. Experimental determination of partition coefficients for rare earth and high-field-strength elements between clinopyroxene, garnet, and basaltic melt at high pressures. *Contributions to Mineralogy and Petrology*, *133*(1-2), 60-68.

Juvigne, E. (1992). Studies on the age of 2 volcanic lacustrine craters of Auvergne (France). *COMPTES RENDUS DE L ACADEMIE DES SCIENCES SERIE II*, *314*(4), 401-404.

Kaliwoda, M., Ludwig, T., Altherr, R., 2008. A new SIMS study of Li, Be, B and δ 7 Li in mantle xenoliths from Harrat Uwayrid (Saudi Arabia). *Lithos*, *106*(3), 261-279.

Khedr, M. Z., Arai, S., Python, M., 2013. Petrology and chemistry of basal lherzolites above the metamorphic sole from Wadi Sarami central Oman ophiolite. *Journal of Mineralogical and Petrological Sciences*, *108*(1), 13-24.

Klemme, S., Van der Laan, S. R., Foley, S. F., Günther, D., 1995. Experimentally determined trace and minor element partitioning between clinopyroxene and carbonatite melt under upper mantle conditions. *Earth and Planetary Science Letters*, *133*(3), 439-448.

Köhler, T. P., Brey, G., 1990. Calcium exchange between olivine and clinopyroxene calibrated as a geothermobarometer for natural peridotites from 2 to 60 kb with applications. *Geochimica et Cosmochimica Acta*, *54*(9), 2375-2388.

Lenoir, X., Garrido, C. J., Bodinier, J. L., Dautria, J. M., 2000. Contrasting lithospheric mantle domains beneath the Massif Central (France) revealed by geochemistry of peridotite xenoliths. *Earth and Planetary Science Letters*, *181*(3), 359-375.

Li, P., Xia, Q, K., Deloule, E., 2012. Anomalous lithium isotopic compositions of the Cenozoic lithospheric mantle beneath Penglai, Shandong Province: the ion probe analyses of peridotite xenoliths. *Geological Journal of China Universities*, *18*(1), 62-73.

Lundstrom, C. C., Chaussidon, M., Hsui, A. T., Kelemen, P., Zimmerman, M., 2005. Observations of Li isotopic variations in the Trinity Ophiolite: evidence for isotopic fractionation by diffusion during mantle melting. *Geochimica et Cosmochimica Acta*, *69*(3), 735-751.

Magna, T., Wiechert, U., Halliday, A. N., 2006. New constraints on the lithium isotope compositions of the Moon and terrestrial planets. *Earth and Planetary Science Letters*, *243*(3), 336-353.

Marschall, H. R., von Strandmann, P. A. P., Seitz, H. M., Elliott, T., Niu, Y., 2007. The lithium isotopic composition of orogenic eclogites and deep subducted slabs. *Earth and Planetary Science Letters*, *262*(3), 563-580.

McDonough, W. F., Sun, S. S., 1995. The composition of the Earth. *Chemical geology*, *120*(3), 223-253.

Menzies, M., Hawkesworth, C., 1986. Mantle metasomatism.

Mercier, J. C., Nicolas, A., 1975. Textures and fabrics of upper-mantle peridotites as illustrated by xenoliths from basalts. *Journal of Petrology*, *16*(2), 454-487.

Michon, L., Merle, O., 2001. The evolution of the Massif Central Rift; spatio-temporal distribution of the volcanism. *Bulletin de la Société géologique de France*, *172*(2), 201-211.

Mundl, A., Ntaflos, T., Ackerman, L., Bizimis, M., Bjerg, E. A., Wegner, W., Hauzenberger, C. A., 2015. Geochemical and Os–Hf–Nd–Sr Isotopic Characterization of North Patagonian Mantle Xenoliths: Implications for Extensive Melt Extraction and Percolation Processes. *Journal of Petrology*, egv048.

Nishio, Y., Nakai, S. I., Yamamoto, J., Sumino, H., Matsumoto, T., Prikhod'ko, V. S., Arai, S., 2004. Lithium isotopic systematics of the mantle-derived ultramafic xenoliths: implications for EM1 origin. *Earth and Planetary Science Letters*, *217*(3), 245-261.

Norman, M. D., 1998. Melting and metasomatism in the continental lithosphere: laser ablation ICPMS analysis of minerals in spinel lherzolites from eastern Australia. *Contributions to Mineralogy and Petrology*, *130*(3-4), 240-255.

O'Reilly, S. Y., Griffin, W. L., 2011. Rates of magma ascent: constraints from mantle-derived xenoliths. In *Timescales of Magmatic Processes* (pp. 116-124). John Wiley and Sons, Ltd.

Ottolini, L., Le Fèvre, B., Vannucci, R., 2004. Direct assessment of mantle boron and lithium contents and distribution by SIMS analyses of peridotite minerals. *Earth and Planetary Science Letters*, *228*(1), 19-36.

Ottolini, L., Laporte, D., Raffone, N., Devidal, J. L., Le Fèvre, B., 2009. New experimental determination of Li and B partition coefficients during upper mantle partial melting. *Contributions to Mineralogy and Petrology*, *157*(3), 313-325.

Parkinson, I. J., Hammond, S. J., James, R. H., Rogers, N. W., 2007. High-temperature lithium isotope fractionation: insights from lithium isotope diffusion in magmatic systems. *Earth and Planetary Science Letters*, *257*(3), 609-621.

Richter, F., Watson, B., Chaussidon, M., Mendybaev, R., Ruscitto, D., 2014. Lithium isotope fractionation by diffusion in minerals. Part 1: Pyroxenes. *Geochimica et Cosmochimica Acta*, *126*, 352-370.

Rudnick, R. L., McDonough, W. F., Chappell, B. W., 1993. Carbonatite metasomatism in the northern Tanzanian mantle: petrographic and geochemical characteristics. *Earth and Planetary Science Letters*, *114*(4), 463-475.

Rudnick, R. L., Gao, S., Ling, W. L., Liu, Y. S., McDonough, W. F., 2004. Petrology and geochemistry of spinel peridotite xenoliths from Hannuoba and Qixia, North China craton. *Lithos*, *77*(1), 609-637.

Rudnick, R. L., Tomascak, P. B., Njo, H. B., Gardner, L. R., 2004. Extreme lithium isotopic fractionation during continental weathering revealed in saprolites from South Carolina. *Chemical Geology*, *212*(1), 45-57.

Rudnick, R. L., Ionov, D. A., 2007. Lithium elemental and isotopic disequilibrium in minerals from peridotite xenoliths from far-east Russia: product of recent melt/fluid–rock reaction. *Earth and Planetary Science Letters*, *256*(1), 278-293.

Ryan, J. G., Langmuir, C. H., 1987. The systematics of lithium abundances in young volcanic rocks. *Geochimica et Cosmochimica Acta*, *51*(6), 1727-1741.

Ryu, J. S., Vigier, N., Lee, S. W., Lee, K. S., Chadwick, O. A., 2014. Variation of lithium isotope geochemistry during basalt weathering and secondary mineral transformations in Hawaii. *Geochimica et Cosmochimica Acta*, *145*, 103-115.

Seitz, H. M., Woodland, A. B., 2000. The distribution of lithium in peridotitic and pyroxenitic mantle lithologies—an indicator of magmatic and metasomatic processes. *Chemical Geology*, *166*(1), 47-64.

Seitz, H. M., Brey, G. P., Lahaye, Y., Durali, S., Weyer, S., 2004. Lithium isotopic signatures of peridotite xenoliths and isotopic fractionation at high temperature between olivine and pyroxenes. *Chemical Geology*, *212*(1), 163-177.

Shaw, C. S., Heidelbach, F., Dingwell, D. B., 2006. The origin of reaction textures in mantle peridotite xenoliths from Sal Island, Cape Verde: the case for "metasomatism" by the host lava. *Contributions to Mineralogy and Petrology*, *151*(6), 681-697.

Sneeringer, M., Hart, S. R., Shimizu, N., 1984. Strontium and samarium diffusion in diopside. *Geochimica et Cosmochimica Acta*, *48*(8), 1589-1608.
Su, B. X., Zhang, H. F., Sakyi, P. A., Yang, Y. H., Ying, J. F., Tang, Y. J., Qin, K. ZH., Xiao, Y., Zhao, X. M., Mao, Q., Ma, Y. G., 2011. The origin of spongy texture in minerals of mantle xenoliths from the Western Qinling, central China. *Contributions to Mineralogy and Petrology*, *161*(3), 465-482.
Su, B. X., Zhang, H. F., Deloule, E., Sakyi, P. A., Xiao, Y., Tang, Y. J., Hu, Y., Ying, J. F., Liu, P. P., 2012. Extremely high Li and low δ 7 Li signatures in the lithospheric mantle. *Chemical Geology*, *292*, 149-157.
Su, B. X., Zhang, H. F., Deloule, E., Vigier, N., Hu, Y., Tang, Y. J., Xiao, Y., Sakyi, P. A., 2014. Distinguishing silicate and carbonatite mantle metasomatism by using lithium and its isotopes. *Chemical Geology*, *381*, 67-77.
Su, B. X., Gu, X. Y., Deloule, E., Zhang, H. F., Li, Q. L., Li, X. H., Vigier, N., Tang, Y. J., Tang, G. Q., Liu, Y., Pang, K. N., Brewer, A., Mao, Q., Ma, Y. G., 2015. Potential Orthopyroxene, Clinopyroxene and Olivine Reference Materials for In Situ Lithium Isotope Determination. *Geostandards and Geoanalytical Research*.
Tang, Y. J., Zhang, H. F., Nakamura, E., Moriguti, T., Kobayashi, K., Ying, J. F., 2007. Lithium isotopic systematics of peridotite xenoliths from Hannuoba, North China Craton: implications for melt–rock interaction in the considerably thinned lithospheric mantle. *Geochimica et Cosmochimica Acta*, *71*(17), 4327-4341.
Tang, Y. J., Zhang, H. F., Deloule, E., Su, B. X., Ying, J. F., Santosh, M., Xiao, Y., 2014. Abnormal lithium isotope composition from the ancient lithospheric mantle beneath the North China Craton. *Scientific reports*, *4*.
Teng, F. Z., McDonough, W. F., Rudnick, R. L., Dalpé, C., Tomascak, P. B., Chappell, B. W., Gao, S., 2004. Lithium isotopic composition and concentration of the upper continental crust. *Geochimica et Cosmochimica Acta*, *68*(20), 4167-4178.
Tian, S., Hou, Z., Su, A., Qiu, L., Mo, X., Hou, K., Zhao, Y., Hu, W., Yang, Z., 2015. The anomalous lithium isotopic signature of Himalayan collisional zone carbonatites in western Sichuan, SW China: Enriched mantle source and petrogenesis. *Geochimica et Cosmochimica Acta*, *159*, 42-60.
Tomascak, P. B., Tera, F., Helz, R. T., Walker, R. J., 1999. The absence of lithium isotope fractionation during basalt differentiation: new measurements by multicollector sector ICP-MS. *Geochimica et Cosmochimica Acta*, *63*(6), 907-910.
Tomascak, P. B., 2004. Developments in the understanding and application of lithium isotopes in the earth and planetary sciences. *Reviews in Mineralogy and Geochemistry*, *55*(1), 153-195.
Tomascak, P. B., Langmuir, C. H., le Roux, P. J., Shirey, S. B., 2008. Lithium isotopes in global mid-ocean ridge basalts. *Geochimica et Cosmochimica Acta*, *72*(6), 1626-1637.
Touron, S., Renac, C., O'Reilly, S. Y., Cottin, J. Y., Griffin, W. L., 2008. Characterization of the metasomatic agent in mantle xenoliths from Deves, Massif Central (France) using coupled in situ trace-element and O, Sr and Nd isotopic compositions. *Geological Society, London, Special Publications*, *293*(1), 177-196.
Uenver-Thiele, L., Woodland, A. B., Downes, H., Altherr, R., 2014. Oxidation state of the lithospheric mantle below the Massif Central, France. *Journal of Petrology*, *55*(12), 2457-2480.
Vlastélic, I., Koga, K., Chauvel, C., Jacques, G., Télouk, P., 2009. Survival of lithium isotopic heterogeneities in the mantle supported by HIMU-lavas from Rurutu Island, Austral Chain. *Earth and Planetary Science Letters*, *286*(3), 456-466.
Von Strandmann, P. A. P., Elliott, T., Marschall, H. R., Coath, C., Lai, Y. J., Jeffcoate, A. B., Ionov, D. A., 2011. Variations of Li and Mg isotope ratios in bulk chondrites and mantle xenoliths. *Geochimica et Cosmochimica Acta*, *75*(18), 5247-5268.
Wagner, C., Deloule, E., 2007. Behaviour of Li and its isotopes during metasomatism of French Massif Central lherzolites. *Geochimica et Cosmochimica Acta*, *71*(17), 4279-4296.

Walter, M. J., 2003. Melt extraction and compositional variability in mantle lithosphere. *Treatise on geochemistry*, *2*, 363-394.

Werling, F., Altherr, R., 1997. Thermal evolution of the lithosphere beneath the French Massif Central as deduced from geothermobarometry on mantle xenoliths. *Tectonophysics*, *275*(1), 119-141.

Wilson, M., Downes, H., 1991. Tertiary—Quaternary extension-related alkaline magmatism in western and central Europe. *Journal of Petrology*, *32*(4), 811-849.

Workman, R. K., Hart, S. R., 2005. Major and trace element composition of the depleted MORB mantle (DMM). *Earth and Planetary Science Letters*, *231*(1), 53-72.

Wunder, B., Meixner, A., Romer, R. L., Heinrich, W., 2006. Temperature-dependent isotopic fractionation of lithium between clinopyroxene and high-pressure hydrous fluids. *Contributions to Mineralogy and Petrology*, *151*(1), 112-120.

Xu, Y. G., Menzies, M. A., Bodinier, J. L., Bedini, R. M., Vroon, P., Mercier, J. C., 1998. Melt percolation and reaction atop a plume: evidence from the poikiloblastic peridotite xenoliths from Borée (Massif Central, France). *Contributions to Mineralogy and Petrology*, *132*(1), 65-84.

Yaxley, G. M., Green, D. H., Kamenetsky, V., 1998. Carbonatite metasomatism in the southeastern Australian lithosphere. *Journal of Petrology*, *39*(11-12), 1917-1930.

Yoshikawa, M., Kawamoto, T., Shibata, T., Yamamoto, J., 2010. Geochemical and Sr–Nd isotopic characteristics and pressure–temperature estimates of mantle xenoliths from the French Massif Central: evidence for melting and multiple metasomatism by silicate-rich carbonatite and asthenospheric melts. *Geological Society, London, Special Publications*, *337*(1), 153-175.

Zack, T., Tomascak, P. B., Rudnick, R. L., Dalpé, C., McDonough, W. F., 2003. Extremely light Li in orogenic eclogites: the role of isotope fractionation during dehydration in subducted oceanic crust. *Earth and Planetary Science Letters*, *208*(3), 279-290.

Zanetti, A., Mazzucchelli, M., Rivalenti, G., Vannucci, R., 1999. The Finero phlogopite-peridotite massif: an example of subduction-related metasomatism. *Contributions to Mineralogy and Petrology*, *134*(2-3), 107-122.

Zangana, N. A., Downes, H., Thirlwall, M. F., Hegner, E., 1997. Relationship between deformation, equilibration temperatures, REE and radiogenic isotopes in mantle xenoliths (Ray Pic, Massif Central, France): an example of plume-lithosphere interaction?. *Contributions to Mineralogy and Petrology*, *127*(1-2), 187-203.

964 Fig. 1 Simplified geological map of the French Massif Central (Michon and Merle, 2001; Downes et
965 al., 2003). The sampling locality of Allègre belonging to Dèves (2) is shown by the red circle. The
966 boundary between two domains (the horizontal black line) is also drawn.
967
968 Fig. 2 (a) Instrumental mass fractionation plotted against Mg# of olivine standards. As the R^2 values
969 are much lower than one, there should be no compositional influence on Δ_i. We used the averaged Δ_i
970 of individual standard minerals (pyroxenes in red and Ol in blue) to calculate the δ^7Li values of the
971 corresponding sample minerals. (b) Lithium ion yields ([Li]) plotted against Mg# of Ol standards. No
972 co-variation exists. For calculation, the averages of individual phases are utilized.
973
974 Fig. 3 Modal compositions of samples in this study (AL××) compared with literature data of the
975 southern domain of the FMC (smaller blue symbols). The data of the southern domain are from Lenoir
976 et al. (2000) and Zangana et al. (1997).
977
978 Fig. 4 (a) Protogranular-textured sample AL56 under polarized light. (b) A cluster composed of Cpx,
979 Ol, Opx and Spl in sample AL56 under reflected light. (c) Porphyroclastic-textured sample AL37P1
980 under polarized light. Fined-grained Ol and Cpx are included in an Opx porphyroclast of about 4 mm
981 across. (d) Spinel with spongy-textured rim in sample AL47P1 under reflected light. The zones d2 and
982 d3 have been investigated in detail using the back-scattered electron (BSE) images, shown in e and f,
983 respectively. (e) The BSE image of spongy texture around one spinel grain (d2 in d). (f) The BSE
984 image of a thin spongy-textured zone between a Spl grain and an adjacent Opx grain (d3 in d). Ol
985 olivine; Opx orthopyroxene; Cpx clinopyroxenes; Plag plagioclase; Spl spinel.
986
987 Fig. 5 Co-variation of major element compositions in minerals. In (a-e), circles represent
988 protogranular samples and squares represent porphyroclastic samples. Filled symbols denote
989 harzburgites and empty symbols denote lherzolites. The zone for the subcontinental peridotites (b, in
990 grey color) is delineated according to Arai (1994). OSMA represents the olivine-spinel mantle array.
991 In (f-g), data from this study are plotted with literature data for the northern domain (Downes et al.,
992 2003) and southern domain of the FMC (Xu et al., 1998; Touron et al., 2008; Yoshikawa et al., 2010).
993 The oxide content ranges for the northern domain and the southern domain are from Downes et al.
994 (2003)

Fig. 6 Plots of olivine Mg# versus abundances of La, Sm and Lu in Cpx (a, b and c, respectively) and Cr# of spinel versus abundance of Lu in Cpx (d).

Fig. 7 REE composition patterns normalized to Chondrite (a) and extended trace element composition patterns normalized to the primitive mantle (b). The dashed lines in (b) represent three samples from other localities in the southern domain for comparison with samples from Allegre (ML40 from Touron et al. (2008); BR4 and BU5 from Yoshikawa et al. (2010)). Normalized values are from McDonough and Sun (1995).

Fig. 8 The fractional melting modeling results based on Y and Yb contents in Cpx (symbols as in Fig. 6). According to the model of Norman (1998), the initial contents of these two elements are chosen as the primitive mantle compositions from McDonough and Sun (1995). Experimentally constrained partition coefficients between Cpx and melts by Hart and Dunn (1993) are used in the model (0.467 for Y; 0.43 for Yb). The modal composition of Cpx is assumed to be 20%, similar to Norman (1998). The letter 'n' denotes normalization to primitive mantle compositions (McDonough and Sun, 1995). Cpx of sample AL56 contains enough Y and Yb that it plots outside the modeling zone (not shown here). The number in blue beside each symbol is the result calculated from Cr# of Spl.

Fig. 9 Variation of $(La/Yb)_N$ versus Ti/Eu (a) and Zr^* (b) in Cpx from Allègre. The Ti/Eu ratio of the primitive mantle (McDonough and Sun, 1995) is also shown in black filled square for comparison. Coltorti et al. (1999) suggested the co-relation between $(La/Yb)_N$ and Ti/Eu in Cpx could be regarded as an indictor to distinguish the carbonatite metasomatism(a; the zone surrounded by the blue lines) from the silicate metasomatism.

Fig. 10 The primitive mantle-normalized trace element distribution patterns of the hypothetical silicate and carbonatite melts in equilibrium with Cpx from sample AL56. The partition coefficients of trace elements between carbonatitic melts and Cpx refer to Hart and Dunn (1993) and the partition coefficients of trace elements between silicate melts and Cpx refer to Johnson (1998). The trace element compositions of representative alkaline basalts in the FMC are also shown for comparison (42450 from Wilson and Downes (1991)).

Fig. 11 Li concentration in samples including the minimum and maximum values compared with the Li concentration ranges estimated for the normal mantle (Seitz and Woodland, 2000; Ottolini et al., 2004).

Fig. 12 Li partitioning between Ol and Cpx (a), between Opx and Cpx (b) (symbols as in Fig. 6a). The equilibrated lines are plotted according to the equilibrated partition coefficients from Seitz and Woodland (2000), $D_{Ol/Cpx}$=1.5-2.0 and $D_{Opx/Cpx}$=0.5-1.1. The Li contents of individual mineral phases in the normal upper mantle are delimitated by a small red square. The metasomatic tendency is according to Seitz and Woodland (2000) and Su et al. (2014).

Fig. 13 (a) The Li concentration plotted against Mg# measured at the same position in Ol cores (symbols as in Fig. 6a). Grains from one single sample are represented by the same symbol. The grey field represents the estimated Li concentrations in olivine from the normal mantle. (b) δ^7Li against Li concentrations in the olivine grain cores (symbols as in Fig. 6a). The red square shows the estimated Li concentration and isotopic composition range of the normal mantle.

Fig. 14 Variation of δ^7Li versus Li concentration in Cpx (a) and Ol (b) from Allègre compared with literature data. In each plot, the values concerning the present study include the whole data set of Ol and Cpx. The Li concentration and isotopic composition ranges of the upper mantle are delineated by red and blue lines, respectively. Small blue filled diamonds represent literature data (Aulbach and Rudnick, 2009; Ionov and Seitz, 2008; Magna et al., 2008; Rudnick and Ionov, 2007; Seitz et al., 2004; Su et al., 2014; Tang et al., 2007, 2014; Wagner and Deloule, 2007).

Fig. 15 A schematic diagram modeling the evolution of the lithospheric mantle beneath Allègre.

Supplementary Fig. 1 The Li elemental and isotopic profiles within every analyzed grain. r, rim; c, core.

Supplementary Table 1 Core-to-rim variations of trace element abundances in grains analyzed at both cores and rims.

1058 Supplementary Table 2 The whole data set of the Li concentrations and δ^7Li in this study.
1059

Title: Melt-rock interaction signatures in peridotite from sub-continental mantle (French Massif Central): A trace element, H, Li and δ^7Li approach

Keywords: Sub-continental mantle; French Massif Central; Peridotite xenoliths; Melt-rock interaction; trace elements; Li concentrations; δ^7Li; Water contents

Abstract

Peridotite xenoliths sampled from two volcanoes erupting in different modes in two localities, Allègre and Mont Coupet, in the southern domain of the French Massif Central (FMC), have been investigated to constrain the evolution of the sub-continental lithospheric mantle beneath the FMC and the behaviors of Li and H during melt-rock reactions.

Negative HFSE anomalies and markedly high LREE/HREE ratios reflect a carbonatite-related metasomatism following an earlier partial melting process in the lithospheric mantle under Allègre. The Ti and Nb negative anomalies in Cpx from all the Mont Coupet samples and Zr-Hf negative anomalies in Cpx from two most strongly metasomatized samples MC38 and MC34 also point to a carbonatite-related mantle metasomatism. Amp in samples MC36 and MC53, whose origin should be associated with fluids from the subducting slab, have equilibrated most of the trace element composition with coexisting Cpx and the modal metasomatism responsible for the Amp genesis haven't refertilized Cpx in LREE and LILE.

Lithium isotope systematics indicates that Allègre xenoliths were overprinted by (at least) a two-stage metasomatism by melts of different origins. Exceptionally high Li concentrations in Cpx (up to 50 ppm by weight) and slightly increased Li contents at Ol rims are ascribed to a diffusive Li uptake from infiltrating melts derived from the host magma. On the other hand, extremely light Li isotopic compositions preserved in Ol cores (with δ^7Li as low as -25‰) suggest another metasomatic event prior to xenolith entrainment by the host magma. In contrast, xenoliths from Mont Coupet have Li concentrations in constituent minerals similar to the normal mantle, and display nearly equilibrated inter-mineral Li partitioning and homogeneous intragranular Li distribution in every phase. The negative δ^7Li values of Cpx and Opx in some samples were brought by the exchange with a small-volume melt with Li concentration similar to the normal mantle and light Li isotopic compositions. The preservation of inter-mineral large Li isotopic fractionation currently observed in these samples indicates that the percolation of the melt should occur shortly prior to the entrainment of Mont Coupet peridotite xenoliths by the host magmas. The metasomatic agents, accounting for negative δ^7Li values in Ol cores in Allègre xenoliths and in Cpx and Opx in some Mont Coupet xenoliths, are related to a subduction environment. In the regional framework of the FMC, the subduction event most likely occurred during the Variscan orogeny.

Water content in Allègre xenoliths ranges from 10.6 to 12.4 ppm in weight, much lower than the water content in the MORB source mantle. It implies that water were lost during the degassing of the host magma during slow cooling of the lava lake. No core-rim variations from profile analysis suggest that xenoliths have achieved water diffusive equilibrium with the host magmas. Peridotite xenoliths from Mont Coupet have retained their original water content from the mantle depths. Partial melting has controlled the water content in most samples from Mont Coupet. However, the subsequent carbonatite-related metasomatism has affected the sample MC34, which had the highest water content among the Mont Coupet xenoliths. And the aqueous agent responsible for presence of Amp in samples MC36 and MC53 has not lead to the considerable increase of water content.

Titre : Signatures des interactions fluide-roche dans le manteau souscontinental (Massif Central Français): Une approche H, Li, δ^7Li, et éléments trace

Mots clés: Le manteau sous-continental ;Massif Central Français ;Les xénolites de péridotite ; Interactions fluide-roche ;Éléments trace ;Les teneurs en Li ;δ^7Li ;Les teneurs en eau

Résumé

Des xénolites de péridotite provenant de deux localités du sud du Massif Central Français (Allègre et Mont Coupet), émis avec des modes éruptifs différents, ont été étudiés pour définir l'évolution du manteau sous continentale et pour étudier le comportement de Li et H lors des réactions fluides roches lors de leur remonté vers la surface.

Pour les xénolites d'Allègre, les anomalies négatives en HFSE et les rapports LREE/HREE élevés reflètent un métasomatisme lié à des liquides carbonatitiques, succédant à un processus de fusion partielle du manteau lithosphérique. Pour les échantillons du Mont Coupet, Les anomalies négatives en Ti et Nb des Cpx de tous les échantillons et les anomalies négatives de Zr et Hf pour deux échantillons plus fortement métasomatisés (MC38 et MC34) soulignent également un métasomatisme carbonatitique. Les amphiboles des échantillons MC36 et MC53, dont l'origine doit être associée à des fluides de subduction, sont à l'équilibre avec les Cpx coexistant, ce qui indique que le fluide qui a permis leur formation n'a pas enrichi les Cpx en LREE ou LILE.

La composition isotopique de des xénolites d'Allègre montre qu'ils ont été affectés par un métasomatisme en au moins deux étapes par des fluides différents. Les teneurs très élevées en Li des Cpx (jusqu'à 50 ppm) et l'enrichissement même modéré des bordures des olivines sont attribués à un apport de Li par diffusion depuis le magma hôte. Par contre, les compositions isotopiques pauvres en ^{7}Li préservées au coeur des Ol (δ^7Li jusqu'à -25‰) suggèrent l'existence d'un autre évènement métasomatique ayant affecté les péridotites avant leur remonté vers la surface. En revanche, les minéraux des xénolites de Mont Coupet ont des concentrations en Li similaires à celles du manteau, avec une répartition à l'équilibre entre les minéraux. Cependant les valeurs de δ^7Li négatives observées pour les Cpx et Opx de certains échantillons suggèrent une interaction avec un fluide en quantité limitée et une composition isotopique négative. La préservation du fractionnement isotopique du Li entre les pyroxènes et olivines indique que cette interaction a du avoir lieu peu de temps avant l'entrainement des xénolites vers la surface. Les fluides métasomatiques à l'origine des valeurs de δ^7Li négatives observées à Allègre et à Mont Coupet sont liés à un environnement de subduction, probablement lié à l'orogenèse varisque dans le cadre régional du FMC.

Les teneurs en eau mesurées dans les xénolites d'Allègre vont de 10,6 à 12,4 ppm, des valeurs beaucoup plus faible que celle du manteau source des MORB. Ceci s'explique par une perte d'eau associée au dégazage du magma lors du refroidissement du lac de lave. L'absence de variation cœur-bord montre une distribution de l'eau à l'équilibre entre les xénolites et la lave hôte. A l'inverse, les xénolites du Mont Coupet ont pu conservé leur teneur en eau acquise en profondeur, contrôlée par les processus de fusion partielle qui ont affecté les péridotites. Cependant, l'échantillon MC34, affecté par le métasomatisme carbonatitique, a la plus haute teneur en eau parmi ces xénolites. Inversement, les échantillons MC36 et MC53 qui contiennent des amphiboles, n'ont pas des teneurs en eau élevées, suggérant que l'agent métasomatique responsable de la formation des amphiboles n'a pas enrichi en eau les autres phases de la péridotite.